



HAL
open science

Search for Higgs bosons and for Supersymmetric particles at particle collider experiments

Steve Muanza

► **To cite this version:**

Steve Muanza. Search for Higgs bosons and for Supersymmetric particles at particle collider experiments. High Energy Physics - Experiment [hep-ex]. Aix-Marseille Université, 2015. tel-01220656v2

HAL Id: tel-01220656

<https://hal.science/tel-01220656v2>

Submitted on 12 Nov 2015

HAL is a multi-disciplinary open access archive for the deposit and dissemination of scientific research documents, whether they are published or not. The documents may come from teaching and research institutions in France or abroad, or from public or private research centers.

L'archive ouverte pluridisciplinaire **HAL**, est destinée au dépôt et à la diffusion de documents scientifiques de niveau recherche, publiés ou non, émanant des établissements d'enseignement et de recherche français ou étrangers, des laboratoires publics ou privés.



Distributed under a Creative Commons Attribution - NonCommercial - NoDerivatives 4.0 International License

AIX-MARSEILLE UNIVERSITE

UFR de Physique

pour l'obtention du diplôme

d'Habilitation à Diriger des Recherches

d'Aix-Marseille Université
Spécialité : Physique des Particules

présentée par

Guy Steve Muanza

**Recherche de Bosons de Higgs et de Particules
Supersymétriques avec des Détecteurs situés
auprès de Collisionneurs de Particules**

Soutenue publiquement le 9 octobre 2015 devant le jury composé par :

Dr. E. Kajfasz	CPPM, Marseille	(Président du Jury)
Pr. M. Talby	Aix-Marseille Université, Marseille	(Examinateur)
Pr. J.R. Ellis	King's College, London	(Examinateur)
Dr. D. Denisov	FNAL, Batavia	(Rapporteur)
Dr. D. Froidevaux	CERN, Geneva	(Rapporteur)
Dr. Marta Felcini	University College, Dublin	(Rapporteur)

Acknowledgements

Je voudrais remercier M. Eric Kajfasz, Directeur du CPPM Marseille, qui m'a beaucoup encouragé, avec confiance et bienveillance, à passer cette habilitation. Je le remercie d'en avoir présidé le jury.

Je remercie M. Mossadek Talby d'avoir été mon tuteur pour cette habilitation. Je le remercie pour ses encouragements et ses décryptages des procédures universitaires.

Je sais gré à mes rapporteurs d'avoir lu et commenté mon document cet été. Je remercie M. Daniel Froidevaux, qui était déjà rapporteur dans mon jury de thèse, pour avoir accepté de ré-itérer cet exercice. Je regrette qu'il n'ait pu assister à la soutenance... mais je lui réserve sa bouteille de champagne¹. Je remercie Mme Marta Felcini d'avoir accepté de se replonger dans la physique "propre" du LEP où nous courrions après un boson de Higgs encore un peu trop évasif... malgré les mirages. I warmly thank Mr Dmitri Denisov to have traveled from Chicago for my defense. It has been a pleasure and a great experience for me to work in the D0 collaboration, and even more so under his cheerful leadership.

And, last but not least, je suis très reconnaissant envers John Ellis d'avoir apporté l'éclairage critique d'une encyclopédie vivante de la phénoménologie de la physique des particules sur mes travaux d'habilitation, après l'avoir fait pour ma thèse. L'Ecole Africaine de Physique que nous co-organisons est un projet très enrichissant dans lequel j'ai régulièrement le plaisir de le retrouver.

Je dédie ce travail à ma famille: à mon épouse pour son soutien et sa patience, à mes enfants pour leur curiosité et leur enthousiasme. Je remercie chaleureusement mes parents à qui je dois l'essentiel de ce que je suis. Je remercie mes frères et soeurs pour leur confiance et leur soutien. Je remercie enfin mes amis et mes collègues, au CPPM et au-delà, amateurs de physique, de jazz, de bons vins, d'énormes grillades ou de débats,..., chacun se reconnaîtra.

¹objet fort intéressant dont le fond ressemble au potentiel de Higgs, dont l'ensemble constitue une chambre à bulles et dont le breuvage altère toutes nos mesures!

Contents

Acknowledgements	i
Contents	ii
1 Introduction	1
1.1 Quick Overview of the History of Particle Physics	1
2 Theoretical Framework	2
2.1 Standard Model	2
2.1.1 Lagrangian Formalism	2
2.1.2 Anatomy	4
2.1.2.1 External and Internal Symmetries	4
2.1.2.2 Particle Content	5
2.1.2.2.a Fermion Sector	5
2.1.2.2.b Gauge Sector	6
2.1.2.2.c Higgs Sector	7
2.1.3 Lagrangian Density	8
2.1.4 Electroweak Symmetry Breaking	8
2.1.5 Experimental Tests of the Standard Model	11
2.1.6 Standard Model Limitations	13
2.2 Supersymmetric Extension of the Standard Model	14
2.2.1 Introduction to Supersymmetry	14
2.2.1.1 Definition	14
2.2.1.2 Super-Poincaré Algebra	15
2.2.1.2.a Chiral Supermultiplet	16
2.2.1.2.b Vector Supermultiplet	17
2.2.2 Supersymmetric Quantum Field Theory	18
2.2.2.0.c Wess-Zumino Model	18
2.2.2.0.d Chiral supermultiplet interactions	18
2.2.2.0.e Vector supermultiplet interactions	19
2.2.3 The Minimal Supersymmetric Standard Model	19
2.2.3.1 Global SUSY Sector	20
2.2.3.2 Soft SUSY Breaking Sector	21
2.2.3.3 Electroweak Symmetry Breaking in the MSSM	22
2.2.3.3.a Scalar Potential	22
2.2.3.3.b The Higgs bosons in the MSSM	23
2.2.3.4 The Scalar Fermions Sector in the MSSM	25
2.2.3.5 The Gaugino Sector in the MSSM	25
2.2.4 The Assests of Supersymmetry	26

3	Search for Higgs Bosons at LEP	29
3.1	Instrumental Aspects	29
3.1.1	LEP	29
3.1.2	L3 Detector	30
3.1.2.1	Silicon Microvertex Detector	31
3.1.2.2	Central Tracking Chambers	31
3.1.2.3	Electromagnetic Calorimeter	32
3.1.2.4	Scintillators	32
3.1.2.5	Hadron Calorimeter	33
3.1.2.6	Muon Detector	33
3.1.2.7	Luminosity Monitor	34
3.1.2.8	Trigger System	34
3.2	Phenomenology of the Higgs Boson at LEP	34
3.2.1	Production Mechanisms	34
3.2.2	Decay Modes	34
3.2.3	Search for the Standard Model Higgs Boson	36
3.2.3.1	Introduction	36
3.2.3.2	Data and Monte Carlo samples	37
3.2.3.3	Analysis procedures	37
3.2.3.3.a	The $Hq\bar{q}$ analysis	38
3.2.3.3.b	The $H\nu\bar{\nu}$ analysis	40
3.2.3.3.c	The $H\ell^+\ell^-$ and $\tau^+\tau^-q\bar{q}$ analyses	41
3.2.3.4	Results	41
3.2.4	Search for a Higgs Boson Decaying Invisibly	51
3.2.4.1	Introduction	51
3.2.4.2	Event simulation	51
3.2.4.3	Search in the hadronic channel	52
3.2.4.3.a	Preselection	52
3.2.4.3.b	Heavy Higgs boson selection	52
3.2.4.3.c	Light Higgs boson selection	53
3.2.4.4	Search in the leptonic channels	53
3.2.4.5	Systematic uncertainties	55
3.2.4.6	Results	55
4	Search for Gluinos at TEVATRON	62
4.1	General Considerations about Hadron Collisions	62
4.2	Instrumental Aspects	62
4.2.1	TEVATRON	62
4.2.2	D0 Detector	63
4.2.3	Search for Gluino Pairs at the TEVATRON Run 2	65
4.2.3.1	Introduction	66
4.2.3.2	Data and Monte Carlo Samples	66
4.2.3.2.a	Data Samples	66
4.2.3.2.b	Monte Carlo Samples	68
4.2.3.3	Data and Monte Carlo Samples Treatment	77
4.2.3.3.a	Samples Fixing	77
4.2.3.3.b	Data Quality	77
4.2.3.3.c	Data Skimming	78
4.2.3.3.d	Jet Energy Scale	78
4.2.3.3.e	Missing Transverse Energy	78
4.2.3.3.f	Bad Jets	78
4.2.3.3.g	Reweighting of the Number of Primary Vertices	78
4.2.3.3.h	Tracks Based Confirmation of the Jets	79

4.2.3.3.i	B-Tagging	82
4.2.3.4	Event Selection	84
4.2.3.5	Analysis Strategy	84
4.2.3.6	Trigger Conditions	85
4.2.3.7	Trigger Efficiencies	86
4.2.3.8	Event preselection in the $2b - jets + \cancel{E}_T$ topology	86
4.2.3.9	Event preselection in the $4b - jets + \cancel{E}_T$ topology	87
4.2.3.10	Estimation of the QCD Background	87
4.2.3.11	Suppression of the QCD Background	89
4.2.3.12	Rejection of Isolated Leptons	91
4.2.3.13	Optimization of the Final Selection	93
4.2.3.14	Analysis Interpretation	96
4.2.3.15	Conclusions	97
4.2.3.16	Appendix: Verifications of the physics background	100
4.2.3.16.a	Verifications prior to the b-tagging	100
4.2.3.16.b	Verifications including to the b-tagging	105
4.2.3.17	Acknowledgments	105
5	Search for Electroweakinos at LHC	107
5.1	Instrumental Aspects	107
5.1.1	LHC	107
5.1.2	ATLAS Detector	108
5.1.3	Using a Higgs Boson to Search for SUSY	110
5.1.3.1	Introduction	111
5.1.3.2	Monte Carlo simulation	112
5.1.3.3	Event reconstruction	113
5.1.3.4	One lepton and two b -jets channel	115
5.1.3.4.a	Event selection	115
5.1.3.4.b	Background estimation	116
5.1.3.5	One lepton and two photons channel	118
5.1.3.5.a	Event Selection	118
5.1.3.5.b	Background estimation	120
5.1.3.6	Same-sign dilepton channel	122
5.1.3.6.a	Event Selection	122
5.1.3.6.b	Background estimation	123
5.1.3.7	Systematic uncertainties	126
5.1.3.8	Results and interpretations	127
5.1.3.9	Conclusions	130
5.1.4	New Method to Measure the Mass of a Chargino-Neutralino Pair	131
5.1.4.1	Introduction	131
5.1.4.2	Inclusive Production of $W^\pm \rightarrow \ell^\pm \nu$	135
5.1.4.2.a	Theoretical Prediction of $A_C(W^\pm \rightarrow \ell^\pm \nu)$	135
5.1.4.2.b	Experimental Measurement of $A_C(W^\pm \rightarrow \ell^\pm \nu)$	140
5.1.4.2.c	Indirect Determination of M_{W^\pm}	153
5.1.4.2.d	Final Result for MRST2007lomod	153
5.1.4.2.e	Final Results for the Other Parton Density Functions	154
5.1.4.2.f	Summary of the M_{W^\pm} Measurements and their Accuracy	157
5.1.4.3	Inclusive Production of $\tilde{\chi}_1^\pm + \tilde{\chi}_2^0 \rightarrow 3\ell^\pm + \cancel{E}_T$	159
5.1.4.3.a	Theoretical Prediction of $A_C(\tilde{\chi}_1^\pm + \tilde{\chi}_2^0)$	159
5.1.4.3.b	Experimental Measurement of $A_C(\tilde{\chi}_1^\pm + \tilde{\chi}_2^0 \rightarrow 3\ell^\pm + \cancel{E}_T)$	168
5.1.4.3.c	Indirect Determination of $M(\tilde{\chi}_1^\pm) + M(\tilde{\chi}_2^0)$	173
5.1.4.3.d	Final Result for MRST2007lomod	179

5.1.4.3.e	Summary of the $M(\tilde{\chi}_1^\pm) + M(\tilde{\chi}_2^0)$ Measurements and their Accuracy	180
5.1.4.4	Conclusions	182
5.1.4.5	Prospects	184
5.1.4.6	Appendix: Toy Models for the Evolution of A_C	186
5.1.4.6.a	Numerical Example of Evolution of the PDFs, the Quark Currents and A_C	186
5.1.4.6.b	Toy Models for the Main Properties of A_C^{Fit}	186
5.1.4.6.c	Polynomials of $Log(x)$	189
5.1.4.6.d	Polynomials of $Log(Log(x))$	189
5.1.4.6.e	Laguerre Polynomials $L_n(x)$	190
A	Rapport Détaillé sur l'Activité Post-Doctorale	191
A.1	Formation Doctorale	191
A.2	Recherches Post-Doctorales	191
A.2.1	Entrée au CNRS	191
A.2.2	Expérience CMS au LHC du CERN	191
A.2.3	Expérience L3 au LEP du CERN	192
A.2.3.1	Désintégrations Invisibles du boson de Higgs	192
A.2.3.2	Désintégrations du boson de Higgs en quarks b	192
A.2.4	Expérience D0 au TEVATRON du FNAL	193
A.2.4.1	L'étalonnage hors-ligne des objets calorimétriques	193
A.2.4.2	Les outils de prédictions théoriques	194
A.2.4.3	La recherche de la Supersymétrie	195
A.2.5	Expérience ATLAS au LHC du CERN	197
A.2.5.1	ATLAS Authorship Project	198
A.2.5.1.a	Validation of Tauola++	198
A.2.5.1.b	Setup for CKKW-L matching	198
A.2.5.1.c	Validation of Photos++	199
A.2.6	Groupements de Recherche sur la Physique Au-Delà du Modèle Standard	199
A.2.6.1	GDR 501 sur la Supersymétrie	199
A.2.6.2	EuroGDR 2305 sur la Supersymétrie	200
A.2.6.3	GDR 2305 sur la Supersymétrie	200
A.2.6.4	GDR 3262 Terascale	200
A.2.6.5	Prolongement du GDR 3262 Terascale	200
A.3	Encadrement	200
A.3.1	Stages de M1	200
A.3.2	Stages de M2	201
A.3.3	Thèses	201
A.3.4	Jurys	202
A.4	Enseignement	202
A.5	Séminaires, Ateliers et Conférences	203
A.5.0.1	Séminaires	203
A.5.0.2	Ateliers	204
A.5.0.3	Conférences	205
A.6	Administration de la Recherche	206
A.7	Vulgarisation de la Recherche	207
	Bibliography	208

Chapter 1

Introduction

1.1 Quick Overview of the History of Particle Physics

The first elementary particle, the electron e^- , was discovered more than a century ago in 1897 by J.J. Thomson. During the first half of the 20th century other particles were discovered, some now considered as elementary, the photon γ (its name was proposed by G.N. Lewis in 1926 after its theoretical foundations had been set by A. Einstein in 1905), the positron e^+ in 1932 by C.N. Anderson, the muon μ^- by C.N. Anderson and S. Neddermeyer in 1936. And a few non elementary, such as the proton p by E. Rutherford in 1919, the neutron n in 1932 by J. Chadwick, and the first mesons in cosmic rays in 1947. Thereby, C.F. Powell, C. Lattes and G. Occhialini discovered the charged pion π^\pm , and G.D. Rochester and C.C. Butler discovered the kaons K^0 and K^\pm .

During these few decades, the theoretical framework of atomic and subatomic physics also developed. What are now known as the key concepts started with quantum physics initiated by M. Planck in 1900 and with special relativity introduced by A. Einstein in 1905. Quantum physics turned to be crucial to cope with physical systems whose action \mathcal{S} are much larger than the Planck constant h . Whereas special relativity enabled to properly describe physical systems for which the velocity v cannot be neglected with respect to speed of light in the vacuum c . These two fundamental breakthroughs, which are the two pillars of modern fundamental physics, were followed by tremendous developments, first separate, then combined within relativistic quantum field theories.

However particle physics as a discipline rather started in the 1950's with a rapid extension of the particles zoo owed to the significant progresses of particles acceleration and detection techniques and the further theoretical developments aimed at classifying the particles and at explaining their fundamental interactions.

Chapter 2

Theoretical Framework

2.1 Standard Model

2.1.1 Lagrangian Formalism

In particle physics the theory relies on relativistic quantum field theories which generally use a lagrangian formalism analogous to that of classical mechanics.

In the latter, the classical lagrangian is defined as the difference between the kinetic and the potential energies:

$$L = T - V \tag{2.1}$$

Here the physical system is described within a 3 dimensional (3-D) euclidian space and consists in a series of N mass points (of mass m_i). Associated to these mass points are:

- a set of "generalized coordinates": $\mathbf{q}_i(t)$, with $i = 1, \dots, N$
- a set of "generalized momenta": $\mathbf{p}_i(t) = \frac{\partial L}{\partial \dot{q}_i}$ (where the upper dot represents the time derivative)

The system kinetic energy is given by

$$T = \frac{1}{2} \sum_{i=1}^N m_i \dot{q}_i^2 \tag{2.2}$$

and one can define an action

$$\mathcal{S} = \int_{t_1}^{t_2} L dt \tag{2.3}$$

which is a functional of the system path. According to the Hamilton's variational principle the action corresponding to the system actual trajectory has an extremum: $\delta \mathcal{S} = 0$. From this, one can derive the Euler-Lagrange equations:

$$\frac{\partial L}{\partial \mathbf{q}} - \frac{d}{dt} \frac{\partial L}{\partial \dot{\mathbf{q}}} = 0 \tag{2.4}$$

which in this form are the equations of motion for the free system.

This classical formalism can be generalized into the formalism of a quantum field theory (QFT) by trading:

- $\mathbf{q}_i(t)$ for a set of fields depending on the space-time coordinates $\phi(x_\mu) \equiv \phi(x)$, hence a finite set of degrees of freedom for continuous coordinates, and
- $\dot{\mathbf{q}}_i(t)$ for $\frac{\partial\phi(x)}{\partial t}$.

Using these notations, the derivative with respect to space-time writes: $\partial_\mu\phi(x) = \frac{\partial\phi(x)}{\partial x^\mu}$, and the action $\mathcal{S} = \int \mathcal{L}d^4x$, where \mathcal{L} is the lagrangian density.

Consequently the Euler-Lagrange equation writes:

$$\partial_\mu \left(\frac{\partial \mathcal{L}}{\partial(\partial_\mu \phi_i)} \right) = \frac{\partial \mathcal{L}}{\partial \phi_i} \quad (2.5)$$

The field of a spin $\frac{1}{2}$ particle of mass m is represented by a Dirac spinor ψ . Its lagrangian is:

$$\mathcal{L} = \bar{\psi}(i\gamma^\mu\partial_\mu - m)\psi \quad (2.6)$$

where $\bar{\psi} = \psi^\dagger\gamma^0$, the γ^μ being the Dirac matrices with $\mu = 0, \dots, 3$. For a free particle, this is the Dirac equation:

$$(i\gamma^\mu\partial_\mu - m)\psi(x) = 0. \quad (2.7)$$

One important concept utilized in field theory is the Noether's theorem, which states that to each continuous symmetry of \mathcal{L} corresponds a conserved current $\partial_\mu j^\mu = 0$, henceforth a conserved charge $Q = \int j^0 d^3x$. Therefore observing some conserved quantities in a system phenomenology implies this system has corresponding global symmetries. Note that the Noether's theorem holds only for on-shell particles, it needs to be generalized into the Ward-Takahashi identities [1][2] in QED and further into the Slavnov-Taylor identities [3][4] in a general QFT.

Starting from Eq. 2.7, we introduce the key method for including the fundamental interactions: rendering a global symmetry local, the invariance of the \mathcal{L} requires to introduce a gauge interaction term. Local gauge invariance transforms ψ as follows:

$$\psi \rightarrow \psi' = e^{i\theta(x)}\psi \quad (2.8)$$

where $\theta(x)$ is a function of space-time, and plugging ψ' into Eq. 2.7, implies to add to ∂_μ the iqA_μ term. This additional term corresponds to a particle of charge q lying in an electromagnetic (EM) 4-potential A_μ . If this 4-potential A_μ and the derivative ∂_μ transform as:

$$\begin{cases} A_\mu \rightarrow A'_\mu = A_\mu - \frac{1}{q}\partial_\mu\theta(x) \\ \partial_\mu \rightarrow D_\mu = \partial_\mu + iqA_\mu \end{cases} \quad (2.9)$$

one indeed finds an invariant form of Eq. 2.7: $(i\gamma^\mu D_\mu - m)\psi(x) = 0$. D_μ is called the covariant derivative. Writting the EM field tensor based upon its 4-potential: $F_{\mu\nu} = \partial_\mu A_\nu - \partial_\nu A_\mu$, the lagrangian of a charged particle within an EM field writes:

$$\mathcal{L}_{QED} = \bar{\psi}(i\gamma^\mu D_\mu - m)\psi - \frac{1}{4}F_{\mu\nu}F_{\nu\mu} \quad (2.10)$$

This actually corresponds to the lagrangian of Quantum ElectroDynamics (QED).

The gauge transformations (Eq. 2.8) of ψ belong to the unitary group $U(1)$. $e^{i\theta}$ is considered as a unitary 1×1 matrix U , where unitary means: $U^\dagger U = \mathbb{1}$.

2.1.2 Anatomy

The Standard Model (SM) of particle physics describes the matter we know as made of elementary particles which are fermions. Out of the four fundamental interactions, the SM describes three which are the electromagnetic (EM), the weak and the strong interactions, the fourth one, gravity, is negligible (at least for energies that can be probed at particle colliders) and therefore not treated in this model. The fundamental interactions undergone by the fermions proceed via the exchange of gauge bosons.

2.1.2.1 External and Internal Symmetries

The SM [5][6][7] is a relativistic QFT that obeys the external space-time continuous symmetries of the Poincaré group [8][9] These symmetries implies the SM lagrangian is invariant with respect to:

- the rotations and the boosts in the Minkowski space-time (these constitute the Lorentz group [10]) and,
- the space-time translations.

Like all relativistic QFTs, the SM conserves the CPT product of discrete symmetries. C stands for the charge conjugation (exchanging any particle by its antiparticle), P stands for space parity [11] (exchanging the sign of the space coordinates) and T stands for time reversal (exchanging the sign of the time coordinate). Though for a long time each of these discrete symmetries were thought to be exact, the violation of P in weak decays was conjectured by Lee and Yang in 1956 [12] and experimetically discovered a year later [13][14]. Then for some time, the product of CP was thought to be a good symmetry of the SM, but was eventually found to be violated in neutral kaon decays in 1964 [15]. And finally it was first stated [16], and soon after more formally demonstrated [17][18][19][20], that any invariant relativistic QFT with a local and hermetian hamiltonian is invariant under the CPT product.

In addition, the SM is invariant with respect to a gauge group describing its internal quantum symmetries:

$$G_{SM} = SU(3)_C \times SU(2)_L \times U(1)_Y \quad (2.11)$$

$SU(3)_C$ represents the gauge group for the strong interactions and $SU(2)_L \times U(1)_Y$ that of the electroweak (EW) interactions, made of $SU(2)_L$ the group of weak isospin and $U(1)_Y$ the group of weak hypercharge.

2.1.2.2 Particle Content

2.1.2.2.a Fermion Sector

This sector describes the building blocks of matter. It is composed of spin $J = \frac{1}{2}$ particles that belong to the fundamental representation of G_{SM} and obey the Fermi-Dirac statistics. Their corresponding quantum numbers are collected in table 2.1. These are quarks and leptons replicated into 3 generations.

The weak interactions are chiral: this means that the weak couplings between gauge bosons and the left-handed (L) fermions, represented by $SU(2)_L$ doublets, are different than between these gauge bosons and the right-handed (R) fermions, represented by $SU(2)_L$ singlets.

Fermion	Field	$SU(2)_L$ Multiplet	Quantum Numbers
Leptons	L_{iL}	$\begin{pmatrix} \nu_e \\ e^- \end{pmatrix}_L \begin{pmatrix} \nu_\mu \\ \mu^- \end{pmatrix}_L \begin{pmatrix} \nu_\tau \\ \tau^- \end{pmatrix}_L$	(1,2,-1)
	ℓ_{iR}	e_R^-, μ_R^-, τ_R^-	(1,1,-2)
Quarks	$\begin{pmatrix} U_\alpha^i \\ D_\alpha^i \end{pmatrix}_L$	$\begin{pmatrix} u^i \\ d^i \end{pmatrix}_L \begin{pmatrix} c^i \\ s^i \end{pmatrix}_L \begin{pmatrix} t^i \\ b^i \end{pmatrix}_L$	(3,2,1/3)
	$U_{\alpha R}^i$	u_R^i, c_R^i, t_R^i	(3,1,4/3)
	$D_{\alpha R}^i$	d_R^i, s_R^i, b_R^i	(3,1,-2/3)

TABLE 2.1: Field content for the SM fermion sector. The colour index is denoted α , the family index is denoted i and the chirality indices are L or R . The quantum numbers quoted are those under the SM gauge group: $SU(3)_C \times SU(2)_L \times U(1)_Y$.

Here we omit the possibility of having a right-handed neutrino ν_R since the neutrino mass will not play a major role in this document.

For each fermion the weak hypercharge Y , the third component of the weak isospin I_3 and the electric charge Q are related by the Gell-Mann Nishijima formula:

$$Q_f = I_{3f} + \frac{Y_f}{2} \quad (2.12)$$

In each generation, the two following relations:

$$\begin{cases} \sum_f Q_f = 0 \\ \sum_f Y_f = 0 \end{cases} \quad (2.13)$$

prevent to have Adler-Jackiw-Bell anomalies [21][22] in the SM and therefore preserve its renormalizability.

2.1.2.2.b Gauge Sector

This sector describes the particles carrying 3 of the fundamental interactions:

- the strong interaction is transported by 8 gluons g
- the electromagnetic (EM) interaction is transported the photon γ
- the weak interactions are transported by the W^\pm and the Z^0 bosons

These particles are vector bosons of spin $J = 1$ belonging to the adjoint representation of G_{SM} , they obey the Bose-Einstein statistics. Their corresponding quantum numbers and their coupling constants are collected in table 2.2.

Gauge Boson	Field	Gauge Group	Coupling Constant	Quantum Numbers
B Boson	B_μ	$U(1)_Y$	g_1 or g'	(1,1,0)
W Bosons	W_μ^i	$SU(2)_L$	g_2 or g	(1,3,0)
Gluons	G_μ^a	$SU(3)_C$	g_3 or g_S	(8,1,0)

TABLE 2.2: Field content for the SM gauge sector. The indices $a = 1, \dots, 8$ refer to the different gluons, $i = 1, \dots, 3$ to the different weak boson field components and $\mu = 0, \dots, 3$ to the space-time coordinates. The quantum numbers quoted are those under the SM gauge group: $G_{SM} = SU(3)_C \times SU(2)_L \times U(1)_Y$ and the gauge coupling constants g_3 , g_2 , and g_1 , are those of the respective sub-groups.

The gauge fields are:

- B_μ : corresponds to the single generator of weak hypercharge Y , such that $[Y, Y] = 0$
- W_μ^i : corresponds to the 3 generators of weak isospin I , such that $[T^i, T^j] = i \cdot \epsilon^{ijk} T^k$
- G_μ^a : corresponds to the 8 generators of colour, such that $[T^a, T^b] = i \cdot f^{abc} T^c$

their corresponding strength tensors are defined by:

$$B_{\mu\nu} = \partial_\mu B_\nu - \partial_\nu B_\mu \quad (2.14)$$

$$W_{\mu\nu}^i = \partial_\mu W_\nu^i - \partial_\nu W_\mu^i + g_2 \epsilon^{ijk} W_\mu^j W_\nu^k \quad (2.15)$$

$$G_{\mu\nu}^a = \partial_\mu G_\nu^a - \partial_\nu G_\mu^a + g_3 f^{abc} G_\mu^b G_\nu^c \quad (2.16)$$

Here, ϵ^{ijk} and f^{abc} are the antisymmetric structure constants of $SU(2)_L$ and $SU(3)_C$ and the corresponding generators can be expressed, in terms of the 2×2 Pauli matrices and of the 3×3 Gell-Mann matrices, respectively: $\tilde{W}_\mu = \frac{1}{2} W_\mu^a \tau^a$ and $\tilde{A}_\mu = \frac{1}{2} A_\mu^b \lambda^b$. Hence the covariant

derivatives write:

$$D_\mu L_{iL} = (\partial_\mu + i\tilde{W}_\mu - i\frac{1}{2}B_\mu)L_{iL} \quad (2.17)$$

$$D_\mu \ell_{iR} = (\partial_\mu + iB_\mu)\ell_{iR} \quad (2.18)$$

$$D_\mu Q_{\alpha L}^i = (\partial_\mu + i\tilde{A}_\mu + i\tilde{W}_\mu + i\frac{1}{6}B_\mu)Q_{\alpha L}^i \quad (2.19)$$

$$D_\mu u_{\alpha R}^i = (\partial_\mu + i\tilde{A}_\mu^* - i\frac{2}{3}B_\mu)u_{\alpha R}^i \quad (2.20)$$

$$D_\mu d_{\alpha R}^i = (\partial_\mu + i\tilde{A}_\mu^* + i\frac{1}{3}B_\mu)d_{\alpha R}^i \quad (2.21)$$

and enable to complete the fermionic part of the SM lagrangian:

$$\mathcal{L}_{Dirac} = \sum_{i=1}^3 \left(L_i^\dagger \sigma_\mu D_\mu L_i + \ell_i^\dagger \sigma_\mu D_\mu \ell_i + Q_i^\dagger \sigma_\mu D_\mu Q_i + u_i^\dagger \sigma_\mu D_\mu u_i + d_i^\dagger \sigma_\mu D_\mu d_i \right) \quad (2.22)$$

where index i runs over the 3 generations.

The interactions between the charged fermions and the Higgs field are contained in:

$$\mathcal{L}_{Yukawa} = y_{\alpha\beta}^l \bar{L}_\alpha l_\beta \Phi + y_{\alpha\beta}^d \bar{D}_{R\alpha} D_{\beta} \Phi + y_{\alpha\beta}^u \bar{U}_{R\alpha} U_\beta \tilde{\Phi} \quad (2.23)$$

where $\tilde{\Phi} = i\tau_2 \Phi^\dagger$ and the $y_{\alpha\beta}^f$ are the Yukawa coupling matrices.

The weak interactions can be sub-divided into charged and neutral currents. The charged currents, carried by the W^\pm boson, couple exclusively to the left-handed fermions. This property was introduced in the theory of weak interactions to account for the experimentally established parity violation in some weak decays. The neutral currents, carried by the Z^0 boson, couple to both fermion chiralities yet with different strengths. It is the weak isospin I of the $SU(2)_L$ symmetry group that distinguishes the different fermions, it takes the value of $I = 1/2$ for f_L and $I = 0$ for f_R .

Note that the quark doublets of weak isospin do not coincide with the quark mass eigenstates. The quark mixing is described by the unitary Cabbibo-Kobayashi-Maskawa (CKM) matrix which is conventionally written for the down quarks:

$$\begin{pmatrix} d' \\ s' \\ b' \end{pmatrix} = V_{CKM} \begin{pmatrix} d \\ s \\ b \end{pmatrix} \quad (2.24)$$

2.1.2.2.c Higgs Sector

We'll justify in the next paragraph the need to introduce an additional $SU(2)_L$ doublet of scalar ($J = 0$) complex fields with $Y = +1$:

$$\Phi = \begin{pmatrix} \phi^+ = \phi_1^+ - i\phi_2^+ \\ \phi^0 = \phi_3^0 - i\phi_4^0 \end{pmatrix} \quad (2.25)$$

where the components ϕ_i ($i = 1, \dots, 4$) are real.

2.1.3 Lagrangian Density

The SM lagrangian density can be written as:

$$\mathcal{L}_{SM} = \mathcal{L}_{Yang-Mills} + \mathcal{L}_{Higgs} + \mathcal{L}_{Fermions} \quad (2.26)$$

where

- $\mathcal{L}_{Yang-Mills}$: contains the kinetic terms of the gauge fields
- \mathcal{L}_{Higgs} : describes the Higgs field dynamics and the EW symmetry breaking (EWSB)
- $\mathcal{L}_{Fermions}$: contains two sets of fermion terms
 - \mathcal{L}_{Dirac} : for free Dirac fermions plus their interactions with gauge bosons
 - \mathcal{L}_{Yukawa} : the interactions between the Higgs field and the fermions

Here we do not explicit the Fadeev-Popov terms and the gauge fixing terms appearing in the quantization of field theories.

The fermionic part has been developed above. The gauge part is:

$$\mathcal{L}_{Yang-Mills} = -\frac{1}{4g_1^2} B_{\mu\nu} B^{\mu\nu} - \frac{1}{4g_2^2} W_{\mu\nu}^j W^{i\ \mu\nu} - \frac{1}{4g_3^2} G_{\mu\nu}^a G^{a\ \mu\nu} \quad (2.27)$$

it represents the kinetic terms of the gauge bosons. Finally, \mathcal{L}_{Higgs} will be detailed in the next paragraph.

2.1.4 Electroweak Symmetry Breaking

Given that QFTs explain the fundamental interactions through the exchange vector bosons that actually carry the interaction. We can derive an estimate of the range of these interactions from the time-energy Heisenberg's inequality. This leads the so-called "reduced Compton's wavelength": $\lambda_c = \frac{\hbar}{M \cdot c}$ where M is the mass of the interaction carrier.

Following this argument a major contradiction arises when one examines the quantum properties of the fundamental interactions and the mass of their carriers.

On the one hand, for a given interaction, the gauge invariance prevents from writing a mass term for the vector boson carrying this interaction. Only massless interaction carriers, i.e. infinite range interactions, are compatible with gauge invariance.

The previous argument perfectly fits the observed properties of the photon which the carrier of the EM interactions. However it obviously do not match the experimental properties of the strong and the weak interactions which experimentally happen to be short-ranged. The latter

suggesting they have very massive vector bosons; two cases in apparent contradiction with gauge invariance.

A specific property of strong interaction, is to have a very high coupling constant at low energy. This causes the confinement of quarks within the hadrons and prevents one to observe free particles bearing a color charge at low energy. Because of this, it's actually possible to explain many features of the strong interactions through the exchange of $q\bar{q}$ bound states, which are mesons. Historically, this is how in 1934 H. Yukawa introduced the first theory of strong interactions between hadrons via the exchange of light mesons called pions. Yukawa predicted the carrier of the strong interaction should have about 200 times the mass of the electron, this was later confirmed with the discovery of the pion in cosmic ray observations. The mass of the pion is perfectly compatible with the range of the strong interaction.

However for the weak interactions, there are no such things as confinement, therefore it is mandatory to introduce a brand new mechanism to fix the apparent contradiction between gauge invariance and the short-ranged weak interactions. This will lead to a mechanism of spontaneous breaking of the electroweak symmetry.

Let's start with preliminary remarks regarding the mass generation within the SM:

- in QED and QCD the gauge invariance prevents from writing an explicit mass term for the photon or the gluons,
- chirality also prevents from writing mass terms for the fermions.

Therefore if all the SM gauge symmetries were exact, this model would only contain massless particles! The solution to this puzzle (and to that of the range of weak interactions) are the justifications for introducing the Higgs doublet described in sub-section 2.1.2.2.c.

This Higgs doublet adds-up 4 degrees of freedom in the theory. This doublet has the following potential:

$$V(\Phi) = \mu^2|\Phi|^2 + \lambda|\Phi|^4 \quad (2.28)$$

which, for $\mu^2 < 0$, has a non-trivial minimum at $|\Phi|_{min} = \sqrt{\frac{-\mu^2}{2\lambda}}$. Hence we choose its vacuum expectation value (vev) as

$$\langle 0|\Phi|0 \rangle = \begin{pmatrix} 0 \\ v/\sqrt{2} \end{pmatrix} \quad (2.29)$$

where $v \approx 246$ GeV ¹. The minimum of the Higgs potential is shown in Fig. 2.1 down the "mexican-hat" shape. We note that there is an infinity of degenerate minima (all at the same potential energy). There are two types of excitations of the Higgs field. On one hand, there are modes that go along a circle at the minimum of the potential, their movement do not cost energy, therefore these modes are massless and associated to the Goldstone bosons. On the other hand there's a mode oscillating vertically around a minimum of the potential, its movement requires energy since it climbs (and falls down) the potential, this is the Higgs boson.

¹value derivable from the measure of G_F , the coupling in the Fermi's theory of weak, in $\mu^\pm \rightarrow e^\pm \bar{\nu}_e \nu_\mu$ decays

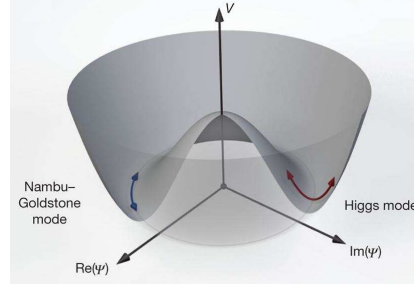


FIGURE 2.1: Higgs potential with its famous "mexican hat" shape. The Higgs field excitations around the vertical axis represents the Goldstone bosons, whilst its excitations along the potential valley represents the Higgs boson.

When the Higgs field acquires a vev, it spontaneously breaks the EW symmetry down to the QED symmetry group:

$$SU(2)_L \times U(1)_Y \rightarrow U(1)_{EM} \quad (2.30)$$

For an equivalent breaking of N_G generators of a global symmetry, the Goldstone theorem states that N_G massless bosons appear in the mass spectrum of the theory. For $SU(2)_L \times U(1)_Y$ there are 4 generators and there's just 1 for $U(1)_{EM}$, therefore there would be 3 Goldstone bosons.

The mechanism of the electroweak symmetry breaking (EWSB), is called the Brout-Englert-Higgs mechanism² [23][24][25][26]. In this mechanism, the field is re-written with 4 real components ξ_j with $j = 1, 2, 3$ and H as:

$$\Phi = e^{i\xi_j \frac{\tau_j}{2}} \begin{pmatrix} 0 \\ \frac{v+H}{\sqrt{2}} \end{pmatrix} \quad (2.31)$$

It follows that the kinetic term writes:

$$\begin{aligned} |D_\mu \Phi|^2 &= \left| \left(\partial_\mu - ig_2 \frac{\tau_i}{2} W_\mu^i - ig_1 \frac{1}{2} B_\mu \right) \Phi \right|^2 \\ &= \frac{1}{2} (\partial_\mu H)^2 + \frac{1}{8} g_2^2 (v+H)^2 \cdot |W_\mu^1 + iW_\mu^2|^2 + \frac{1}{8} (v+H)^2 \cdot |g_2 W_\mu^3 - g_1 B_\mu|^2 \end{aligned} \quad (2.32)$$

and one can also re-write the EW gauge fields:

$$W^\pm \text{ boson : } W_\mu^\pm = \frac{(W_\mu^{1\pm} \mp iW_\mu^{2\pm})}{\sqrt{2}} \quad (2.33)$$

$$\text{photon : } A_\mu = B_\mu \cos\theta_w + W_\mu^3 \sin\theta_w \quad (2.34)$$

$$Z^0 \text{ boson : } Z_\mu = -B_\mu \sin\theta_w + W_\mu^3 \cos\theta_w \quad (2.35)$$

where θ_w is the mixing angle between the EM and the weak interaction, known as the Weinberg angle and relating the gauge coupling constants with e : $g_1 = \frac{e}{\cos\theta_w}$ and $g_2 = \frac{e}{\sin\theta_w}$.

²Also due to P.W. Anderson, C.R. Hagen, T. Kibble and G. Guralnik

In terms of gauge symmetry, at the electroweak scale, the following transition occurs:

$$SU(3)_C \times SU(2)_L \times U(1)_Y \longrightarrow SU(3)_C \times U(1)_{EM} \quad (2.36)$$

and, the 3 Goldstone bosons do not appear in the mass spectrum, as they would have in the spontaneous symmetry breaking (SSB) of a global $SU(2)_L \times U(1)_Y$. In a SSB of a gauge symmetry, due to the choice of the gauge, the Goldstone bosons are "eaten" by W^\pm and Z^0 bosons: they provide their longitudinal polarization and therefore enable them to get a mass.

It's interesting at this stage to summarize how the different types of SM particles acquire their mass.

- Gauge bosons:
 - $M_W = g_2 \frac{v}{\sqrt{2}}$ and $M_Z = \sqrt{g_1^2 + g_2^2} \frac{v}{\sqrt{2}}$ (EW couplings to Φ)
 - $M_\gamma = 0$ and $M_g = 0$ (No direct coupling to Φ)
- Higgs boson: $M_H = \sqrt{2\lambda}v$ (EW coupling to Φ)
- Charged fermions: $M_f = y_f \frac{v}{\sqrt{2}}$ (Yukawa couplings to Φ)

We see that there are couplings of 2 different types, yet one common feature holds: the larger the coupling to Φ , the larger the mass. Since the Higgs potential parameters λ and μ nor the Yukawas couplings are not predicted, the SM is actually not predictive regarding the mass of its particles.

2.1.5 Experimental Tests of the Standard Model

Over the past five decades there's been a very extensive set of experimental tests of the SM. None of these tests, including precision measurements, found the SM in fault as it is illustrated in Fig. 2.2 [27].

The success of the SM culminated in 2012 with the announcement by the ATLAS [28] and the CMS [29] collaborations of the discovery of the Higgs boson 48 years after its theoretical conjecture.



FIGURE 2.2: Pulls of a global fit of the SM to collider data.

2.1.6 Standard Model Limitations

Even though the SM is quite successful, a few experimental observations as well as a few theoretical considerations assure us that it is not the ultimate theory.

We'll just detail the naturalness problem of the Higgs boson in the SM and give a non-exhaustive list of other open questions at the end of this paragraph.

As already mentioned, contrarily to the gauge bosons and the charged fermions in the SM, the Higgs boson mass is not protected by any symmetries. At the 1-loop level, its bare mass M_H^0 gets contributions from fermion loops (almost exclusively from the top quark), from the W^\pm and Z gauge bosons and from itself. Its renormalized mass writes:

$$M_H^2 = (M_H^0)^2 + \frac{3\Lambda^2}{8\pi^2 v^2} [M_H^2 + 2M_W^2 + M_Z^2 - 4M_t^2] \quad (2.37)$$

where Λ is the ultraviolet cut-off is the loop integral over the momenta. This situation is often referred to as non natural, in the sense that the corrections can be much larger than the bare mass and that setting this bare mass to zero does not increase the symmetry of the SM. M_H^2 has a quadratic divergence with respect to Λ that could destabilized the Higgs boson mass for example in the presence of a high energy fundamental scale (i.e. the Grand Unification scale 10^{16} GeV or the Planck mass 10^{18} GeV) and drag it away from the EW scale, below which a unitary upper bound maintains it. This is known as the Higgs boson hierarchy problem. When one extrapolates the SM at very high energies, one is forced to fine-tune its parameters to a very unsatisfactory degree. So even though it is technically viable, it is not an appealing scenario.

Experimental Problems:

- Non-zero neutrino mass from neutrino oscillations
- Gravitational evidence of Cold Dark Matter
- Astrophysical evidence of Dark Energy

Theoretical Problems:

- Naturalness Issues:
 - Strong CP problem (possible, yet unobserved, CP violation in QCD)
 - SM Higgs sector: fine tuning?
- Gauge Interactions:
 - Larger gauge group: Grand Unification?,...
 - Landau pole at high energy for weak hypercharge
 - Quantum gravity
- Flavour Puzzle:

- Why 3 generations?
- Why such a large fermion mass hierarchy (especially for neutrinos)?
- Space-Time Structure & Symmetries:
 - More the 3 dimensions of space?
 - Supersymmetry?

On top of these open questions, another aspect of the SM that makes it unsatisfactory is the following list of its 19 free parameters:

- 3 gauge couplings: g_1, g_2 (or $\sin^2\theta_w$), g_3
- 9 Yukawa couplings: 3 for charged leptons, 6 for quarks
- 2 parameters of the Higgs potential: λ and μ (or M_H , or v)
- 3 elements of V_{CKM} , plus 1 phase (CP violation)
- 1 parameter θ_{QCD} for "strong CP violation": $\mathcal{L} \sim \frac{g_s^2}{64\pi^2} \theta_{QCD} F_a^{\mu\nu} \epsilon_{\mu\nu\alpha\beta} F^{a\alpha\beta}$

2.2 Supersymmetric Extension of the Standard Model

2.2.1 Introduction to Supersymmetry

2.2.1.1 Definition

Supersymmetry (SUSY) is an hypothetical, yet very interesting, new symmetry between the fermions and the bosons. Let's consider an operator Q acting on a field of spin S , Q is an operator of SUSY if:

$$Q|S\rangle = |S \pm 1/2\rangle \quad (2.38)$$

Eq. 2.38 means that Q shifts (upwards or downwards) the spin S by half a unit of \hbar , this implies that Q is a fermionic (anti-commuting) operator.

Historically SUSY was introduced in the early 1970's in attempts to extend the external symmetries (Poincaré group) by the internal quantum symmetries [30][31]. These attempts were dramatically stopped when S. Coleman and J. Mandula [32] demonstrated in 1967 a famous "no-go" theorem [32] stating that with Lie algebra, it is not possible to extend non-trivially the Poincaré group. This show-stopper was eventually circumvented in 1975 by R. Haag, J. Lopuszanski, and M. Sohnius [33] who showed that the use of graded Lie algebra, which mixes the usual bosonic operators with fermionic ones, actually permits a non-trivial extension of the Poincaré algebra.

2.2.1.2 Super-Poincaré Algebra

Let's adopt the following notations:

- $M_{\mu\nu} = i(x_\mu\partial_\nu - x_\nu\partial_\mu)$ ³: the 6 generators of the Lorentz group
- $P_\mu = i\partial_\mu$: the generator of the space-time translations
- T_a : the N generators of a gauge group
- Q_α : SUSY generators (left-handed spinor with spinorial indices $\alpha, \dot{\alpha} = 1, 2$)
- $\bar{Q}_\alpha = (Q^T\gamma^0)_\alpha$: SUSY generators (right-handed spinor)

The Poincaré algebra is defined by:

$$[M_{\mu\nu}, M_{\rho\sigma}] = -i(\eta_{\nu\sigma}M_{\rho\mu} - \eta_{\mu\sigma}M_{\rho\nu} + \eta_{\nu\rho}M_{\mu\sigma} - \eta_{\mu\rho}M_{\nu\sigma}) \quad (2.39)$$

$$[M_{\mu\nu}, P_\rho] = -i(\eta_{\nu\rho}P_\mu - \eta_{\mu\rho}P_\nu) \quad (2.40)$$

$$[P_\mu, P_\nu] = 0 \quad (2.41)$$

The gauge algebra is as usual and its generators T^a commute with Poincaré operators:

$$[T_a, T_b] = i \cdot f_{abc}T_c \quad (2.42)$$

$$[T_a, P_\mu] = [T_a, M_{\mu\nu}] = 0 \quad (2.43)$$

And the Super-Poincaré algebra includes the Poincaré and the gauge algebra adding to them the following relations:

$$[M_{\mu\nu}, Q_\alpha] = i(\sigma_{\mu\nu})_\beta^\alpha Q_\beta \quad (2.44)$$

$$[M_{\mu\nu}, \bar{Q}_{\dot{\alpha}}] = -i(\bar{\sigma}_{\mu\nu})_{\dot{\beta}}^{\dot{\alpha}} \bar{Q}_{\dot{\beta}} \quad (2.45)$$

$$[P_\mu, Q_\alpha] = [P_\mu, \bar{Q}_{\dot{\alpha}}] = 0 \quad (2.46)$$

$$\{Q_\alpha, \bar{Q}_{\dot{\beta}}\} = 2\sigma_{\alpha\dot{\beta}}^\mu P_\mu \quad (2.47)$$

$$\{Q_\alpha, Q_\beta\} = \{Q_{\dot{\alpha}}, Q_{\dot{\beta}}\} = 0 \quad (2.48)$$

The irreducible representations of this algebra are supermultiplets that contain fields with the same quantum numbers but different spins (i.e. SM fields and their SUSY partners). We'll now present the most important consequences of this algebra on the supermultiplets.

Eq. 2.47 enables to interpret the meaning of the SUSY generator Q_α : two consecutive applications (i.e. Q^2) of this generator is equivalent to a translation in space-time. Therefore Q_α is somewhat the "square root of a space-time translation". This equation has also profound consequence in the context of local SUSY. Indeed a theory invariant under local SUSY transformations is also invariant wrt space-time translations, i.e. invariant with respect to changes of

³ $+\frac{i}{4}[\gamma_\mu, \gamma_\nu]$ for $J = 1/2$

local coordinates, which is a definition of General Relativity. That's why local SUSY theories, called theories of supergravity (SUGRA), naturally embed General Relativity.

The number \mathcal{N} of different SUSY generators $Q_{i\alpha}$ is limited to:

- $\mathcal{N} = 4$ for a flat-space renormalizable theory,
- $\mathcal{N} = 8$ for supergravity.

This is due to the fact that for an extended SUSY \mathcal{N} the supermultiplets can only contain particles with spin larger than $\frac{\mathcal{N}}{4}$. And also because gravity cannot consistently couple with $J > 2$ and because flat-space theories are renormalizable only if they contain fields with $J \leq 1$. We remind that the criterion to figure whether a lagrangian is renormalizable is:

$$\Delta_{renorm} = 4 - d - \sum_i n_i (s_i + 1) \geq 0 \quad (2.49)$$

where d is the number of field derivatives, n_i the number of fields of spin s_i .

SUSY theories with $\mathcal{N} > 1$ are called extended SUSY theories. We'll not discuss that further because of a phenomenological limitations of these theories: their algebra don't have representations to include chiral fermions. The only possibility is to have an extended SUSY at very high energy that has to breakdown into $\mathcal{N} = 1$ say at the TeV scale, the latter having to breakdown to the SM, i.e. to no apparent SUSY at the EW scale. In addition, it can be shown that for unbroken SUSY, the number of fermionic and bosonic degrees of freedom within the same supermultiplet are equal.

Finally, it's also interesting to consider the two Casimir invariants of the Poincaré group:

- $P^2 = P^\mu P_\mu$: the mass, $[P^2, Q_\alpha] = 0$ meaning there's a mass degeneracy amongst the fields in the same supermultiplet
- $W^2 = W^\mu W_\mu$, where $W^\mu = \frac{1}{2} \epsilon^{\mu\nu\rho\sigma} P_\nu M_{\rho\sigma}$ is the Pauli-Lubanski spin vector, here $[W^2, Q_\alpha] \neq 0$ meaning that for different fields within the same supermultiplet the spins differ

Therefore, if the SM has to be supersymmetrized, the SUSY partners of the SM particles are yet undiscovered particles, most probably much heavier ones.

We can now start building the representations of the super-Poincaré group. For $\mathcal{N} = 1$ they just two representations labelled by $|j, m\rangle$ which is the eigenvector common to the J^2 and J_3 operators for a spin \mathbf{J} .

2.2.1.2.a Chiral Supermultiplet

This fundamental representation $|j = 0, m\rangle$ is called the chiral (or scalar) supermultiplet Ψ . It contains:

- 1 scalar complex field ϕ
- 1 fermionic field ψ (Weyl spinor)

As shown in the previous paragraph, for SUSY to be preserved we need between these scalars and these fermions equal masses and equal numbers of degrees of freedom (N_{dof}). This is clearly achieved in the on-shell case: $P^2 = M^2$ and $N_{dof}(\phi) = N_{dof}(\psi) = 2$. However to always maintain $N_{dof}(\phi) = N_{dof}(\psi)$, in particular within loops where particles could be off-shell, we need to use an important technical subtlety which consists in introducing an additional complex scalar field F having 2 degrees of freedom ($N_{dof}(F) = 2$). The reason is that the Weyl fermion has:

- on-shell: $N_{dof}(\psi) = 2$
- off-shell: $N_{dof}(\psi) = 4$

and F , the auxiliary field, compensates the $\Delta N_{dof} = 2$ in the off-shell case. F is not a physical field, it does not propagate (no kinetic term). It can be eliminated using its equation of motion: $F = F^* = 0$.

So, finally, the chiral supermultiplet content is:

$$\Psi = (\phi, \psi_\alpha, F) \tag{2.50}$$

2.2.1.2.b Vector Supermultiplet

This second representation $|j = 1/2, m\rangle$ is called the vector (or gauge) supermultiplet Φ . It contains:

- 1 massless gauge boson A_a^μ (a is the gauge group index)
- 1 fermionic field with λ_α^a (Weyl spinor: the gaugino)

As for the chiral supermultiplet, we add an auxiliary real scalar field D^a . Henceforth:

$$\Phi = (\lambda_\alpha^a, A_a^\mu, D^a) \tag{2.51}$$

All the SM fields and their SUSY partner fields fit in these 2 representations, on which we shall base the SUSY QFT. Note that SUSY is global so far and shall stay this way as long as we don't discuss the way it is broken.

2.2.2 Supersymmetric Quantum Field Theory

2.2.2.0.c Wess-Zumino Model

The simplest action derivable from the chiral supermultiplet as that of the Wess-Zumino model [34]:

$$S = \int d^4x (\mathcal{L}_{scalar} + \mathcal{L}_{fermion} + \mathcal{L}_{aux}^{off-shell}) \quad (2.52)$$

where

$$\mathcal{L}_{scalar} = -(\partial^\mu \phi)(\partial_\mu \phi^*) \quad (2.53)$$

$$\mathcal{L}_{fermion} = -i(\psi^\dagger \bar{\sigma}^\mu \partial_\mu \psi) \quad (2.54)$$

$$\mathcal{L}_{aux}^{off-shell} = F^* F \quad (2.55)$$

2.2.2.0.d Chiral supermultiplet interactions

Now we introduce the interactions between the scalar and the fermion within the chiral supermultiplet. This interaction term needs obviously to be invariant under global SUSY and to be renormalizable. These requirements constrain its form to:

$$\mathcal{L}_{int} = \frac{-1}{2} W^{ij}(\phi) \psi_i \psi_j + V(\phi, \phi^*) + h.c. \quad (2.56)$$

The W^{ij} can be derived from an analytic function of ϕ (i.e. not of ϕ^*) called the superpotential $W(\phi)$:

$$W^{ij} = \frac{\partial^2 W(\phi)}{\partial \phi_i \partial \phi_j} \quad (2.57)$$

where the most general renormalizable superpotential is:

$$W(\phi) = \frac{1}{2} M^{ij} \phi_i \phi_j + \frac{1}{6} y^{ijk} \phi_i \phi_j \phi_k \quad (2.58)$$

in which M^{ij} are the fermions mass matrix and y^{ijk} the matrix of the Yukawa couplings between the scalar and the fermions. The superpotential is not an usual "potential energy" term, it's an analytic function that collects all types of interactions, but the gauge interactions. Its invariance under global SUSY imposes the form of a scalar potential V (which plays the usual role of "potential energy"). The auxiliary fields F_i are related to the superpotential through their equations of motion:

$$F_i = -\frac{\partial W(\phi)}{\partial \phi^i} = -W_i^* \quad (2.59)$$

$$F^{*i} = -\frac{\partial W(\phi)}{\partial \phi_i} = -W^i \quad (2.60)$$

and the scalar potential can then be written as:

$$V = F_i F^{i*} = W_i^* W^i \quad (2.61)$$

Finally, \mathcal{L}_{int} writes:

$$\mathcal{L}_{int} = -(\partial^\mu \phi)(\partial_\mu \phi^* + i\psi^\dagger \bar{\sigma}^\mu \partial_\mu \psi) - \frac{1}{2}(M^{ij} \psi^i \psi^j + M_{ij}^* \psi^{i\dagger} \psi^{j\dagger}) - V - \frac{1}{2}(y^{ijk} \phi_i \psi_j \psi_k + y_{ijk}^* \phi^{i*} \psi^{j\dagger} \psi^{k\dagger}) \quad (2.62)$$

2.2.2.0.e Vector supermultiplet interactions

This part of the lagrangian contains the gauge interactions. It writes:

$$\mathcal{L}_{gauge} = -\frac{1}{4} F_{\mu\nu}^a F^{a\mu\nu} - i\lambda^{a\dagger} \bar{\sigma}^\mu D_\mu \lambda^a + \frac{1}{2} D^a D_a - V \quad (2.63)$$

The usual derivatives need to be replaced by the covariant derivatives:

$$F_{\mu\nu}^a = \partial_\mu A_\nu^a - \partial_\nu A_\mu^a - g \cdot f^{abc} A_\mu^b A_\nu^c \quad (2.64)$$

$$D_\mu \lambda^a = \partial_\mu \lambda^a - g \cdot f^{abc} A_\mu^b \lambda^c \quad (2.65)$$

and the auxiliary field equation of motion is: $D^a = -g\phi^* T^a \phi$. And the full scalar potential (including F and D terms) now writes:

$$V = F_i F^{i*} + \frac{1}{2} \sum_a D^a D_a = W_i^* W^i + \frac{1}{2} \sum_a (g\phi^* T^a \phi)^2 \quad (2.66)$$

and contains the Yukawa interactions (F terms) and the gauge interactions (D terms).

2.2.3 The Minimal Supersymmetric Standard Model

Let's now use all the tools for a SUSY QFT mentioned above to supersymmetrize the SM. Before proceeding, we could ask whether the SM as is manifests invariance under SUSY transformations. The answer is clearly no, it directly follows from the SUSY algebra when trying to apply it within the SM framework. Had we SUSY in this context, among other things, we would have a partner of the electron with the same mass and a spin shifted by $\pm 1/2$, i.e. obeying Bose-Einstein statistics, therefore violating the Pauli exclusion principle. This obviously contradicts experimental observations. Besides we would have the same number of degrees of freedom for fermionic and bosonic fields. Again the former largely exceed over the latter. Therefore we need to associate new, yet undiscovered (hence probably much heavier), fields to each fields in the SM so as to match separately $N_{dof}(\text{SM fermions})$ and $N_{dof}(\text{SM bosons})$. For the naming scheme, we'll add an "s" prefix and an "ino" suffix to the respective SUSY partners of the SM fermions and bosons. And for more compact and convenient notations, we'll also introduce the superfields which contain SM fields and their SUSY partners, they will be denoted with a hat: i.e. the chiral superfield \hat{Q}_L contains both the (u_L, d_L) and the $(\tilde{u}_L, \tilde{d}_L)$ doublets of $SU(2)_L$.

We'll now describe how a SUSY version of the SM can be achieved in a minimal way, leading to the Minimal Supersymmetric Standard Model (MSSM), which is minimal in a few senses:

- $\mathcal{N} = 1$ global SUSY

Boson	Fermion	Superfields	Quantum numbers
Gauge Fields			
$J = 1$	$J = 1/2$		
G_μ^a	\tilde{G}^a	\hat{G}^a	(8,1,0)
W_μ^i	\tilde{W}^a	\hat{W}^a	(1,3,0)
B_μ	\tilde{B}	\hat{B}	(1,1,0)
Matter Fields			
$J = 0$	$J = 1/2$		
\tilde{Q}_L^a	Q_L^a	\hat{Q}_L^a	(3,2,1/6)
\tilde{U}_R^a	U_R^a	\hat{U}_R^a	($\bar{3}$,1,-2/3)
\tilde{D}_R^a	D_R^a	\hat{D}_R^a	($\bar{3}$,1,1/3)
\tilde{L}_L^i	L_L^i	\hat{L}_L^i	(1,2,-1/2)
$\tilde{\ell}_R^i$	ℓ_R^i	$\hat{\ell}_R^i$	(1,1,1)
EWSB Fields			
$J = 0$	$J = 1/2$		
Φ_d	$\tilde{\Phi}_d$	$\hat{\Phi}_d$	(1,2,-1/2)
Φ_u	$\tilde{\Phi}_u$	$\hat{\Phi}_u$	(1,2,1/2)

TABLE 2.3: Field content of the MSSM

- $G_{MSSM} = G_{SM}$ (no new fundamental interactions)
- minimal particle content

Regarding the particle content, we need to double the SM mass spectrum. However in the Higgs sector, we need to introduce 2 doublets instead of one: Φ_u couples to charged fermions and up quarks, whilst Φ_d couples to down quarks. A first justification to that lies in the analyticity of the superpotential which prevents from writing consistent Yukawa couplings to up and down quarks using a single Higgs doublet. The second reason is that the SUSY partner of Higgs fields are fermions which contribute to Adler-Jackiw-Bell anomalies. The way out of the latter issue is to introduce 2 Higgs doublets with opposite hypercharges so as to cancel out their contributions to chiral anomalies.

The MSSM lagrangian can be sub-divided into two parts:

$$\mathcal{L}_{MSSM} = \mathcal{L}_{SUSY} + \mathcal{L}_{\cancel{SUSY}} \quad (2.67)$$

2.2.3.1 Global SUSY Sector

The first part is globally supersymmetric and invariant under G_{SM} . As we already mentioned it contains the Yukawa interactions which are related to the SM ones, yet not strictly identical. All the interactions, but the gauge interactions, are contained in the superpotential:

$$W_{RP} = -Y_u^{ij} \hat{U}_{Ri} \hat{Q}_{Lj} \hat{\Phi}_u + Y_d^{ij} \hat{D}_{Ri} \hat{Q}_{Lj} \hat{\Phi}_d + Y_e^{ij} \hat{\ell}_{Ri} \hat{L}_{Lj} \hat{\Phi}_d + \mu \hat{\Phi}_u \hat{\Phi}_d \quad (2.68)$$

where Y_f^{ij} are the 3×3 flavours Yukawa matrices.

In principle some terms violating the conservation of the lepton and the baryon numbers, but still globally supersymmetric and invariant under G_{SM} , can be added to the superpotential as

written in Eq. 2.68:

$$W_{\cancel{RP}} = W_{\Delta L=1} + W_{\Delta B=1}, \text{ with} \quad (2.69)$$

$$W_{\Delta L=1} = \lambda_{ijk} \hat{L}_L^i \hat{L}_L^j \hat{\ell}_R^k + \lambda'_{ijk} \hat{L}_L^i \hat{Q}_L^j \hat{D}_R^k + \mu_i \hat{L}_L^i \hat{\Phi}_u, \text{ and} \quad (2.70)$$

$$W_{\Delta B=1} = \lambda''_{ijk} \hat{U}_R^i \hat{D}_R^j \hat{D}_R^k. \quad (2.71)$$

However, no violations of the lepton or the baryon numbers have been observed so far and if both $\lambda' \neq 0$ and $\lambda'' \neq 0$, the proton could rapidly decay via the $e^+\pi^0$ channel for example. In order to remove the $W_{\cancel{RP}}$ part of the superpotential, one introduces a new quantum number called "R-parity":

$$R_P = (-1)^{L+2S+3B} \quad (2.72)$$

where L is the lepton number, B is the baryon number and S the spin; consequently:

$$\begin{cases} R_P(SM) = +1, \text{ and} \\ R_P(SUSY) = -1. \end{cases} \quad (2.73)$$

Imposing the multiplicative conservation of R-parity, protects the proton from fast decays and has important phenomenological implications:

- SUSY particles (Sparticles) are produced by pair,
- a Sparticle can only decay into an odd number of lighter Sparticles,
- the lightest Sparticle is stable (hence a good candidate for Cold Dark Matter).

\mathcal{L}_{SUSY} is just the straight application to the MSSM particle content of the

$$\mathcal{L} = \mathcal{L}_{scalar} + \mathcal{L}_{fermion} + \mathcal{L}_{gauge} + \mathcal{L}_{int}$$

described in the previous paragraph.

To sum up, this part of the lagrangian is responsible for the EW symmetry breaking (i.e. generating the masses of the SM particles) and for the gauge and the Yukawa interactions, it contains the 19 free parameters of the SM.

2.2.3.2 Soft SUSY Breaking Sector

Contrarily to \mathcal{L}_{SUSY} , $\mathcal{L}_{\cancel{SUSY}}$ explicitly violates SUSY. We remember the SM does not exhibit SUSY. Therefore breaking SUSY is mandatory. Technically if we knew the underlying mechanism to break SUSY we would apply a spontaneous (or a dynamical) SUSY breaking. Historical attempts to spontaneously break global SUSY in the 1970's all led to unviable phenomenologies [35][36]. It was even demonstrated under general hypotheses that a "supertrace theorem" [37] implies in each supermultiplet the following constraints:

$$\sum_J (-1)^{2J} (2J+1) M_J^2 = 0, \text{ i.e. :} \quad (2.74)$$

$$M^2(\tilde{e}_R^\pm) + M^2(\tilde{e}_L^\pm) - 2M^2(e^\pm) = 0 \quad (2.75)$$

which are obviously not verified experimentally. The way out was found by H. Georgi and S. Dimopoulos in 1981 [38], their key idea was that the so-called "hidden sector", responsible for SUSY breaking, is at very high energy and completely decoupled from the "visible sector" composed by the SM and by the TeV scale SUSY.

Not knowing the SUSY breaking mechanism, we're left with the option of parametrizing this ignorance with a collection of terms that explicitly break SUSY in \mathcal{L}_{SUSY} , the limitations being the gauge invariance and the so-called soft SUSY breaking. The soft SUSY breaking means that no quadratic divergences can arise from \mathcal{L}_{SUSY} . In this way, broken SUSY can solve the hierarchy problem. Note that the only observable consequence of the SUSY breaking in the visible sector is the lift of the mass degeneracy for all pairs of bosons and fermions in the supermultiplets.

Let's now describe the "low-energy" (typically of O(1 TeV)) parametrization of the SUSY breaking.

$$\begin{aligned} \mathcal{L}_{SUSY} = & \frac{1}{2}(M_1\tilde{B}\tilde{B} + M_2\tilde{W}\tilde{W} + M_3\tilde{g}\tilde{g} + h.c.) \\ & + \tilde{Q}_L^\dagger M_{Q_L}^2 \tilde{Q}_L + \tilde{U}_R^\dagger M_{U_R}^2 \tilde{U}_R + \tilde{D}_R^\dagger M_{D_R}^2 \tilde{D}_R + \tilde{L}_L^\dagger M_{L_L}^2 \tilde{L}_L + \tilde{\ell}_R^\dagger M_{\ell_R}^2 \tilde{\ell}_R \\ & + (\tilde{U}_R^\dagger A_{U_R}^2 \tilde{Q}_L \Phi_u - \tilde{D}_R^\dagger A_{D_R}^2 \tilde{Q}_L \Phi_d - \tilde{\ell}_R^\dagger A_{\ell_R}^2 \tilde{L}_L \Phi_d + h.c.) \\ & + M_{\Phi_u}^2 \Phi_u^* \Phi_u + M_{\Phi_d}^2 \Phi_d^* \Phi_d + (B\mu\Phi_u\Phi_d + h.c.) \end{aligned} \quad (2.76)$$

where

- M_1, M_2, M_3 : the gaugino masses (bino, wino, gluino, respectively)
- $M_{Q_L}, M_{Q_R}, M_{L_L}, \dots$: hermitian 3×3 mass matrices
- B, A : bilinear and trilinear complex couplings among scalars

To sum up, this part of the lagrangian is responsible for parametrizing the SUSY breaking, i.e. generating the masses of the SUSY particles. And it introduces 105 additional free parameters on top of the 19 of the SM included within \mathcal{L}_{SUSY} .

2.2.3.3 Electroweak Symmetry Breaking in the MSSM

2.2.3.3.a Scalar Potential

As seen in Tab. 2.3, the MSSM has two Higgs doublets:

$$\Phi_u = \begin{pmatrix} \phi_u^+ \\ \phi_u^0 \end{pmatrix} \text{ and } \Phi_d = \begin{pmatrix} \phi_d^0 \\ \phi_d^- \end{pmatrix} \quad (2.77)$$

The scalar potential receives contributions from the different sources evoked in the previous paragraphs:

$$V_{Higgs} = V_D + V_F + V_{SUSY}$$

. V_D gathers the contributions from the quartic Higgs interactions from the D-terms, V_F contains the F-term contribution from the superpotential, and $V_{\cancel{SUSY}}$ provides the contribution from the soft SUSY breaking terms. Quantitatively, at tree level, we have:

$$V_D = \frac{g_1^2}{8} [|\Phi_u|^2 - |\Phi_d|^2]^2 + \frac{g_2^2}{8} [4|\Phi_d^\dagger \Phi_u|^2 - 2|\Phi_d|^2 |\Phi_u|^2 + (|\Phi_u|^2 |\Phi_d|^2)^2] \quad (2.78)$$

$$V_F = \mu^2 (|\Phi_u|^2 + |\Phi_d|^2) \quad (2.79)$$

$$V_{\cancel{SUSY}} = M_{\Phi_d}^2 \Phi_d^\dagger \Phi_d + M_{\Phi_u}^2 \Phi_u^\dagger \Phi_u + B\mu(\Phi_u \Phi_d + h.c.) \quad (2.80)$$

The EW symmetry breaking is triggered by the vev's acquired by Φ_u and Φ_d :

$$\langle 0|\Phi_u|0 \rangle = v_u \text{ and } \langle 0|\Phi_d|0 \rangle = v_d \quad (2.81)$$

which are related to the SM Higgs vev (v) by:

$$v^2 = v_u^2 + v_d^2 = \frac{2M_Z^2}{g_1^2 + g_2^2} = (246 \text{ GeV})^2 \quad (2.82)$$

and the relative contributions of Φ_u and Φ_d to this vev are controlled by:

$$\tan\beta = \frac{v_u}{v_d}, \text{ with } 0 < \beta < \frac{\pi}{2}. \quad (2.83)$$

The minimum of the scalar potential breaks $SU(2)_L \times U(1)_Y$ while preserving $U(1)_{EM}$, and one may choose:

$$\frac{\partial V_{Higgs}}{\partial \phi_u^0} = \frac{\partial V_{Higgs}}{\partial \phi_d^0} = 0. \quad (2.84)$$

2.2.3.3.b The Higgs bosons in the MSSM

The two Higgs doublets (of complex scalar fields) represent $N_{dof} = 8$, 3 of which are "eaten" by W_L^\pm and Z_L^0 . Therefore the MSSM spectrum has 5 physical Higgs bosons:

- 2 neutral and CP even: h^0 and H^0 (with $M_{h^0} < M_{H^0}$),
- 1 neutral and CP odd: A^0 , and
- 2 charged: H^\pm

To find these physical states, ones needs to develop the Higgs fields components from Eq. 2.77 around V_{Higgs}^{min} into their real and imaginary parts:

$$\Phi_u = \frac{1}{\sqrt{2}} \begin{pmatrix} \phi_u^+ \\ \phi_u^0 = v_u + \phi_u^0 + iP_u^0 \end{pmatrix} \text{ and } \Phi_d = \begin{pmatrix} \phi_d^0 \\ \phi_d^- = v_d + \phi_d^0 + iP_d^0 \end{pmatrix} \quad (2.85)$$

where the real parts correspond to the CP-even Higgs bosons, whilst the CP-odd correspond to the Goldstone bosons. Around V_{Higgs}^{min} , we have:

$$\langle 0|\phi_u^0|0\rangle = v_u/\sqrt{2} \quad (2.86)$$

$$\langle 0|\phi_d^0|0\rangle = v_d/\sqrt{2} \quad (2.87)$$

$$\langle 0|\phi_{u/d}^\pm|0\rangle = 0 \quad (2.88)$$

In these conditions, the Higgs mass matrices are defined by the V_{Higgs} second derivatives:

$$\mathcal{M}^2 = \frac{1}{2} \left(\frac{\partial^2 V_{Higgs}}{\partial \phi_u^0 \partial \phi_d^0} \right)_{Min.Cond.} \quad (2.89)$$

In the basis $(Re(\Phi_u)/\sqrt{2}, Re(\Phi_d)/\sqrt{2})$, this gives:

$$\mathcal{M}_{Re}^2 = \begin{pmatrix} -B\mu \tan\beta + M_Z^2 \cos^2\beta & B\mu - M_Z^2 \sin\beta \cos\beta \\ B\mu - M_Z^2 \sin\beta \cos\beta & -B\mu \cot\beta + M_Z^2 \sin^2\beta \end{pmatrix} \quad (2.90)$$

and in the basis $(Im(\Phi_u)/\sqrt{2}, Im(\Phi_d)/\sqrt{2})$:

$$\mathcal{M}_{Im}^2 = \begin{pmatrix} -B\mu \tan\beta & B\mu \\ B\mu & -B\mu \cot\beta \end{pmatrix} \quad (2.91)$$

This latest matrix has a determinant $Det(\mathcal{M}_{Im}^2) = 0$ with one null eigenvalue corresponding to the Goldstone boson and the other eigenvalue given by:

$$M_{A^0}^2 = \frac{B\mu}{\sin 2\beta} \quad (2.92)$$

The latest, injected in the \mathcal{M}_{Re}^2 matrix, leads to its eigenvalues:

$$M_{h^0, H^0}^2 = \frac{1}{2} \left[(M_A^2 + M_Z^2) \mp \sqrt{(M_A^2 + M_Z^2)^2 - 4M_A^2 M_Z^2 \cos^2(2\beta)} \right] \quad (2.93)$$

The same developments can be made with the charged components, leading to the tree level relation:

$$M_{H^\pm}^2 = M_A^2 + M_{W^\pm}^2 \quad (2.94)$$

In addition to the eigenvalues of the mass matrices, we also get a strong mass hierarchy at tree level:

$$M_{H^0} > Max(M_A, M_Z) \quad (2.95)$$

$$M_{H^\pm} > M_{W^\pm} \quad (2.96)$$

$$M_{h^0} \leq Min(M_A, M_Z) \cdot |\cos(2\beta)| \leq M_Z \quad (2.97)$$

Note that the latest inequality implies a Higgs boson lighter than the Z boson. However this tree level prediction is strongly modified by radiative corrections that push this upper bound to about 130 GeV.

At tree level, just two independent parameters are sufficient to describe the MSSM Higgs sector. The usual choice is: $\tan\beta$ and M_A .

2.2.3.4 The Scalar Fermions Sector in the MSSM

The procedure to get the masses of the physical states detailed in 2.2.3.3.b can be applied to the different sectors of the MSSM. For the scalar fermions, in the basis $(\tilde{f}_L, \tilde{f}_R)$, the mass matrix writes:

$$M_{\tilde{f}}^2 = \begin{pmatrix} M_{\tilde{f}}^2 + M_{LL}^2 & M_{\tilde{f}}^2 \cdot X_f \\ M_{\tilde{f}}^2 \cdot X_f & M_{\tilde{f}}^2 + M_{RR}^2 \end{pmatrix} \quad (2.98)$$

with

$$M_{LL}^2 = M_{\tilde{f}_L}^2 + (I_{3L}^f - Q^f \sin^2\theta_W) M_Z^2 \cos(2\beta) \quad (2.99)$$

$$M_{RR}^2 = M_{\tilde{f}_R}^2 + Q^f \sin^2\theta_W M_Z^2 \cos(2\beta) \quad (2.100)$$

$$X_f = A_f - \mu(\tan\beta)^{-2I_{3L}^f} \quad (2.101)$$

The mass eigenvalues are:

$$M_{\tilde{f}_{1,2}}^2 = M_f^2 + \frac{1}{2} \left[(M_{LL}^2 + M_{RR}^2) \mp \sqrt{(M_{LL}^2 - M_{RR}^2)^2 + 4M_{\tilde{f}}^2 X_f^2} \right] \quad (2.102)$$

Given that the off-diagonal entry in the mass matrices is proportional to the corresponding SM fermion mass, we can expect a strong mixing for the SUSY partners of the heavy fermions: especially the stops, but also the sbottoms and the staus. In such case, say for the stops, the eigenvalues $M_{\tilde{t}_{1,2}}$ ⁴ have a large mass splitting, rendering the lightest stop \tilde{t}_1 much lighter than the other squarks.

For the sleptons, we have the tree level relation: $M_{\tilde{\ell}_L}^2 = M_{\tilde{\nu}_L}^2 - M_W^2 \cos(2\beta)$ which is always well observed for the selectron and the smuons, but might be broken in case of a large splitting for the staus.

At tree level, 5 or 6 independent parameters are necessary to describe the MSSM sfermion sector per flavour. For the squarks, these parameters are: $\tan\beta$, μ , $M_{\tilde{Q}_L}$, $M_{\tilde{U}_R}$, $M_{\tilde{D}_R}$, and A_f . And for the sleptons, one may take: $\tan\beta$, μ , $M_{\tilde{L}_L}$, $M_{\tilde{\ell}_R}$, and A_f .

2.2.3.5 The Gaugino Sector in the MSSM

There is no mixing in the case of the gluinos for which the $SU(3)_C$ eigenvectors are identical to the mass eigenvectors. In this case, we just have at tree level: $M_{\tilde{g}} = M_3$ and this single parameter is sufficient.

This situation does not prevail for the SUSY partners of the SM EW bosons. The charged ones, the 2 charged higgsinos $\tilde{\phi}_{u,d}^\pm$ and winos $\tilde{W}_{1,2}^\pm$, mix to form the 2 charginos $\tilde{\chi}_{1,2}^\pm$. In a basis where $\psi^{+T} = (-i\tilde{W}^+, \tilde{\phi}_u^+)$ and $\psi^{-T} = (-i\tilde{W}^-, \tilde{\phi}_d^-)$, the mass matrix writes:

⁴the convention in the MSSM is that the index increases with the mass

$$M_C = \begin{pmatrix} M_2 & \sqrt{2}M_W \sin\beta \\ \sqrt{2}M_W \cos\beta & \mu \end{pmatrix} \quad (2.103)$$

Since this matrix is not symmetric (unless $\tan\beta = 1$), two separate unitary matrices U and V are necessary to diagonalize M_C :

$$\text{Diag}(M_C) = U^* M_C V^{-1} \quad (2.104)$$

$$\begin{pmatrix} \tilde{\chi}_1^- \\ \tilde{\chi}_2^- \end{pmatrix} = U \begin{pmatrix} \tilde{W}^- \\ \tilde{\phi}_d^- \end{pmatrix} \quad (2.105)$$

$$\begin{pmatrix} \tilde{\chi}_1^+ \\ \tilde{\chi}_2^+ \end{pmatrix} = V \begin{pmatrix} \tilde{W}^+ \\ \tilde{\phi}_u^+ \end{pmatrix} \quad (2.106)$$

The eigenvalues are:

$$M_{\tilde{\chi}_{1,2}^\pm}^2 = \frac{1}{2} \left[(M_2^2 + \mu^2 + 2M_W^2) \mp \sqrt{(M_2^2 + \mu^2 + 2M_W^2)^2 - 4(\mu M_2 - M_W^2 \sin(2\beta))^2} \right] \quad (2.107)$$

At tree level, 3 independent parameters are necessary to describe the MSSM chargino sector. These parameters are: $\tan\beta$, μ , and M_2 .

Similarly, the 2 neutral higgsinos $\tilde{\phi}_{u,d}^0$ and the neutral bino \tilde{B} and the neutral wino \tilde{W}_3^0 , mix to form the 4 neutralinos $\tilde{\chi}_{1,2,3,4}^0$. In a basis where $\psi^0 = (-i\tilde{B}, -i\tilde{W}_3^0, \tilde{\phi}_d^0, \tilde{\phi}_u^0)$, the neutralino mass matrix is:

$$M_N = \begin{pmatrix} M_1 & 0 & -M_Z \cos\beta \sin\theta_W & M_Z \sin\beta \sin\theta_W \\ 0 & M_2 & M_Z \cos\beta \cos\theta_W & -M_Z \sin\beta \cos\theta_W \\ -M_Z \cos\beta \sin\theta_W & M_Z \cos\beta \cos\theta_W & 0 & -\mu \\ M_Z \sin\beta \sin\theta_W & -M_Z \sin\beta \cos\theta_W & -\mu & 0 \end{pmatrix} \quad (2.108)$$

A single unitary matrix N is sufficient to diagonalize M_N :

$$\text{Diag}(M_{\tilde{\chi}_1^0}, M_{\tilde{\chi}_2^0}, M_{\tilde{\chi}_3^0}, M_{\tilde{\chi}_4^0}) = N^* M_N N^{-1} \quad (2.109)$$

The analytic expression of the eigenvalues is quite long. It was established for the first time in Ref. [39].

At tree level, 4 independent parameters are necessary to describe the MSSM neutralino sector. These parameters are: $\tan\beta$, μ , M_1 , and M_2 .

2.2.4 The Assessts of Supersymmetry

Like in the section describing the SM, we'll detail the situation of the Higgs boson mass radiative corrections (illustrated with just generic scalars and fermions hereafter) in the MSSM and just give a non-exhaustive list of SM open questions for which SUSY can provide a solution.

In the MSSM with N_S scalars of mass M_S , and trilinear and quadrilinear couplings of $v\lambda_S$ and λ_S , the radiative correction to M_h is:

$$\Delta M_h^2(S) = \frac{\lambda_S N_S}{16\pi^2} \left[-\Lambda^2 + \lambda_S v^2 + 2(M_S^2 - \lambda_S v^2) \text{Log}\left(\frac{\Lambda}{M_S}\right) \right] \quad (2.110)$$

In contrast, the corresponding contribution from the fermion loops writes:

$$\Delta M_h^2(f) = \frac{\lambda_f^2 N_f}{8\pi^2} \left[-\Lambda^2 + 2M_f^2 \left(3\text{Log}\left(\frac{\Lambda}{M_f}\right) - 1 \right) \right] \quad (2.111)$$

The quadratic divergences are still manifest in both contributions. However, by expliciting the SUSY hypotheses:

- "Opposite" Higgs couplings: $\lambda_f^2 = \frac{2M_f^2}{v^2} = -\lambda_S$
- Equal N_{dof} : $N_S = 2N_f$

one gets a sum of these contributions that writes:

$$\Delta M_h^2(Total) = \frac{\lambda_f^2 N_f}{4\pi^2} \left[(M_f^2 - M_S^2) \text{Log}\left(\frac{\Lambda}{M_f}\right) + 3M_f^2 \text{Log}\left(\frac{M_S}{M_f}\right) \right] \quad (2.112)$$

in which the quadratic divergences have cancelled out and where we're left with a logarithmic dependence on Λ . If SUSY was an exact low energy symmetry, $M_S = M_f$ and the above contributions would exactly cancel each other. With a broken SUSY, the constraint of keeping M_h at the EW scale, impose a constraint on $M_f^2 - M_S^2$ which must remains smaller than about 1 TeV².

Nowadays, SUSY is still considered to be the favourite venue beyond the SM. Here is a list of motivations:

- It could be the largest symmetry of space-time (non-trivial with respect to gauge symmetries).
- Local SUSY sets a framework for a quantum theory of gravity and SUSY is a key ingredient for superstring and M-theories.
- In large fractions of the MSSM parameter space, $\tilde{\chi}_1^0$ is the lightest SUSY particle (LSP). Provided that R-parity is conserved, the LSP is an excellent candidate for Cold Dark Matter.
- In the MSSM one needs a light Higgs boson (lighter than 130 GeV): this is compatible with the discovery of the Higgs boson with $M_h = 125$ GeV.
- When extrapolating the the strong, weak and EM coupling constants at high energy, their unification is achieved in the framework of SUSY, whilst it fails in that of the SM.
- In the SM the μ^2 parameter in the Higgs potential is arbitrary. In the MSSM it is related to the EW coupling constants.

-
- In SUSY Grand Unified models, there's a dynamically induced EW symmetry breaking essentially due to the top and stop renormalization.
 - Because fermion and boson loops have opposite signs (spin-statistics theorem), SUSY can solve the SM hierarchy problem, provided that some of its particles are not too heavy with respect to the TeV scale.

Chapter 3

Search for Higgs Bosons at LEP

3.1 Instrumental Aspects

3.1.1 LEP

The LEP was the former e^+e^- collider that was used at CERN between 1989 and 2000. It was built in a tunnel with a radius $R=4.25$ km, at the french-swiss border, about 100 m underground. This collider was dismantled in 2001 in order to mount the current LHC in the same tunnel.

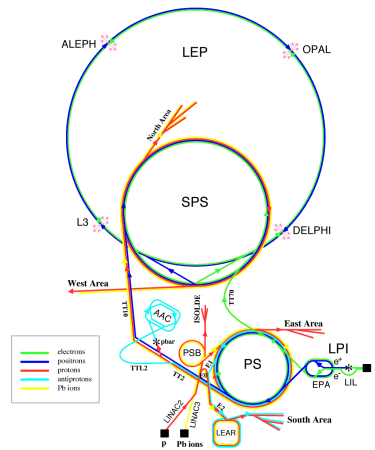


FIGURE 3.1: LEP accelerator complex at CERN.

The electron and the positron beams were accelerated in the injection complex made of the LIL ($E_{beam} = 600$ MeV), the EPA accumulation ring ($R=125.7$ m), the PS with $E_{beam} = 3.5$ GeV ($R=628.5$ m), the SPS with $E_{beam} = 22$ GeV ($R=6.9$ km).

Overall the LEP delivered about an integrated luminosity of about $\int \mathcal{L} dt \approx 2.5 fb^{-1}$ to the 4 experiments (ALEPH, DELPHI, L3 and OPAL) at center-of-mass energies: $189 \leq \sqrt{s} \leq 209$ GeV between 1998 and 2000.

Two different acceleration schemes were used. In the first, electrons and positrons were arranged in 2×4 bunches along the LEP ring. The distance between two bunches was $\Delta t_X = 22 \mu\text{s}$. In the second scheme, the so called "bunch train regime", the bunches were replaced by trains of up to 4 smaller bunchlets, which have a $\Delta t_X = 250$ ns.

The integrated luminosity delivered to the L3 experiment is given in Tab. 3.1.

\sqrt{s} (GeV)	189	192	196	200	202	202-206	206-209
$\int \mathcal{L} dt$ (pb^{-1})	176.4	29.8	84.1	83.3	37.1	145.3	72.0

TABLE 3.1: Integrated luminosities delivered to the L3 experiment as a function of the center-of-mass energy of the e^+e^- collisions. These numbers include the data quality requirements for the L3 analyses.

3.1.2 L3 Detector

The L3 detector has been designed to optimize the energy resolution for the electrons and the photons as well as the momentum resolution for muons above 2 GeV. Fig. 3.2 shows a sketch of this detector. The origin of the right-handed coordinate system is in the geometric centre of the detector. The positive z -axis coincides with the direction of the electron beam. The y -axis points vertically upwards and the x -axis towards the centre of the LEP ring. The distance between a point in the x - y plane and the geometric centre of the detector is the radius r . The azimuthal angle between the radius vector r and the positive x -axis is denoted ϕ . The polar angle between the direction of a particle and the electron direction is called θ . The particles produced at the interaction point and their decay products encounter the following sub-detectors while traversing L3:

- SMD: silicon microvertex detector
- TEC: time expansion wire chamber (and Z chambers)
- EM calorimeter: made of BGO crystals
- Scintillators
- HCAL: hadronic calorimeter
- MUCH: muon chambers
- Luminosity monitor

All the sub-detectors except for the muon chambers are contained inside the 32 m long steel support tube with a diameter of 4.45 m. A solenoid coil with an inner radius of 5.9 m produces a magnetic field along the z -axis of 0.5 Tesla in which all sub-detectors (except for the forward backward muon chambers) are placed. This magnetic field forces a charged particle onto a helicoidal trajectory. The curvature of this trajectory is used to determine the particle's charge and the momentum transverse to the beam direction. The various sub-detectors will be described in more detail in the subsequent sections.

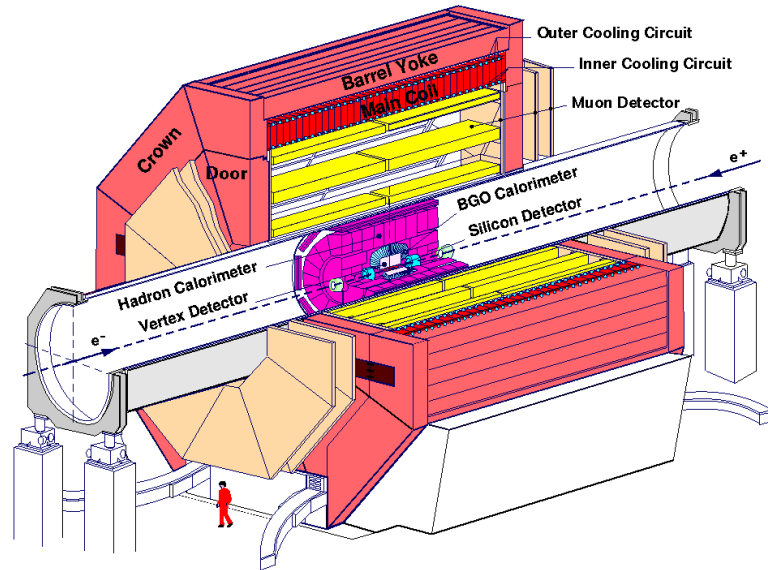


FIGURE 3.2: L3 Detector

3.1.2.1 Silicon Microvertex Detector

The Silicon Microvertex Detector (SMD) is directly attached to the beryllium beam pipe of LEP which has a radius of 5.3 cm. This detector is used to measure charged particles at a close distance of the interaction point to resolve possible secondary vertices which arise from the decay of short-lived particles such as hadrons containing b quarks. The SMD is made up of two cylindrical layers. The mean radius of the cylinders amounts 6 cm and 8 cm, respectively. The length of the SMD is 30 cm which yields a polar angle coverage of $22^\circ \leq \theta \leq 158^\circ$. Each of the layers has 12 modules (ladders) which are made up of two electrically independent half-ladders. The half-ladders consist of two double-sided silicon sensors. Each of these sensors is 70 mm long, 40 mm wide and made of 300 μm thick high purity n-type silicon. On one side (junction side) of the sensors there are implantation strips every 25 μm with a readout pitch of 50 μm . They run parallel to the beam axis and allow therefore the determination of the $r - \phi$ coordinate. On the other side the implantation strips are arranged perpendicular to the junction side strips with a pitch of 50 μm . The readout pitch is 200 μm for $0.53 \leq |\cos\theta| \leq 0.93$ and 150 μm for $|\cos\theta| \leq 0.53$. These strips are used for the z measurement. A resolution of 7.5 μm in $r - \phi$ and 14.3 μm in z is obtained.

3.1.2.2 Central Tracking Chambers

The central tracking chambers allow the reconstruction of charged tracks in $r - \phi$ and z . For the $r - \phi$ measurement two concentric drift chambers are used which operate in a time expansion mode. The drift chambers are subdivided into sectors. The anode and cathode wires are drawn in the z direction. The inner drift chamber consists of 12 sectors with 8 anode wires each. The outer drift chamber is subdivided into 24 sectors with 54 wires each. The inner and the outer radius of the TEC is 9.15 cm and 45.6 cm respectively. The length is 126 cm. The anode planes are surrounded by grid planes which divide the drift regions in areas of different field strength. The

small field strength between the cathode and the grid plane leads to a small drift velocity which results in a very good spatial resolution. In the region of high field strength gas amplification occurs and the electron avalanche is detected by the anodes. In order to resolve the left right ambiguity additional wires in the grid plane are read out. The gas mixture consists of 80% of CO₂ and of 20% isobutane. The drift velocity is 6 $\mu\text{m}/\text{ns}$. In $r - \phi$ a resolution of (50-60) μm is obtained. Some anode wires are read out on both sides. These signals are used to obtain a rough z coordinate (resolution of a few cm's) by means of the charge division principle. Particles with a polar angle between 42° and 138° will pass through the Z chamber. This detector supplements the measurements of the TEC and the SMD with a z coordinate at $r = 50$ cm. It consists of two multiwire proportional chambers with cathode readout. The anode wires are aligned in z direction. The two chambers contain two cathode layers each. The cathode layers are made of 240 strips with a pitch of 4.45 mm. The strips of two of the layers are arranged perpendicular to the z direction (z layer) and the strips of the other two layers run under a stereo angle of $\pm 69^\circ$. The gas mixture consists of 80% of argon, 16% of CO₂ and of 4% of isobutane. A charged particle traversing the chamber ionizes the gas. The resulting electron avalanche around the anode wire induces image charges on the cathode layers. The relative amount of the signal measured on the individual cathode strips is used for the coordinate determination. The ϕ component of the stereo layer allows the matching of the cluster with a TEC track. The z layers are used for the measurement of the z coordinate. The resolution varies depending on the polar angle. At $\cos\theta = 0$ the resolution is about 200 μm whereas at $|\cos\theta| = 0.74$ the resolution is 1000 μm . The special design of the readout electronics can be used to tag the interacting bunchlet when LEP is operating in the bunch train mode.

3.1.2.3 Electromagnetic Calorimeter

The electromagnetic calorimeter (BGO) allows the very precise measurement of electrons and photons with energies between 100 MeV and 100 GeV. It consists of bismuth germanate ($\text{Bi}_4\text{Ge}_3\text{O}_{12}$) crystals pointing to the interaction region. The crystals have a length of 24 cm, a front face of 2×2 cm² and a rear face of 3×3 cm². In the central part of the detector (barrel) there are 7680 crystals. They cover the polar angle $42^\circ \leq \theta \leq 138^\circ$. In the forward-backward region (endcap) of the detector there are 2×1527 BGO crystals which cover the angles $11.6^\circ \leq \theta \leq 38^\circ$ and $142^\circ \leq \theta \leq 168.4^\circ$. The scintillation light of the BGO crystals is collected by two photodiodes which are mounted at the rear face of the crystals. The energy resolution is 5% at 100 MeV and less than 2% at energies larger than 1 GeV. The gaps between the barrel and the endcap BGO crystals are filled with lead-scintillating fibre calorimeters (SPACAL). They consist of 24 modules (bricks) containing a lead structure filled with scintillating fibres. The scintillation light is collected by phototriodes glued on the rear site of the bricks. The resolution of the SPACAL is 15% at 45 GeV.

3.1.2.4 Scintillators

The scintillator system consists of 30 single plastic counters in the barrel and 2×16 in the endcaps. They were located between the ECAL and the HCAL. The time resolution is about

800 ps in the barrel and 1.9 ns in the endcaps. The scintillators therefore allow the discrimination of cosmic muons with respect to collision muons. When the LEP was operating in the bunch train mode they were used to tag the bunchlet.

3.1.2.5 Hadron Calorimeter

The energy of hadrons is measured in the hadron calorimeter. As in the case of the BGO, it also consists of a barrel and two endcap parts. The barrel calorimeter allows the energy measurement within $35^\circ \leq \theta \leq 145^\circ$ whereas the endcap calorimeters cover the angles $5.5^\circ \leq \theta \leq 35^\circ$ and $145^\circ \leq \theta \leq 174.5^\circ$ in the forward-backward region of the detector. The central part of the hadron calorimeter contains 9 rings with 16 modules. These modules consist of depleted uranium absorber plates with a width of 5.5 mm interspersed with proportional wire chambers. There are in total 7968 chambers in the barrel part. The two endcaps are each built up of one outer and two inner rings. Each of these rings contains 12 modules. The material, which a particle arising from the interaction point, has to traverse depends on the polar angle and varies between 6 and 7 nuclear absorption lengths. A muon filter, mounted on the inside wall of the support tube, adds an additional absorption length which suppresses the flow of secondary particles produced in the hadron calorimeter into the muon chambers. The hadron jet energy resolution of the calorimeter is $\frac{\sigma_E}{E} = \frac{55\%}{\sqrt{E}} + 8\%$, where E is measured in GeV. The direction of the jet axis can be measured with a angular resolution of about 2.5° .

3.1.2.6 Muon Detector

The muon chamber system is the largest detector in the L3 experiment. It envelopes all other detector components. It was designed to measure muon momenta with very high precision. The barrel part of the detector covers the polar angle range from 44° to 136° . It consists of two halves with a gap at $z = 0$. Each of the halves is subdivided into octants. Each octant consists of five precision drift chambers (P-chambers) which are arranged in three layers. The outer and inner chambers contain 16 wires each whereas the middle chambers are equipped with 24 wires. In order to determine the z -coordinate of a muon track, there is a set of Z-chambers mounted on the top and the bottom of the inner and the outer layer. The design resolution for muons measured in all 3 layers is $\frac{\sigma_z}{p} \approx 2.5\%$ at 45 GeV. The barrel part of the muon detector is complemented with a forward-backward spectrometer covering the polar angles $24^\circ \leq \theta \leq 44^\circ$ and $136^\circ \leq \theta \leq 156^\circ$. Three rings consisting of 16 drift chambers are attached to the magnet doors. They are triggered by Resistive Plate Counters (RPCs) which are mounted at the rings. The magnet doors are wrapped up with coils producing a toroidal magnetic field of 1.2 T. The resolution depends on the polar angle or, more precisely, whether the inner and middle layers of the barrel detector were also hit by the muon. The momentum resolution varies from 6% at $\theta = 43^\circ$ to 35% at $\theta = 28^\circ$.

3.1.2.7 Luminosity Monitor

A precise knowledge of the luminosity is very important for most of the measurements made at LEP. This is achieved by measuring low-angle Bhabha scattering and comparing the measured rate with a precise theoretical calculation. The L3 luminosity monitor consists of two electromagnetic calorimeters complemented with two silicon trackers. These two sets are located at $z = \pm 2.7$ m and cover the polar angles $24.93 \leq \theta \leq 69.94$ mrad.

3.1.2.8 Trigger System

An efficient trigger system is needed to separate interesting physics events from those events which just contain energy deposits caused by beam-gas, beam-wall interactions, synchrotron radiation or detector noise. All sub-detectors are prepared for data taking by the beam crossing signal ($\approx 1.7\mu\text{s}$ before the electron and the positron bunches are expected to collide). The number of events written to tape is reduced in 3 steps. The first step (level-1 trigger) takes individual information from the sub-detectors into account. These are track information from the TEC (inner and outer TEC triggers), energy deposits in the calorimeters (energy trigger), scintillator hits (scintillator trigger), energy deposits in the luminosity monitor (luminosity trigger) and tracks in the muon chamber (muon trigger). If one of these triggers has fired, the event is passed to the level-2 trigger, where more time is available to make a first cross check between the individual triggers. This removes already a large fraction of the background events mentioned above. If an event was accepted by more than one trigger, the event is not rejected. At the trigger level-3 the full information of an event is available. The correlation between the individual sub-detector information is exploited and tighter requirements on the individual decisions can be made. Events with multiple positive decisions on trigger level-1 or with luminosity trigger are not rejected. All events passing the trigger level-3 decision are written to tape.

3.2 Phenomenology of the Higgs Boson at LEP

3.2.1 Production Mechanisms

The dominant production mechanism for the Higgs boson is the s-channel Higgs-strahlung process. There's also a contribution from the t-channel VV fusion (where $V = W^\pm$ or Z^0) as shown in Fig. 3.3 (left). The resulting cross sections are displayed in Fig. 3.3 (right) as a function of the Higgs boson mass.

3.2.2 Decay Modes

Since the coupling of the Higgs boson to any SM particle is proportional to that particle mass (be it a gauge boson or a fermion), the Higgs boson will decay dominantly into pairs of the heaviest particles compatible with the available phase space. The dominant decay modes of the Higgs boson (plus a rare one) and their branching ratios are displayed in Fig. 3.4.

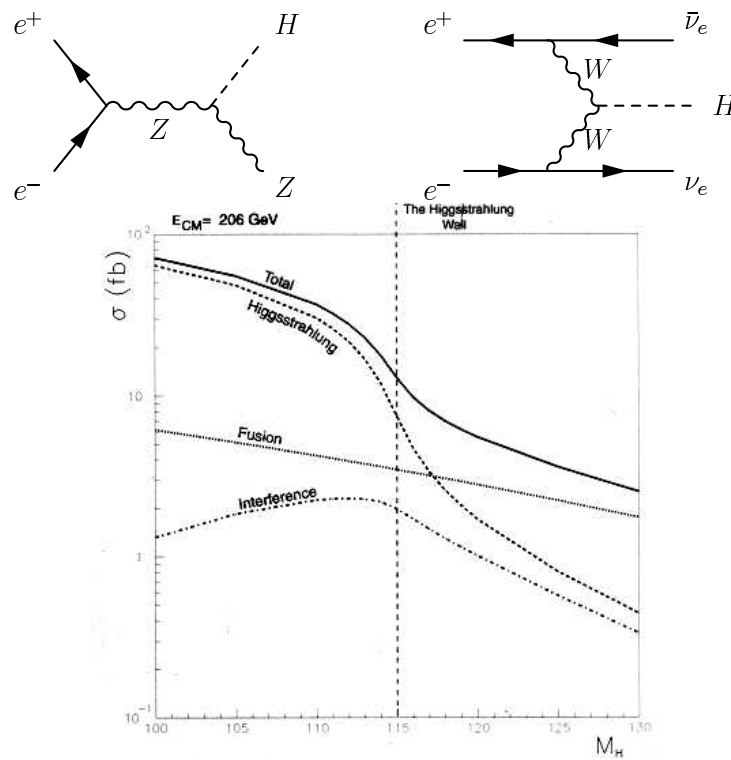


FIGURE 3.3: Higgs boson production mechanism (left) and cross section at $\sqrt{s} = 206$ GeV (right).

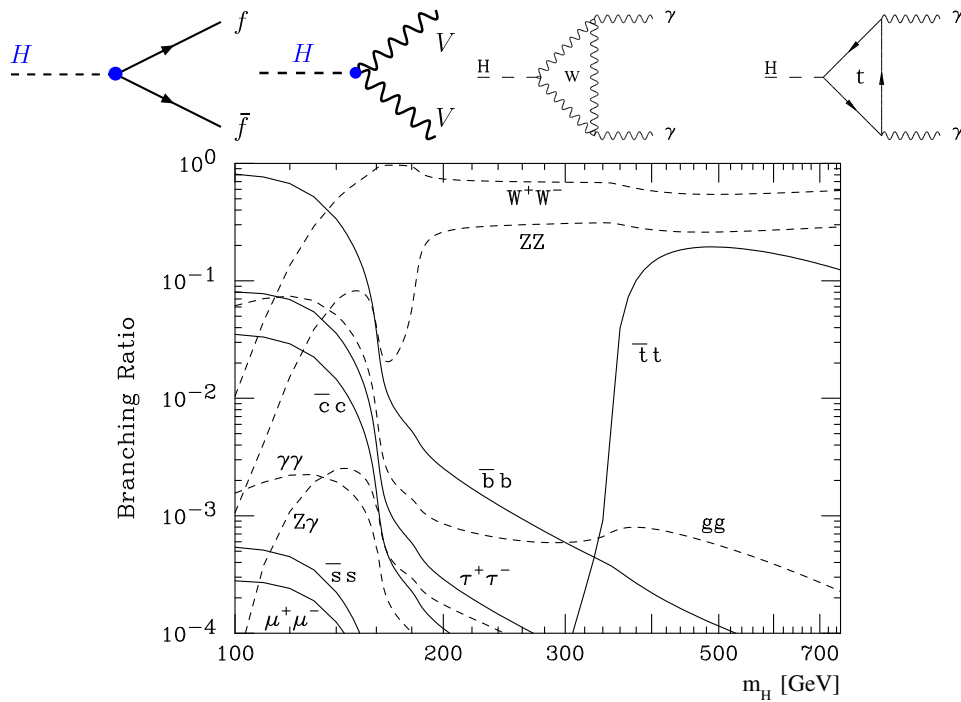


FIGURE 3.4: Higgs boson decay modes and their branching ratios.

3.2.3 Search for the Standard Model Higgs Boson

Standard Model Higgs Boson with the L3 Experiment at LEP L3 Collaboration

Abstract

Final results of the search for the Standard Model Higgs boson are presented for the data collected by the L3 detector at LEP at centre-of-mass energies up to about 209 GeV. These data are compared with the expectations of Standard Model processes for Higgs boson masses up to 120 GeV. A lower limit on the mass of the Standard Model Higgs boson of 112.0 GeV is set at the 95% confidence level. The most significant high mass candidate is a $H\nu\bar{\nu}$ event. It has a reconstructed Higgs mass of 115 GeV and it was recorded at $\sqrt{s} = 206.4$ GeV.

3.2.3.1 Introduction

One of the most important goals of the L3 experiment at the LEP e^+e^- collider was to find the Higgs boson. In the Standard Model this particle is associated to the Higgs field, expected to provide mass to all the observed elementary particles. The mass of the Higgs boson, m_H , is not predicted by the theory. Before the advent of LEP, there was no solid experimental information about the Higgs mass. The L3 experiment has carried out the search for the Higgs boson at LEP in very large data samples collected at the Z resonance [198] and at ever increasing centre-of-mass energies and luminosities [199–203] greatly extending the Higgs mass range investigated.

A fit that includes L3 electroweak precision measurements results in an upper limit on m_H of 133 GeV [204] at the 95% confidence level. Previous L3 direct searches for the Standard Model Higgs boson excluded the mass range up to 107 GeV [202]. Similar results were also reported by other LEP experiments [205]. Results of the Standard Model Higgs search obtained shortly after the end of the LEP data taking in the year 2000 were also published by L3 [203] and by the other LEP experiments [206].

The Standard Model Higgs boson is produced at LEP mainly via the Higgs-strahlung process $e^+e^- \rightarrow HZ$. The processes of WW and ZZ fusion contribute, with smaller rate, to the Higgs production in the $H\nu\bar{\nu}$ and He^+e^- channels, respectively. The largest sources of background are four-fermion final states from W and Z pair production, as well as quark pair production $e^+e^- \rightarrow q\bar{q}(\gamma)$.

In this letter, the final results of the Standard Model Higgs search performed on the data collected by L3 at LEP at a centre-of-mass energy, \sqrt{s} , up to about 209 GeV are reported. These results include the full luminosity collected in the year 2000 and the corrected LEP beam energies. In the year 2000 LEP was run at several values of \sqrt{s} . The slight beam energy adjustments significantly affect the signal expectation at the highest Higgs masses, close to the kinematic limit for HZ production, $m_H = \sqrt{s} - m_Z$, where m_Z is the Z boson mass. The effect of the Z width in the Higgs mass reconstruction close to the HZ kinematic limit is also taken into account. Final calibrations of all subdetectors are applied. The signal and background expectations are evaluated on a finer grid of \sqrt{s} values, with larger samples of simulated events, thus reducing

statistical and systematic uncertainties. Therefore, the results reported in this letter are affected by total uncertainties smaller than in Reference [203].

3.2.3.2 Data and Monte Carlo samples

The data were collected by the L3 detector [207] at LEP during the year 2000 at several centre-of-mass energies. The total collected luminosity amounts to 217.3 pb^{-1} . The data are grouped into seven samples corresponding to average centre-of-mass energies between 202.8 GeV and 208.6 GeV. The integrated luminosities corresponding to these samples are given in Table 3.2.

The Higgs production cross sections and branching ratios are calculated using the HZHA generator [208]. Efficiencies are determined using Monte Carlo samples of Higgs events, generated with PYTHIA [209]. Since the Higgs production cross sections and efficiencies depend strongly on \sqrt{s} , in particular for m_H close to the HZ kinematic limit, samples of Higgs events are simulated at each centre-of-mass energy shown in Table 3.2. Higgs events are generated with m_H between 105 and 120 GeV, in steps of 1 GeV. For each mass and each search channel, between 2000 and 10000 events are generated.

The Standard Model background estimates rely on the following Monte Carlo programs: KK2f [210] for $e^+e^- \rightarrow q\bar{q}(\gamma)$, KORALW [211] for $e^+e^- \rightarrow W^+W^-$, PHOJET [212] for two-photon processes ($e^+e^- \rightarrow e^+e^-q\bar{q}$) and EXCALIBUR [213] for other four-fermion final states. The number of simulated events for the dominant backgrounds is at least 100 times the number of events expected for such processes.

The response of the L3 detector is simulated using the GEANT program [214], taking into account the effects of multiple scattering, energy loss and showering in the detector. Hadronic interactions in the detector are modelled using the GHEISHA program [215]. Time dependent detector inefficiencies, as monitored during the data taking period, are also simulated.

3.2.3.3 Analysis procedures

The search for the Standard Model Higgs boson is based on the study of four distinct event topologies: $HZ \rightarrow q\bar{q}q\bar{q}$, $HZ \rightarrow q\bar{q}\nu\bar{\nu}$, $HZ \rightarrow q\bar{q}\ell^+\ell^-$ ($\ell = e, \mu, \tau$) and $HZ \rightarrow \tau^+\tau^-q\bar{q}$.

In the following they are denoted as $Hq\bar{q}$, $H\nu\bar{\nu}$, $H\ell^+\ell^-$ and $\tau^+\tau^-q\bar{q}$, respectively. With the exception of the $HZ \rightarrow \tau^+\tau^-q\bar{q}$ decay mode, all the analyses are optimised for the $H \rightarrow b\bar{b}$ decay. This mode represents about 80% of the Higgs branching fraction in the mass range of interest.

All the search channels are analysed in three stages. First, a high multiplicity hadronic event selection is applied to reduce the large background from two-photon processes, while preserving most of the Higgs signal. In a second stage, topological and kinematical variables together with b-tag variables are either used to construct an event likelihood or fed into a neural network, to further discriminate between signal and background events. A b-tag variable is calculated for each hadronic jet using a neural network [199] which exploits three-dimensional decay lengths,

properties of semileptonic b decays and jet-shape variables. The tracking and b-tagging performance in the Monte Carlo simulation are tuned using 4 pb^{-1} of calibration data collected at $\sqrt{s} \sim m_Z$ in the year 2000. The b-tagging performance for the high-energy data is verified with samples of $e^+e^- \rightarrow q\bar{q}(\gamma)$ events. The efficiency for tagging light flavoured hadrons is verified with $W^+W^- \rightarrow q\bar{q}\ell\nu$ events. The agreement of data with the simulation of Standard Model processes in the jet b-tag variable based on neural network is shown in Figure 3.5 for the $e^+e^- \rightarrow q\bar{q}(\gamma)$ and the $W^+W^- \rightarrow q\bar{q}\ell\nu$ events. The expectation from the Standard Model Monte Carlo describes the data within the statistical uncertainty.

The neural network b-tag variables are combined into an event b-tag variable. First, the probability is calculated for each jet to be compatible with the distribution for light quarks determined from Monte Carlo. Then, the event b-tag variable is defined as the negative log-likelihood of these probabilities.

The last part of the analysis is the construction of a final discriminant for each topology. It is built from a combination of the event likelihood, or the neural network output, with the reconstructed Higgs mass. For each Higgs mass hypothesis, the final discriminants are computed for the data and for the expected background and signal. The distributions of the final discriminants are then used to calculate the likelihood ratio, Q , as a function of m_H . This is the ratio of the probability of observing the data in the presence of both the signal and the background, “signal+background” hypothesis, to the probability of observing the data in the presence of only the background, “background-only” hypothesis. The quantity used to evaluate the compatibility of the data with the signal is the log-likelihood ratio defined by [216]:

$$-2\ln Q \equiv 2 \sum_i [s_i - n_i \ln(1 + s_i/b_i)] .$$

In this expression, i indicates the i -th bin of the final discriminant of each channel and at each \sqrt{s} ; n_i , s_i and b_i indicate respectively the number of observed events, the expected Higgs signal and the Standard Model background, in the i -th bin. Each event in the sum has a weight $\ln(1 + s/b)$ which depends on the signal-to-background ratio, s/b , in the bin where it is found. This weight depends on the Higgs mass hypothesis. For each given m_H , the value of the log-likelihood ratio in the data is compared to the expected distributions of $-2\ln Q$ in a large number of simulated experiments under the “background-only” and the “signal+background” hypotheses. The results for each search channel are then presented in terms of $-2\ln Q$ for the data compared to the expected median values for the two hypotheses, as a function of m_H .

3.2.3.3.a The $Hq\bar{q}$ analysis

The $Hq\bar{q}$ analysis aims to select and study events with four jets, two of which contain b hadrons, while the other two must be consistent with the decay of a Z boson. Background from Standard Model processes comes mainly from $q\bar{q}$ final states with hard gluon radiation, W^+W^- and ZZ events, especially those where one of the Z bosons decays into b quarks.

After a high multiplicity hadronic preselection, the events are forced into four jets with the DURHAM algorithm [231] and a kinematic fit requiring four-momentum conservation is performed. Several discriminating variables, x_i , are combined into a single likelihood which is then used to select the final sample. In this combination, each final state is considered as an event class j ($j=HZ, ZZ, WW, q\bar{q}$). For each class, probability density functions $f^j(x_i)$ are derived from Monte Carlo. The probability for an event to belong to the event class j , based on the value of the variable x_i , is defined as $p^j(x_i) = f^j(x_i) / \sum_k f^k(x_i)$, where k runs over all classes.

The individual probabilities are combined into a likelihood: $L_{HZ} = \prod_i p^{HZ}(x_i) / \sum_k \prod_i p^k(x_i)$, where i runs over all variables considered and k over all event classes. Ten variables are used to calculate the likelihood. They are:

- the number of tracks,
- the event b-tag,
- the maximum energy difference between any two jets,
- the minimum jet energy,
- the parameter of the DURHAM algorithm for which the event is resolved from three jets into four jets,
- the maximal triple-jet boost, defined as the maximum three-jet boost obtained from the four possibilities to construct a one-jet against three-jet configuration in a four-jet event,
- the minimum opening angle between any two jets,
- the event sphericity,
- the mass from a 5C kinematic fit imposing energy and momentum conservation and equal dijet masses, M_{eq}^{5C} ,
- the absolute value of the cosine of the production polar angle, $|\cos \Theta|$, assuming the production of a pair of bosons.

The distributions of the event b-tag, M_{eq}^{5C} , $|\cos \Theta|$ and L_{HZ} for the events selected in the $Hq\bar{q}$ search channel with $\sqrt{s} > 206$ GeV, compared to the expectation for Standard Model processes, are shown in Figure 3.6.

Events are selected into the final sample if the value of L_{HZ} exceeds a threshold optimised for each centre-of-mass energy and each Higgs mass hypothesis. In addition, the compatibility of each event with a Higgs mass hypothesis m_H is tested by the variable $\chi_{HZ}^2 = (\Sigma_i - (m_H + m_Z))^2 / \sigma_{\Sigma_{HZ}}^2 + (\Delta_i - |m_H - m_Z|)^2 / \sigma_{\Delta_{HZ}}^2$. In this expression, Σ_i and Δ_i are the dijet mass sum and dijet mass difference, respectively, for the i -th of the three possible jet pairing combinations, while $\sigma_{\Sigma_{HZ}}$ and $\sigma_{\Delta_{HZ}}$ are the corresponding resolutions for Higgs events. The jet pairing with the best χ^2 is chosen. Finally, only events with the χ^2 probability above 0.01 are selected. As an example, for $m_H = 110$ GeV, 179 events are selected in the data with 172 expected from background processes and 12.8 events expected from the Higgs signal; for $m_H = 115$ GeV, 149 events are observed with 142 from background and 3.2 from the Higgs signal.

For these events a final discriminant is constructed. At first, the events are classified into three categories depending on the values of the b-tag of the two jets assigned to the Higgs boson. The first category contains events where none of these jets has the highest value of the b-tag among the four jets of the event. The second category is composed of events where one of these jets has the highest b-tag value. The third category contains events where the two jets assigned to the Higgs boson have the highest b-tag values. The χ_{HZ}^2 probability, the b-tag values of the individual jets and the event category are then combined into the final discriminant.

3.2.3.3.b The $H\nu\bar{\nu}$ analysis

The $H\nu\bar{\nu}$ search is based on the selection of events with two jets containing b hadrons, with large missing energy and missing mass consistent with m_Z . A neural network is used for the $H\nu\bar{\nu}$ analysis, very similar to the one previously reported [202, 203]. However, tighter cuts on radiative photons and on the jet polar angle are applied to reduce the $e^+e^- \rightarrow q\bar{q}(\gamma)$ background and ensure the best jet energy and b-tag measurements. The signal efficiency is slightly reduced by a few percent relative but the search performance is not significantly modified. In addition, the neural network is trained with the final, high statistics, signal and background Monte Carlo samples, at each \sqrt{s} value, to maximise the sensitivity of the analysis.

In the first step of the analysis, high multiplicity hadronic events are selected and forced into two jets using the DURHAM algorithm. The dijet invariant mass must exceed 40 GeV. These requirements reduce contributions from two-photon interactions, while retaining a significant fraction of hadronic events from $e^+e^- \rightarrow q\bar{q}(\gamma)$ and W-pair production. These backgrounds are then reduced by requiring the visible mass to be less than 140 GeV and the mass recoiling against the hadronic system to lie between 50 GeV and 130 GeV.

Events from $e^+e^- \rightarrow q\bar{q}(\gamma)$ are further suppressed by requiring the longitudinal missing energy to be less than $0.6\sqrt{s}$ and the missing momentum vector to be at least 16° away from the beam axis. The energy in the forward luminosity calorimeter is required to be below 20 GeV. The acollinearity is required to be smaller than 65° . The distribution of the event b-tag after the above cuts is shown in Figure 3.7 a. A loose cut requiring the event b-tag to be larger than 0.5 is then applied, without further loss of signal efficiency. After this set of cuts, there are 123 events in the data, while 130 are expected from background processes with 4.3 and 1.3 events expected for $m_H = 110$ GeV and 115 GeV, respectively.

A kinematic fit imposing four-momentum conservation and requiring the missing mass to be consistent with m_Z is performed to compute the reconstructed Higgs mass from the two jets. The output of a mass independent neural network [200] is then combined with the reconstructed Higgs mass to build the final discriminant. The distributions of the reconstructed Higgs mass, the missing mass and the neural network output for the events selected in the $H\nu\bar{\nu}$ search channel with $\sqrt{s} > 206$ GeV, compared to the expectation for Standard Model processes, are shown in Figure 3.7. General agreement between the data and the expected contributions from Standard Model processes is observed in all the distributions.

3.2.3.3.c The $H\ell^+\ell^-$ and $\tau^+\tau^-q\bar{q}$ analyses

The signatures for the He^+e^- and $H\mu^+\mu^-$ processes are a pair of high energy electrons or muons with an invariant mass compatible with m_Z and two hadronic jets with b quark content. In $H\tau^+\tau^-$ events the tau pair invariant mass must also be compatible with m_Z . For these events, the mass resolution is worse than in the other $H\ell^+\ell^-$ channels due to the missing neutrinos from the tau decays. Events with Higgs decaying into tau leptons, $\tau^+\tau^-q\bar{q}$, have similar signature to the $H\tau^+\tau^-$ events, with the difference that the hadronic jet mass must be compatible with m_Z and that the b-tag content of the event is reduced.

The analyses are very similar to those described in Reference [202]. The selections require high multiplicity events. In the He^+e^- and $H\mu^+\mu^-$ analyses two well identified electrons or muons are also required. In the tau analyses, tau leptons are identified either by their decay into electrons or muons, or as an isolated low-multiplicity jet with one or three tracks and unit charge. The identified leptons must have a large opening angle and must be well isolated from the hadronic jets. For all $H\ell^+\ell^-$ selections, the invariant mass of the leptons after a kinematic fit imposing four-momentum conservation must be consistent with m_Z within a mass range depending on the dilepton mass resolution. In the $\tau^+\tau^-q\bar{q}$ selection the mass of the two hadronic jets after kinematic fit must be consistent with m_Z .

After the $H\ell^+\ell^-$ selection, 18 events are observed with 16.7 expected from background processes and 1.7 or 0.32 signal events expected for $m_H=110$ GeV or 115 GeV, respectively. After the $\tau^+\tau^-q\bar{q}$ selection, 8 events are observed with 7.8 expected from background and 0.66 or 0.15 signal events expected for $m_H=110$ GeV or 115 GeV, respectively.

The distributions of the dilepton mass and the reconstructed Higgs mass in the He^+e^- and $H\mu^+\mu^-$ channels are shown in Figure 3.8a and 3.8b. The distributions of the reconstructed Higgs mass in the $H\tau^+\tau^-$ and $\tau^+\tau^-q\bar{q}$ channels are shown in Figure 3.8c and 3.8d, respectively.

In the $H\ell^+\ell^-$ selections, the dijet mass after the fit is combined with the b-tag values of the two jets, to form the final discriminant. For the $\tau^+\tau^-q\bar{q}$ selection, the mass of the tau pair, calculated by constraining the invariant mass of the two other jets to m_Z , is used as the final discriminant.

3.2.3.4 Results

Figure 3.9 shows the observed $-2\ln Q$ compared to the expectation for the “background-only” and the “signal+background” hypotheses, as a function of m_H , for each of the search channels. An observed value of $-2\ln Q$ larger than the median expected value for the background indicates a deficit of events with respect to the expected background while an observed $-2\ln Q$ value below the median expected background value indicates an excess. Good agreement between the observation and the expected background is observed in all channels within one standard deviation from the background expectation. A slight excess of events above one standard deviation from the background is observed in the $H\nu\bar{\nu}$ channel for m_H above 100 GeV. The observed and expected log-likelihood ratio $-2\ln Q$ for all channels combined as a function of m_H is shown in Figure 3.10.

These results are used to evaluate confidence levels for the “background-only” and the “signal+background” hypotheses. The confidence level for the “background-only” hypothesis, CL_B [216], is the probability of observing in a large sample of simulated “background-only” experiments a more signal-like value of the log-likelihood ratio than is actually observed. The distribution of CL_B in a large sample of “background-only” experiments is uniform between 0 and 1, thus its median expected value is 0.5. An observed value of CL_B lower than 0.5 indicates an excess of events in data compared to the expected background. Similarly, the “signal+background” confidence level CL_{S+B} is defined as the probability in a sample of “signal+background” experiments of observing a less signal-like value of the log-likelihood ratio than is actually observed. To exclude a signal, an additional quantity is defined, $CL_S = CL_{S+B}/CL_B$ [216]. The signal hypothesis is excluded at 95% confidence level when CL_S has a value smaller or equal to 5%.

The statistical and systematic uncertainties on the signal and background expectations are included in the calculations of the combined confidence levels. Statistical uncertainties on the background and signal predictions, arising from the finite number of generated Monte Carlo events, are evaluated to be up to 8% for the background and 4% for the signal. The systematic uncertainties are derived using a similar procedure to the one adopted in previous Standard Model Higgs searches [202]. In addition, a systematic uncertainty on the $q\bar{q}$ background, which affects mostly the search region close to the HZ kinematic limit in the $H\nu\bar{\nu}$ and $Hq\bar{q}$ channels, is included depending on m_H . Thus the systematic uncertainty on the number of background events is estimated to be from 6% up to 15% for m_H close and beyond the HZ kinematic limit. The systematic uncertainty on the number of signal events is estimated to be between 3% and 6%, for m_H close to and beyond the HZ kinematic limit, to take into account the spread of \sqrt{s} values in the different data samples.

The statistical uncertainty is uncorrelated from bin to bin in the final discriminant distributions and has little effect on the confidence level. Bins of the final discriminant distributions with a s/b ratio below 0.05 are not considered in the calculation of the confidence levels, as they degrade the search sensitivity once systematic uncertainties are included in the calculation. The number of selected and expected events for all the analyses after such a s/b cut are summarised in Table 3.3 for the data, the background and the Higgs signals for $m_H = 110$ GeV and 115 GeV. The number of signal events includes cross-efficiencies from other channels, fusion processes and charm and gluonic Higgs decays.

The confidence level for the “background-only” hypothesis $1-CL_B$ and the confidence level for the signal hypothesis CL_S as a function of m_H are shown in Figure 3.11. They are computed following the procedure of Reference [216]. The results of the L3 Standard Model Higgs searches at lower centre-of-mass energies [201, 202] are included in the calculation of these confidence levels. Values of m_H below 107 GeV are excluded in the Standard Model with a confidence level greater than 99.5%.

The observed lower limit on m_H is 112.0 GeV at the 95% confidence level, for an expected lower limit of 112.4 GeV. This new value improves upon and supersedes our previously published limit. For $m_H=112.0$ GeV, where CL_S is 5%, the background probability $1-CL_B$ is 40%. For $m_H=115$

GeV, the background probability is 32%. The previously published background probability estimates [203] are consistent with the final results presented here, given the size of the uncertainties affecting the signal and background estimate in the vicinity of the kinematic limit.

The most significant candidate for $m_H=115$ GeV is a $H\nu\bar{\nu}$ event. It has a reconstructed Higgs mass of 115 GeV and it was recorded at $\sqrt{s}=206.4$ GeV. The kinematic properties of this event were described in detail in Reference [203].

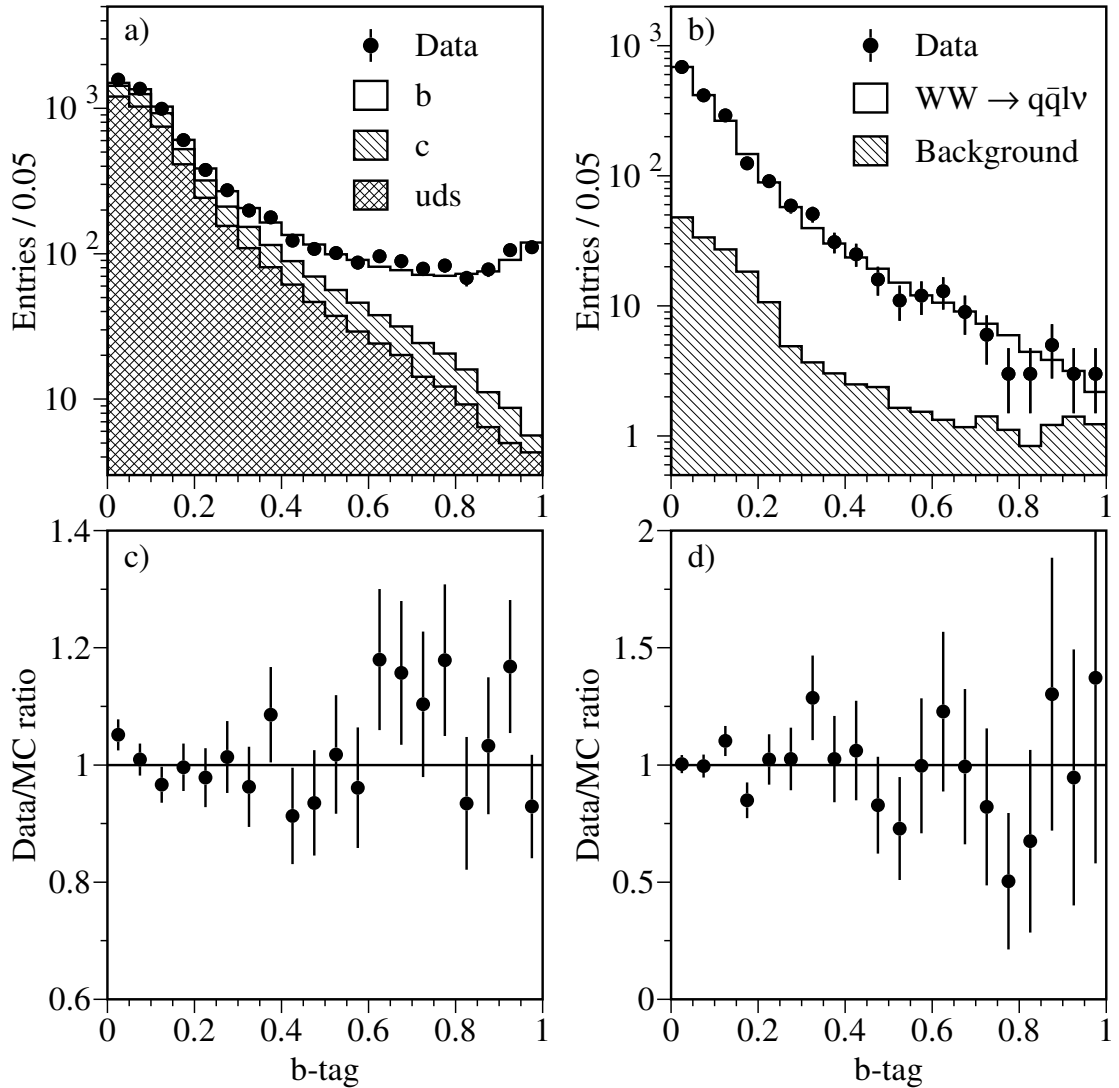


FIGURE 3.5: Distribution of the neural network jet b-tag variable in a sample of a) $e^+e^- \rightarrow q\bar{q}(\gamma)$ and b) $W^+W^- \rightarrow q\bar{q}l\nu$ events selected from the high-energy data collected in the year 2000. Two entries per event contribute to the distributions. The data are compared to the simulation of Standard Model processes. The bin-by-bin ratio of the data to the simulated events is displayed in c) and d).

\sqrt{s} (GeV)	202.8	203.8	205.1	206.3	206.6	208.0	208.6
Luminosity (pb^{-1})	2.7	7.6	68.1	66.9	63.7	8.2	0.1

TABLE 3.2: The average centre-of-mass energies and the corresponding integrated luminosities of the data samples collected in the year 2000.

$200 \leq \sqrt{s} \leq 209$ GeV	Mass hypothesis					
	$m_H = 110$ GeV			$m_H = 115$ GeV		
Selection	N_D	N_B	N_S	N_D	N_B	N_S
$Hq\bar{q}$	49	51.5	11.7	12	9.4	1.8
$H\nu\bar{\nu}$	13	10.7	3.3	5	3.3	0.66
He^+e^-	0	0.66	0.58	0	0.38	0.14
$H\mu^+\mu^-$	0	0.38	0.45	0	0.26	0.11
$H\tau^+\tau^-$	0	0.53	0.19	1	0.14	0.03
$\tau^+\tau^-q\bar{q}$	3	2.3	0.51	0	0.84	0.15
Total	65	66.1	16.7	18	14.3	2.9

TABLE 3.3: The number of observed candidates (N_D), expected background (N_B) and expected signal (N_S) events for the data collected in the year 2000, after a cut on the final discriminant corresponding to a signal-to-background ratio greater than 0.05. This cut is used to calculate the confidence levels.

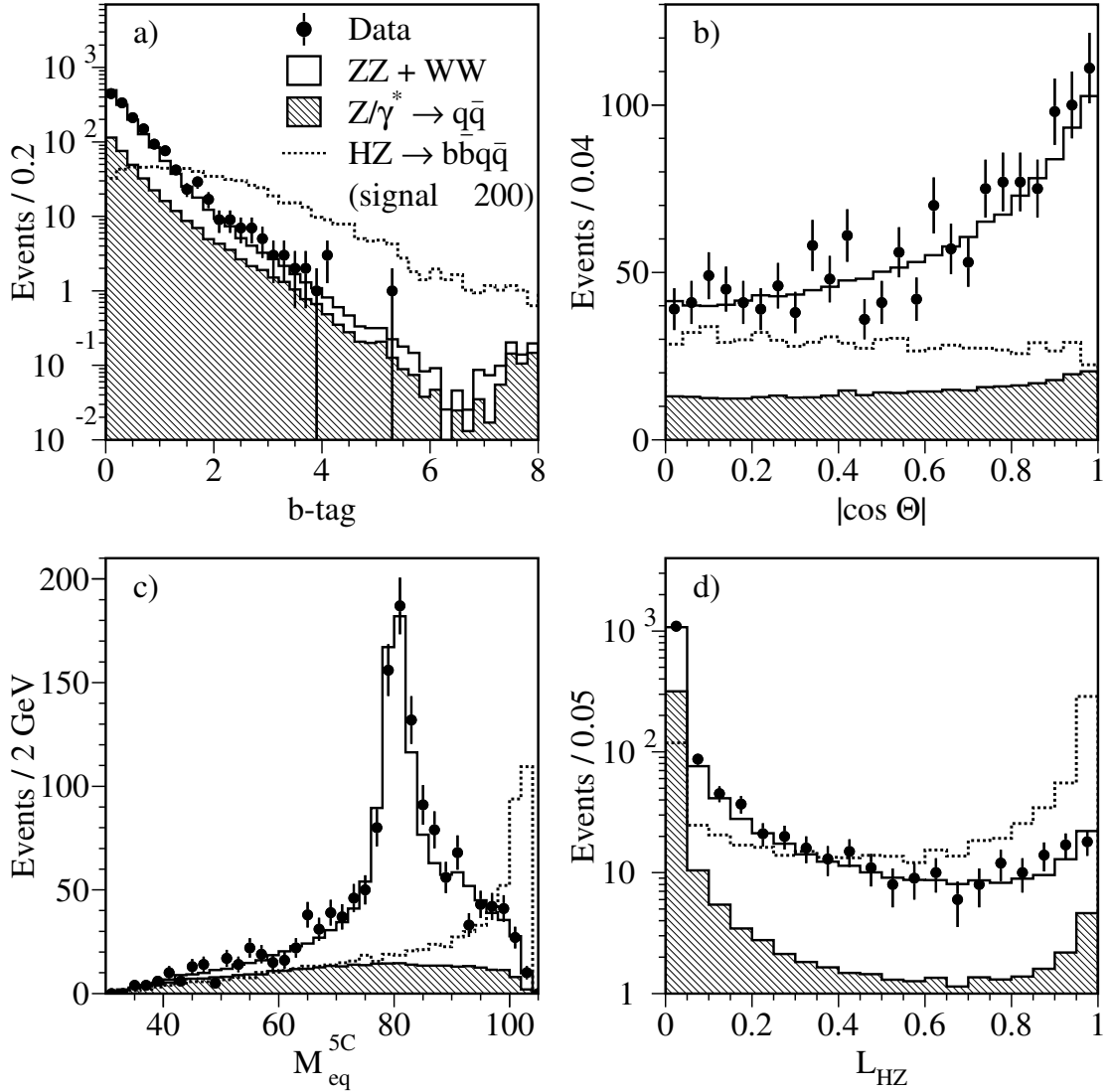


FIGURE 3.6: Distribution of a) the event b-tag, b) the cosine of the boson production angle, c) the mass from the 5C equal-mass fit and d) the likelihood for the events selected in the $Hq\bar{q}$ search channel. The points correspond to the data collected at $\sqrt{s} > 206$ GeV. The open and hatched histograms are the expected backgrounds from Standard Model processes. The dashed line is the distribution expected for a 115 GeV Higgs signal, multiplied by a factor of 200.

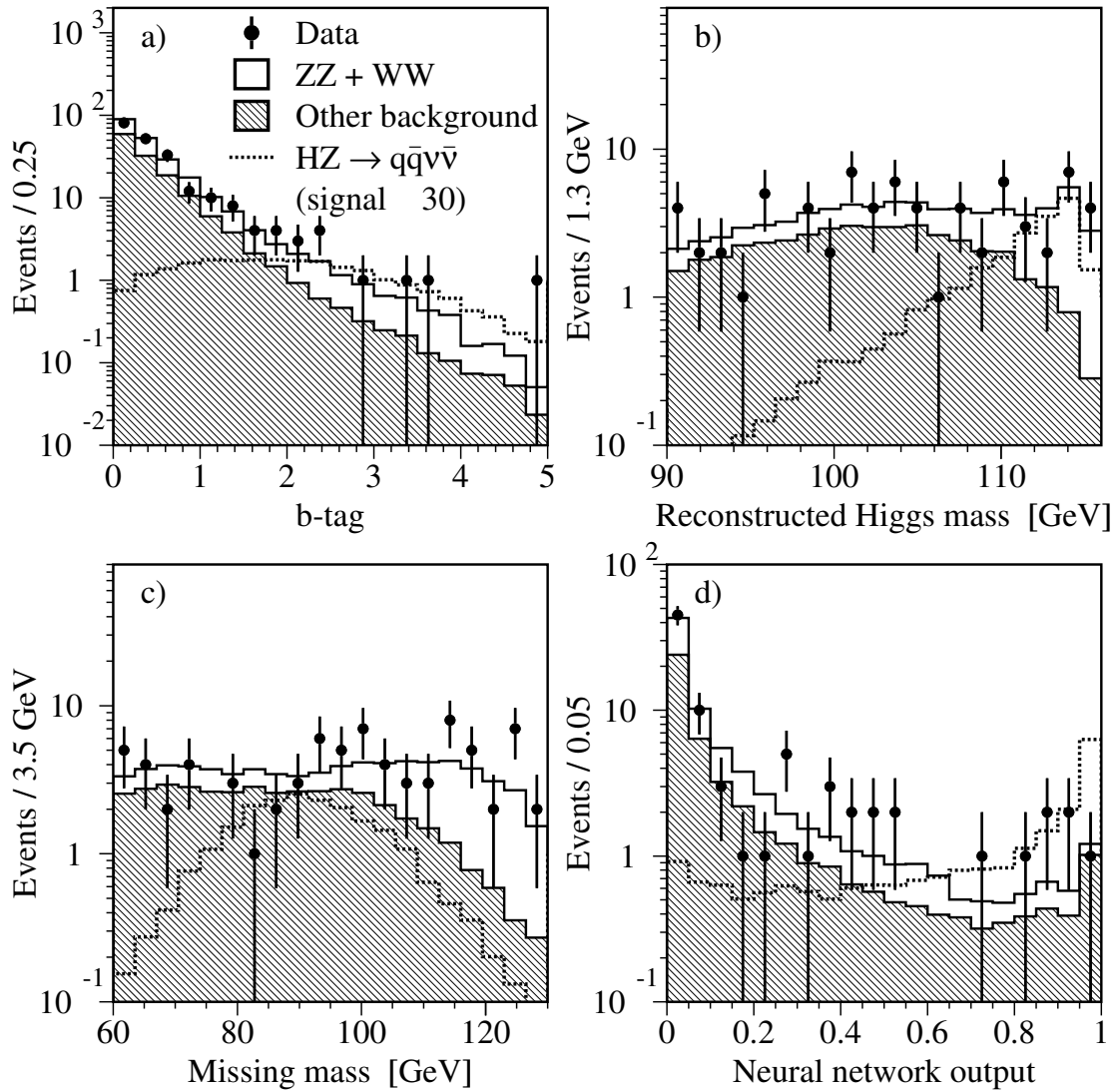


FIGURE 3.7: Distribution of a) the event b-tag, b) the reconstructed Higgs mass, c) the missing mass and d) the neural network output, for the events selected in the $H\nu\bar{\nu}$ search channel. The points represent the data collected at $\sqrt{s} > 206$ GeV. The open and hatched histograms are the expected backgrounds. The dashed line is the expected Higgs signal with $m_H = 115$ GeV, multiplied by a factor of 30.

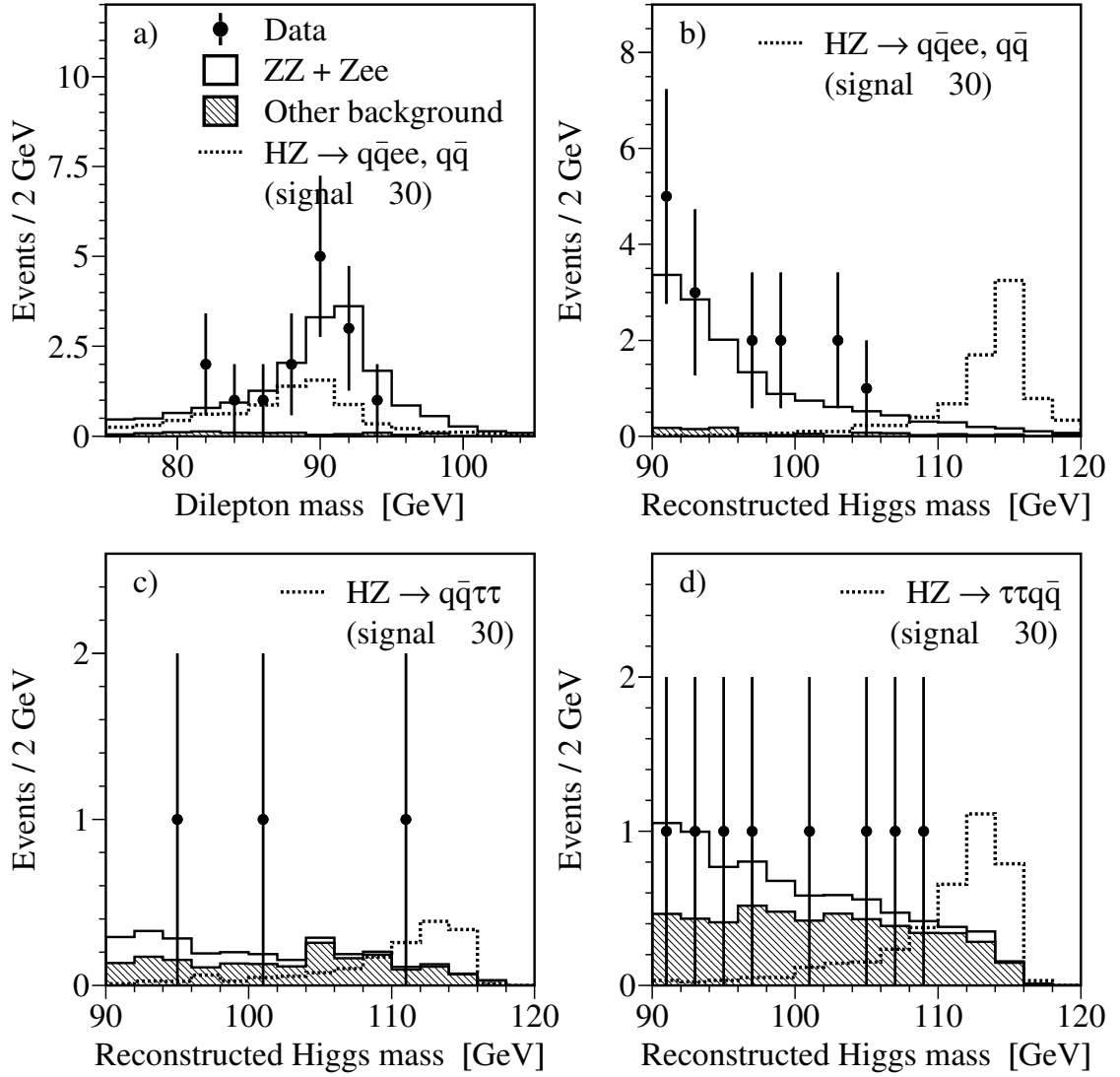


FIGURE 3.8: Distributions of a) the dilepton mass and the reconstructed Higgs mass in the b) He^+e^- and $H\mu^+\mu^-$, c) $H\tau^+\tau^-$ and d) $\tau^+\tau^-q\bar{q}$ channels. The points are the data and the open and hatched histograms the expected backgrounds. The dashed line is the expected Higgs signal with $m_H = 115$ GeV, multiplied by a factor of 30, in each channel.

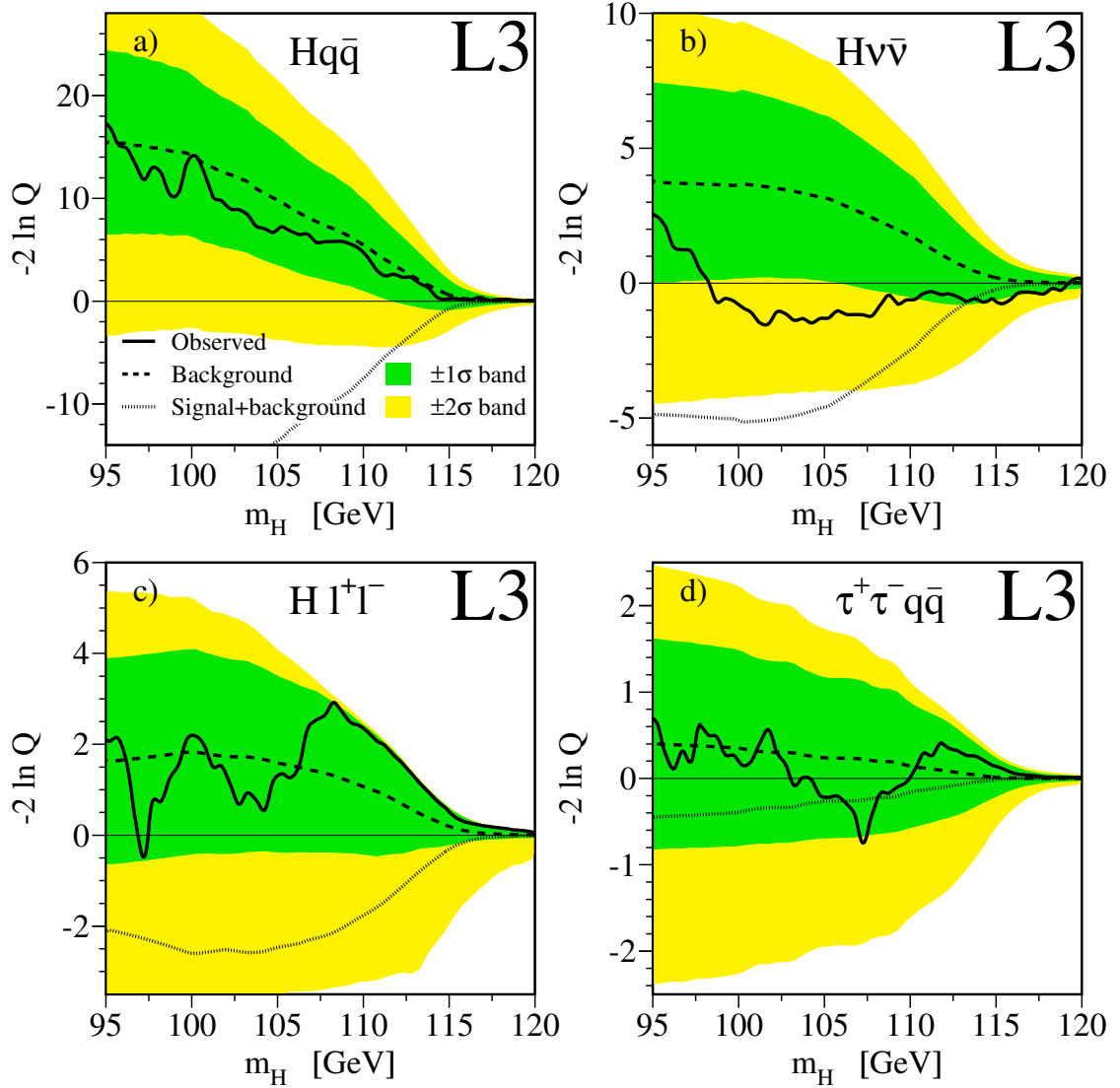


FIGURE 3.9: The log-likelihood ratio, $-2\ln Q$, as a function of the Higgs mass hypothesis, m_H , for the search channels a) $Hq\bar{q}$, b) $H\nu\bar{\nu}$, c) $H\ell^+\ell^-$ and d) $\tau^+\tau^-q\bar{q}$. The solid line shows the observed $-2\ln Q$. The dashed line shows the expected median value of $-2\ln Q$ for the “background-only” hypothesis. The dark and light shaded bands show the 68% and 95% probability intervals centred on the background expected median value. The dotted line is the median expected value for the “signal+background” hypothesis.

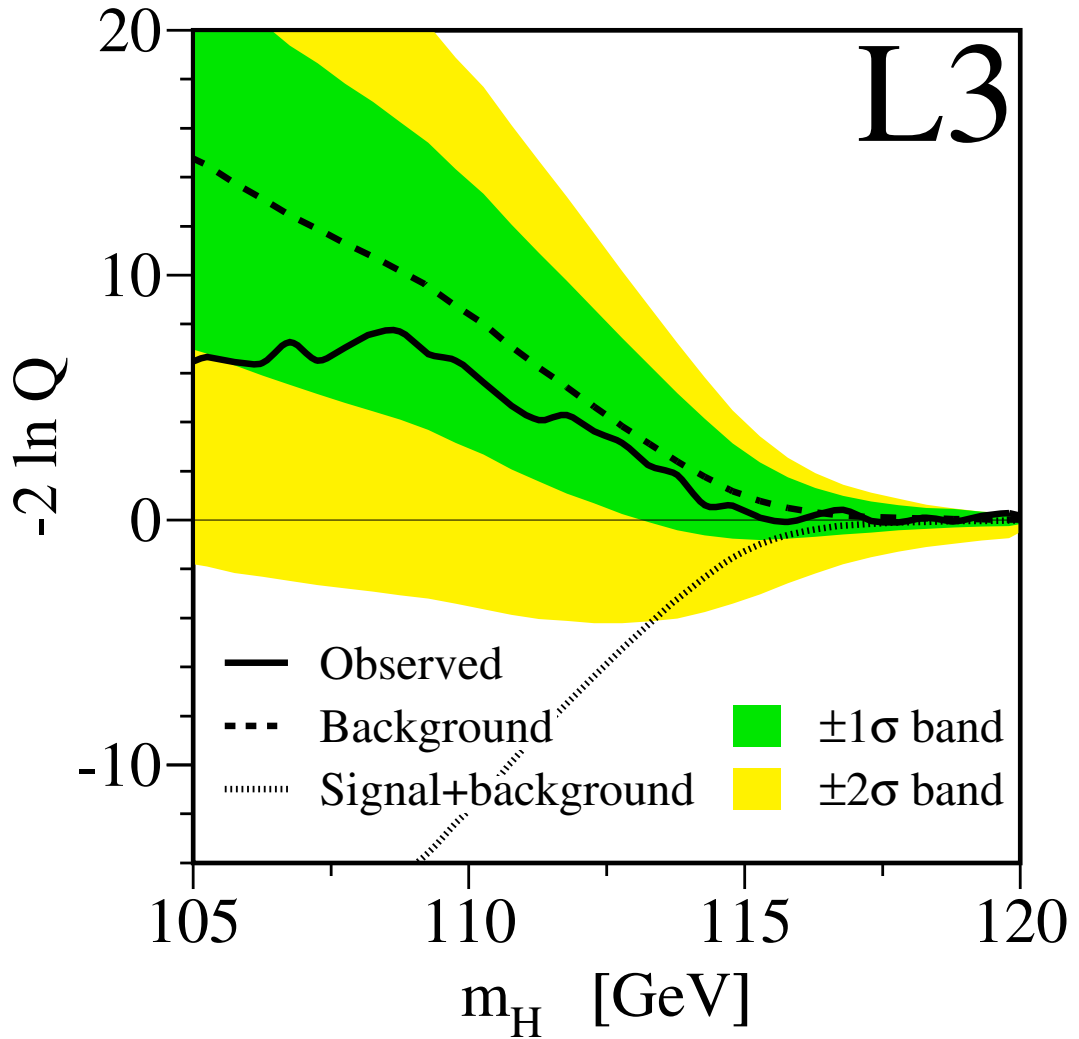


FIGURE 3.10: The log-likelihood ratio, $-2\ln Q$, as a function of the Higgs mass hypothesis, m_H , for all the search channels combined. The solid line shows the observed $-2\ln Q$. The dashed line shows the expected median value of $-2\ln Q$ for the “background-only” hypothesis. The dark and light shaded bands show the 68% and 95% probability intervals centred on the background expected median value. The dotted line is the median expected value for the “signal+background” hypothesis.

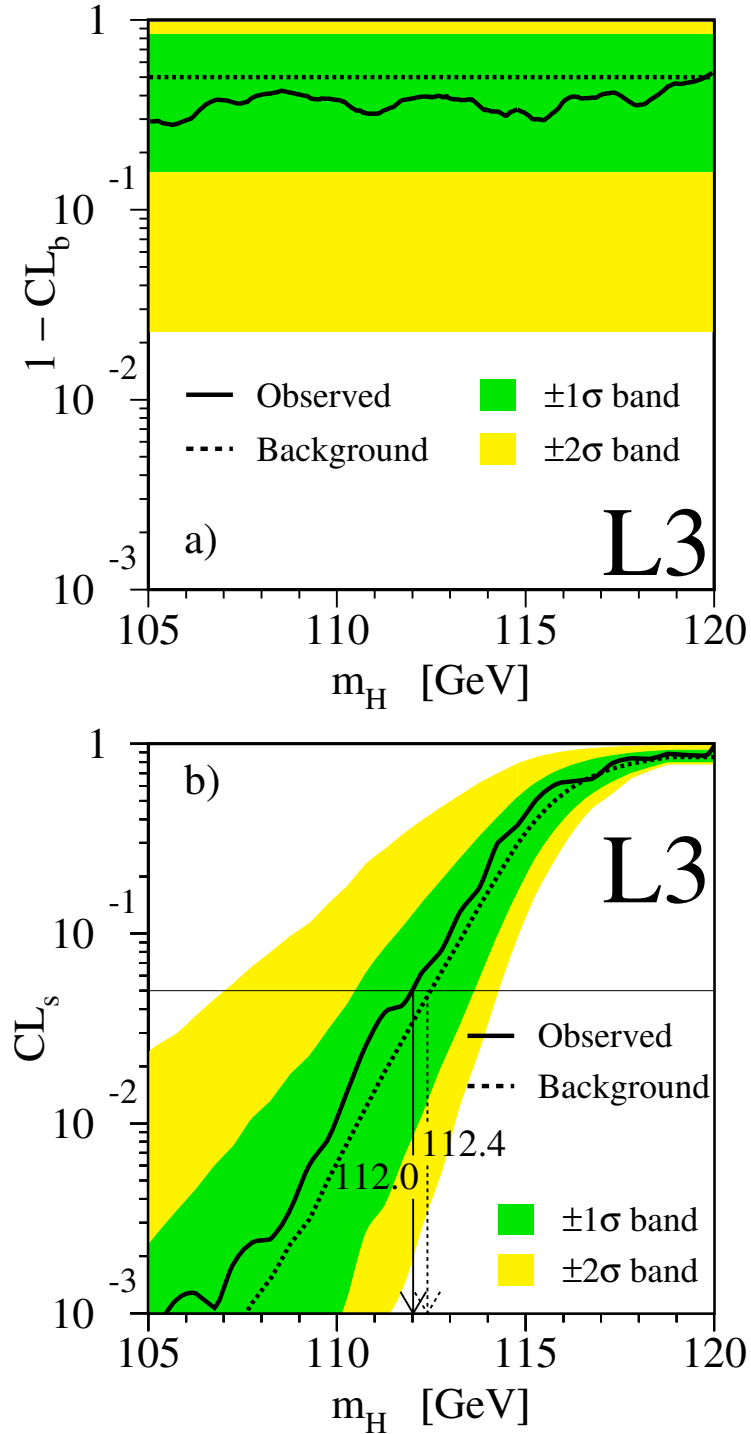


FIGURE 3.11: a) The background confidence level CL_B and b) the signal confidence level, CL_S , as a function of the Higgs mass hypothesis, m_H , for all the search channels combined. The data collected at $189 \leq \sqrt{s} \leq 202$ GeV [201, 202] are also included in the combination. The solid line shows the observed value. The dashed line shows the median expected value in a large number of simulated “background-only” experiments. The dark and light shaded bands show the expected 68% and 95% probability intervals centred on the background expected median value. The observed lower limit on the Higgs mass is set at 112.0 GeV, with an expected median value of 112.4 GeV, at the 95% confidence level.

3.2.4 Search for a Higgs Boson Decaying Invisibly

Search for an invisibly decaying Higgs boson
in e^+e^- collisions at $\sqrt{s} = 183 - 189$ GeV

L3 Collaboration

Abstract

A search for a Higgs boson decaying into invisible particles is performed using the data collected at LEP by the L3 experiment at centre-of-mass energies of 183 GeV and 189 GeV. The integrated luminosities are respectively 55.3 pb^{-1} and 176.4 pb^{-1} . The observed candidates are consistent with the expectations from Standard Model processes. In the hypothesis that the production cross section of this Higgs boson equals the Standard Model one and the branching ratio into invisible particles is 100%, a lower mass limit of 89.2 GeV is set at 95% confidence level.

3.2.4.1 Introduction

In some extensions of the Standard Model the Higgs boson can decay into stable weakly interacting particles, thus yielding invisible final states [218]. For example the minimal supersymmetric extension of the Standard Model predicts that the Higgs boson can decay into a pair of invisible neutralinos.

A search is performed for a Higgs boson produced through the Higgs-strahlung process, $e^+e^- \rightarrow Z^* \rightarrow hZ$. The Z boson decays into fermion pairs yielding two different investigated topologies: two acoplanar jets plus missing energy, corresponding to the Z boson hadronic decays, and two acoplanar charged leptons plus missing energy, corresponding to decays of the Z boson into electrons or muons. Data collected by the L3 experiment [219] at LEP centre-of-mass energies of $\sqrt{s} = 183$ GeV and 189 GeV are analysed. The corresponding integrated luminosities are respectively 55.3 pb^{-1} and 176.4 pb^{-1} . Results at lower centre-of-mass energies have been reported by L3 [220] and by the other LEP experiments [221].

3.2.4.2 Event simulation

To determine the signal efficiency, samples of Higgs boson events are generated using the PYTHIA Monte Carlo program [222] for masses between 55 GeV and 100 GeV.

For the background studies the following Monte Carlo programs are used: PYTHIA ($e^+e^- \rightarrow q\bar{q}(\gamma)$, $e^+e^- \rightarrow Z/\gamma^*Z/\gamma^*$ and $e^+e^- \rightarrow Ze^+e^-$), KORALW [223] ($e^+e^- \rightarrow W^+W^-$), KORALZ [224] ($e^+e^- \rightarrow \mu^+\mu^-(\gamma)$, $e^+e^- \rightarrow \tau^+\tau^-(\gamma)$), PHOJET [225] ($e^+e^- \rightarrow e^+e^-q\bar{q}$), DIAG36 [226] ($e^+e^- \rightarrow e^+e^-\ell^+\ell^-$), BHWIDE [227] ($e^+e^- \rightarrow e^+e^-\gamma$), and EXCALIBUR [228] for the other four-fermion final states. For each centre-of-mass energy, the number of simulated background events corresponds to at least 50 times the number of expected events except for the two-photon interactions ($e^+e^- \rightarrow e^+e^-\bar{f}f$) and Bhabha scattering ($e^+e^- \rightarrow e^+e^-$) for which twice and seven times the collected luminosity are simulated, respectively.

The L3 detector response is simulated using the GEANT 3.15 program [229], which takes into account the effects of energy loss, multiple scattering and showering in the detector. The GHEISHA program [230] is used to simulate hadronic interactions in the detector. Small time-dependent inefficiencies of the different subdetectors are taken into account in the simulation procedure.

3.2.4.3 Search in the hadronic channel

A cut-based analysis is used to select events in the hadronic channel. After a common preselection two sequential selections are separately optimised for light (below 80 GeV) and heavy (above 80 GeV) Higgs boson masses. Unless otherwise stated, the events are constrained to have two jets using the DURHAM algorithm [231].

3.2.4.3.a Preselection

High-multiplicity hadronic events are selected at $\sqrt{s} = 189$ GeV. Events coming from QCD processes and hadronic decays of W and Z boson pairs are rejected by requiring a missing momentum larger than 10 GeV. The absolute values of the cosine of the polar angle of the jets and of the missing momentum vector have to be less than 0.9, to reject events with a high-energy initial-state radiation photon emitted close to the beam axis. In addition, events with large energy depositions in the forward calorimeters are vetoed to reduce the background contribution from the Ze^+e^- and $q\bar{q}(\gamma)$ processes and from residual two-photon interactions. Coplanar events are rejected to further suppress these last processes.

Events with energetic and isolated charged leptons are removed to decrease the contamination from semi-leptonic decays of W boson pairs. This cut is designed to keep signal events with semi-leptonic decays of b or c hadrons produced in Z decays.

The larger of the jet masses is required to be in the range from 6 GeV up to 50 GeV and the lower one greater than 4 GeV. The upper mass limit further removes some semi-leptonic W boson pair decays and the lower bounds reject two-photon interactions with tau leptons in the final state.

Figure 3.12 shows the comparison between data and Monte Carlo expectations for the distribution of the visible mass, M_{vis} of the preselected events.

3.2.4.3.b Heavy Higgs boson selection

In addition to the preselection described above, the correlation between the visible and the missing mass, M_{mis} , is used to select heavy Higgs boson candidates in the $\sqrt{s} = 189$ GeV data sample. We define the variable $R = (M_{\text{vis}} + M_{\text{mis}})/(M_{\text{vis}} - M_{\text{mis}})$ and we require $R < -3.5$ or $R > 7$, since the signal has a broad R distribution while for the background R is close to zero.

A heavy Higgs boson is characterised by relatively low momentum, hence the missing momentum of the event should not exceed 40 GeV. The background due to the $q\bar{q}(\gamma)$ and two-photon interaction processes is suppressed by rejecting collinear events and by requiring a large value of the event thrust, together with a moderate value of the sum of the inter-jet angles, Θ_{123} , when

the events are constrained to have three jets. In order to reject the residual contributions from the W pair and the single W processes, an isolation criterion on the missing momentum vector is applied. In addition, the upper cut on the maximum value of the jet masses is tightened to 30 GeV while the minimum has to be less than 20 GeV.

The recoiling mass, M_h^{rec} , is calculated by constraining the visible mass to the Z boson mass and imposing energy-momentum conservation [220]; its distribution is plotted in Figure 3.13(a) for the data and the background. With this kinematical constraint, the recoil mass resolution is 3.5 GeV in the hypothesis of a Higgs boson mass of 90 GeV.

After applying the selection described above the dominant process in the remaining background is the Z boson pair production.

3.2.4.3.c Light Higgs boson selection

The production of a light invisible Higgs boson at $\sqrt{s} = 189$ GeV is characterised by three main features, exploited by the following selection criteria: mass of the hadronic system close to the Z mass $|M_{vis} - M_Z| < 20$ GeV, at least 40% but not more than 60% of the centre-of-mass energy visible in the detector and missing momentum in the window from 30 GeV up to 55 GeV. This last requirement reduces part of the background arising from Z boson pair production and two-photon interactions, the latter being further suppressed by an upper cut on Θ_{123} . Events from $q\bar{q}(\gamma)$ are rejected by requiring a large value of the event thrust and the longitudinal momentum imbalance to be less than 40% of the visible energy. The residual contribution from W pair production is reduced by a cut on the threshold y_{23} at which the DURHAM algorithm resolves the event into three jets from a two-jet topology.

The distribution of M_h^{rec} for events selected in the data and the Monte Carlo samples is displayed in Figure 3.13(b).

The selection of the hadronic channel at $\sqrt{s} = 183$ GeV is similar to this light Higgs boson selection. A cut on the transverse momentum imbalance replaces the cut on the y_{23} parameter and the values of the selection requirements reflect the different centre-of-mass energies. The final M_h^{rec} spectrum for data and Monte Carlo is shown in Figure 3.13(c). Table 3.4 summarises the yields of all the selections described above.

After applying the two selections described above the dominant process in the remaining background is the W^+W^- production.

3.2.4.4 Search in the leptonic channels

The search for an invisibly decaying Higgs boson produced in association with a Z boson decaying into leptons is designed to be almost independent of the Higgs boson mass in the investigated range. Low multiplicity events with a pair of high energy muons or electrons are selected. These are separated from fermion pair production events by requiring large acoplanarity and visible energy between 5% and 70% of the centre-of-mass energy. The lepton energy has to be less than

	$\sqrt{s} = 189 \text{ GeV}$			$\sqrt{s} = 183 \text{ GeV}$
	Preselection	Heavy Higgs boson	Light Higgs boson	Final Selection
Data	304	30	27	8
Background MC	300.3	25.8	23.6	8.5
ϵ (%) ($M_h = 65 \text{ GeV}$)	53.1	3.0	19.2	22.0
ϵ (%) ($M_h = 85 \text{ GeV}$)	54.0	30.2	20.0	28.0
ϵ (%) ($M_h = 90 \text{ GeV}$)	54.1	37.8	7.6	18.5
ϵ (%) ($M_h = 95 \text{ GeV}$)	46.6	32.2	2.1	–

TABLE 3.4: Number of events expected from Standard Model processes compared to the number of data events selected by the hadronic selections. The signal efficiencies (ϵ) for several Higgs boson masses M_h are also shown.

90% of the beam energy to further reject Bhabha scattering events. Two-photon interactions are suppressed by requiring the lepton pair invariant mass to be larger than 30 GeV and low energy depositions in the forward calorimeters. Events with muons should have at least one scintillator in time with the beam crossing in order to remove cosmic-ray background. The yield of this preselection is presented in Table 3.5, while Figure 3.14 displays the spectra of the lepton pair invariant mass, $M_{\ell\ell}$, for data and Standard Model Monte Carlo events.

	Electrons		Muons	
	Preselection	Final selection	Preselection	Final selection
Data	38	2	34	2
Background MC	41.4	2.2	36.5	1.6
ϵ (%) ($M_h = 65 \text{ GeV}$)	52.9	36.5	42.1	19.1
ϵ (%) ($M_h = 85 \text{ GeV}$)	55.4	41.3	42.3	20.9
ϵ (%) ($M_h = 90 \text{ GeV}$)	55.4	39.6	45.8	25.1
ϵ (%) ($M_h = 95 \text{ GeV}$)	55.3	42.1	47.7	30.2

TABLE 3.5: Number of events observed and expected from Standard Model processes at $\sqrt{s} = 189 \text{ GeV}$ after the preselections and the final selections. Signal efficiencies (ϵ) for different Higgs mass hypotheses are also shown. The background to the final selected sample is composed of one third Z boson-pair events and two thirds W boson-pair events.

Residual events due to the radiative return to the Z resonance where the photon remains undetected in the beam pipe are rejected by requiring the missing momentum to point away from the beam axis. Tau pair production can yield acoplanar lepton pairs that satisfy the selection criteria described above. In the hypothesis that the lepton pair originates from a single particle, we require the cosine of the most energetic lepton emission angle θ^* in the Z boson rest frame not to exceed 0.95.

The contribution from two-photon interactions is eliminated by tightening the cut on the lepton invariant masses, $70 \text{ GeV} < M_{\ell\ell} < 110 \text{ GeV}$; this is also effective against a significant portion of the fully leptonic decays of W bosons. Final states with an electron or muon pair and two neutrinos, produced by Z boson pairs, constitute an irreducible background but their cross section is relatively low.

The visible energy E_{vis} , $\cos \theta^*$, $M_{\ell\ell}$ and the velocity β of the dilepton system are combined into a single likelihood variable G , defined as:

$$G = \sum_i \log(P_S^i(x)) - \log(P_B^i(x)).$$

The index i runs over the four variables and $P_S^i(x)$ and $P_B^i(x)$ are the probability densities for the i -th variable to have a value x in the signal or background hypotheses, respectively. These densities are calculated for each event by interpolating between the two signal Monte Carlo samples whose generated Higgs masses are closer to the event missing mass which is taken as the Higgs boson mass hypothesis. The Z boson pair background is not included in this calculation. Figure 3.15 shows distributions of G for the data and the expected Monte Carlo background and signal for a Higgs boson mass of 95 GeV.

The number of selected events and the signal efficiency after the optimization [232] of a cut on G are reported in Table 3.5. The observed resolution on the missing mass is 1.1 GeV in the electron channel, and 5.1 GeV in the muon channel for a Higgs boson mass of 90 GeV.

A cut-based analysis is developed for the $\sqrt{s} = 183$ GeV data sample making use of the following selection criteria: $30 \text{ GeV} < E_{\text{vis}} < 120 \text{ GeV}$, $\cos \theta^* < 0.95$, $80 \text{ GeV} < M_{\ell\ell} < 100 \text{ GeV}$ and $0.05 < \beta < 0.55$. In the electron channel, the signal efficiency is 45% and 4 events are observed for 1.4 expected background events. In the muon channel, the signal efficiency is 28% and no events are observed while 1.7 background events are expected. Figure 3.16 displays the missing mass distributions for the search in the leptonic channel for the combined $\sqrt{s} = 183$ GeV and $\sqrt{s} = 189$ GeV samples.

3.2.4.5 Systematic uncertainties

Two sources of systematic uncertainties, summarised in Table 3.6, can affect the results. The first is the limited amount of Monte Carlo statistics, which gives the systematic errors on the signal and background efficiencies listed as ‘‘MC Stat.’’ in Table 3.6. The second is the quality of the Monte Carlo description of the background processes. This is studied using data and Monte Carlo samples containing essentially W^+W^- and ZZ background events. These samples contain about 1100 events for the hadronic channel and 500 for the leptonic ones. The data distributions in these new samples of each selection variable i , except the likelihood G , are compared with those of the Monte Carlo, determining their systematic shifts s_i and the corresponding statistical errors σ_i . All the selection cuts are then shifted by $s_i \pm \sigma_i$, where the sign of σ_i is chosen so as to obtain the lowest efficiency for the single cut on the variable i . The difference between the efficiency of the selection using the shifted cuts and that of the nominal one is taken as the systematic uncertainty. These errors are summarised as ‘‘Syst.’’ in Table 3.6 and are summed in quadrature with the Monte Carlo statistical uncertainties to obtain the total systematic uncertainty, listed as ‘‘Total’’ in Table 3.6.

3.2.4.6 Results

No indication of the production of a Higgs boson with invisible decays is found. As both the production cross section and the branching ratios are model dependent, it is useful to introduce the ratio $R_{\text{inv}} = \text{BR}(h \rightarrow \text{invisible particles}) \times \sigma(e^+e^- \rightarrow hZ) / \sigma(e^+e^- \rightarrow H_{\text{SM}}Z)$, where H_{SM} is

	Background			Signal		
	MC Stat.	Syst.	Total	MC Stat.	Syst.	Total
Heavy hadronic	1.0	5.0	5.0	3.0	2.5	4.0
Light hadronic	1.0	5.0	5.0	4.0	5.5	7.0
Electrons	6.0	1.5	6.0	5.0	2.0	5.5
Muons	6.5	5.0	8.0	6.0	3.5	7.0

TABLE 3.6: Relative systematic uncertainties in percent on the signal and background efficiencies for each analysis.

the Standard Model Higgs boson. A limit on R_{inv} is calculated [233] as a function of the Higgs boson mass making use of the mass distributions presented in Figures 3.13 and 3.16. In the determination of the limit the Standard Model Higgs boson cross section as given by the HZHA generator [234] is used and the signal and background efficiencies are lowered by their systematic uncertainties. Results obtained at lower energies [220] are included. Figure 3.17 shows the 95% confidence level (CL) upper limit on R_{inv} as a function of the Higgs mass M_h . For the value of $R_{\text{inv}} = 1$ the 95% CL lower limit on the Higgs boson mass is:

$$M_h > 89.2 \text{ GeV.}$$

The expected lower limit is 92.6 GeV.

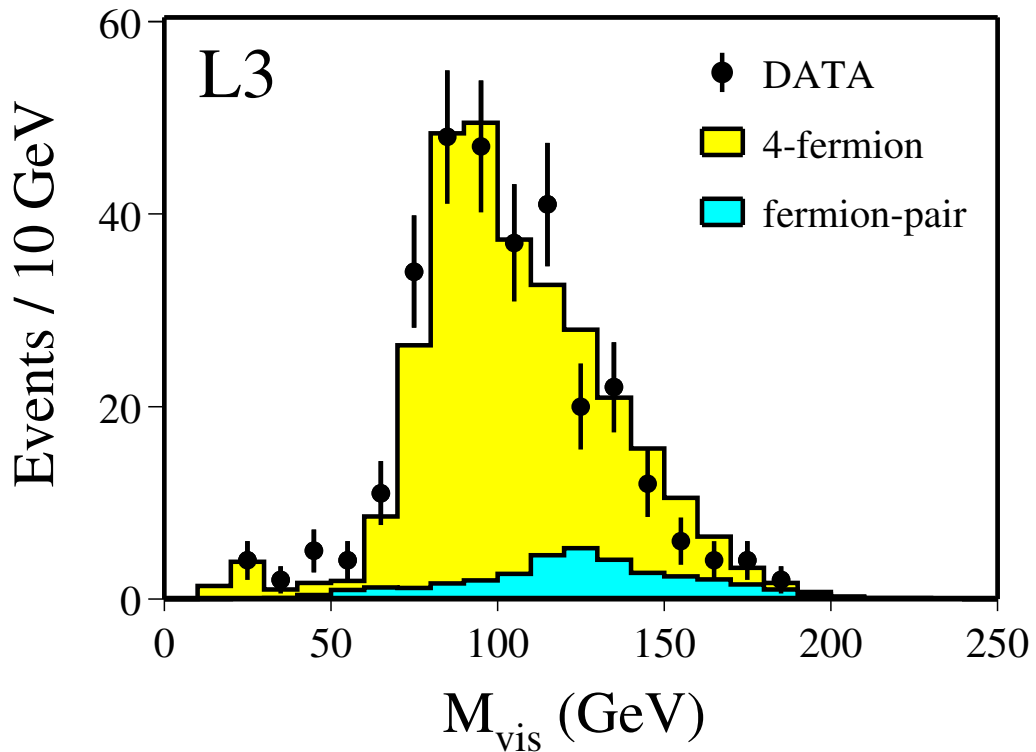


FIGURE 3.12: Distribution of the visible mass after the hadronic preselection at $\sqrt{s} = 189$ GeV.

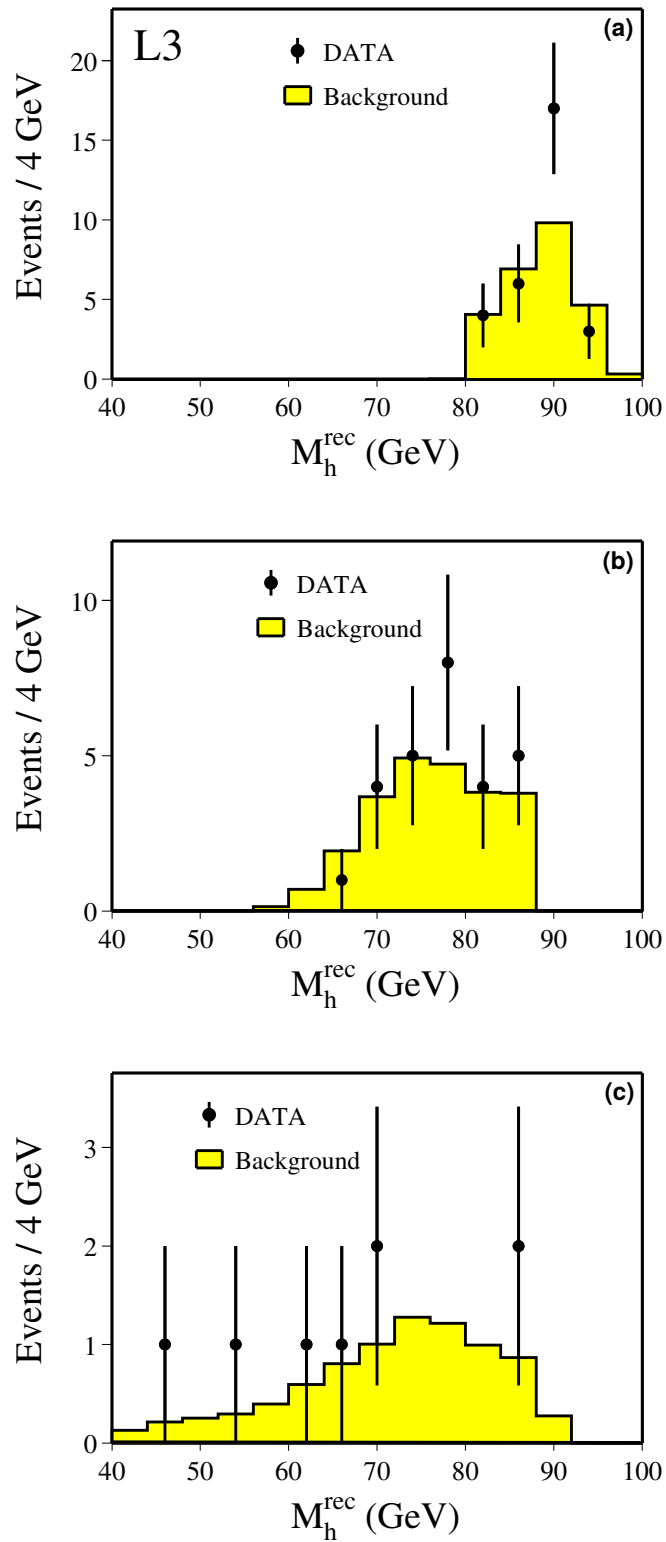


FIGURE 3.13: Distribution of the recoil mass (a) after the heavy Higgs boson selection at $\sqrt{s} = 189$ GeV, (b) after the light Higgs boson selection at $\sqrt{s} = 189$ GeV and (c) after the final selection at $\sqrt{s} = 183$ GeV.

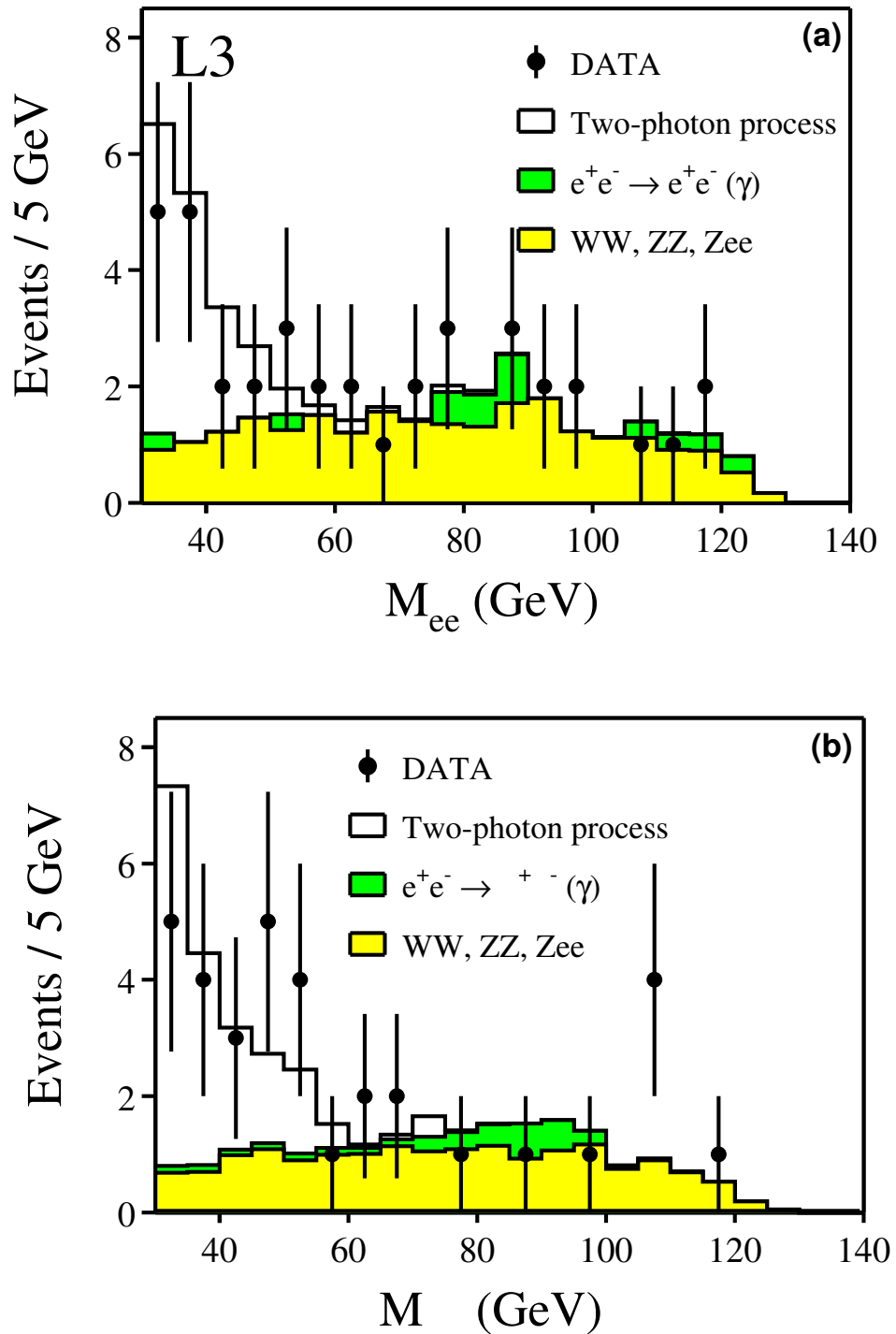


FIGURE 3.14: Distribution of (a) the dielectron and (b) the dimuon invariant mass at $\sqrt{s} = 189$ GeV after the preselection is applied.

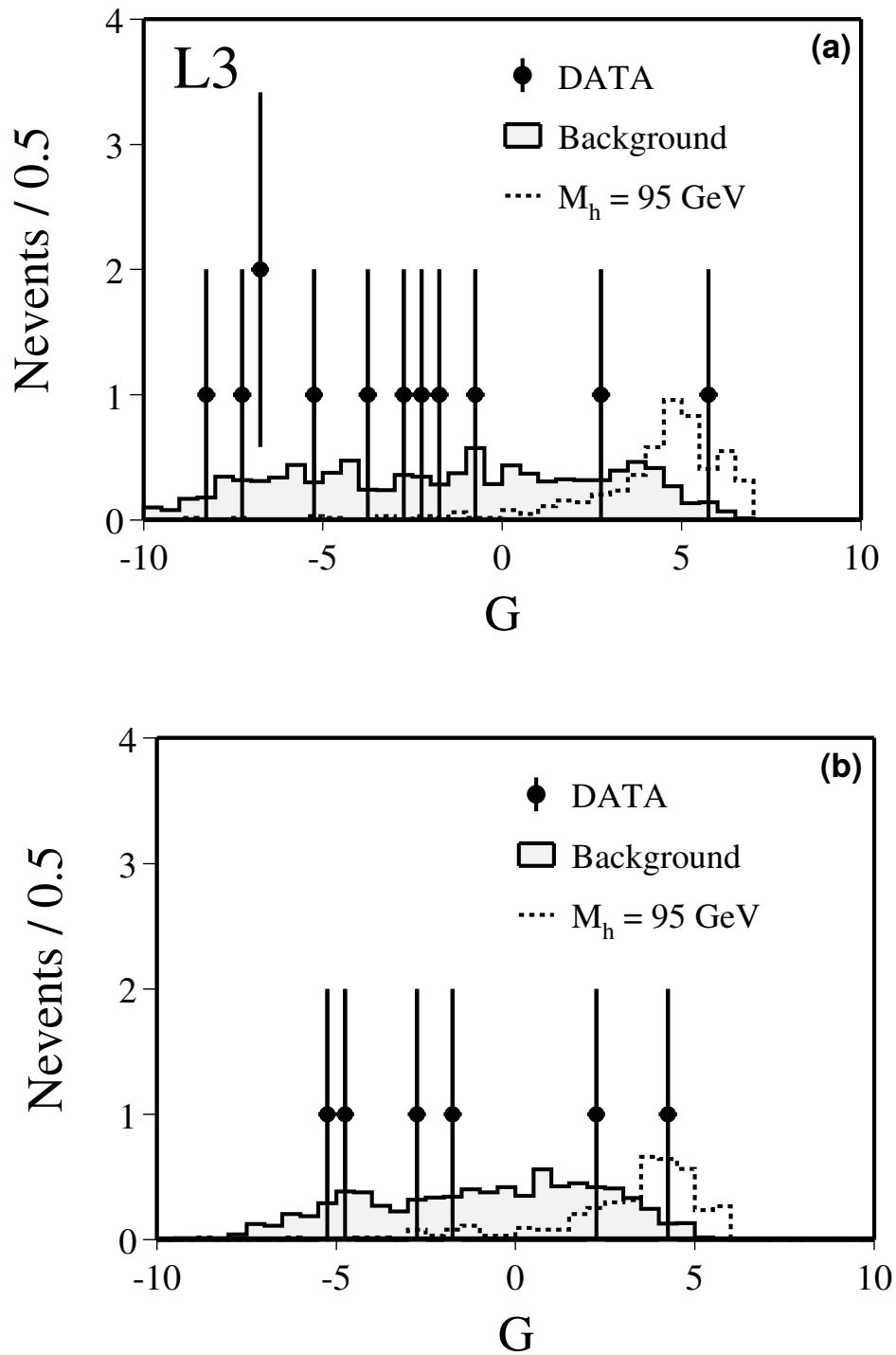


FIGURE 3.15: Distributions of the final likelihood variable, G , (a) for the electron and (b) for the muon selections at $\sqrt{s} = 189$ GeV, for data and the expected background. A possible Higgs signal ($M_h = 95$ GeV) with an arbitrary cross section is also shown.

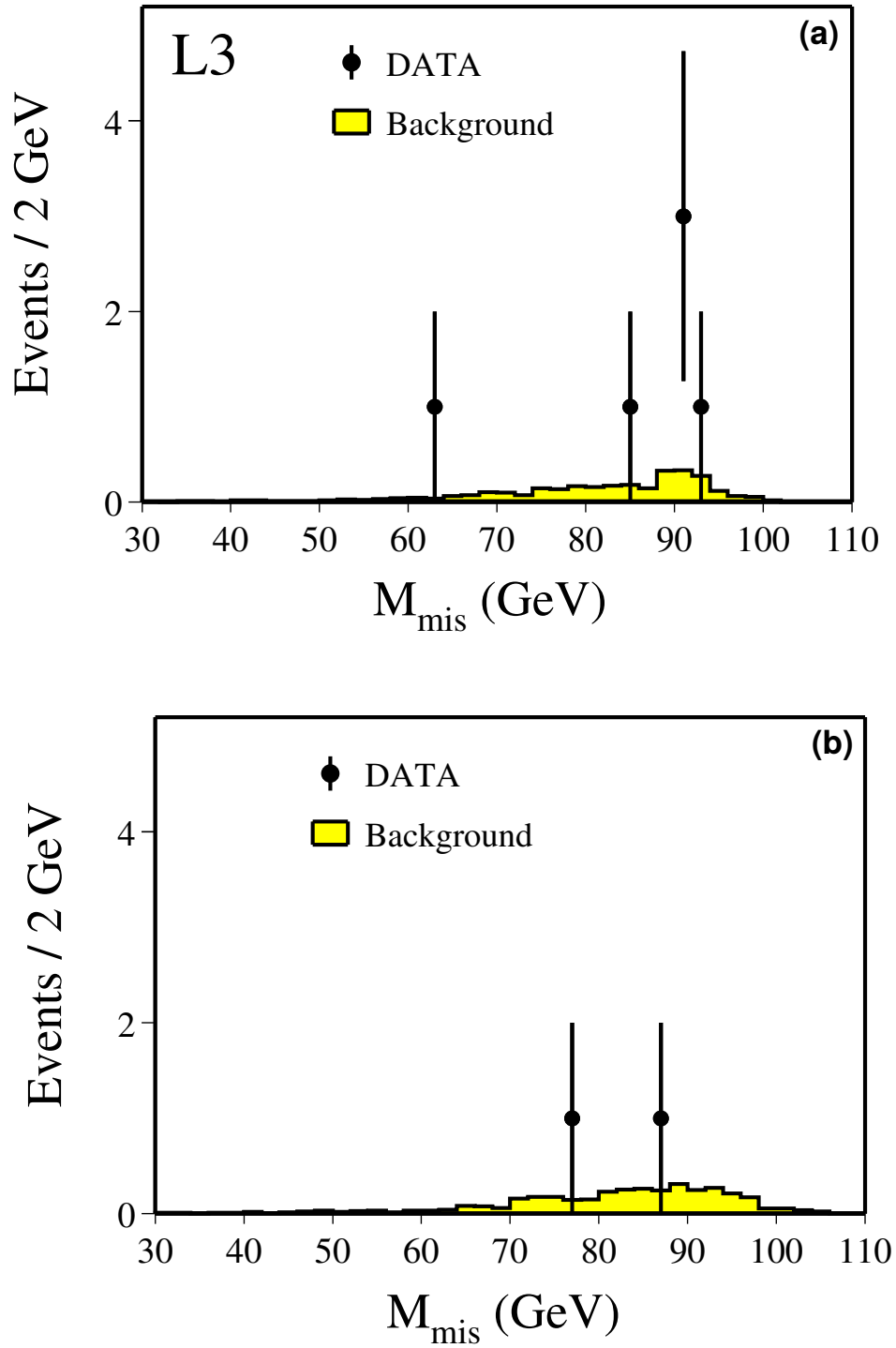


FIGURE 3.16: Missing mass distributions (a) in the electron channel and (b) in the muon channel for the combined $\sqrt{s} = 183$ GeV and 189 GeV data samples.

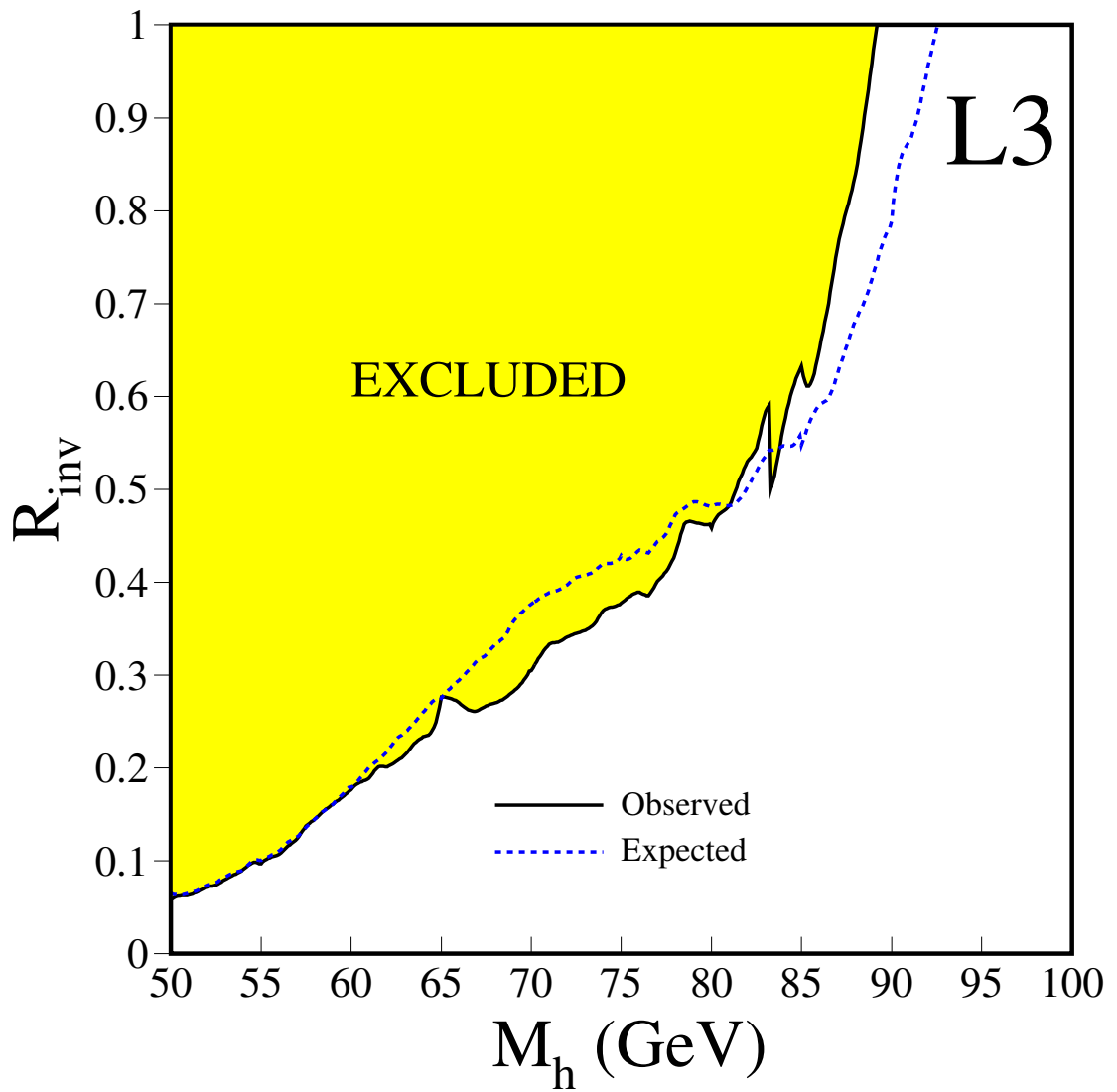


FIGURE 3.17: Observed and expected upper limits on the ratio of the invisibly-decaying Higgs boson cross section to that of the Standard Model Higgs boson, as function of the Higgs boson mass. The shaded area is excluded at least at 95% confidence level.

Chapter 4

Search for Gluinos at TEVATRON

4.1 General Considerations about Hadron Collisions

4.2 Instrumental Aspects

4.2.1 TEVATRON

The TEVATRON was the highest energy proton-antiproton ever built. It was in use at FER-MILAB between 1983 and 2011. It was constructed about 8 m underground and was formed by a $R = 1$ km.

There were two experiments within which the $p\bar{p}$ collisions were made: CDF and D0.

The injection chain of the TEVATRON consisted in:

- Cockcroft-Walton: gets gaseous H , creates H^- ions in a polarized Cs chamber, accelerates H^- to $E_{beam} = 750$ keV
- LINAC: accelerates H^- to $E_{beam} = 400$ MeV (140 m long)
- Electron stripping: passage of the H^- through a carbon foil, get a proton beam
- Booster: circular accelerator raising the proton energy to $E_{beam} = 8$ GeV ($R = 75$ m)
- Antiprotons: steer a proton beam onto a fixed nickel target, select antiprotons among the secondary particles, accumulate and cool the antiprotons
- Main Injector: accelerate p and \bar{p} beams up to $E_{beam} = 150$ GeV ($R \approx 500$ m)
- TEVATRON: accelerate p and \bar{p} beams up to $E_{beam} = 980$ GeV ($R = 1km$), make head-on collisions

During the Run I (1992-1996), the D0 experiment collected about $\int \mathcal{L} dt \approx 100 \text{ pb}^{-1}$ of $p\bar{p}$ collisions at $\sqrt{s} = 1.8 \text{ TeV}$. The instantaneous luminosity went up to $\mathcal{L} = 2 \times 10^{31} \text{ cm}^{-2}\text{s}^{-1}$ with bunches distant of $\Delta t_X = 3.5 \mu\text{s}$. The highlight of the Run I was the discovery of the top quark in 1995 by the CDF and D0 collaborations.

During the Run II (2001-2011), the D0 experiment collected about $\int \mathcal{L} dt \approx 11 \text{ fb}^{-1}$ of $p\bar{p}$ collisions at $\sqrt{s} = 1.96 \text{ TeV}$. The instantaneous luminosity went up to $\mathcal{L} = 4 \times 10^{32} \text{ cm}^{-2}\text{s}^{-1}$. The working configuration was 36 p and \bar{p} bunches distributed into 3 trains of 12 bunches separated by $\Delta t_X = 396 \text{ ns}$.



FIGURE 4.1: Aerial view of the TEVATRON for the Run II at FERMILAB.

4.2.2 D0 Detector

The DØ detector (see Fig. 4.2) consists of a magnetic central-tracking system, comprised of a silicon microstrip tracker (SMT) and a central fiber tracker (CFT), both located within a 2 T superconducting solenoidal magnet [85]. The SMT has $\approx 800,000$ individual strips, with typical pitch of $50 - 80 \mu\text{m}$, and a design optimized for tracking and vertexing capability at pseudorapidities of $|\eta| < 2.5$. The system has a six-barrel longitudinal structure, each with a set of four layers arranged axially around the beam pipe, and interspersed with 16 radial disks. The CFT has eight thin coaxial barrels, each supporting two doublets of overlapping scintillating fibers of 0.835 mm diameter, one doublet being parallel to the collision axis, and the other alternating by $\pm 3^\circ$ relative to the axis. Light signals are transferred via clear fibers to solid-state photon counters (VLPC) that have $\approx 80\%$ quantum efficiency.

Central and forward preshower detectors located just outside of the superconducting coil (in front of the calorimetry) are constructed of several layers of extruded triangular scintillator strips that are read out using wavelength-shifting fibers and VLPCs. The next layer of detection involves three liquid-argon/depleted uranium calorimeters: a central section (CC) covering $|\eta|$

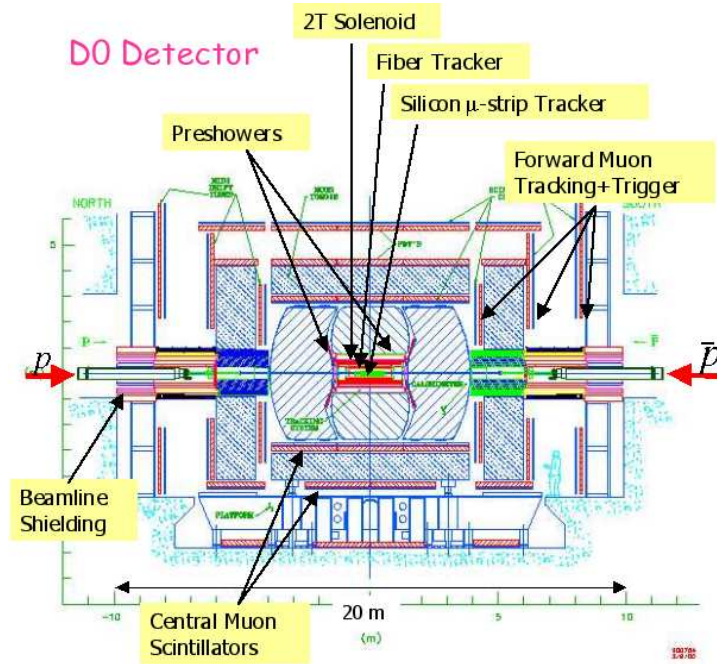


FIGURE 4.2: The D0 detector.

up to ≈ 1.1 , and two end calorimeters (EC) that extend coverage to $|\eta| \approx 4.2$, all housed in separate cryostats [84]. In addition to the preshower detectors, scintillators between the CC and EC cryostats provide sampling of developing showers at $1.1 < |\eta| < 1.4$.

A muon system [86] resides beyond the calorimetry, and consists of a layer of tracking detectors and scintillation trigger counters before 1.8 T toroids, followed by two similar layers after the toroids. Tracking at $|\eta| < 1$ relies on 10 cm wide drift tubes [84], while 1 cm mini-drift tubes are used at $1 < |\eta| < 2$.

Luminosity is measured using plastic scintillator arrays located in front of the EC cryostats, covering $2.7 < |\eta| < 4.4$. A forward-proton detector, situated in the Tevatron tunnel on either side of the interaction region, consists of a total of 18 Roman pots used for measuring high-momentum charged-particle trajectories close to the incident beam directions.

Trigger and data acquisition systems are designed to accommodate the high luminosities of Run II. Based on preliminary information from tracking, calorimetry, and muon systems, the output of the first level of the trigger is used to limit the rate for accepted events to ≈ 2 kHz. At the next trigger stage, with more refined information, the rate is reduced further to ≈ 1 kHz. These first two levels of triggering rely mainly on hardware and firmware. The third and final level of the trigger, with access to all the event information, uses software algorithms and a computing farm, and reduces the output rate to ≈ 50 Hz, which is written to tape.



4.2.3 Search for Gluino Pairs at the TEVATRON Run 2

Search for Gluino Pairs in Events with $4b + \cancel{E}_T$ at the TEVATRON

In this sub-section, I'll describe the search for gluino pairs in the $4b + \cancel{E}_T$ inclusive topology in the D0 Run 2A dataset. This is just an internal D0 Note, that we did not have the time to finalize and to publish. However a complete version of it is reported in detail within the PhD thesis of Thomas Millet, who was co-tutored for the analysis by myself and by Patrice Verdier. I was especially in charge of the analysis strategy and of all the MC samples for the signal and for the background processes, I also calculated all the cross sections for the signal and the background processes at least up to the NLO accuracy.

Search for gluino pairs decaying into b quarks with the DØ detector at $\sqrt{s} = 1.96$ TeV in the Run 2a data

Thomas Millet, G. Steve Muanza, Patrice Verdier

IPN Lyon, CNRS-IN2P3, Université de Lyon

The DØ Collaboration

Abstract

A search for gluino pairs is performed in a $\int \mathcal{L} dt \approx 1fb^{-1}$ dataset from the Fermilab Tevatron Run 2a collected with the DØ detector. In this analysis the following cascade decay for gluinos is assumed: each gluino first decays into a pair formed of a scalar b quark and a b quark, and each scalar b quark subsequently decays into a b quark and the lightest neutralino. The resulting inclusive topology, analyzed for the first time at DØ consists of events with multiple b-jets and a large transverse missing energy. This search is complementary to the generic "flavor blind" searches for gluino and squark pairs. No evidence of signal is found, therefore preliminary exclusion limits up to $m_{\tilde{g}} > 308$ GeV at the 95% confidence level are set. Under the above hypothesized gluino cascade decay, this improves the sensitivity with respect to the flavor blind gluino searches.

4.2.3.1 Introduction

In this analysis we search for gluinos which are fermionic partners of the gluons as predicted by the supersymmetry (SUSY)[232].

Previous studies [77][78][79] have searched gluinos (\tilde{g}) produced either in association with scalar quarks or by pairs. So far, at $D\bar{O}$ these searches were purely topological and did not use the flavor tagging of the jets coming from the \tilde{g} decay. In the rest of the note, we'll refer to them as "flavor blind" searches.

In the current analysis, we complement these searches by taking advantage of the possibly large content in heavy flavor quarks subsequent to the \tilde{g} decay. Namely we look for the following signal (or any partial C-conjugate of it since gluinos are majorons):

$$p\bar{p} \rightarrow \tilde{g} + \tilde{g} \rightarrow \tilde{b}_1 + \bar{b} + \tilde{b}_1 + b \rightarrow \tilde{\chi}_1^0 + b + \bar{b} + \tilde{\chi}_1^0 + \bar{b} + b,$$

leading to a $4b + \cancel{E}_T$ inclusive final state. The \cancel{E}_T is mainly due to the lightest neutralinos $\tilde{\chi}_1^0$ that are supposed to be the lightest supersymmetric particles (LSP) and which escape detection since they are neutral and exclusively weakly interacting.

The decay of a gluino into a scalar b quark (sbottom) can occur in large parts of SUSY models parameter space. Indeed in case of a large mixing in the sbottom sector, the lightest sbottom, denoted \tilde{b}_1 can be much lighter than the other squarks. Precisely, this special condition is fulfilled when $m_b(A_b - \mu \times \tan\beta)$ is large with respect to $m_{\tilde{b}_{L/R}}^2$. Whenever the lightest sbottom is the only squark lighter than the gluino, the later decays almost exclusively into the following two-body mode: $\tilde{g} \rightarrow \tilde{b}_1 + \bar{b}$. In this analysis, we'll consider that: $BR(\tilde{g} \rightarrow \tilde{b}_1 + \bar{b}) = 100\%$ and $BR(\tilde{b}_1 \rightarrow b\tilde{\chi}_1^0) = 100\%$ as well. Parameter space exclusions in any specific SUSY model, would require to correct the limit or the measured signal cross sections for the actual values of these branching ratios.

In this note a gluino search is performed using a sample of $\int \mathcal{L}dt \approx 1fb^{-1}$ of the Run 2a data collected with the $D\bar{O}$ detector [85].

The data and Monte Carlo samples utilized are described in section 4.2.3.2. The different treatments (event quality selection, corrections, resolutions smearing,...) applied on these samples are evoked in section 4.2.3.3. Section 4.2.3.4 contains all the steps of the offline event selection. And finally interpretations and the conclusions of the analysis are drawn in sections 4.2.3.14 and 4.2.3.15, respectively.

4.2.3.2 Data and Monte Carlo Samples

4.2.3.2.a Data Samples

Jets+ \cancel{E}_T triggers

The data samples studied in this note were selected using dedicated unrescaled jets+ \cancel{E}_T triggers.

These triggers are essentially calorimeter based. At the level 1 (L1), they count the numbers of trigger towers (with a granularity of $\Delta\eta \times \Delta\phi = 0.2 \times 0.2$) above a given E_T threshold. At the level 2 (L2) and level 3 (L3), more complex quantities are calculated. Among those are jets reconstructed with a simple cone algorithm (at L3) and global event variables (at L2 and L3) like:

$$H_T = \sum_{jets} |p_T^{\vec{}}| : \text{ the scalar sum of the jets transverse energy,}$$

$$\cancel{H}_T = \left| \sum_{jets} \vec{p}_T^{\vec{}} \right| : \text{ the missing } E_T \text{ calculated with the jets (denoted MHT).}$$

Two periods can be distinguished in the implementation of these triggers during the Run 2a.

The first period started with the introduction of the so called MHT30_CJT(3,5) trigger in the trigger list version 11 (v11) in late march 2003. This trigger remained barely modified till the trigger list v12 up to late june 2004. A total integrated luminosity of $321 pb^{-1}$ was recorded during this period for the run range [174845-194597] with typical instantaneous peak luminosities around $\mathcal{L} = 5 \times 10^{31} cm^{-2} s^{-1}$.

During the second period, from late june 2004 till february 2006, new triggers were introduced in order to cope with the steadily increasing instantaneous luminosity. We use two of them, that we'll denote JT1_ACO_MHT_HT and JT2_MHT25_HT, and this will lead to the use of two distinct streams respectively called JT1 and JT2 for the offline analysis. During this second period, total integrated luminosities of $814 pb^{-1}$ and $811 pb^{-1}$ were recorded with these respective triggers. This corresponds to the run range [194567-215670] and to typical instantaneous peak luminosities around $\mathcal{L} = 7.5 \times 10^{31} cm^{-2} s^{-1}$.

Tables 4.1, 4.2 and 4.3 summarize the main features of the highest luminosity versions of these jets+ \cancel{E}_T triggers.

TABLE 4.1: The version 12.3 of the MHT30_CJT(3,5) trigger

Online Selection Level	Trigger Term	Corresponding Cuts
L1	CJT(3,5)	3 towers w/ $E_T > 5 GeV$
L2	MJT_20	$\cancel{H}_T > 20 GeV$
L3	MHT_30	$\cancel{H}_T > 30 GeV$

The trigger towers cover a pseudo-rapidity range of $|\eta_{det}| < 3.6$. At the L2, the \cancel{H}_T is calculated from jets reconstructed from 5×5 tower clusters with an E_T threshold of 10 GeV.

At the L3, the equivalent quantity is calculated from simple cone jets of radius $\Delta R = 0.5$, $|\eta_{det}| < 3.6$ and $p_T > 9$ GeV. A primary vertex is reconstructed based on L3 tracks with $p_T > 1$ GeV. The z_{PV} is used for the jets reconstruction.

Offline Reconstruction of the Data Samples

We used the full "PASS3" [87] data samples (see 4.2.3.3.a) that were reconstructed with p17 versions of d0reco [88].

Online Selection Level	Trigger Term	Corresponding Cuts
L1	CJT(3,5)	3 towers w/ $E_T > 5 \text{ GeV}$
	CJT(3,4eta2.6)	3 towers w/ $E_T > 4 \text{ GeV}$ and $ \eta_{det} < 2.6$
	CJT(1,7eta1.8)	1 tower w/ $E_T > 7 \text{ GeV}$ and $ \eta_{det} < 1.8$
L2	MJT_20	$\cancel{H}_T > 20 \text{ GeV}$
	ACOP	$0^\circ < \Delta\phi(j_1, j_2) < 168.75^\circ$
L3	N_{jets}	$N_{jets} \geq 1$
	MJT_30	$\cancel{H}_T > 30 \text{ GeV}$
	ACOP	$0^\circ < \Delta\phi(j_1, j_2) < 170^\circ$
	$\Delta\phi_{min}$	$25^\circ < \Delta\phi(\cancel{H}_T, jets) < 180^\circ$
	HT	$H_T > 50 \text{ GeV}$

TABLE 4.2: The version 14.92 of the JT1_ACO_MHT_HT trigger. j_1, j_2 represent the leading and next-to-leading p_T jets.

Online Selection Level	Trigger Term	Corresponding Cuts
L1	CJT(3,5)	3 towers w/ $E_T > 5 \text{ GeV}$
	CJT(3,4eta2.6)	3 towers w/ $E_T > 4 \text{ GeV}$ and $ \eta_{det} < 2.6$
	CJT(1,7eta1.8)	1 tower w/ $E_T > 7 \text{ GeV}$ and $ \eta_{det} < 1.8$
L2	N_{jets}	$N_{jets} \geq 3$
	$p_T(jets)$	$p_T(jets) > 6 \text{ GeV}$ and $ \eta_{det} < 2.6$
	HT	$H_T > 75 \text{ GeV}$
L3	N_{jets}	$N_{jets} \geq 3$
	$p_T(jets)$	$p_T(jets) > 20 \text{ GeV}$
	MJT_25	$\cancel{H}_T > 25 \text{ GeV}$
	HT	$H_T > 125 \text{ GeV}$

TABLE 4.3: The version 14.92 of the JT2_MHT25_HT trigger.

4.2.3.2.b Monte Carlo Samples

Generation Settings

To produce the MC samples we used the p17 Common Samples Monte Carlo (CSMC) [107] settings which main features are recalled below.

The signal samples were generated using Pythia v6.323 [94], pertaining details are given in the next paragraph. This generator was also used to produce the di-boson and the light flavour (LF) QCD samples.

The rest of the background processes were produced with "Fixed Order Matrix Element" (FOME) generators: for the single-top processes we used Comphep v4.1.10 [101] and for the V+LF-jets, V+HF-jets (HF: heavy flavour), $t + \bar{t}$, and the HF QCD samples. The parton shower (PS), the parton fragmentation and the LF hadron decays were handled by Pythia for all the Alpgen samples. In order to remove the contributions from the PS and the ME where they overlap in the processes phase space, the MLM matching prescription [289][290] was applied.

The tau decay and the C/B-hadron decays were handled respectively by the Tauola [345] and by the EvtGen [346] specialized programs.

The proton/antiproton parton density function used for these generations based on leading order (LO) matrix elements (ME) was CTEQ6L1 (aka CTEQ6LL) [98].

The masses for the heavy quarks were: $m_t = 172.5$ GeV, $m_b = 4.75$ GeV, $m_c = 1.55$ GeV and the parton level cut $|\hat{\eta}| < 5$ was applied on all the samples unless otherwise stated.

Signal Process

The *MCpythia.x* executable was used to read the mass spectrum using the "SUSY Les Houches Accord" (SLHA) [95] interface and the cascade decay of interest was forced within the *pythia.cards* files. Note that the bug on the SUSY particles lifetime was fixed using the p17-br-17 *mcpp-gen* branch [96] to recompile *MCpythia.x*.

The signal was produced with a full p17.09.06 simulation chain (generator, d0gstar, d0sim, d0reco). The zero-bias data samples from the "temp_Zerobias_p17_06_03MC_events8_9_18_19_28and29" SAM dataset were overlaid on top of the MC hard-scatter so as to simulate the effect of the multiple $p\bar{p}$ collisions in each beam crossings.

We produced the signal in the most model-independent way: we just chose the following mass triplet $m_{\tilde{g}}, m_{\tilde{b}_1}, m_{\tilde{\chi}_1^0}$, (with $m_{\tilde{g}} > m_{\tilde{b}_1} > m_{\tilde{\chi}_1^0}$) from an SLHA SUSY mass spectrum file and we set both branching ratios (BRs) of the following $\tilde{g} \rightarrow \tilde{b}_1 + \bar{b}$ and $\tilde{b}_1 \rightarrow b\tilde{\chi}_1^0$ decays to be 100%. Therefore the signals acceptance and efficiencies are model-independent. The interpretation of the analysis results in any specific realization of a gravity-mediated SUSY breaking model essentially requires to adjust the number of expected signal events for the actual values of the aforementioned BRs. The only model dependent assumptions are that the $\tilde{\chi}_1^0$ is the LSP and the conservation of the R-parity makes it stable.

Within the MSSM the mapping of the mass triplets to the parameters writes as follow:

$$\begin{cases} m_{\tilde{g}}(M_3) \\ m_{\tilde{b}_1}(m_{\tilde{b}_R}, A_b, \mu, \tan\beta) \\ m_{\tilde{\chi}_1^0}(M_1, \mu, \tan\beta). \end{cases}$$

But one has also to take into account the mean (first and second generation) squark mass, defined as $\langle m_{\tilde{q}} \rangle = (m_{\tilde{u}} + m_{\tilde{d}} + m_{\tilde{s}} + m_{\tilde{c}})/4$, in order to evaluate the gluino pair production cross section, even at the LO. This is due to the destructive interference between two following dominant graphs (see Fig. 4.3). The higher the mean squark mass the lesser the interference. In this note, we set its default value to $\langle m_{\tilde{q}} \rangle = 1$ TeV and we explored the impact of lighter masses: $\langle m_{\tilde{q}} \rangle = 500$ GeV and $\langle m_{\tilde{q}} \rangle = 400$ GeV.

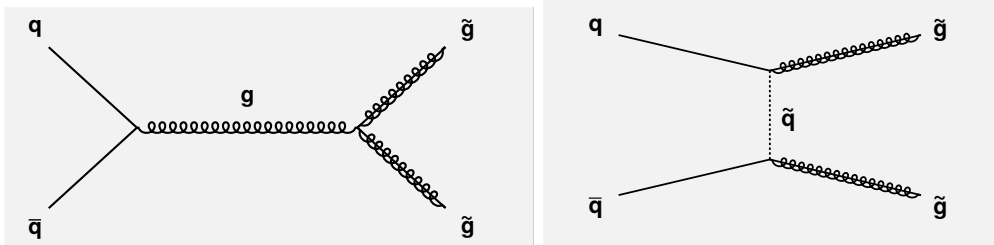


FIGURE 4.3: The dominant LO mechanisms for gluino pairs production.

The main properties of the generated signal samples are in tables 4.4 and 4.5.

In the following tables describing the signal and background MC samples, the N'_{gen} represents the number of remaining generated events after the data quality (see 4.2.3.3.b) cuts have been applied and N_{gen} is the total number of generated events after the heavy flavour quarks skimming (HFS), when it was necessary. The HFS procedure consists in building exclusive HF event topologies for the QCD and the V+jets samples. In practice, the MC samples are filtered out to remove any HF quarks from the parton shower that would be in overlap with same flavor quarks from the Matrix Element.

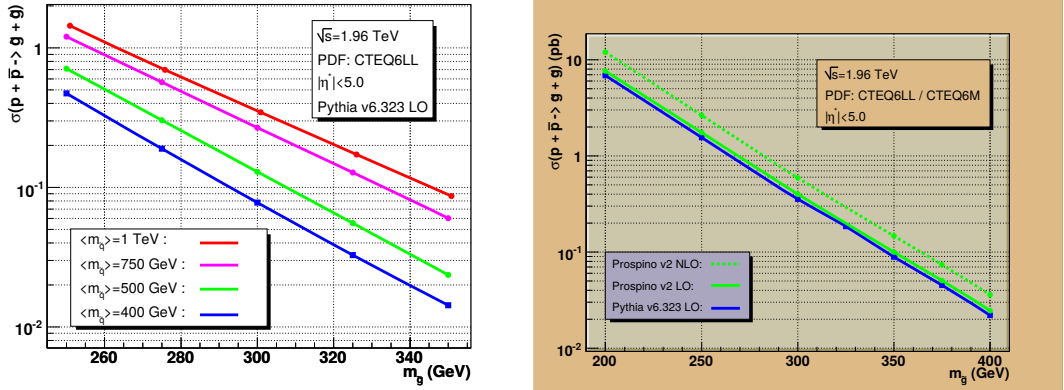
$m_{\tilde{g}}$ (GeV)	$m_{\tilde{b}_1}$ (GeV)	N'_{gen}/N_{gen}	σ_{LO} (pb)	K-factor
200.	95.	8731/9235	6.860	1.57
200.	105.	8973/9487		
200.	150.	9443/9976		
200.	175.	11647/12228		
200.	180.	9234/9734		
200.	195.	7573/7987		
205.	200.	8757/9233	5.838	1.564
210.	200.	8471/8979	4.965	1.561
225.	105.	9189/9735	3.223	1.544
225.	175.	11593/12227		
225.	200.	9201/9738		
225.	215.	8510/8987		
225.	220.	9178/9734		
230.	225.	6356/6739	2.778	1.538
250.	85.	8962/9486	1.598	1.509
250.	95.	8947/9474		
250.	105.	9406/9982		
250.	150.	9200/9730		
250.	175.	10397/10980		
250.	200.	8724/9233		
250.	225.	8971/9484		
250.	230.	8962/9490		
250.	240.	18377/19459		
250.	245.	18163/19206		
255.	250.	8939/9478	1.305	1.502
260.	250.	8670/9229	1.140	1.497
275.	95.	9443/9983	0.730	1.484
275.	105.	8737/9233		
275.	150.	8532/8985		
275.	175.	9193/9734		
275.	200.	9209/9737		
275.	225.	9187/9733		
275.	250.	8544/8988		
275.	265.	9469/9989		
275.	270.	9176/9729		
290.	230.	7575/7992	0.474	1.477
300.	85.	8506/8985	0.355	1.475
300.	95.	6131/6492		
300.	105.	9454/9984		
300.	150.	9193/9728		
300.	175.	6396/6737		
300.	200.	7566/7985		
300.	225.	8966/9482		
300.	250.	7990/8490		
300.	280.	9448/9978		
300.	290.	8716/9230		
300.	295.	8496/8981		
325.	150.	9208/9731	0.185	1.474
325.	175.	3064/3246		
325.	200.	8984/9480		
325.	225.	9487/9988		
325.	250.	7083/7481		
325.	305.	8967/9477		
325.	320.	8236/8736		
350.	105.	8500/8985	0.089	1.470
350.	150.	8991/9477		
350.	175.	5911/6241		
350.	200.	8983/9484		
350.	330.	9460/9986		
350.	345.	7796/8230		
375.	150.	9198/9733	0.045	1.460
375.	175.	8034/8483		
375.	250.	8988/9484		
375.	355.	9484/9990		
375.	370.	7558/7983		
400.	175.	6635/6989	0.022	1.460
400.	250.	8025/8483		
425.	175.	9244/9738	0.011	1.455

TABLE 4.4: Description of the signal MC samples with $m_{\tilde{\chi}_1^0} = 75$ GeV

The K-factor calculated with Prospino is defined as $\text{K-factor} = \frac{\sigma_{NLO}(\tilde{g}\tilde{g})}{\sigma_{LO}(\tilde{g}\tilde{g})}$.

We used the p17 "Common Samples MC" setting [107]. In particular, we used the following masses for the heavy quark masses: $m_b = 4.75$ GeV and $m_c = 1.55$ GeV, $|\hat{\eta}| < 5$. The CTEQ6M1 (resp. CTEQ6L1, aka CTEQ6LL) parton density functions (PDF) are utilized to calculate the NLO (resp. LO) cross sections. The $\hat{\eta}$ symbols refer to the center-of-mass frame

$m_{\tilde{g}}$ (GeV)	$m_{\tilde{b}_1}$ (GeV)	$m_{\tilde{\chi}_1^0}$ (GeV)	N'_{gen}/N_{gen}
200.	150.	50.	8981/9482
250.	100.	50.	7993/8487
250.	150.	50.	9432/9984
275.	100.	50.	8257/8741
275.	150.	50.	9430/9986
290.	230.	50.	9454/9979
290.	230.	60.	7772/8235
300.	100.	50.	8528/8986
300.	150.	50.	3764/3994
300.	200.	50.	9431/9974
300.	150.	100.	9465/9985
300.	150.	125.	8526/8975
300.	150.	145.	9226/9727
325.	150.	50.	7999/8488
325.	305.	50.	9213/9733
350.	150.	50.	8714/9229
375.	150.	50.	8275/8733
400.	150.	50.	8994/9483

TABLE 4.5: Description of the signal MC samples with $m_{\tilde{\chi}_1^0} \neq 75$ GeVFIGURE 4.4: $\sigma(p\bar{p} \rightarrow \tilde{g}\tilde{g})$ in pb as a function of $m_{\tilde{g}}$ in GeV. The impact of the squark mass on $\sigma_{LO}(p\bar{p} \rightarrow \tilde{g}\tilde{g})$ (left) and the comparison between $\sigma_{LO}(p\bar{p} \rightarrow \tilde{g}\tilde{g})$ and $\sigma_{NLO}(p\bar{p} \rightarrow \tilde{g}\tilde{g})$ (right) from which we derived the K-Factor 4.2.3.2.b.

of the partons collision. This setting was used for the Prospino calculations but with $m_t = 175.0$ GeV.

One should note the different choices for the renormalization (Q_R) and factorization (Q_F) scales in Pythia and Prospino. The later has the fixed scale defined as $Q_R = Q_F = m(\tilde{g})$ whereas the former has the following dynamical scale $Q_R = Q_F = \hat{m}_T(\tilde{g}) = \sqrt{\hat{m}^2(\tilde{g}) + \hat{p}_T^2(\tilde{g})}$. This systematically lower scale for Prospino explains its systematically higher LO cross section with respect to that of Pythia as shown in Figure 4.4.

Physics Background Processes

The QCD instrumental background is estimated from a data-driven method as well as from MC samples.

Process	Decay Channel	ReqID	N'_{gen}/N_{gen}	σ_{LO} (pb)	K-factor
$t + \bar{t} + 0lp$ (excl)	$2b + 4lpc$	88040-88043	749973/798098	1.300	1.374
	$2\ell + \nu\bar{\nu} + 2b$	88032-88035	712962/761025	0.324	1.374
	$\ell\nu + 2b + 2lp$	88036-88039	749957/798773	1.300	1.374
$t + \bar{t} + 1lp$ (excl)	$2b + 5lpc$	88058-88060	474181/507835	0.538	1.374
	$2\ell + \nu\bar{\nu} + 2b + 1lp$	88052-88054	467608/499376	0.135	1.374
	$\ell\nu + 2b + 3lp$	88055-88057	479485/509914	0.540	1.374
$t + \bar{t} + 2lp$ (incl)	$2b + 6lpc$	88065-88066	283927/302951	0.254	1.374
	$2\ell + \nu\bar{\nu} + 2b + 2lp$	88061-88062	307694/326796	0.063	1.374
	$\ell\nu + 2b + 4lpc$	88063-88064	282541/302964	0.254	1.374

TABLE 4.6: Description of the top pairs background MC samples ($m_t = 172.5$ GeV)

Process	Decay Channel	ReqID	m_t (GeV)	N'_{gen}/N_{gen}	σ_{NLO} (pb)
$t + b$	$\ell^\pm \nu b + b$	85972,86172-86173, 86191-86194	170.0	164452/174842	0.285
$t + b$	$q' \bar{q} b + b$	-	170.0	-	-
$t + b$	$\ell^\pm \nu b + b$	26624-26625,26696,26706, 26715,26808-26809	175.0	182995/197708	0.285
$t + b$	$q' \bar{q} b + b$	30213,30232	175.0	54936/59746	0.595
$t + q + b$	$\ell^\pm \nu b + qb$	26950-26952,27021-27022, 27083,27085,30540-30541, 86195-86205,86207-86210,86212-86218	170.0	924491/995179	
$t + q + b$	$q' \bar{q} b + qb$	-	170.0	-	-
$t + q + b$	$\ell^\pm \nu b + qb$	26950-26952,27021-27022, 27083,27085	175.0	315717/346293	0.642
$t + q + b$	$q' \bar{q} b + qb$	30540-30541	175.0	92938/99744	1.338

TABLE 4.7: Description of the single top background MC samples

QCD higher order corrections to the cross sections

The k-factors are calculated using MCFM v5.1 [102][103] and defined as:

$$\left\{ \text{K - factor} = \frac{[\sigma^{incl}(X+0lp)]_{NLO}}{[\sigma(X+0lp)]_{LO}} \right.$$

as described in Ref. [97] to correct the LO normalizations of the Alpgen, the Pythia and the ComHep samples calculated using the "Common Samples MC" setting, except for the top pair MC samples generated using $m_t = 172.5$ GeV and the single top ones using $m_t = 175.0$ GeV.

Following the CSMC standards, all the NLO cross sections calculations were based on the 41 CTEQ6.1M PDF set and the renormalization and factorization scales were set to be equal: $\mu_0 = \mu_R = \mu_F$.

Theoretical uncertainties on the MC samples

We considered two sources of theory uncertainty for the MC samples: the QCD scales uncertainty and the PDF uncertainty. We considered the impact of both sources on the MC samples normalization and only from the latter source on the samples acceptance.

The impact of the scales uncertainty on the sample normalization was estimated by varying the central scale μ by factors of 1/2 and 2: $\Delta\sigma_{scale}^+ = \sigma(\mu/2)$ and $\Delta\sigma_{scale}^- = \sigma(2\mu)$.

Process	Decay Channel	ReqID	N'_{gen}/N_{gen}	σ_{LO} (pb)	K-factor
$W^\pm + 0lp$ (excl)	$\ell\nu + 0lp$	31063-31069,31070-31075, 31118-31122,31125, 31860-31864,31867-31870, 32019-32034,32082-32086, 32097,32099-32101, 32513-32516,32547-32556, 32680-32689,36766-36770, 37197-37200,37880-37884, 38070-38079,38141, 38144-38145,38419-38422, 38536,38538-38540, 38573-38577,38660-38664, 39248-39257,42188-42192, 43229-43248,78832-78841, 79663-79671	20375772/21867629	4574.36	1.318
$W^\pm + 0lp$ (excl)	$q'\bar{q}\nu + 0lp$	80132	191291/203495	9002.68	1.318
$W^\pm + 1lp$ (excl)	$\ell\nu + 1lp$	29155,30175-30179, 30372-30373,30375-30376, 32092,32094-32096,34944, 36775,37205,37887-37889, 38148,38423-38424, 38426-38427,38542-38544, 38542-38544,38546, 38665-38669,39258-39262, 42193-42197,43249-43252	4774384/5140276	1278.67	1.318
$W^\pm + 1lp$ (excl)	$q'\bar{q}\nu + 1lp$	80133	93345/99779	2556.57	1.318
$W^\pm + 2lp$ (excl)	$\ell\nu + 2lp$	28478,28868,29156-29159, 36776-36778,37206-37208, 37890-37892,38151-38153, 38428-38430,38547,38549, 38670,38672-38674, 39263-39267,42198-42202	4936813/5250195	304.52	1.318
$W^\pm + 2lp$ (excl)	$q'\bar{q}\nu + 2lp$	80134	20843/22435	604.93	1.318
$W^\pm + 3lp$ (excl)	$\ell\nu + 3lp$	29160-29162,36779-36780, 37209-37211,37893, 37893,38154-38155, 38675-38680,39268-39272, 42203-42204	3042755/3244296	39.78	1.318
$W^\pm + 3lp$ (incl)	$q'\bar{q}\nu + 3lp$	80135	18550/19985	196.20	1.318
$W^\pm + 4lp$ (excl)	$\ell\nu + 4lp$	38681-38682,39273-39276, 39278-39282,42205	215672/230301	16.41	1.318
$W^\pm + 5lp$ (incl)	$\ell\nu + 5lp$	34959,36814,37212,37895, 38156,38683-38688, 39283-39285,42206, 48472,48479,78852-78854, 80032-80034	1480885/1574367	7.96	1.318
$W^\pm + c + 0lp$ (excl)	$\ell\nu + c + 0lp$	82754	192967/205588	239.767	1.648
$W^\pm + c + 1lp$ (excl)	$\ell\nu + c + 1lp$	82772-82773	364083/386931	77.010	1.648
$W^\pm + c + 2lp$ (excl)	$\ell\nu + c + 2lp$	82792	96093/101720	14.245	1.648
$W^\pm + c + 3lp$ (excl)	$\ell\nu + c + 3lp$	82832	47225/50426	2.541	1.648
$W^\pm + c + 4lp$ (incl)	$\ell\nu + c + 4lp$	82833	47806/50789	0.597	1.648
$W^\pm + c\bar{c} + 0lp$ (excl)	$\ell\nu + c\bar{c} + 0lp$	73912,81032-81036	1173868/1249158	23.964	1.886
$W^\pm + c\bar{c} + 0lp$ (excl)	$q'\bar{q} + c\bar{c} + 0lp$	80139	189509/202952	47.949	1.886
$W^\pm + c\bar{c} + 1lp$ (excl)	$\ell\nu + c\bar{c} + 1lp$	73913,81052-81054	719436/766617	13.352	1.886
$W^\pm + c\bar{c} + 1lp$ (excl)	$q'\bar{q} + c\bar{c} + 1lp$	80140	140628/149971	26.925	1.886
$W^\pm + c\bar{c} + 2lp$ (excl)	$\ell\nu + c\bar{c} + 2lp$	73916,81072-81073,82792	429025/457287	5.510	1.886
$W^\pm + c\bar{c} + 2lp$ (incl)	$q'\bar{q} + c\bar{c} + 2lp$	80141	95977/101975	16.110	1.886
$W^\pm + c\bar{c} + 3lp$ (incl)	$\ell\nu + c\bar{c} + 3lp$	73917,81092-81093	434022/462460	2.519	1.886
$W^\pm + b\bar{b} + 0lp$ (excl)	$\ell\nu + b\bar{b} + 0lp$	72292,72732,76492-76494	1170159/1245903	9.337	1.881
$W^\pm + b\bar{b} + 0lp$ (excl)	$q'\bar{q} + b\bar{b} + 0lp$	80136	197179/208707	18.682	1.881
$W^\pm + b\bar{b} + 1lp$ (excl)	$\ell\nu + b\bar{b} + 1lp$	72293,72752,76495-76496	616327/658037	4.264	1.881
$W^\pm + b\bar{b} + 1lp$ (excl)	$q'\bar{q} + b\bar{b} + 1lp$	80137	146323/156166	8.554	1.881
$W^\pm + b\bar{b} + 2lp$ (excl)	$\ell\nu + b\bar{b} + 2lp$	72294,72852-72853	226894/242368	1.548	1.881
$W^\pm + b\bar{b} + 2lp$ (incl)	$q'\bar{q} + b\bar{b} + 2lp$	80138	94131/100330	4.795	1.881
$W^\pm + b\bar{b} + 3lp$ (incl)	$\ell\nu + b\bar{b} + 3lp$	74072,76497-76499	252520/269475	0.745	1.881

TABLE 4.8: Description of the W+jets background MC samples

Process	Decay Channel	ReqID	N'_{gen}	σ_{LO} (pb)	K-factor
$\gamma^*/Z + 0lp$ (excl) ($15 < \hat{m} < 60$ GeV)	$\ell^\pm \ell^\mp + 0lp$	32873-32875,32900-32902, 32910-32912	1662879/1791819	336.212	1.329
$\gamma^*/Z + 0lp$ (excl) ($60 < \hat{m} < 130$ GeV)	$\ell^\pm \ell^\mp + 0lp$	29270-29280,36998-36999, 37003-37004,37008-37009, 37407-37410,37412-37415, 38350-38351,38363-38366, 38408-38417,73412-73419, 75192-75200,75654-75661, 78032-78043	10951319/1171201	140.291	1.329
$\gamma^*/Z + 0lp$ (excl) ($130 < \hat{m} < 250$ GeV)	$\ell^\pm \ell^\mp + 0lp$	32618,32621,32626,84192	477671/503395	0.906	1.329
$\gamma^*/Z + 0lp$ (excl) ($250 < \hat{m} < 1960$ GeV)	$\ell^\pm \ell^\mp + 0lp$	33734,33738,33937	283987/308793	0.0701057	1.329
$\gamma^*/Z + 1lp$ (excl) ($15 < \hat{m} < 60$ GeV)	$\ell^\pm \ell^\mp + 1lp$	32876-32878,32903-32905, 32913-32915	907719/972426	39.4202	1.329
$\gamma^*/Z + 1lp$ (excl) ($60 < \hat{m} < 130$ GeV)	$\ell^\pm \ell^\mp + 1lp$	37000,37005,37010, 37416-37418,38360, 38362,38367,73354, 73372,75212-75215, 75232-75233,75662-75663	3436255/3663319	42.270	1.329
$\gamma^*/Z + 1lp$ (excl) ($130 < \hat{m} < 250$ GeV)	$\ell^\pm \ell^\mp + 1lp$	32619,32623,32627,84193	446823/478660	0.365395	1.329
$\gamma^*/Z + 1lp$ (excl) ($250 < \hat{m} < 1960$ GeV)	$\ell^\pm \ell^\mp + 1lp$	33735,33739,33938	265073/294839	0.0369237	1.329
$\gamma^*/Z + 2lp$ (excl) ($15 < \hat{m} < 60$ GeV)	$\ell^\pm \ell^\mp + 2lp$	32879-32880,32906-32907, 32916-32917	494383/526417	10.297	1.329
$\gamma^*/Z + 2lp$ (excl) ($60 < \hat{m} < 130$ GeV)	$\ell^\pm \ell^\mp + 2lp$	37001,37006,37011, 38368-38370,75252-75257	1609582/1716454	10.4663	1.329
$\gamma^*/Z + 2lp$ (excl) ($130 < \hat{m} < 250$ GeV)	$\ell^\pm \ell^\mp + 2lp$	32620,32624,32628, 32647-32649,84194-84195	789129/852571	0.0986418	1.329
$\gamma^*/Z + 2lp$ (excl) ($250 < \hat{m} < 1960$ GeV)	$\ell^\pm \ell^\mp + 2lp$	33736-33737,33740-33741, 33939-33940	386718/419243	0.0118	1.329
$\gamma^*/Z + 3lp$ (incl) ($15 < \hat{m} < 60$ GeV)	$\ell^\pm \ell^\mp + 3lp$	32881-32882,32908-32909, 32918-32919	230226/245426	3.08402	1.329
$\gamma^*/Z + 3lp$ (excl) ($60 < \hat{m} < 130$ GeV)	$\ell^\pm \ell^\mp + 3lp$	43181,43184,44184	323469/343266	3.90446	1.329
$\gamma^*/Z + 3lp$ (incl) ($130 < \hat{m} < 250$ GeV)	$\ell^\pm \ell^\mp + 3lp$	33737,33741,33940	367747/402636	0.040569	1.329
$\gamma^*/Z + 3lp$ (incl) ($250 < \hat{m} < 1960$ GeV)	$\ell^\pm \ell^\mp + 3lp$	32647-32649,84195	127204/138445	0.0048711	1.329
$\gamma^*/Z + 4lp$ (excl) ($60 < \hat{m} < 130$ GeV)	$\ell^\pm \ell^\mp + 4lp$	29518,43182,43185,44185	270904/289262	0.538130170371	1.329
$\gamma^*/Z + 5lp$ (incl) ($60 < \hat{m} < 130$ GeV)	$\ell^\pm \ell^\mp + 5lp$	43183,43186,44186	106784/114506	0.379501584997	1.329

TABLE 4.9: Description of the $Z(\rightarrow \ell^+ \ell^-) + jets$ background MC samples

The impact of the PDF uncertainty on the sample normalization and acceptance were estimated using the so-called "CTEQ asymmetric prescription" [99]: $\Delta\sigma_{PDF} = \sum_{i=1}^{40} [\sigma_{PDF_i} - \sigma_{PDF_0}]^2$, where σ_{PDF_0} represent the central PDF of the CTEQ6.1M series.

Process	Decay Channel	ReqID	N'_{gen}	σ_{LO} (pb)	K-factor
$Z + 0lp$ (excl)	$\nu\bar{\nu} + 0lp$	29512-29513,41184-41188	1291747/1379060	818.043	1.322
$Z + 1lp$ (excl)	$\nu\bar{\nu} + 1lp$	29515,30605-30608,41189-41198	2694194/2873198	245.504	1.322
$Z + 2lp$ (excl)	$\nu\bar{\nu} + 2lp$	29516-29517,41199-41203	991292/1060008	61.184	1.322
$Z + 3lp$ (excl)	$\nu\bar{\nu} + 3lp$	42625-42626	202745/215956	14.605	1.322
$Z + 4lp$ (excl)	$\nu\bar{\nu} + 4lp$	29518,42627	128380/135929	3.368	1.322
$Z + 5lp$ (incl)	$\nu\bar{\nu} + 5lp$	33160-33161,42628	146812/155651	1.857	1.322

TABLE 4.10: Description of the $Z(\rightarrow \nu\bar{\nu}) + jets$ background MC samples

Process	Decay Channel	ReqID	N'_{gen}/N_{gen}	σ_{LO} (pb)	K-factor
$Z + c\bar{c} + 0lp$ (excl)	$\nu\bar{\nu} + c\bar{c} + 0lp$	81236	196973/208993	17.7439	1.322
$Z + c\bar{c} + 1lp$ (excl)	$\nu\bar{\nu} + c\bar{c} + 1lp$	81237	64689/69783	6.26213	1.322
$Z + c\bar{c} + 2lp$ (incl)	$\nu\bar{\nu} + c\bar{c} + 2lp$	81238	49245/51987	2.51	1.322
$\gamma^*/Z + c\bar{c} + 0lp$ (excl), $15 < \hat{m} < 75$ GeV	$\ell^+\ell^- + c\bar{c} + 0lp$	85112-85114	577621/610871		
$\gamma^*/Z + c\bar{c} + 0lp$ (excl), $75 < \hat{m} < 130$ GeV	$\ell^+\ell^- + c\bar{c} + 0lp$	74418-74420	575897/611984	3.04996	1.329
$\gamma^*/Z + c\bar{c} + 0lp$ (excl), $130 < \hat{m} < 250$ GeV		85461-85463	279948/299413		
$\gamma^*/Z + c\bar{c} + 1lp$ (excl), $15 < \hat{m} < 75$ GeV	$\ell^+\ell^- + c\bar{c} + 1lp$	85132-85134	284524/305523		
$\gamma^*/Z + c\bar{c} + 1lp$ (excl), $75 < \hat{m} < 130$ GeV	$\ell^+\ell^- + c\bar{c} + 1lp$	74415-74417	305244/322332	1.07254	1.329
$\gamma^*/Z + c\bar{c} + 1lp$ (excl), $130 < \hat{m} < 250$ GeV	$\ell^+\ell^- + c\bar{c} + 1lp$	85464-85466	139973/149865		
$\gamma^*/Z + c\bar{c} + 2lp$ (incl), $15 < \hat{m} < 75$ GeV	$\ell^+\ell^- + c\bar{c} + 2lp$	85135-85137	289180/307677		
$\gamma^*/Z + c\bar{c} + 2lp$ (incl), $75 < \hat{m} < 130$ GeV	$\ell^+\ell^- + c\bar{c} + 2lp$	74412-74414	143265/153426	0.438884	1.329
$\gamma^*/Z + c\bar{c} + 2lp$ (incl), $130 < \hat{m} < 250$ GeV	$\ell^+\ell^- + c\bar{c} + 2lp$	8546-85469	141175/149585		
$Z + b\bar{b} + 0lp$ (excl)	$\nu\bar{\nu} + b\bar{b} + 0lp$	81232-81233	377220/401472	5.8059	1.322
$Z + b\bar{b} + 1lp$ (excl)	$\nu\bar{\nu} + b\bar{b} + 1lp$	81234	185063/196132	2.1492	1.322
$Z + b\bar{b} + 2lp$ (incl)	$\nu\bar{\nu} + b\bar{b} + 2lp$	81235	86060/92565	0.8869	1.322
$\gamma^*/Z + b\bar{b} + 0lp$ (excl), $15 < \hat{m} < 75$ GeV	$\ell^+\ell^- + b\bar{b} + 0lp$	84892-84894	630770/668800		
$\gamma^*/Z + b\bar{b} + 0lp$ (excl), $75 < \hat{m} < 130$ GeV	$\ell^+\ell^- + b\bar{b} + 0lp$	73952,73955,73992	568446/603773	0.987807	1.329
$\gamma^*/Z + b\bar{b} + 0lp$ (excl), $130 < \hat{m} < 250$ GeV	$\ell^+\ell^- + b\bar{b} + 0lp$	85452-85454	301022/320615		
$\gamma^*/Z + b\bar{b} + 1lp$ (excl), $15 < \hat{m} < 75$ GeV	$\ell^+\ell^- + b\bar{b} + 1lp$	84912-84914	270383/289433		
$\gamma^*/Z + b\bar{b} + 1lp$ (excl), $75 < \hat{m} < 130$ GeV	$\ell^+\ell^- + b\bar{b} + 1lp$	73953,73956,74012	278437/295399	0.367608	1.329
$\gamma^*/Z + b\bar{b} + 1lp$ (excl), $130 < \hat{m} < 250$ GeV	$\ell^+\ell^- + b\bar{b} + 1lp$	85455-85457	100202/107023		
$\gamma^*/Z + b\bar{b} + 2lp$ (incl), $15 < \hat{m} < 75$ GeV	$\ell^+\ell^- + b\bar{b} + 2lp$	84915-84917	267252/287260		
$\gamma^*/Z + b\bar{b} + 2lp$ (incl), $75 < \hat{m} < 130$ GeV	$\ell^+\ell^- + b\bar{b} + 2lp$	73954,73972,74032	132009/141298	0.152731	1.329
$\gamma^*/Z + b\bar{b} + 2lp$ (incl), $130 < \hat{m} < 250$ GeV	$\ell^+\ell^- + b\bar{b} + 2lp$	85458-85460	126759/134714		

TABLE 4.11: Description of the $\gamma^*/Z + HF - jets$ background MC samples

Process	Decay Channel	ReqID	N'_{gen}/N_{gen}	σ_{LO} (pb)	K-factor
$W^\pm + W^\mp$	incl	33681-33683,38488-38490,38939-38943, 42208-42211,79214,79553	2854003/3044069	7.986	1.414
$W^\pm + W^\mp$	$e^\pm + \nu + q'\bar{q}$	27886	86742/95000	1.163	1.414
$W^\pm + W^\mp$	$\mu^\pm + \nu + q'\bar{q}$	27887	106664/115994	1.160	1.414
$W^\pm + W^\mp$	$\ell^+ \ell^- + \nu\bar{\nu}$	26146-26147,43932,44111,80532,81692	768772/813067	0.84119	1.414
$W^\pm + Z$	incl	30488-30489,33684-33685,30838,38491, 42212,79212,79554	850943/907311	2.38875	1.514
$W^\pm + Z$	$e^+e^- + q'\bar{q}$	30088	92315/103750	0.0542225	1.514
$W^\pm + Z$	$\mu^\pm + \mu^\mp + q'\bar{q}$	30089	95976/99931	0.0545385	1.514
$W^\pm + Z$	$3\ell^\pm + 3\nu$	43930,44109	202074/215772	0.0784225	1.514
$\gamma^*/Z + \gamma^*/Z$	incl	30486-30487,33686-33687, 38492,42213,79213,79552	858532/916903	0.9369	1.442
$\gamma^*/Z + \gamma^*/Z$	$4e^\pm$	30835	25110/25997	0.00104943	1.442
$\gamma^*/Z + \gamma^*/Z$	$4\mu^\pm$	30836	22622/25250	0.00106397	1.442
$\gamma^*/Z + \gamma^*/Z$	$2e^\pm + 2\mu^\pm$	30838	24083/24987	0.00208868	1.442
$\gamma^*/Z + Z$	$2\ell^\pm + \nu\bar{\nu}$	43931,44110,80512	350511/373201	0.0411261624	1.442

TABLE 4.12: Description of the di-boson background MC samples

4.2.3.3 Data and Monte Carlo Samples Treatment

4.2.3.3.a Samples Fixing

Data Fixing

With the p17 releases, the Run 2a data samples were reconstructed with the p17.03.03, p17.05.01 versions of d0reco. These versions did not have a hadronic calibration of the calorimeter unlike the p17.09.00 version. Therefore the p17.03.03 and the p17.05.01 thumbnails (TMB) needed to be fixed unlike the p17.09.00 ones. A problem known as a gain "cable swap" [121] affecting the EC south ($0.98 < \phi < 1.57$ rad) occurred at the end of the Run 2a. This was from december 2005 till february 2006, for the run range [213064-214999]. The samples not affected by this problem were not re-reconstructed and were reskimmed. The samples affected by this problem were re-reconstructed with the p17.09.06 version of d0reco.

The actual treatments applied in the TMB fixing were:

- HCAL calibration and propagation to all CAL objects
- adaptative revertexing [106]
- improve material description, refit the tracks, redo the track matching wrt relevant objects

Finally, our data samples correspond to the following SAM datasets:

- CSskim-NP-PASS3-p17.09.03
- refixed
- CSskim-NP-PASS3-p17.09.06
- reco'd w/ p17.09.00, unfixed and re-reco'd w/ p17.09.06 (cable swap)
- CSskim-NP-PASS3-p17.09.06b
- unfixed and re-reco'd (non cable swap)

MC Fixing

Most of our MC samples were produced with the p17.09.01 release and then fixed with p17.09.05. Some of those samples were directly produced with p17.09.06 and did not require any fixing; this was in particular the case for our signal samples produced privately using mc_runjob v06-05-26.

4.2.3.3.b Data Quality

In order to ensure the data are not affected by some detector malfunctions, some data quality requirements are imposed. They are based on the global quality of the runs as defined by the sub-detectors experts and on the quality of one minute sub-units of the runs called luminosity blocks (LB) and on the removal of the known of calorimeter noises and problems.

The two first types of criteria are taken into account for the integrated luminosity computation. Whereas the inefficiency due the rejection of events with calorimeter noise is estimated on a zero bias data sample and found to be $97.14 \pm 0.003\%$. This inefficiency is then applied to correct that of the MC samples.

4.2.3.3.c Data Skimming

The data samples were skimmed according mainly to the fired trigger bits. For this analysis we used the so-called "NP" skim that requires one of the following triggers: MHT30_CJT(3,5), or JT1_ACO_MHT_HT, or JT2_MHT25_HT trigger and $\cancel{E}_T > 15 \text{ GeV}$ in addition.

4.2.3.3.d Jet Energy Scale

This analysis is based on the JCCB jets reconstructed with a Run 2 cone algorithm, with a radius of 0.5. We used the p17 certified jet identification [117] and the p17 Jet Energy Scale (JES) [113]. Furthermore, the MC jet were corrected for their relative JES difference between data and MC. The "Smearing, Shifting and Removing" (SSR) method [118] was applied exactly with the same provisions as in Ref. [79].

4.2.3.3.e Missing Transverse Energy

We used the METB definition of the \cancel{E}_T , which is calculated on all the calorimeter cells excepting those from the Coarse Hadronic (CH) layer [120]. For the EM clusters, (respectively for the good jets), the EM scale (respectively the JES) is propagated to the \cancel{E}_T with a special care for overlapping cases between both type of objects. For the MC samples, the smearing of the EM energies as well as the jet SSR corrections were also propagated to the \cancel{E}_T .

4.2.3.3.f Bad Jets

The jet candidates not passing the jet ID cuts [117] are called bad jets. These bad jets may be seeded or largely made of calorimeter noise. Or they can simply be badly reconstructed jets that fail the ID cuts and therefore are not corrected for the Jet Energy Scale. Hence they distort the events p_T balance and contribute to the fake \cancel{E}_T .

4.2.3.3.g Reweighting of the Number of Primary Vertices

The zero bias (ZB) data samples used for a realistic simulation the $p\bar{p}$ multiple interactions do not reproduce the luminosity profile of the Run 2a data samples. Therefore, in order to apply the jet confirmation by the tracks and the b-tagging without introducing a bias, it is necessary to adjust the MC luminosity profile to that of the data. This adjustment is realized by reweighting the MC samples by the ratio of the N_{PV} distributions in the data and in the MC.

Figure 4.6 show the distributions of the N_{PV} for the JT1 (top) and the JT2 (bottom) streams for the data and the MC background (left) and for the data and the MC signal (right). The data are the full dots. The SM background before and after the reweighting are respectively the stack histogram and the empty triangles. The MC signals before and after the reweighting are respectively the full histogram and the empty triangles.

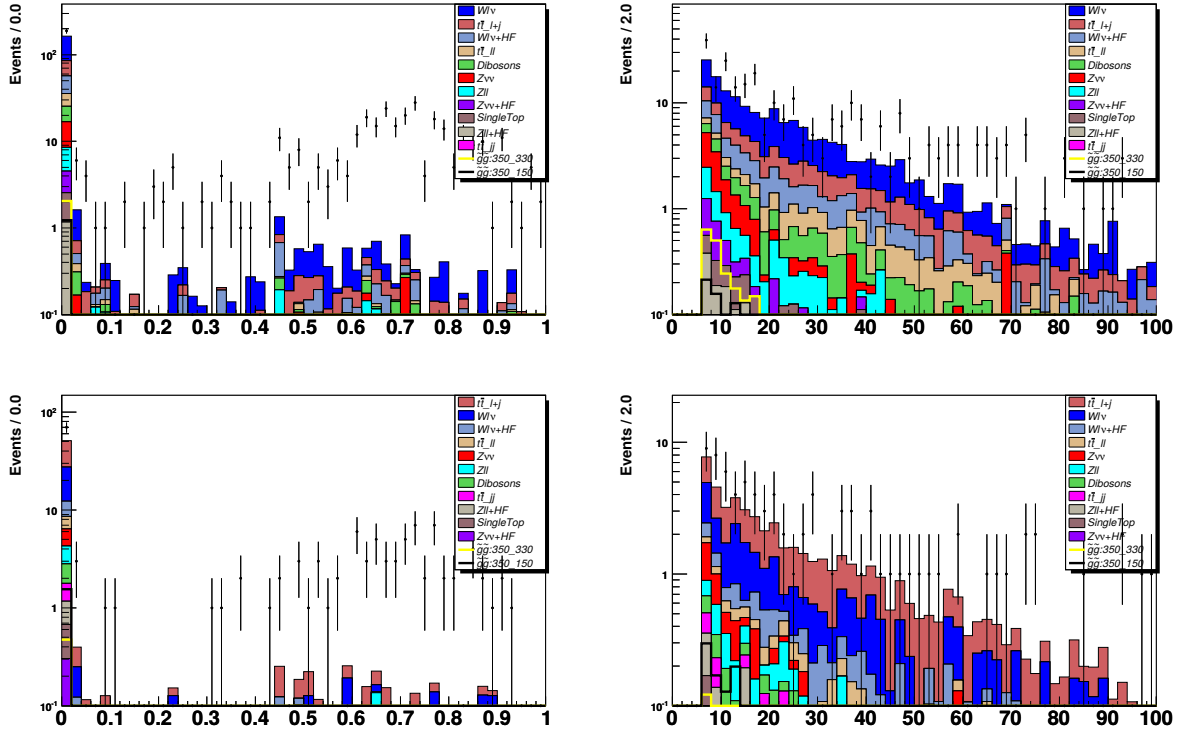


FIGURE 4.5: The coarse hadronic fraction (left) and the p_T (right) of the bad jets. The bad jets of the JT1 and the JT2 analysis streams are respectively displayed in the top and the bottom row.

N_{PV}	Correction Factor			
	JT1		JT2	
1	0.707	0.749	0.580	0.618
2	1.085	1.112	1.212	1.224
3	1.960	1.580	2.293	1.975
4	2.612	1.578	2.025	1.307
6	7.332	3.185	4.523	2.422
≥ 6	19.750	3.945	14.826	3.108

TABLE 4.13: The MC background correction factors derived from the N_{PV} "data/MC" reweighting after the "JT1 C2" cuts.

4.2.3.3.h Tracks Based Confirmation of the Jets

In order to increase the data samples quality with respect to the calorimeter noise, the mismeasured jets and the cosmic rays depositing large amount of energy in the calorimeter, we impose a confirmation of the leading jets by the tracks. We use the so-called CPF_0 variable based on tracks and primary vertices (PV) and defined for the jet i and the PV j as

$$CPF(j_i, PV_j) = \frac{\sum_{trk} p_T^{trk}(j_i, PV_j)}{\sum_{k=1}^{N_{PV}} \sum_{trk} (j_i, PV_k)}$$

where the track of index trk , attached to the primary vertex PV_j , lies within the jet j_i cone.

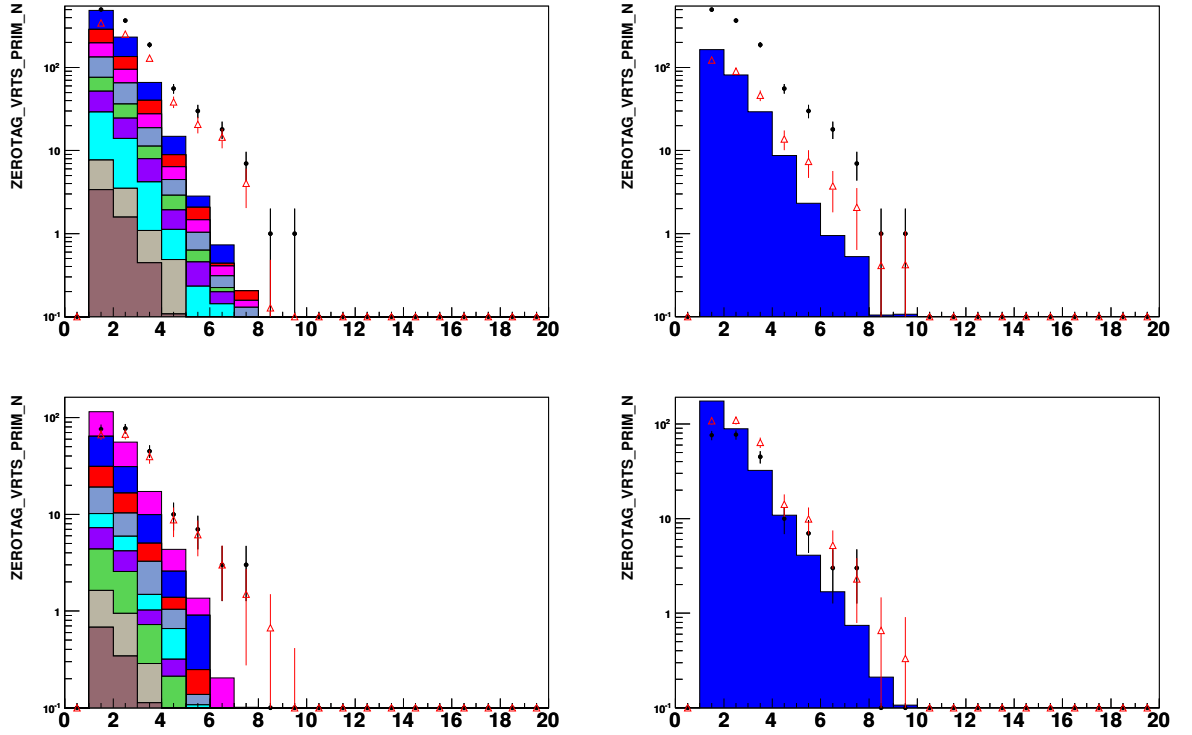


FIGURE 4.6: Distributions of the N_{PV} for the JT1 (top) and the JT2 (bottom) streams for the data and the MC background (left) and for the data and the MC signal (right). The data are the full dots, the SM background before and after the reweighting are respectively the stack histogram and the empty triangles. The MC signals before and after the reweighting are respectively the full histogram and the empty triangles.

For a given jet, CPF_0 corresponds to the above ratio relative to the best PV. CPF_0 can take the following values.

$$\begin{cases} CPF_0 = -1 & \text{no tracks associated to any vertex} \\ CPF_0 = 0 & \text{all jet tracks don't point towards the best PV} \\ CPF_0 = 1 & \text{all jet tracks point towards the best PV} \\ 0 < CPF_0 < 1 & \text{otherwise} \end{cases}$$

It should be noted that for events with only one reconstructed PV, $|CPF_0| = 1$.

Since the detector simulation cannot reproduce the tracking efficiencies measured in the data, we had to determine MC to data scale factors. These scale factors enable to obtain the same efficiencies when applying the CPF_0 cut on data and on MC.

They were derived using data samples from the QCD skim based on the following triggers: JT8, JT15 and JT25; and QCD MC samples with parton p_T intervals: $[40 - 80]$, $[80 - 160]$, $[160 - 320]$, $[320 - 980]$. The following event selection was applied:

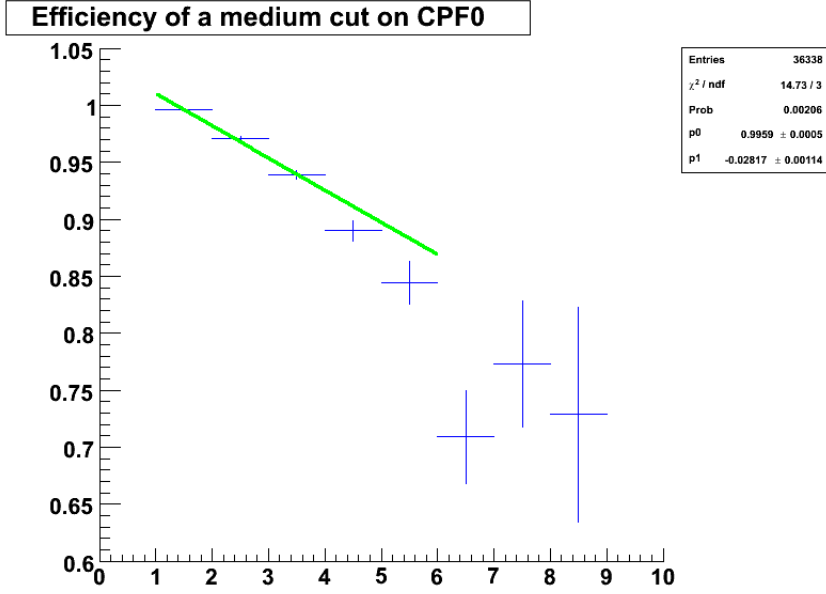


FIGURE 4.7: MC correction factor ($\epsilon_{Data}/\epsilon_{MC}$) for a medium cut on CPF_0 ($CPF_0 > 0.85$) as a function of the number of PV.

$$\left\{ \begin{array}{ll} \text{Data Quality} & \\ 1 \text{ PV} & w/ |z_{PV}| < 60 \text{ cm} \\ N_j = 2 & w/ |\eta_{\text{det}}(j_1, j_2)| < 0.8 \text{ and } p_T(j_2) > 40 \text{ GeV} \\ \Delta\phi(j_1, j_2) > 170^\circ & \end{array} \right.$$

Parametrizations of the efficiency were derived as a function of the number of PV, for the leading jet:

$$\left\{ \begin{array}{ll} CPF_0 \neq 0 : & 1. - 0.003467(N_{PV} - 1) \\ CPF_0 \neq -1 : & 0.9958 - 0.0003442(N_{PV} - 1) \\ CPF_0 > 0.85 : & 0.9959 - 0.02817(N_{PV} - 1) \end{array} \right.$$

and for the next-to-leading jet, knowing the first is confirmed,

$$\left\{ \begin{array}{ll} CPF_0 \neq 0 : & 0.9975 - 0.0007508(N_{PV} - 1) \\ CPF_0 \neq -1 : & 1. - 0.00004998(N_{PV} - 1) \\ CPF_0 > 0.85 : & 0.9976 - 0.01426(N_{PV} - 1) \end{array} \right.$$

Figure 4.7 illustrates one of these parametrizations for the hardest jet for $CPF_0 > 0.85$, a medium cut.

4.2.3.3.i B-Tagging

We use the b-tagging to exploit the large heavy flavor (HF) content of our signal. We first determine different jets taggabilities from our data samples depending on our events topology (see 4.2.3.5). We parametrize these taggabilities as (independent) functions of the jets η_{det} , ϕ , p_T and z_{PV} and correct the MC samples for the data versus MC efficiency differences. Note that no special treatments are applied to jets identified as hadronic taus.

The data and MC samples after the following loose preselection cuts are used for these taggability studies:

$$\left\{ \begin{array}{l} \text{For the acoplanar dijet topology :} \\ \text{Triggers : MHT30_CJT(3, 5) or JT1_ACO_MHT_HT} \\ \text{Data quality cuts} \\ \text{At least one reco'd PV, with } |z_{PV}| < 60 \text{ cm} \\ \text{2 good jets w/ } p_T(j_2) > 15 \text{ GeV and } |\eta_{det}(j_1, j_2)| < 2.5 \\ \cancel{E}_T > 40 \text{ GeV} \\ \Delta\phi(j_1, j_2) < 165^\circ \\ \Delta\phi_{min}(\cancel{E}_T, jets) > 40^\circ \\ \text{CPF}_0(j_1, j_2) > 0.85 \end{array} \right.$$

or

$$\left\{ \begin{array}{l} \text{For the (more spherical) multijet topology :} \\ \text{Triggers : MHT30_CJT(3, 5) or JT2_MHT25_HT} \\ \text{Data quality cuts} \\ \text{At least one reco'd PV, w/ } |z_{PV}| < 60 \text{ cm} \\ \text{3 good jets w/ } p_T > 15 \text{ GeV and } |\eta_{det}(j_1, j_2, j_3)| < 2.5 \\ \cancel{E}_T > 50 \text{ GeV} \\ \text{CPF}_0(j_1, j_2) > 0.85 \end{array} \right.$$

Figure 4.8 (respectively figure 4.9) shows the taggability dependence on ϕ , p_T and z_{PV} .

Figure 4.10 (respectively figure 4.11) displays the closure tests that compare the corrected simulated taggable jets to the data taggable jets and the parametrizations as a function of z_{PV} , p_T and ϕ .

Once the taggabilities are known and the MC efficiencies are corrected, we apply the Tag Rate Functions (TRF) corresponding to the probability of tagging a given MC jet as determined from the p17 neural network (NN) selection in Ref. [123]. We used three different operating points "loose", "medium" and "tight" defined therein. For the multi-b-tags, we only considered the combinations of identical operating points.

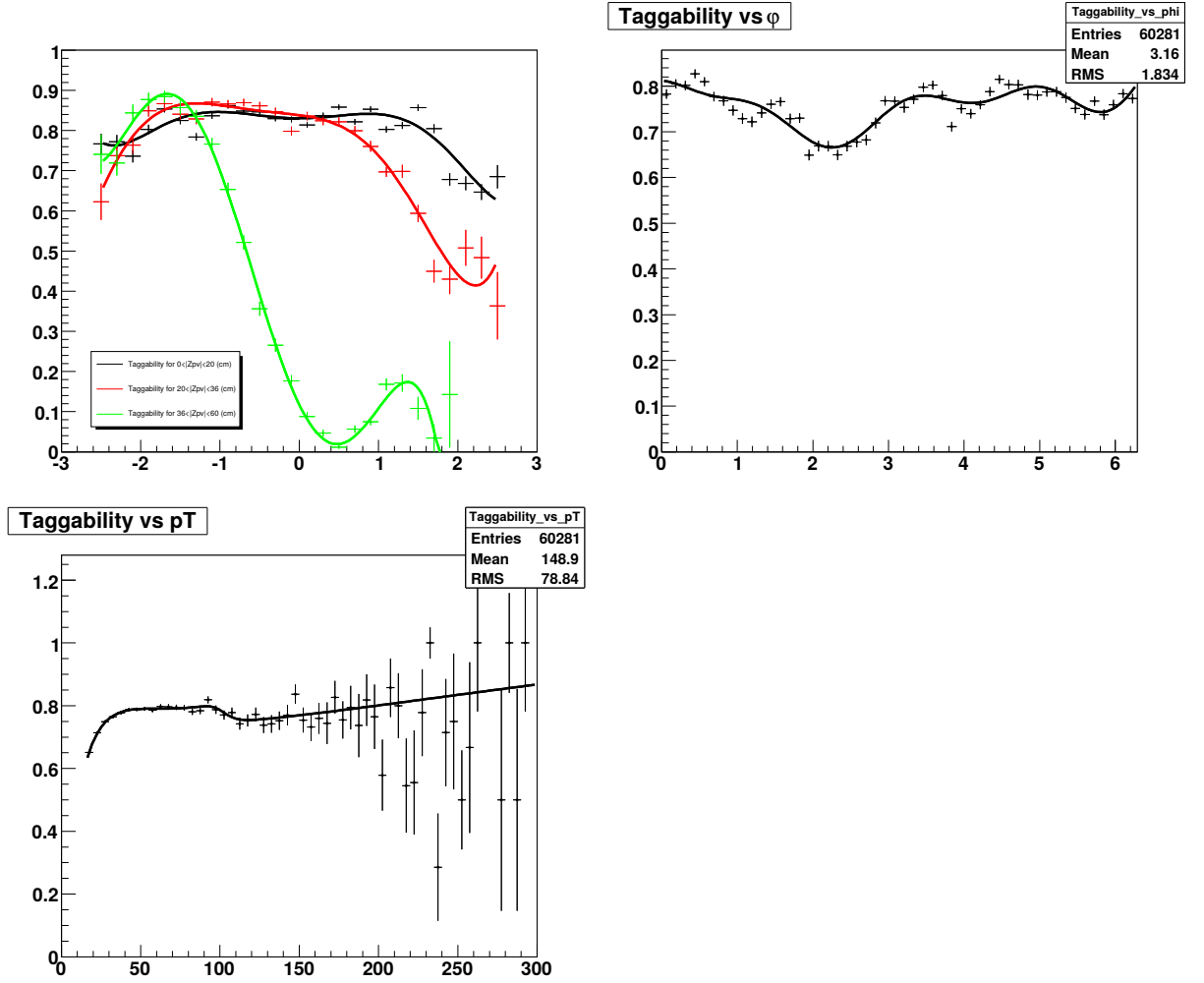


FIGURE 4.8: Taggabilities for the acoplanar dijet topology as functions of z_{PV} (top left), ϕ (top right) and p_T (bottom).

Note that the $W + jets$, $W + b\bar{b} + jets$, $\gamma^*/Z + jets$, $\gamma^*/Z + b\bar{b} + jets$ samples were filtered out from their events containing:

$$\left\{ \begin{array}{l} c\bar{c} \text{ pairs in the ME (} W + jets, \gamma^*/Z + jets \text{)} \\ c\bar{c} \text{ and } b\bar{b} \text{ pairs in the PS (} W + jets, \gamma^*/Z + jets \text{)} \\ c\bar{c} \text{ pairs in the PS (} W + b\bar{b} + jets, \gamma^*/Z + b\bar{b} + jets \text{)} \end{array} \right.$$

as advocated in Ref. [122]. The abbreviations ME and PS stand for matrix element and parton shower respectively. The cross sections were re-scaled according to the proportion of rejected events. This heavy flavor skimming is meant to avoid double counted contributions from different sub-processes to the $W + c\bar{c} + jets$ and $\gamma^*/Z + c\bar{c} + jets$ background samples.

Control regions designed to verify the impact of the b-tagging on the data vs MC agreement are presented in sub-section 4.2.3.16.

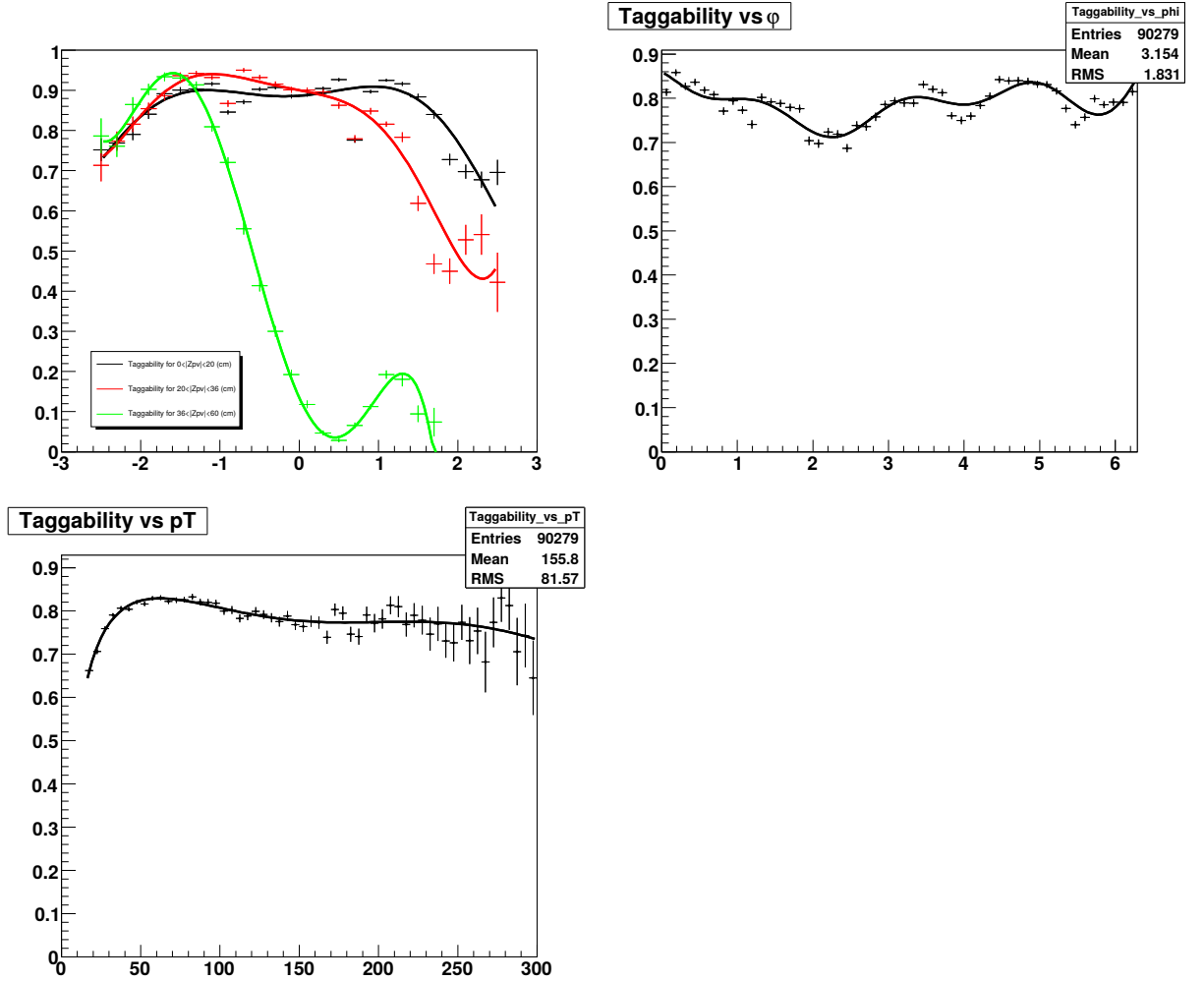


FIGURE 4.9: Taggability for the multijet topology as functions of z_{PV} (top left), ϕ (top right) and p_T (bottom).

4.2.3.4 Event Selection

4.2.3.5 Analysis Strategy

The search topology depends drastically on the mass splittings between the SUSY particles as illustrated in figure 4.12. We denote the upper and lower mass splittings: $\Delta M = m_{\tilde{g}} - m_{\tilde{b}_1}$ and $\Delta m = m_{\tilde{b}_1} - m_{\tilde{\chi}_1^0}$. We can distinguish two cases:

1. either, ΔM , Δm are both large (typically larger than 50 GeV)
2. or, one of them is small (typically less than 10-20 GeV)

In the first case, we can expect a final state made of 4 hard jets which will be most of the time taggable; this corresponds to a "4b-jets + \cancel{E}_T " inclusive search topology. Whereas in the second case, because of their small phase space volumes, two of the jets will either turn out to be below the good jets p_T threshold or not to be taggable. This will therefore lead to a "2b-jets + \cancel{E}_T " inclusive search topology.

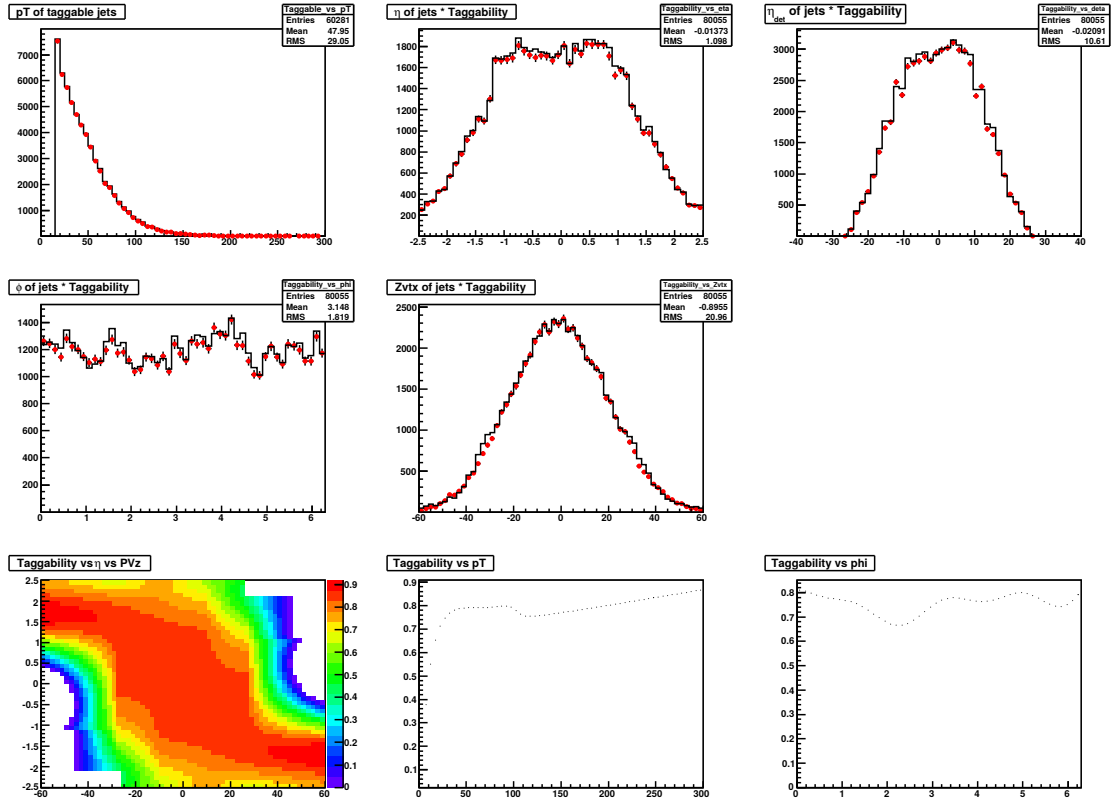


FIGURE 4.10: Closure tests for the acoplanar dijet taggabilities (5 top plots). Taggabilities parametrizations as functions of z_{PV} , p_T and ϕ (3 bottom plots).

Obviously when both ΔM and Δm are small, we are in a "compressed SUSY spectrum" scenario where the sensitivity to the signal is strongly reduced, unabling the search for the signal altogether.

4.2.3.6 Trigger Conditions

For the first period of Run 2a data taking only the "MHT30_3CJT5" trigger condition is utilized, irrespective of the above cited topologies. For the further periods, the "JT1_ACO_MHT_HT" and the "JT2_MHT25_HT" trigger conditions take over to collect events corresponding to the $2jets + \cancel{E}_T$ and the $4jets + \cancel{E}_T$ inclusive topologies, respectively.

These two inclusive data streams lead us to apply the two following event preselections that both aim at selecting events compatible with our search topologies with large trigger efficiencies and to start reducing the rate of the instrumental background essentially coming from QCD mis-reconstructed events.

These different trigger conditions were simulated for the MC samples [111][90]. Starting from data samples a parametrization of the p_T of the reconstructed objects. The number of trigger towers above the L1 trigger term, the p_T of level 2 and level 3 jets as a function of the p_T of off-line jets are determined. This way we can estimate the trigger efficiencies for the MC events. The systematic uncertainties for the trigger terms of interest for this analysis were determined

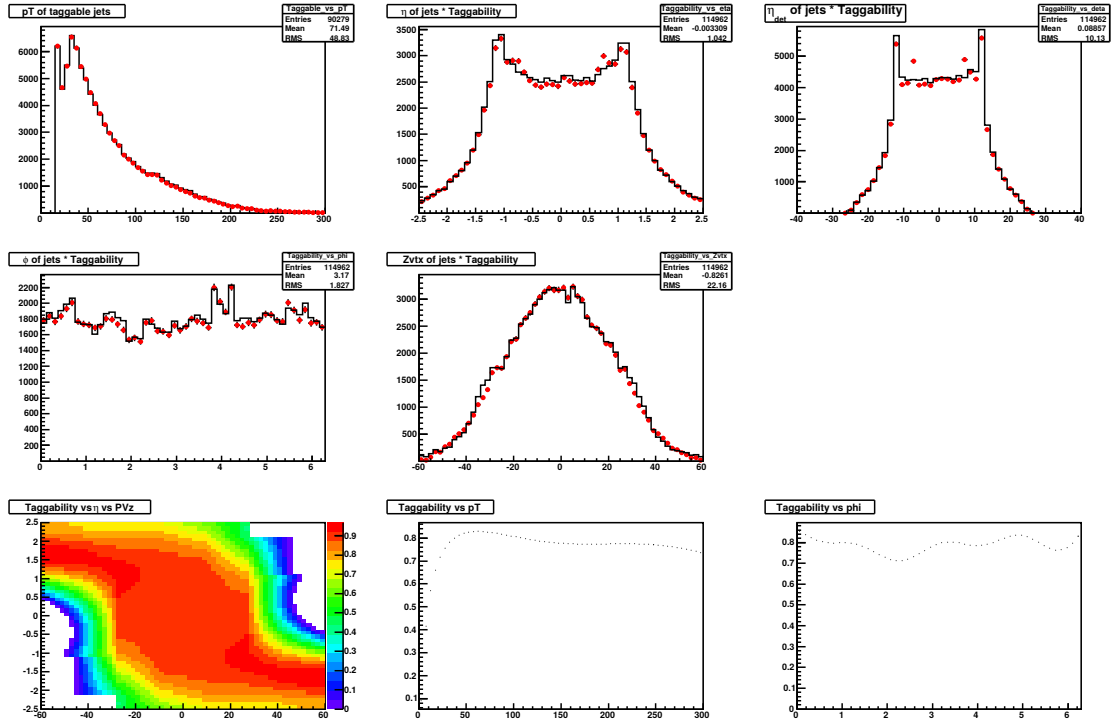


FIGURE 4.11: Closure tests for the multijet taggabilities (5 top plots). Taggabilities parametrizations as functions of z_{PV} , p_T and ϕ (3 bottom plots).

in [90]. An overall conservative systematic uncertainty of 2% on these trigger efficiencies was applied to our analysis.

4.2.3.7 Trigger Efficiencies

4.2.3.8 Event preselection in the $2b - jets + \cancel{E}_T$ topology

The event preselection applied in this case retains only events passing the following cuts:

$$\left\{ \begin{array}{l} \text{Trigger terms : "MHT30_3CJT5" or "JT1_ACO_MHT_HT"} \\ \text{Data quality requirements} \\ \text{At least one primary vertex (PV) with : } |z_{PV}| < 60 \text{ cm} \\ \text{At least two jets (j}_1 \text{ and j}_2 \text{) each with } E_T > 40 \text{ GeV \& } |\eta| < 0.8 \\ \cancel{E}_T > 50 \text{ GeV} \\ \cancel{H}_T > 50 \text{ GeV} \\ \Delta\phi(j_1, j_2) < 165^\circ \\ \Delta\phi(\cancel{E}_T, \text{jets}) > 40^\circ \end{array} \right.$$

the event yields and efficiencies are presented in table 4.16

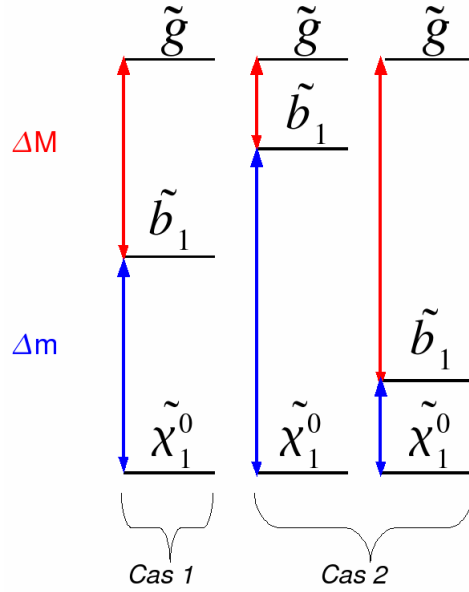


FIGURE 4.12: . Mass splittings in the signal.

4.2.3.9 Event preselection in the $4b - jets + \cancel{E}_T$ topology

The event preselection applied in this case retains only events passing the following cuts:

$$\left\{ \begin{array}{l} \text{Trigger terms : "MHT30_3CJT5" or "JT2_MHT25_HT"} \\ \text{Data quality requirements} \\ \text{At least one primary vertex (PV) with : } |z_{PV}| < 60 \text{ cm} \\ \text{At least three jets (j}_1, \text{j}_2, \text{ and j}_3) \text{ each with } E_T(\text{jets}) > 40 \text{ GeV \& with } |\eta(\text{j}_1, \text{j}_2)| < 0.8, |\eta(\text{j}_3)| < 2.5 \\ \cancel{E}_T > 50 \text{ GeV} \\ \cancel{H}_T > 50 \text{ GeV} \\ H_T > 180 \text{ GeV} \end{array} \right.$$

the event yields and efficiencies are presented in table 4.17

4.2.3.10 Estimation of the QCD Background

The instrumental background, essentially due to QCD processes, was not simulated with the MC. Instead it was estimated via a data-driven method. A event selection was applied to the data and MC samples using the "JT1" and the "JT2" preselection to which a common cut was added: $\cancel{E}_T > 50 \text{ GeV}$. Knowing that the QCD background just yields large \cancel{E}_T through the mis-measurement of some jets in the events, we measured its shape in the low end of the distribution, namely $50 < \cancel{E}_T < 120 \text{ GeV}$. Then, in order to estimate how much this background contaminates the signal regions at much higher \cancel{E}_T , we used two different functional forms to extrapolate its shape:

(Sub-)Process	Decay Mode	Efficiency (%)
$t + \bar{t} + 0lp(excl.)$	$2\ell^\pm + 2\nu + 2b + 0lp$	91.47 ± 0.14
	$\ell^\pm + \nu + 2b + 2lp$	90.67 ± 0.10
$t + \bar{t} + 1lp(excl.)$	$2\ell^\pm + 2\nu + 2b + 1lp$	91.15 ± 0.20
	$\ell^\pm + \nu + 2b + 3lp$	89.99 ± 0.20
$t + \bar{t} + 2lp(incl.)$	$2\ell^\pm + 2\nu + 2b + 2lp$	89.97 ± 0.14
	$\ell^\pm + \nu + 2b + 4lp$	88.65 ± 0.20
$t + q + \bar{b}$	$e^\pm \nu b + qb$	89.85 ± 0.43
	$\mu^\pm \nu b + qb$	92.06 ± 0.17
	$\tau^\pm \nu b + qb$	91.67 ± 0.22
$t + b$	$e^\pm \nu b + b$	89.52 ± 0.31
	$\mu^\pm \nu b + b$	94.42 ± 0.17
	$\tau^\pm \nu b + b$	92.26 ± 0.20
$W^\pm + 2lp(excl.)$	$\ell^\pm \nu + 2lp$	87.57 ± 0.37
$W^\pm + 3lp(excl.)$	$\ell^\pm \nu + 3lp$	89.98 ± 0.26
$W^\pm + 4lp(excl.)$	$\ell^\pm \nu + 4lp$	90.16 ± 0.17
$W^\pm + 5lp(incl.)$	$\ell^\pm \nu + 5lp$	91.44 ± 0.43
$W^\pm + c + 3lp(incl.)$	$\ell^\pm \nu + c + 3lp$	89.36 ± 0.40
$W^\pm + c\bar{c} + 2lp(excl.)$	$\ell^\pm \nu + c\bar{c} + 2lp$	91.37 ± 0.41
$W^\pm + c\bar{c} + 3lp(incl.)$	$\ell^\pm \nu + c\bar{c} + 3lp$	90.24 ± 0.31
$W^\pm + b\bar{b} + 2lp(excl.)$	$\ell^\pm \nu + b\bar{b} + 2lp$	90.87 ± 0.46
$W^\pm + b\bar{b} + 3lp(incl.)$	$\ell^\pm \nu + b\bar{b} + 3lp$	90.59 ± 0.30
$\gamma^*/Z + 2lp(excl.)$	$\tau^\pm \tau^\mp + 2lp$ ($250 < \hat{m} < 1960$ GeV)	80.46 ± 0.66
$\gamma^*/Z + 3lp(incl.)$	$\mu^\pm \mu^\mp + 3lp$ ($60 < \hat{m} < 130$ GeV)	93.13 ± 0.26
	$\mu^\pm \mu^\mp + 3lp$ ($130 < \hat{m} < 250$ GeV)	92.45 ± 0.41
	$\mu^\pm \mu^\mp + 3lp$ ($250 < \hat{m} < 1960$ GeV)	93.82 ± 0.30
	$\tau^\pm \tau^\mp + 3lp$ ($130 < \hat{m} < 250$ GeV)	81.85 ± 0.64
	$\tau^\pm \tau^\mp + 3lp$ ($250 < \hat{m} < 1960$ GeV)	81.17 ± 0.45
$Z + 4lp(excl.)$	$\nu\bar{\nu} + 4lp$	93.65 ± 0.40
$Z + 5lp(incl.)$	$\nu\bar{\nu} + 5lp$	94.41 ± 0.28
$Z + b\bar{b} + 2lp(incl.)$	$\nu\bar{\nu} + b\bar{b} + 2lp$	93.80 ± 0.40
$W^\pm + W^\mp$	incl.	87.78 ± 0.33
$W^\pm + Z$	incl.	88.78 ± 0.43
$\gamma^*/Z + \gamma^*/Z$	incl.	90.23 ± 0.42
Signal Samples ($m_{\tilde{g}}, m_{\tilde{b}_1}, m_{\tilde{\chi}_1^0}$) GeV		
(350,330,75)		97.71 ± 0.26
(325,305,75)		97.53 ± 0.14
(300,280,75)		96.76 ± 0.31
(275,265,75)		97.57 ± 0.14
(250,230,75)		96.51 ± 0.36

TABLE 4.14: Efficiencies for the $MHT30_3CJT5$ and $JT1_ACO_MHT_HT$ triggers. The uncertainties are statistical.

- $f(E_T) = A_{pow} \times E_T^{B_{pow}}$
- $g(E_T) = A_{exp} \times e^{-E_T \times B_{exp}}$

The first functional form supposes a power law decrease of the number of QCD events with the increasing missing transverse energy. The second one relies on the hypothesis that this decrease is exponential. The parameters A_{pow} , B_{pow} , A_{exp} , and B_{exp} are determined by two fits to the data which are dominated by the QCD background at low E_T . These fits are performed after the physics background (which is simulated) has been subtracted from the data. The central value for our estimate of the number of QCD events in the signal regions is the mean of the estimates based upon the power law and the exponential functional forms; the uncertainty is

(Sub-)Process	Decay Mode	Efficiency (%)
$t + \bar{t} + 0lp(excl.)$	$2\ell^\pm + 2\nu + 2b + 0lp$	92.13 ± 0.41
	$\ell^\pm + \nu + 2b + 2lp$	93.59 ± 0.10
	$2b + 4lp$	74.72 ± 0.71
$t + \bar{t} + 1lp(excl.)$	$2\ell^\pm + 2\nu + 2b + 1lp$	93.44 ± 0.40
	$\ell^\pm + \nu + 2b + 3lp$	94.29 ± 0.17
	$2b + 5lp$	75.74 ± 0.65
$t + \bar{t} + 2lp(incl.)$	$2\ell^\pm + 2\nu + 2b + 2lp$	94.56 ± 0.17
	$\ell^\pm + \nu + 2b + 4lp$	94.60 ± 0.14
	$2b + 6lp$	78.10 ± 1.07
$t + q + b$	$\mu^\pm \nu b + qb$	91.92 ± 0.46
	$\tau^\pm \nu b + qb$	91.46 ± 0.59
$t + b$	$e^\pm \nu b + b$	90.25 ± 0.76
	$\mu^\pm \nu b + b$	92.84 ± 0.61
	$\tau^\pm \nu b + b$	91.04 ± 0.54
	$q' \bar{q} b + b$	77.31 ± 0.90
$W^\pm + 4lp(excl.)$	$\ell^\pm \nu + 4lp$	90.98 ± 0.52
$W^\pm + 5lp(incl.)$	$\ell^\pm \nu + 5lp$	92.38 ± 0.66
$W^\pm + bb + 3lp(incl.)$	$\ell^\pm \nu + bb + 3lp$	91.55 ± 0.56
$\gamma^*/Z + 3lp(incl.)$	$\tau^\pm \tau^\mp + 3lp$ ($250 < \hat{m} < 1960$ GeV)	90.12 ± 0.52
$Z + 5lp(incl.)$	$\nu \bar{\nu} + 5lp$	93.77 ± 0.53
Signal Samples ($m_{\tilde{g}}, m_{\tilde{b}_1}, m_{\tilde{\chi}_1^0}$) GeV		
(350,200,75)		96.82 ± 0.17
(350,150,75)		96.37 ± 0.31
(325,250,75)		96.56 ± 0.20
(325,200,75)		96.18 ± 0.17
(325,150,75)		95.96 ± 0.17
(300,200,75)		96.35 ± 0.20
(300,150,75)		95.52 ± 0.37

TABLE 4.15: Efficiencies for the *MHT30_3CJT5* and *JT2_MHT25_HT* triggers. The uncertainties are statistical.

taken as half of the difference between these two estimates:

$$N_{QCD} = \left[\frac{\int_{\cancel{E}_T^{Cut}}^{980\text{GeV}} f(x)dx + \int_{\cancel{E}_T^{Cut}}^{980\text{GeV}} g(x)dx}{2} \right] \pm \left[\frac{\int_{\cancel{E}_T^{Cut}}^{980\text{GeV}} f(x)dx - \int_{\cancel{E}_T^{Cut}}^{980\text{GeV}} g(x)dx}{2} \right]$$

, where \cancel{E}_T^{Cut} is the actual lower bound on the missing transverse energy that defines one of the signal regions. figure 4.13 illustrates this procedure after the preselection cuts. The procedure will be repeated after the final event selection so as to establish the final estimates of the QCD contamination into the two signal regions.

4.2.3.11 Suppression of the QCD Background

At this stage, the QCD background is dominant both in the JT1 and the JT2 event selections. We also note that it has a large uncertainty. It is therefore mandatory to apply specific cuts to suppress this background. Firstly we strengthen the quality requirements for the reconstructed jets in order to reduce the contamination of "bad jets" described in sub-section 4.2.3.3.f. We reject events with bad jets that have either $E_T > 20$ GeV or a coarse hadronic fraction $CHF > 0.02$. Secondly, the main source of \cancel{E}_T in QCD events, is the mis-measurement of a hard jet in

(Sub-)Process	Number of events
$W^\pm(\rightarrow \ell^\pm\nu) + jets$	375.2 ± 0.0
$Z(\rightarrow \nu\bar{\nu}) + jets$	150.8 ± 0.0
$t\bar{t} \rightarrow \ell^\pm\nu + 2b + jets$	109.9 ± 0.6
VV	45.5 ± 0.9
$Z(\rightarrow \ell^\pm\ell^\mp) + jets$	39.6 ± 0.0
$Z(\rightarrow \nu\bar{\nu}) + HF + jets$	39.0 ± 0.3
$t\bar{t} \rightarrow 2\ell^\pm\nu\bar{\nu} + 2b + jets$	23.1 ± 0.2
$Z(\rightarrow \ell^\pm\ell^\mp) + HF + jets$	7.9 ± 0.0
$t + q + b$ & $t + b$	6.3 ± 0.0
$t\bar{t} \rightarrow 2b + jets$	0.0 ± 0.0
QCD Background	706.4 ± 250.2
Total Background	1612.1 ± 252.6
Data	1562
Signal (350,150,75)	$15.9 \pm 0.5, \epsilon = 12.0\%$
Signal (350,330,75)	$24.5 \pm 0.5, \epsilon = 18.5\%$

TABLE 4.16: Event yields after the JT1 preselection and the $\cancel{E}_T > 100$ GeV cuts. "V" and "HF" stand for weak vector bosons and heavy flavor, respectively. The uncertainties are statistical.

(Sub-)Process	Number of events
$t\bar{t} \rightarrow \ell^\pm\nu + 2b + jets$	110.6 ± 0.6
$W^\pm(\rightarrow \ell^\pm\nu) + jets$	78.5 ± 0.0
$Z(\rightarrow \nu\bar{\nu}) + jets$	24.5 ± 0.0
$W^\pm(\rightarrow \ell^\pm\nu) + HF + jets$	23.1 ± 0.1
$Z(\rightarrow \ell^\pm\ell^\mp) + jets$	10.1 ± 0.0
VV	7.3 ± 0.4
$t\bar{t} \rightarrow 2\ell^\pm\nu\bar{\nu} + 2b + jets$	6.2 ± 0.1
$t\bar{t} \rightarrow 2b + jets$	5.9 ± 0.2
$Z(\rightarrow \nu\bar{\nu}) + HF + jets$	5.9 ± 0.1
$Z(\rightarrow \ell^\pm\ell^\mp) + HF + jets$	2.7 ± 0.0
$t + q + b$ & $t + b$	2.4 ± 0.0
QCD Background	253.8 ± 113.5
Total Background	530.9 ± 115.0
Data	638
Signal (350,150,75)	$25.1 \pm 0.5, \epsilon = 19.1\%$
Signal (350,330,75)	$8.1 \pm 0.3, \epsilon = 6.1\%$

TABLE 4.17: Event yields after the JT2 preselection and the $\cancel{E}_T > 100$ GeV cuts. "V" and "HF" stand for weak vector bosons and heavy flavor, respectively. The uncertainties are statistical.

the event. In this case the direction of the missing transverse energy in the transverse plane tends to be aligned with that of the jet. Therefore, we apply the following additional topological cuts:

$$\left\{ \begin{array}{l} \text{For JT1 :} \\ \Delta\phi_{min}(\cancel{E}_T, jets) > 100^\circ \end{array} \right. \quad \left\{ \begin{array}{l} \text{For JT2 :} \\ \Delta\phi(\cancel{E}_T, j_1) > 80^\circ \\ \Delta\phi(\cancel{E}_T, j_2) > 20^\circ \\ \Delta\phi(\cancel{E}_T, j_3) > 20^\circ \end{array} \right.$$

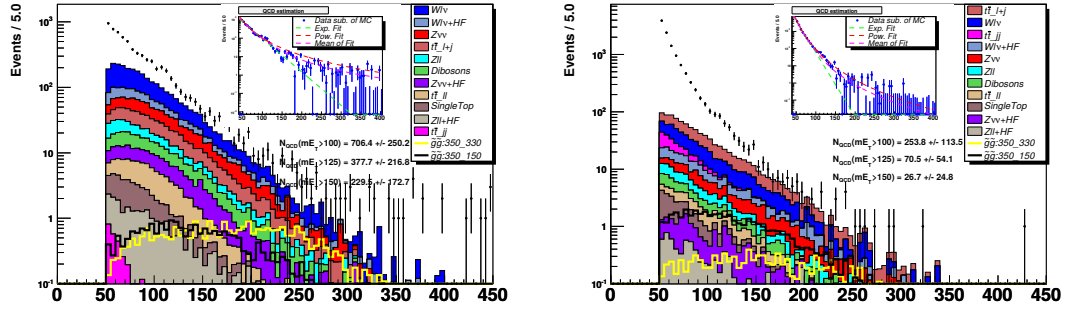


FIGURE 4.13: Estimates of the number of QCD events in the JT1 (right) and the JT2 (left) signal regions after the preselection cuts. In both cases, the stack of histograms at the bottom of the plots represent the contribution of the physics background, the data are the black dots, and the signal samples are the black and yellow open histograms overlaid on the stack. The smaller windows at the top of the plots represent the data (blue dots) after the physics background subtraction. The red, green and pink lines represent the power law fit, the exponential fit and the mean between the two fits.

Thirdly, an important source of the QCD jets comes from noise-induced jets as well as jets from the multiple $p\bar{p}$ interactions at each beam crossing. To suppress that latter source of jets, we apply the $CPF_0 > 0.85$ on the 2 leading jets on the JT1 and JT2 streams. This cut is applied on MC samples after their luminosity reweighting as described in sub-section 4.2.3.3.h.

4.2.3.12 Rejection of Isolated Leptons

After, the cuts meant to reduce the QCD background, the event yield is shown in table 4.18. The instrumental background is significantly reduced, and the dominant contribution is from the $W^\pm(\rightarrow \ell^\pm\nu) + jets$ process for JT1 signal region and $t\bar{t} \rightarrow \ell^\pm\nu + 2b + jets$ for the JT2 signal region.

(Sub-)Process	JT1 Event Selection	JT2 Event Selection
Data	886	196
Total Background	746.2 ± 2.4	177.8 ± 1.1
$W^\pm(\rightarrow \ell^\pm\nu) + jets$	34%	25%
$Z(\rightarrow \nu\bar{\nu}) + jets$	15%	10%
$W^\pm(\rightarrow \ell^\pm\nu) + HF + jets$	10%	8%
$t\bar{t} \rightarrow \ell^\pm\nu + 2b + jets$	9%	37%

TABLE 4.18: Event yields after the preselection and the QCD suppression. The uncertainties are statistical.

We note that the dominant background processes have a hard isolated lepton in the final state. Hence, we apply a veto against such events. Here are the detailed features of the leptons for which we reject events containing them:

$$\left\{ \begin{array}{l} \text{Electron candidates :} \\ EMF > 0.9 \\ Isolation < 0.2 \\ HMx7 < 50 \\ E_T > 5 \text{ GeV} \\ \text{Track match} \end{array} \right. \quad \left\{ \begin{array}{l} \text{Muon candidates :} \\ \text{Medium quality} \\ N_{segt} = 3 \\ p_T > 5 \text{ GeV} \end{array} \right.$$

The distribution of the number of isolated electrons and muons for both signal regions are displayed in figure 4.14 and 4.15, respectively.

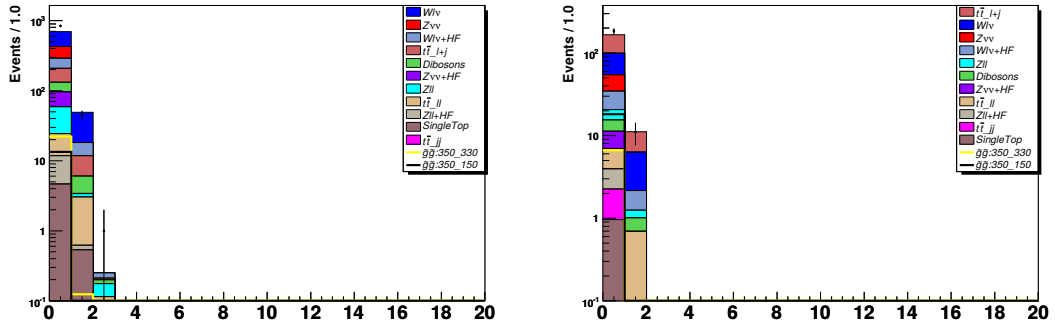


FIGURE 4.14: Distribution of the number of isolated electrons after the preselection and the QCD suppression for the JT1 (right) and the JT2 (left) streams.

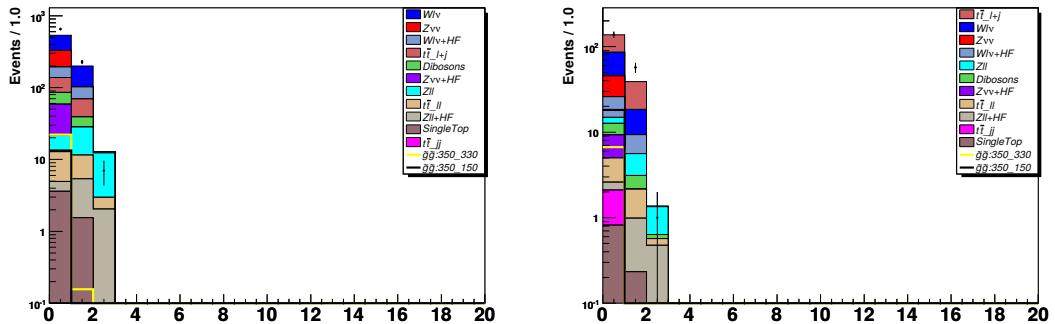


FIGURE 4.15: Distribution of the number of isolated muons after the preselection and the QCD suppression for the JT1 (right) and the JT2 (left) streams.

By reverting the cuts to reject events with isolated leptons, we can verify the normalization and shape of the $V + jets$ and $t\bar{t}$ physics background processes, where $V = W^\pm$ when we request exactly 1 isolated lepton and $V = Z$ when we request exactly 2. We apply the preselection and the QCD suppression cuts and loosen the cut on the missing transverse energy: $\cancel{E}_T > 75$ GeV for $N_{lep} = 1$ and $\cancel{E}_T > 50$ GeV for $N_{lep} = 2$. The distributions in figure 4.16 show that the $W^\pm(\rightarrow \ell^\pm\nu) + jets$ background process is correctly simulated. From Fig. 4.17 we can see a good agreement in a phase space region where the background is dominated by the $t\bar{t} \rightarrow 1\ell^\pm + 2b + \cancel{E}_T$ process. Same conclusions can be drawn from figure 4.18 for the $\gamma^*/Z(\rightarrow \ell^\pm\ell^\mp) + jets$ process.

Sources	Impact on Bkgd	Impact on Signal
Jet Energy Scale (JES)	$\pm 1\sigma : \begin{cases} JT1 : 4 - 13\% \\ JT2 : 6 - 18\% \end{cases}$	$\pm 1\sigma : 7\%$ [133]
Jet ID [133]	2%	2%
Jet Energy Resolution (JER) [133]	5%	5%
Int. Luminosity [105]	6.5%	6.5%
Trigger [90]	2%	2%
Track Confirmed Jets	5%	5%
Jets Taggability	1%	1%
Tag Rate Functions (TRF)	$\pm 1\sigma : \begin{cases} 1b - tag : 4 - 6\% \\ 2b - tags : 6 - 13\% \\ 3b - tags : 15 - 21\% \end{cases}$	$\pm 1\sigma : \begin{cases} 1b - tag : 1 - 5\% \\ 2b - tags : 5 - 14\% \\ 3b - tags : 11 - 23\% \end{cases}$
Cross Sections	15%	-
Impact of PDFs on Acceptance [133]	5%	5%

TABLE 4.19: Sources of experimental systematic uncertainties and their impact on the background and the signal.

$m_{\tilde{g}}$ (GeV)	σ_{LO} (pb)	$\Delta\sigma_{LO}$ (pb)	σ_{NLO} (pb)	$\Delta\sigma_{NLO}$ (pb)	K-Factor
200	7.670	$\begin{cases} Stat : 0.01\% \\ PDF : +19.65_{-13.25} \% \\ Scale : +42.11_{-27.12} \% \\ Total : +46.47_{-30.18} \% \end{cases}$	12.000	$\begin{cases} Stat : 0.01\% \\ PDF : +21.28_{-13.11} \% \\ Scale : +18.33_{-17.00} \% \\ Total : +28.09_{-21.47} \% \end{cases}$	$1.57^{+0.85}_{-0.58}$
250	1.750	$\begin{cases} Stat : 0.05\% \\ PDF : +18.50_{-12.90} \% \\ Scale : +42.29_{-27.49} \% \\ Total : +46.16_{-30.31} \% \end{cases}$	2.640	$\begin{cases} Stat : 0.07\% \\ PDF : +20.36_{-12.38} \% \\ Scale : +18.94_{-18.18} \% \\ Total : +27.81_{-22.00} \% \end{cases}$	$1.51^{+0.81}_{-0.56}$
300	0.400	$\begin{cases} Stat : 0.21\% \\ PDF : +19.54_{-11.81} \% \\ Scale : +43.75_{-28.25} \% \\ Total : +52.08_{-30.62} \% \end{cases}$	0.590	$\begin{cases} Stat : 0.29\% \\ PDF : +20.16_{-12.07} \% \\ Scale : +21.36_{-18.81} \% \\ Total : +29.37_{-22.35} \% \end{cases}$	$1.48^{+0.88}_{-0.56}$
325	0.207	$\begin{cases} Stat : 0.40\% \\ PDF : +20.29_{-11.74} \% \\ Scale : +44.93_{-28.50} \% \\ Total : +49.30_{-30.83} \% \end{cases}$	0.304	$\begin{cases} Stat : 0.57\% \\ PDF : +20.40_{-12.20} \% \\ Scale : +22.37_{-19.41} \% \\ Total : +30.28_{-22.93} \% \end{cases}$	$1.47^{+0.85}_{-0.56}$
350	0.100	$\begin{cases} Stat : 0.82\% \\ PDF : +20.67_{-12.91} \% \\ Scale : +46.00_{-29.00} \% \\ Total : +50.44_{-31.75} \% \end{cases}$	0.147	$\begin{cases} Stat : 1.18\% \\ PDF : +22.01_{-12.02} \% \\ Scale : +23.13_{-20.41} \% \\ Total : +31.95_{-23.72} \% \end{cases}$	$1.46^{+0.88}_{-0.58}$
375	0.051	$\begin{cases} Stat : 1.63\% \\ PDF : +21.98_{-13.13} \% \\ Scale : +45.45_{-29.64} \% \\ Total : +50.51_{-32.46} \% \end{cases}$	0.074	$\begin{cases} Stat : 2.34\% \\ PDF : +22.03_{-13.48} \% \\ Scale : +24.36_{-20.30} \% \\ Total : +32.93_{-24.48} \% \end{cases}$	$1.46^{+0.88}_{-0.59}$
400	0.025	$\begin{cases} Stat : 3.34\% \\ PDF : +23.01_{-14.41} \% \\ Scale : +48.78_{-28.46} \% \\ Total : +54.04_{-32.07} \% \end{cases}$	0.036	$\begin{cases} Stat : 4.82\% \\ PDF : +23.76_{-13.73} \% \\ Scale : +25.07_{-20.89} \% \\ Total : +34.88_{-25.46} \% \end{cases}$	$1.46^{+0.94}_{-0.60}$

TABLE 4.20: Theoretical systematic uncertainties of the signal.

Signal Samples ($m_{\tilde{g}}, m_{\tilde{b}_1}, m_{\tilde{\chi}_1^0}$)	Analysis Filter	Nber of B-Tagged Jets	Kinematic Cuts (GeV)	Efficiency (%)
(375,250,75)	JT2	3 Loose	$\cancel{E}_T > 100 \ \& \ H_T > 300$	5.5
(375,150,75)	JT2	3 Loose	$\cancel{E}_T > 100 \ \& \ H_T > 300$	4.1
(350,330,75)	JT1	1 Tight	$\cancel{E}_T > 200 \ \& \ H_T > 250$	5.3
(350,200,75)	JT2	3 Loose	$\cancel{E}_T > 100 \ \& \ H_T > 300$	4.0
(350,150,75)	JT2	3 Loose	$\cancel{E}_T > 100 \ \& \ H_T > 300$	3.4
(350,105,75)	JT2	3 Loose	$\cancel{E}_T > 100 \ \& \ H_T > 300$	2.2
(325,305,75)	JT1	1 Medium	$\cancel{E}_T > 175 \ \& \ H_T > 225$	6.2
(325,250,75)	JT2	2 Loose	$\cancel{E}_T > 125 \ \& \ H_T > 180$	8.2
(325,200,75)	JT2	3 Loose	$\cancel{E}_T > 100 \ \& \ H_T > 180$	4.5
(325,105,75)	JT2	3 Loose	$\cancel{E}_T > 100 \ \& \ H_T > 300$	2.9
(300,280,75)	JT1	1 Medium	$\cancel{E}_T > 150 \ \& \ H_T > 200$	6.8
(300,250,75)	JT1	2 Loose	$\cancel{E}_T > 125 \ \& \ H_T > 175$	5.3
(300,200,75)	JT2	2 Tight	$\cancel{E}_T > 100 \ \& \ H_T > 180$	6.5
(300,150,75)	JT2	2 Tight	$\cancel{E}_T > 100 \ \& \ H_T > 200$	5.1
(300,105,75)	JT2	3 Loose	$\cancel{E}_T > 100 \ \& \ H_T > 180$	1.8
(290,260,60)	JT1	2 Loose	$\cancel{E}_T > 100 \ \& \ H_T > 225$	5.6
(275,265,75)	JT1	1 Tight	$\cancel{E}_T > 125 \ \& \ H_T > 100$	8.3
(275,250,75)	JT1	1 Tight	$\cancel{E}_T > 125 \ \& \ H_T > 150$	6.6
(275,200,75)	JT2	2 Tight	$\cancel{E}_T > 100 \ \& \ H_T > 180$	5.0
(275,150,75)	JT2	2 Tight	$\cancel{E}_T > 100 \ \& \ H_T > 200$	5.0
(275,105,75)	JT1	2 Loose	$\cancel{E}_T > 100 \ \& \ H_T > 100$	3.1
(250,230,75)	JT1	1 Tight	$\cancel{E}_T > 100 \ \& \ H_T > 125$	6.8
(250,150,75)	JT1	1 Tight	$\cancel{E}_T > 100 \ \& \ H_T > 125$	5.4
(250,105,75)	JT1	1 Loose	$\cancel{E}_T > 100 \ \& \ H_T > 150$	4.3
(250,95,75)	JT1	1 Loose	$\cancel{E}_T > 100 \ \& \ H_T > 150$	4.6
(200,180,75)	JT1	1 Loose	$\cancel{E}_T > 100 \ \& \ H_T > 125$	3.6
(200,150,75)	JT1	1 Tight	$\cancel{E}_T > 100 \ \& \ H_T > 125$	2.1
(200,95,75)	JT1	1 Loose	$\cancel{E}_T > 100 \ \& \ H_T > 125$	2.4

TABLE 4.21: Optimal final cuts and their signal efficiencies.

Table 4.21 presents the optimal final event selection for each signal sample. We can verify therein that the JT2 stream has a good sensitivity to signal mass configurations where $Min(\Delta M, \Delta m)$ is large, typically larger than 50 GeV. On the contrary, when $Min(\Delta M, \Delta m)$ is small, typically less than 50 GeV, the JT1 takes over with a good sensitivity to the signal, especially so in the difficult region where $m_{\tilde{g}} - m_{\tilde{b}_1}$ gets very small, down to 5 GeV.

4.2.3.14 Analysis Interpretation

Based upon this final event selection summarized in table 4.21, and given that no excess of events are observed in the data with respect to the background expectations, we can calculate the 95% confidence level (C.L.) exclusion limits for the different signal hypotheses.

This way, the exclusion limits are calculated for the $m_{\tilde{q}} = 1$ TeV, $m_{\tilde{b}_1} = 105$ GeV, and $m_{\tilde{\chi}_1^0} = 75$ GeV, hypothesis, as shown in figure 4.19. For this mass hypothesis we can exclude $m_{\tilde{g}} < 286$ GeV at the 95% C.L. This procedure is repeated for other mass hypotheses. For instance, figure 4.20, 4.21, 4.22 present the same informations as figure 4.19, but for $m_{\tilde{b}_1} = 150, 200, 250$ GeV, respectively. Similarly, figure 4.23, 4.24 display the limits for $\Delta M = 20, 5$ GeV, respectively.

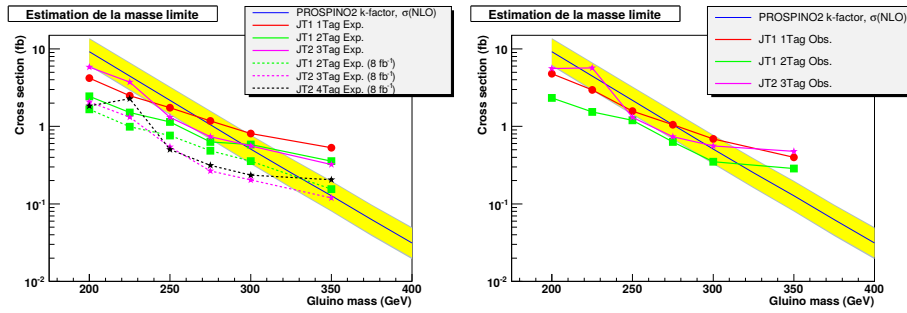


FIGURE 4.19: Limits on the signal cross section for $m_{\tilde{q}} = 1$ TeV, $m_{\tilde{b}_1} = 105$ GeV, and $m_{\tilde{\chi}_1^0} = 75$ GeV, the expected (left) and the observed (right) limits are displayed. An extrapolation of the expected limit for an integrated luminosity of 8 fb^{-1} are also shown in dash lines (left).

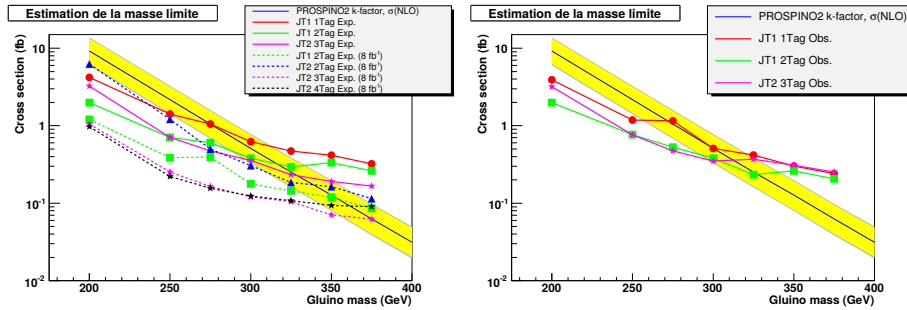


FIGURE 4.20: Limits on the signal cross section for $m_{\tilde{q}} = 1$ TeV, $m_{\tilde{b}_1} = 150$ GeV, and $m_{\tilde{\chi}_1^0} = 75$ GeV, the expected (left) and the observed (right) limits are displayed. The expected limits for $L = 8 \text{ fb}^{-1}$ are also shown in dash lines (left).

The summary of excluded gluino masses for $m_{\tilde{\chi}_1^0} = 75$ GeV are presented in table 4.22 $m_{\tilde{q}} = 1$ TeV, and in table 4.22 for $m_{\tilde{q}} = 500$ GeV. The latter being weaker than the former as expected from the gluino pair production cross section shown in figure 4.3.

From the ensemble of these results we construct the exclusion zone in the $[m_{\tilde{g}}, m_{\tilde{b}_1}]$ plane. This is shown in figure 4.25 for $m_{\tilde{\chi}_1^0} = 75$ GeV as a function of $m_{\tilde{q}}$ (top). The extrapolation for $L = 8 \text{ fb}^{-1}$ is also provided (right).

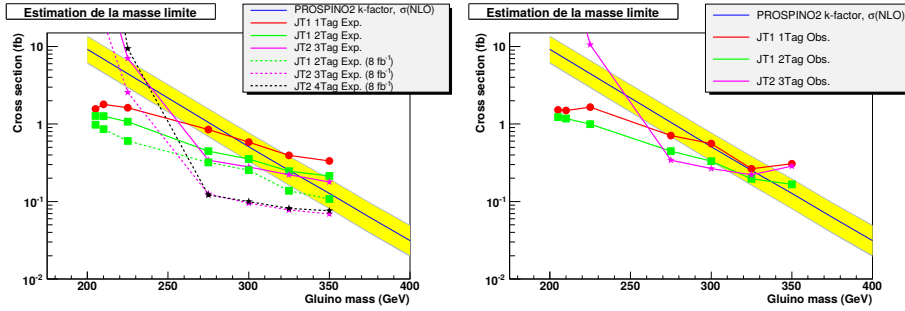


FIGURE 4.21: Limits on the signal cross section for $m_{\tilde{q}} = 1$ TeV, $m_{\tilde{b}_1} = 200$ GeV, and $m_{\tilde{\chi}_1^0} = 75$ GeV, the expected (left) and the observed (right) limits are displayed. The expected limits for $L = 8 fb^{-1}$ are also shown in dash lines (left).

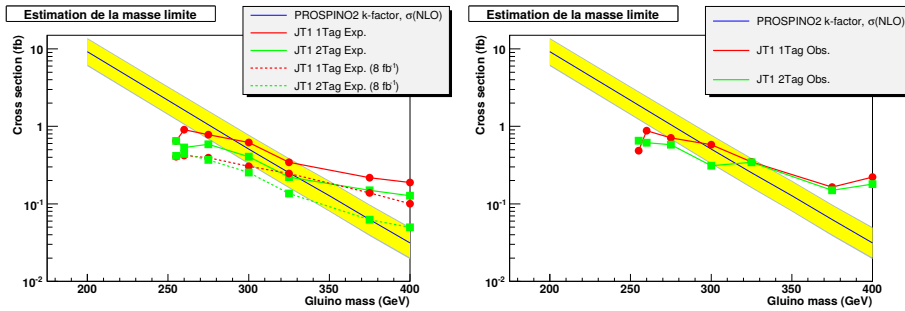


FIGURE 4.22: Limits on the signal cross section for $m_{\tilde{q}} = 1$ TeV, $m_{\tilde{b}_1} = 250$ GeV, and $m_{\tilde{\chi}_1^0} = 75$ GeV, the expected (left) and the observed (right) limits are displayed. The expected limits for $L = 8 fb^{-1}$ are also shown in dash lines (left).

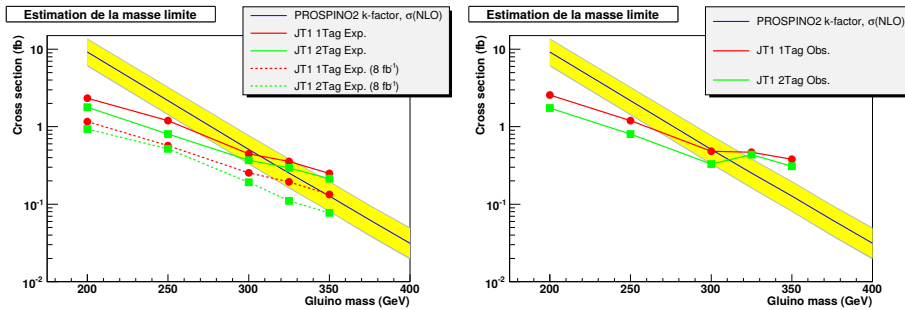


FIGURE 4.23: Limits on the signal cross section for $m_{\tilde{q}} = 1$ TeV, $\Delta M = 20$ GeV, and $m_{\tilde{\chi}_1^0} = 75$ GeV, the expected (left) and the observed (right) limits are displayed. The expected limits for $L = 8 fb^{-1}$ are also shown in dash lines (left).

4.2.3.15 Conclusions

We performed a search for gluino pairs decaying into pairs of bottom quark and bottom squark, leading to a final state made of 4 b-jets and a large missing transverse energy in $L = 1 fb^{-1}$ of the D0 Run 2a data. No such supersymmetric signal was found, the data were compatible with the expectation from the SM. We could therefore derive exclusion limits on the gluino mass up to 309 GeV at the 95 % C.L.

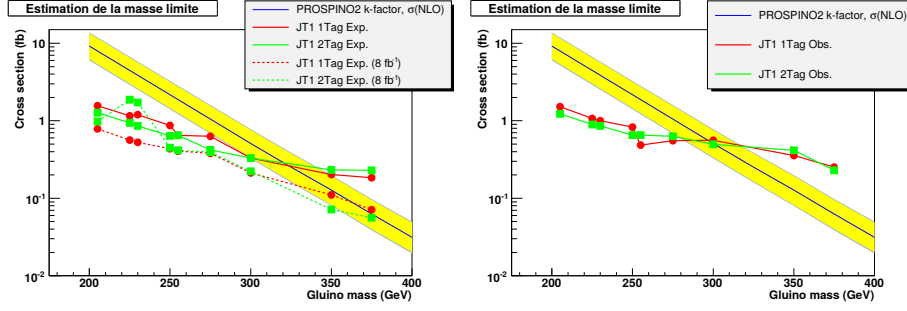


FIGURE 4.24: Limits on the signal cross section for $m_{\tilde{q}} = 1$ TeV, $\Delta M = 5$ GeV, and $m_{\tilde{\chi}_1^0} = 75$ GeV, the expected (left) and the observed (right) limits are displayed. The expected limits for $L = 8 \text{ fb}^{-1}$ are also shown in dash lines (left).

Signal Mass Hypo. (GeV)	Exp. Limit $m_{\tilde{g}} < \text{GeV}$	Obs. Limit $m_{\tilde{g}} < \text{GeV}$	Event Selection
$m_{\tilde{b}_1} = 95$ GeV	261	266	JT1, 2 B-Tags
$m_{\tilde{b}_1} = 105$ GeV	277	286	JT1, 2 B-Tags
$m_{\tilde{b}_1} = 150$ GeV	295	296	JT2, 3 B-Tags
$m_{\tilde{b}_1} = 175$ GeV	289	307	JT2, 3 B-Tags
$m_{\tilde{b}_1} = 200$ GeV	308	309	JT2, 3 B-Tags
$m_{\tilde{b}_1} = 225$ GeV	300	300	JT1, 2 B-Tags
$m_{\tilde{b}_1} = 250$ GeV	285	301	JT1, 2 B-Tags
$m_{\tilde{g}} - m_{\tilde{b}_1} = 5$ GeV	300	281	JT1, 2 B-Tags
$m_{\tilde{g}} - m_{\tilde{b}_1} = 20$ GeV	290	299	JT1, 2 B-Tags

TABLE 4.22: Excpeted and observed exclusion limits for $m_{\tilde{q}} = 1$ TeV and $m_{\tilde{\chi}_1^0} = 75$ GeV.

Signal Mass Hypo. (GeV)	Exp. Limit $m_{\tilde{g}} < \text{GeV}$	Obs. Limit $m_{\tilde{g}} < \text{GeV}$	Event Selection
$m_{\tilde{b}_1} = 95$ GeV	229	236	JT1, 2 B-Tags
$m_{\tilde{b}_1} = 105$ GeV	230	231	JT1, 2 B-Tags
$m_{\tilde{b}_1} = 150$ GeV	253	254	JT2, 3 B-Tags
$m_{\tilde{b}_1} = 175$ GeV	253	256	JT1, 2 B-Tags
$m_{\tilde{b}_1} = 200$ GeV	357	261	JT1, 2 B-Tags
$m_{\tilde{b}_1} = 225$ GeV	248	250	JT1, 2 B-Tags
$m_{\tilde{b}_1} = 250$ GeV	258	256	JT1, 2 B-Tags
$m_{\tilde{g}} - m_{\tilde{b}_1} = 5$ GeV	258	257	JT1, 2 B-Tags
$m_{\tilde{g}} - m_{\tilde{b}_1} = 10$ GeV	254	252	JT1, 2 B-Tags
$m_{\tilde{g}} - m_{\tilde{b}_1} = 20$ GeV	246	250	JT1, 2 B-Tags
$m_{\tilde{g}} - m_{\tilde{b}_1} = 25$ GeV	246	251	JT1, 2 B-Tags

TABLE 4.23: Excpeted and observed exclusion limits for $m_{\tilde{q}} = 500$ GeV and $m_{\tilde{\chi}_1^0} = 75$ GeV.

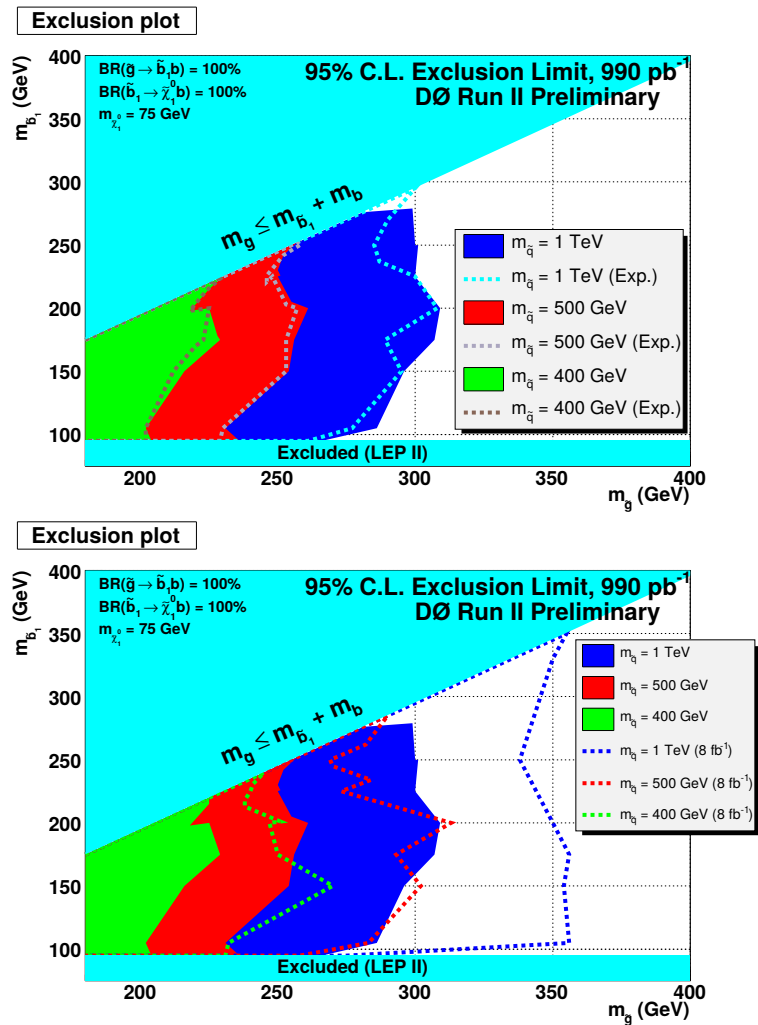


FIGURE 4.25: Exclusion zone in the $m_{\tilde{g}}, m_{\tilde{b}_1}$ plane (top) with the extrapolation for $L = 8 \text{ fb}^{-1}$ (bottom). The plain areas are the observed exclusions whilst the hollow ones correspond to the expected exclusions.

4.2.3.16 Appendix: Verifications of the physics background

Hereafter, we define two control regions for the physics background after the JT1 C4 cuts. The C4 cuts correspond to the preselection and the QCD suppression cuts.

In order to increase the statistics of the isolated single and dilepton samples the \cancel{E}_T cut is loosened down to $\cancel{E}_T > 75$ GeV and $\cancel{E}_T > 50$ GeV respectively.

4.2.3.16.a Verifications prior to the b-tagging

The events yield after applying the JT1 C4, the $\cancel{E}_T > 75$ GeV cuts and the exclusive single electron requirement is presented in Table 4.24. Figure 4.26 essentially confirms that the $W^\pm(\rightarrow \ell^\pm\nu) + jets$ and the $t\bar{t}(\rightarrow \ell^\pm\nu + 2b) + jets$ processes are properly described by the simulation.

Process	N_{exp} or N_{obs}
$W^\pm(\rightarrow \ell^\pm\nu) + jets$	64.0 ± 0.0
$W^\pm(\rightarrow \ell^\pm\nu) + HF + jets$	14.9 ± 0.2
$t\bar{t}(\rightarrow \ell^\pm\nu + 2b) + jets$	10.1 ± 0.2
$t\bar{t}(\rightarrow \ell^+\ell^-\nu\bar{\nu} + 2b) + jets$	4.3 ± 0.1
VV	4.1 ± 0.3
$t + q + b, t + b$	1.31 ± 0.03
$\gamma^*/Z(\rightarrow \ell^+\ell^-) + jets$	0.7 ± 0.0
$Z(\rightarrow \nu\bar{\nu}) + HF + jets$	0.3 ± 0.0
$\gamma^*/Z(\rightarrow \ell^+\ell^-) + HF + jets$	0.3 ± 0.0
$Z(\rightarrow \nu\bar{\nu}) + jets$	0.07 ± 0.0
$Z(\rightarrow \nu\bar{\nu}) + HF + jets$	0.04 ± 0.0
Total background	99.8 ± 0.8
Data	97

TABLE 4.24: The events yield after the JT1 C4, the $\cancel{E}_T > 75$ and the requirement to have exactly one isolated electron per event.

Process	N_{exp} or N_{obs}
$t\bar{t}(\rightarrow \ell^\pm\nu + 2b) + jets$	9.25126 ± 0.176143
$W^\pm(\rightarrow \ell^\pm\nu) + jets$	8.01069 ± 0.0
$W^\pm(\rightarrow \ell^\pm\nu) + HF + jets$	1.94776 ± 0.0
$t\bar{t}(\rightarrow \ell^+\ell^-\nu\bar{\nu} + 2b) + jets$	1.0515 ± 0.0261271
VV	0.525817 ± 0.104261
$\gamma^*/Z(\rightarrow \ell^+\ell^-) + jets$	0.513907 ± 0.0
$t + q + b, t + b$	0.241442 ± 0.0110249
$t\bar{t} \rightarrow 2b + jets$	0.0404395 ± 0.0271588
$\gamma^*/Z(\rightarrow \ell^+\ell^-) + HF + jets$	0.0325661 ± 0.0
Total background	21.6154 ± 0.344715
Data	21

TABLE 4.25: The events yield after the JT2 C4, the $\cancel{E}_T > 75$ and the requirement to have exactly one isolated electron per event.

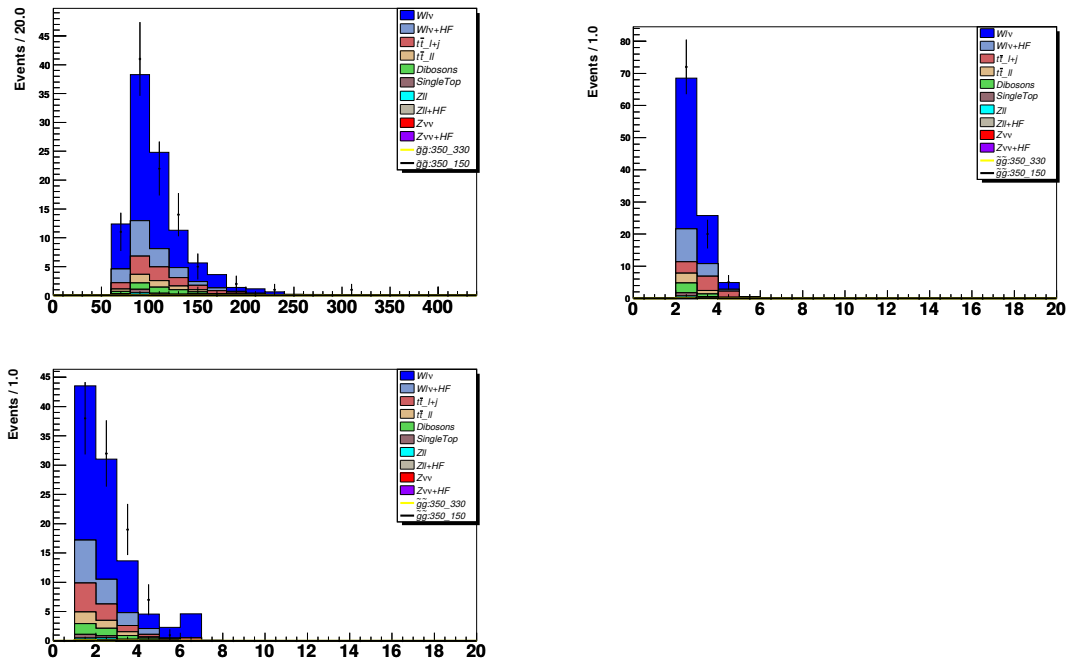


FIGURE 4.26: The $\#E_T$ (top left), the number of central jets (top right) and the N_{PV} (bottom) distributions after the JT1 C4, the $\#E_T > 75$ cuts and the requirement to have exactly one isolated electron per event.

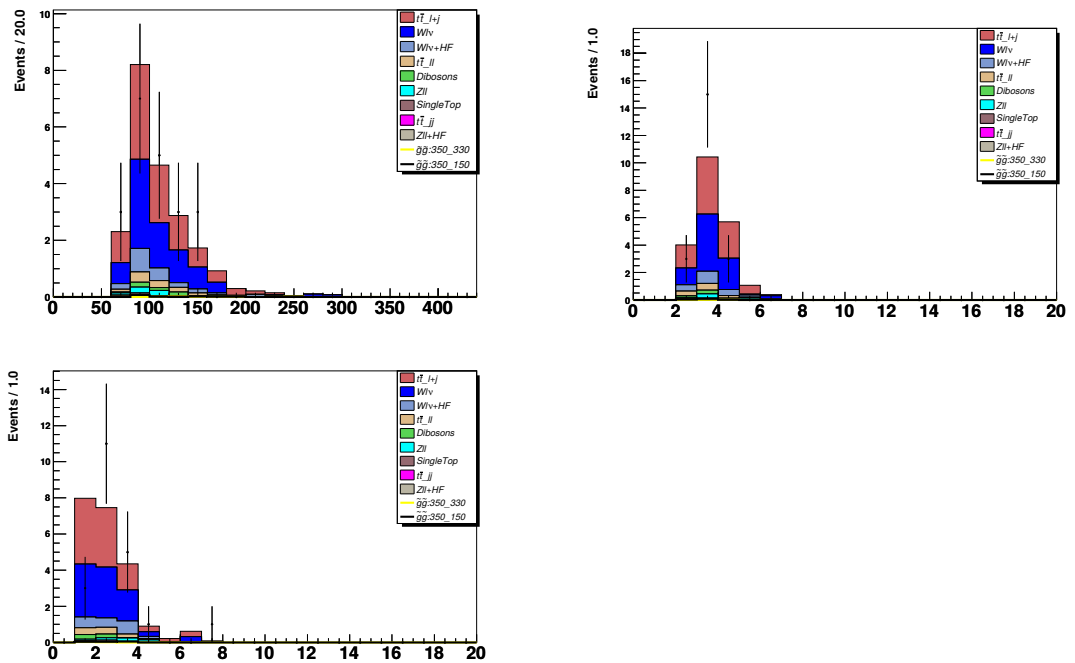


FIGURE 4.27: The $\#E_T$ (top left), the number of central jets (top right) and the N_{PV} (bottom) distributions after the JT2 C4, the $\#E_T > 75$ cuts and the requirement to have exactly one isolated electron per event.

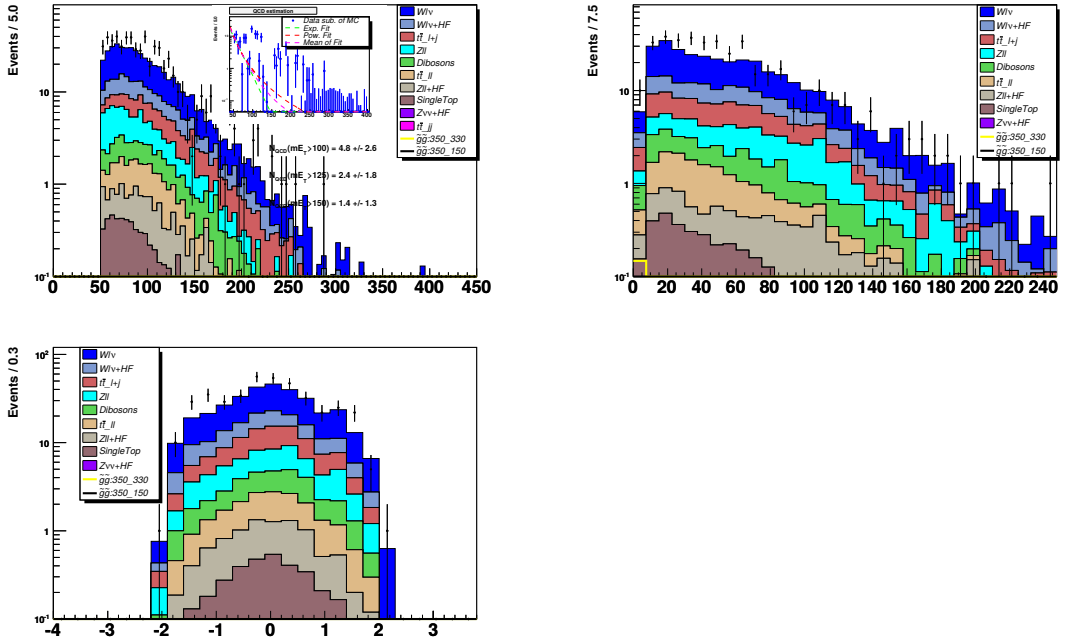


FIGURE 4.28: The marginal E_T , the leading muon p_T and η distributions after the JT1 C4, the $E_T > 75$ cuts and the requirement to have exactly one isolated muon per event.

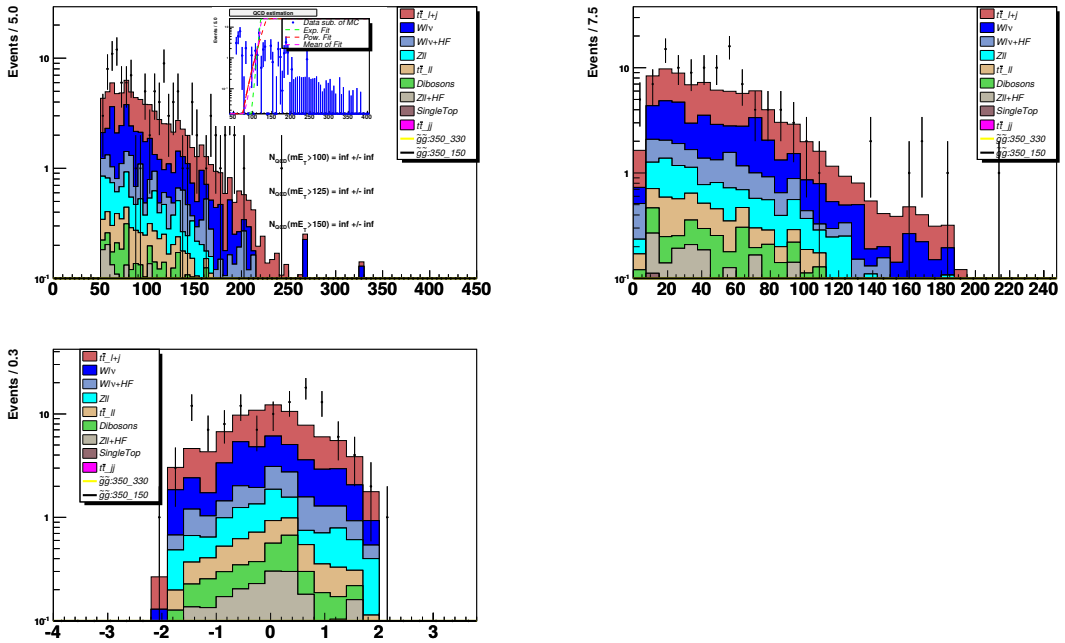


FIGURE 4.29: The marginal E_T , the leading muon p_T and η distributions after the JT2 C4, the $E_T > 75$ cuts and the requirement to have exactly one isolated muon per event.

Process	N_{exp} or N_{obs}
$W^\pm(\rightarrow \ell^\pm\nu) + jets$	170.1 ± 0.0
$W^\pm(\rightarrow \ell^\pm\nu) + HF + jets$	54.4 ± 0.3
$t\bar{t}(\rightarrow \ell^\pm\nu + 2b) + jets$	45.2 ± 0.4
$\gamma^*/Z(\rightarrow \ell^+\ell^-) + jets$	30.9 ± 0.0
VV	16.2 ± 0.6
$t\bar{t}(\rightarrow \ell^+\ell^-\nu\bar{\nu} + 2b) + jets$	10.8 ± 0.1
$\gamma^*/Z(\rightarrow \ell^+\ell^-) + HF + jets$	6.03 ± 0.0
$t + q + b, t + b$	3.228 ± 0.001
$Z(\rightarrow \nu\bar{\nu}) + HF + jets$	0.1 ± 0.0
QCD	7.55 ± 7.55
Total background	344.6 ± 7.7
Data	402

TABLE 4.26: The events yield after the JT1 C4, the $\cancel{E}_T > 75$ and the requirement to have exactly one isolated muon per event.

Process	N_{exp} or N_{obs}
$t\bar{t}(\rightarrow \ell^\pm\nu + 2b) + jets$	31.8 ± 0.3
$W^\pm(\rightarrow \ell^\pm\nu) + jets$	16.3 ± 0.0
$W^\pm(\rightarrow \ell^\pm\nu) + HF + jets$	5.92 ± 0.04
$\gamma^*/Z(\rightarrow \ell^+\ell^-) + jets$	3.81 ± 0.0
$t\bar{t}(\rightarrow \ell^+\ell^-\nu\bar{\nu} + 2b) + jets$	1.87 ± 0.03
VV	1.4 ± 0.2
$\gamma^*/Z(\rightarrow \ell^+\ell^-) + HF + jets$	1.0 ± 0.0
$t + q + b, t + b$	0.390 ± 0.003
Total background	62.5 ± 0.6
Data	77

TABLE 4.27: The events yield after the JT2 C4, the $\cancel{E}_T > 75$ and the requirement to have exactly one isolated muon per event.

The events yield after applying the JT1 C4, the $\cancel{E}_T > 50$ GeV cuts and the exclusive dilepton requirement is presented in Table 4.28. Figure 4.30 essentially confirms that the $\gamma^*/Z(\rightarrow \ell^+\ell^-) + jets$ and the $t\bar{t}(\rightarrow \ell^+\ell^-\nu\bar{\nu} + 2b) + jets$ processes are properly described by the simulation.

Process	N_{exp} or N_{obs}
$\gamma^*/Z(\rightarrow \ell^+\ell^-) + jets$	22.1 ± 0.0
$t\bar{t}(\rightarrow \ell^+\ell^-\nu\bar{\nu} + 2b) + jets$	4.36 ± 0.07
$\gamma^*/Z(\rightarrow \ell^+\ell^-) + HF + jets$	3.9 ± 0.0
VV	0.96 ± 0.05
$t\bar{t}(\rightarrow \ell^\pm\nu + 2b) + jets$	0.30 ± 0.04
$W^\pm(\rightarrow \ell^\pm\nu) + HF + jets$	0.22 ± 0.03
$t + q + b, t + b$	0.016 ± 0.001
Total background	31.8 ± 0.2
Data	30

TABLE 4.28: The events yield after the JT1 C4, the $\cancel{E}_T > 50$ and the requirement to have exactly two isolated leptons per event.

The good agreement found between the MC and the data regarding for the isolated single and dilepton control regions before the b-tagging give some confidence in the quality of the physics

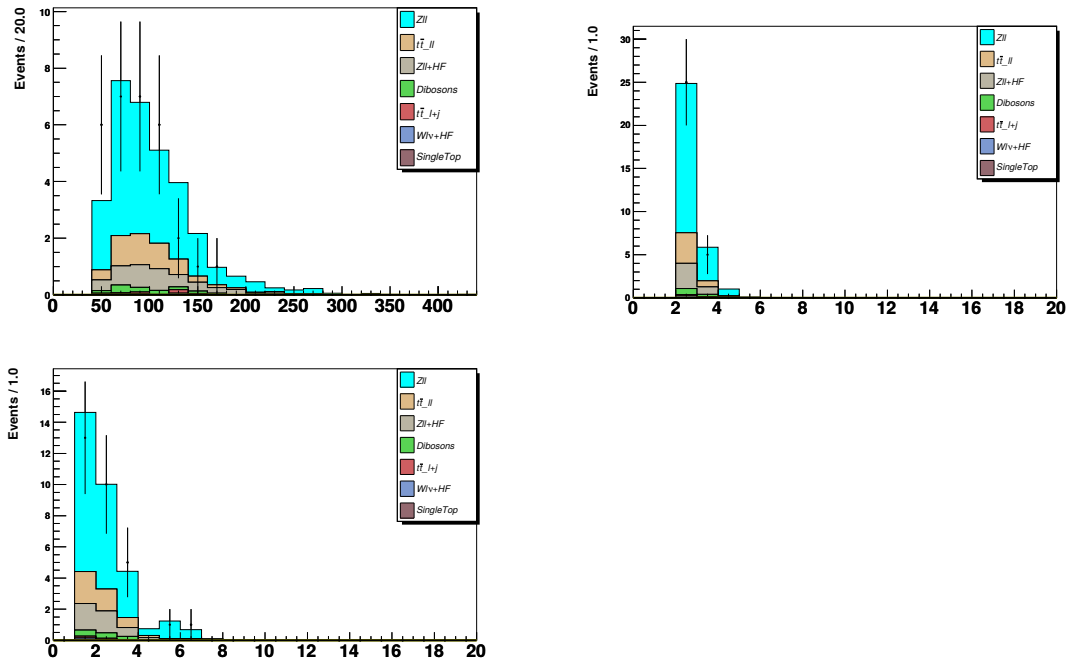


FIGURE 4.30: The \cancel{E}_T (top left), the number of central jets (top right) and the N_{PV} (bottom) distributions after the JT1 C4, the $\cancel{E}_T > 50$ cuts and the requirement to have exactly two isolated leptons per event.

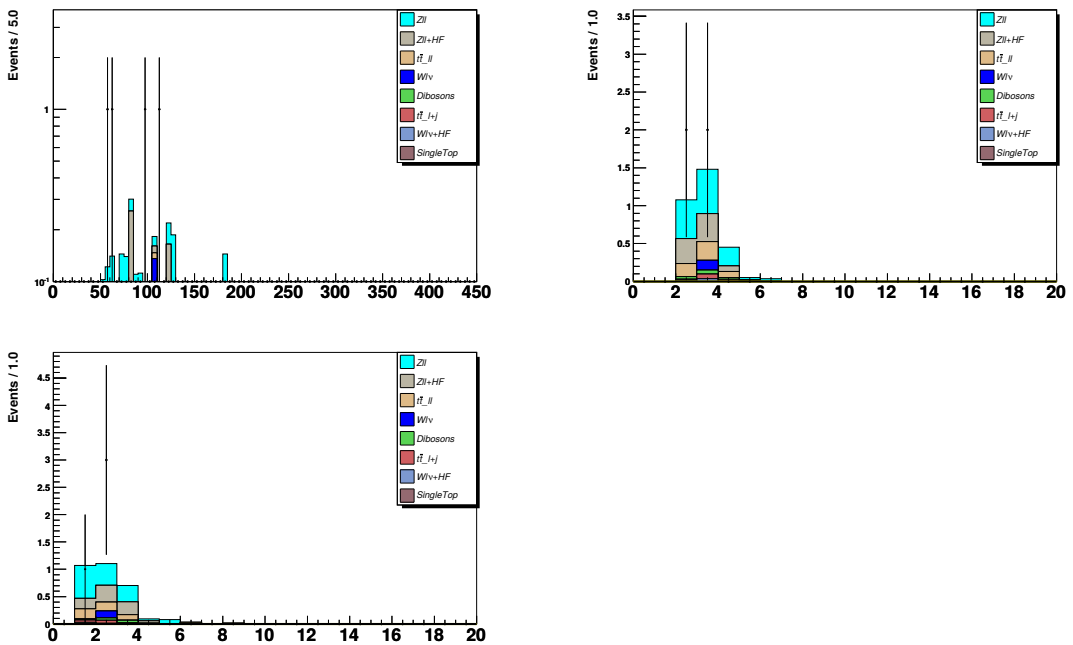


FIGURE 4.31: The \cancel{E}_T (top left), the number of central jets (top right) and the N_{PV} (bottom) distributions after the JT2 C4, the $\cancel{E}_T > 50$ cuts and the requirement to have exactly two isolated leptons per event.

background simulation especially in the tails of the distributions after the JT1 C4 cuts.

4.2.3.16.b Verifications including to the b-tagging

The physics background are also tested after applying a b-tagging with different operating points on one jet. Table 4.29 contains the number of expected and observed events after the JT1 and JT2 C4 cuts and the requirement to have exactly two isolated leptons per event. A good agreement is found between the MC and the data in terms of normalization.

	JT1			JT2		
	L	M	T	L	M	T
N_{exp}	19.1 ± 0.5	15.7 ± 0.5	13.8 ± 0.4	9.5 ± 0.3	8.5 ± 0.2	7.8 ± 0.2
N_{obs}	22	17	16	10	9	9

TABLE 4.29: Events yield after the JT1 and JT2 C4, the $\cancel{E}_T > 75$ GeV (resp. 50 GeV) cuts, the requirement to have exactly two isolated leptons per event and the b-tagging of one jet with different operating points. The L, M and T respectively stand for the "Loose", the "Medium" and the "Tight" b-tagging operating points.

And finally we made some verifications of the b-tagging within the signal region after the JT1 and JT2 C5 cuts.

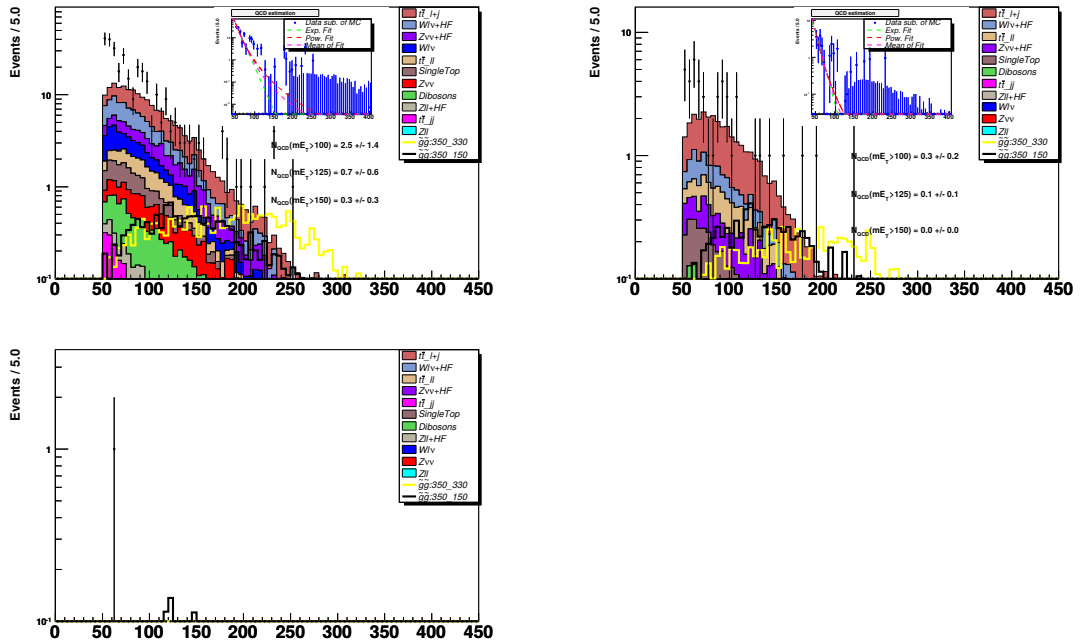


FIGURE 4.32: The \cancel{E}_T distributions after the JT1 C5 and one (top left), two (top right) and three (bottom) medium b-tags.

4.2.3.17 Acknowledgments

We thank the staffs at Fermilab and collaborating institutions, and acknowledge support from the DOE and NSF (USA); CEA and CNRS/IN2P3 (France); FASI, Rosatom and RFBR (Russia); CAPES, CNPq, FAPERJ, FAPESP and FUNDUNESP (Brazil); DAE and DST (India);

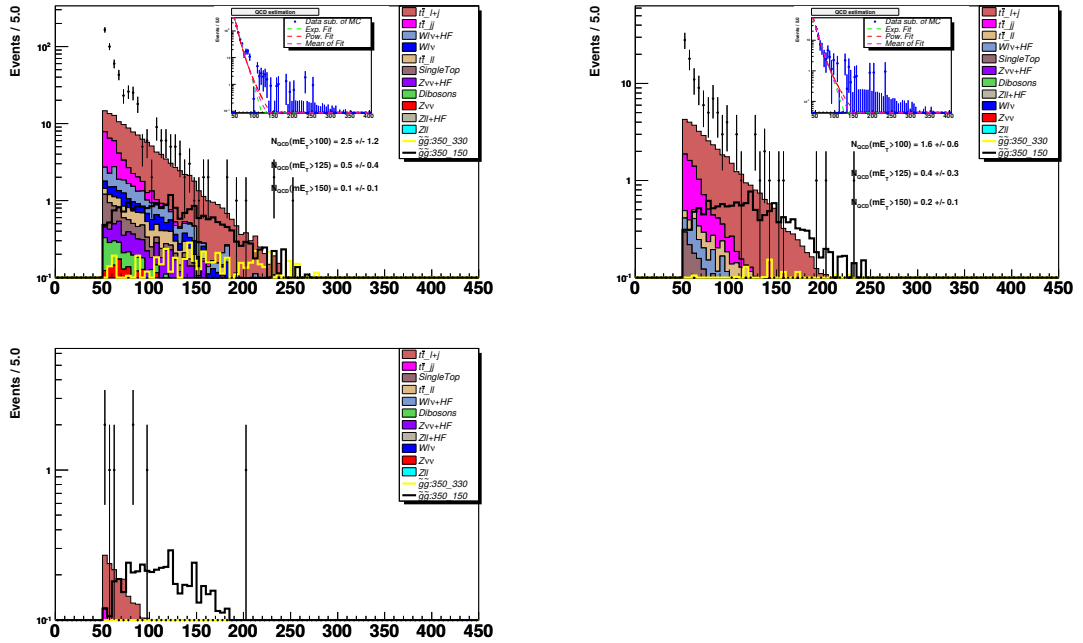


FIGURE 4.33: The E_T distributions after the JT2 C5 and one (top left), two (top right) and three (bottom) medium b-tags.

Colciencias (Colombia); CONACyT (Mexico); KRF and KOSEF (Korea); CONICET and UBA-CyT (Argentina); FOM (The Netherlands); PPARC (United Kingdom); MSMT (Czech Republic); CRC Program, CFI, NSERC and WestGrid Project (Canada); BMBF and DFG (Germany); SFI (Ireland); Research Corporation, Alexander von Humboldt Foundation, and the Marie Curie Program.

Chapter 5

Search for Electroweakinos at LHC

5.1 Instrumental Aspects

5.1.1 LHC

The LHC [41] is the highest energy collider ever built. It was constructed in the former tunnel of the LEP at CERN. Its injection chain consists of:

- Proton source: hydrogen bottle, electrons are stripped out by an electric field to create the proton beam
- LINAC 2: linear accelerator that raise the proton energy up to $E_{beam} = 50$ MeV
- PS Booster: circular machine that accelerates the p up to $E_{beam} = 1.8$ GeV
- PS: proton synchrotron that accelerates the p up to $E_{beam} = 25$ GeV
- SPS: super proton synchrotron that accelerates the p up to $E_{beam} = 450$ GeV
- LHC: accelerates the p up to $E_{beam} = 7$ TeV and collide them head-on at the center of the detectors

Fig. 5.1 displays the injection complex of the LHC.

It can collide protons and heavy ions and delivers its beams to four main experiments: ATLAS, CMS, LHCb and ALICE. The two former are general purpose experiments, whereas LHCb is dedicated to beauty and charm physics and ALICE to heavy ion collisions (that can also be studied in ATLAS and CMS).

The LHC nominal characteristics are:

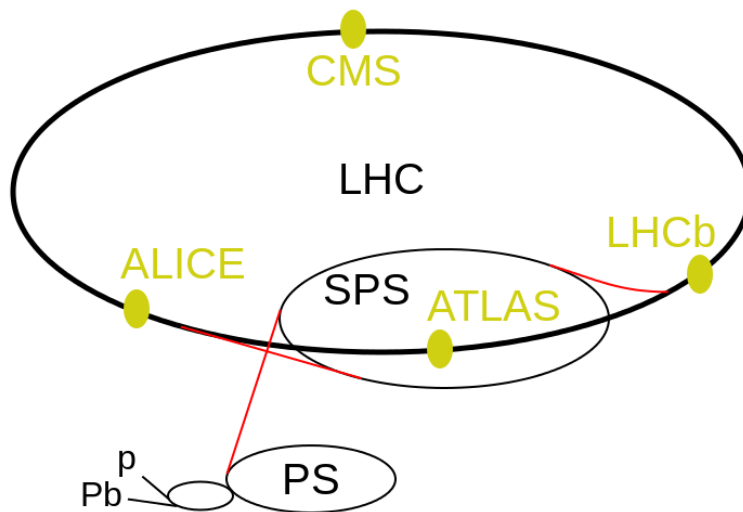


FIGURE 5.1: The LHC injection chain.

- center-of-mass energy for pp collisions: $\sqrt{s} = 14$ TeV
- instantaneous luminosity: $\mathcal{L} = 10^{34} \text{ cm}^{-2}\text{s}^{-1}$
- bunch spacing: $\Delta t_X = 25$ ns

It started operating in 2008 (delivering physics data in 2009) and is scheduled to run for a couple of decades.

5.1.2 ATLAS Detector

The ATLAS experiment [136] at the LHC is a multi-purpose particle detector with a forward-backward symmetric cylindrical geometry and a near 4π coverage in solid angle.¹ It consists of an inner tracking detector surrounded by a thin superconducting solenoid providing a 2 T axial magnetic field, electromagnetic and hadron calorimeters, and a muon spectrometer; Fig. 5.2 shows a sketch of this detector.

The inner tracking detector covers the pseudorapidity range $|\eta| < 2.5$. It consists of silicon pixel, silicon micro-strip, and transition radiation tracking detectors. Lead/liquid-argon (LAr) sampling calorimeters provide electromagnetic (EM) energy measurements with high granularity. A hadron (iron/scintillator-tile) calorimeter covers the central pseudorapidity range ($|\eta| < 1.7$). The end-cap and forward regions are instrumented with LAr calorimeters for both EM and hadronic energy measurements up to $|\eta| = 4.9$. The muon spectrometer surrounds the calorimeters and is based on three large air-core toroid superconducting magnets with eight coils each.

¹ATLAS uses a right-handed coordinate system with its origin at the nominal interaction point (IP) in the centre of the detector and the z -axis along the beam pipe. The x -axis points from the IP to the centre of the LHC ring, and the y -axis points upwards. Cylindrical coordinates (r, ϕ) are used in the transverse plane, ϕ being the azimuthal angle around the z -axis. The pseudorapidity is defined in terms of the polar angle θ as $\eta = -\text{Log}(\tan(\theta/2))$. Angular distance is measured in units of $\Delta R \equiv \sqrt{(\Delta\eta)^2 + (\Delta\phi)^2}$.

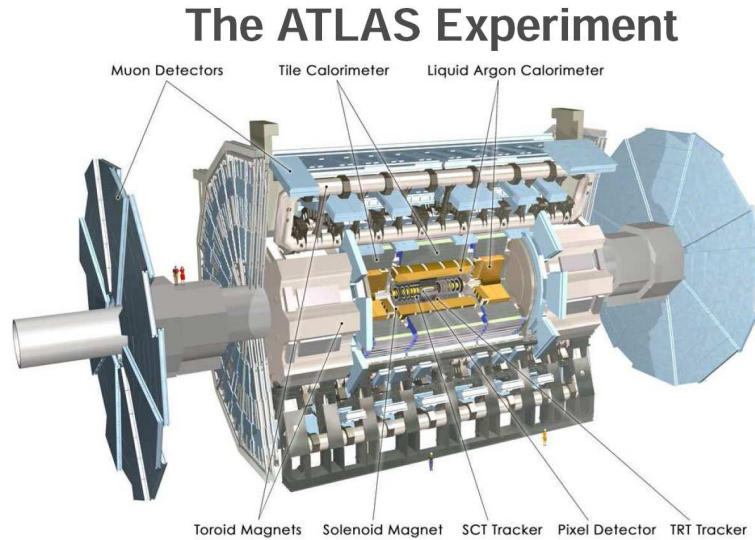


FIGURE 5.2: The ATLAS detector.

Its bending power is in the range from 2.0 to $7.5Tm$. It includes a system of precision tracking chambers and fast detectors for triggering. A three-level trigger system is used to select events. The first-level trigger is implemented in hardware and uses a subset of the detector information to reduce the accepted rate to at most 75 kHz. This is followed by two software-based trigger levels that together reduce the accepted event rate to 400 Hz on average depending on the data-taking conditions during 2012. The ATLAS detector [136] at the LHC covers nearly the entire solid angle around the collision point. It consists of an inner tracking detector surrounded by a thin superconducting solenoid, electromagnetic and hadronic calorimeters, and a muon spectrometer incorporating three large superconducting toroid magnets. The inner-detector system (ID) is immersed in a 2 T axial magnetic field and provides charged particle tracking in the range $|\eta| < 2.5$.

The high-granularity silicon pixel detector covers the vertex region and typically provides three measurements per track, the first hit being normally in the innermost layer. It is followed by the silicon microstrip tracker which usually provides four two-dimensional measurement points per track. These silicon detectors are complemented by the transition radiation tracker, which enables radially extended track reconstruction up to $|\eta| = 2.0$. The transition radiation tracker also provides electron identification information based on the fraction of hits (typically 30 in total) above a higher energy deposit threshold corresponding to transition radiation.

The calorimeter system covers the pseudorapidity range $|\eta| < 4.9$. Within the region $|\eta| < 3.2$, electromagnetic calorimetry is provided by barrel and endcap high-granularity lead/liquid-argon (LAr) electromagnetic calorimeters, with an additional thin LAr presampler covering $|\eta| < 1.8$, to correct for energy loss in material upstream of the calorimeters. Hadronic calorimetry is provided by the steel/scintillating-tile calorimeter, segmented into three barrel structures within $|\eta| < 1.7$, and two copper/LAr hadronic endcap calorimeters. The solid angle coverage is completed with forward copper/LAr and tungsten/LAr calorimeter modules optimised for electromagnetic and hadronic measurements respectively.

The muon spectrometer (MS) comprises separate trigger and high-precision tracking chambers measuring the deflection of muons in a magnetic field generated by superconducting air-core toroids. The precision chamber system covers the region $|\eta| < 2.7$ with three layers of monitored drift tubes, complemented by cathode strip chambers in the forward region, where the background is highest. The muon trigger system covers the range $|\eta| < 2.4$ with resistive plate chambers in the barrel, and thin gap chambers in the endcap regions. A three-level trigger system is used to select interesting events [42]. The Level-1 trigger is implemented in hardware and uses a subset of detector information to reduce the event rate to a design value of at most 75 kHz. This is followed by two software-based trigger levels which together reduce the event rate to about 200 Hz.

5.1.3 Using a Higgs Boson to Search for SUSY

In this sub-section, I'll describe the combination [425][442] of three ATLAS analyses that utilized a Higgs Boson as a tag to search for electroweak gauginos (aka "electroweakinos") within the Run 1 dataset. More precisely, these analyses restrict themselves to the production of $pp \rightarrow \tilde{\chi}_1^\pm \tilde{\chi}_2^0$. Myself, together with my PhD student, Michael Ughetto, took part only in the analysis where the following decay modes are envisaged: $\tilde{\chi}_1^\pm \rightarrow W^\pm (\rightarrow \ell^\pm \nu) \tilde{\chi}_1^0$, and $\tilde{\chi}_2^0 \rightarrow h^0 (\rightarrow b\bar{b}) \tilde{\chi}_1^0$. Note that this was the first such analysis on ATLAS data [423] and that it is the most sensitive channel to search for electroweakinos tagged with a Higgs boson.

Search for direct production of charginos and neutralinos decaying via the 125 GeV Higgs boson in $\sqrt{s} = 8$ TeV pp collisions with the ATLAS detector

ATLAS Collaboration

Abstract

A search for the direct pair production of charginos and neutralinos $pp \rightarrow \tilde{\chi}_1^\pm \tilde{\chi}_2^0$ is presented, where the chargino decays via a W boson $\tilde{\chi}_1^\pm \rightarrow \tilde{\chi}_1^0 (W^\pm \rightarrow \ell^\pm \nu)$, while the neutralino decays via the 125 GeV Higgs boson $\tilde{\chi}_2^0 \rightarrow \tilde{\chi}_1^0 (h \rightarrow b\bar{b}/\gamma\gamma/\ell^\pm \nu qq)$ to the lightest neutralino. The final states considered for the search have large missing transverse momentum, an isolated electron or muon, and one of the following: either two jets identified as originating from bottom quarks, or two photons, or a second electron or muon with the same electric charge. The analysis is based on 20.3 fb^{-1} of $\sqrt{s} = 8$ TeV proton-proton collision data delivered by the Large Hadron Collider and recorded with the ATLAS detector. Observations are consistent with the Standard Model expectations, and limits are set in the context of a simplified supersymmetric model within which, in the case where the $\tilde{\chi}_1^0$ is massless, the direct production of $\tilde{\chi}_1^\pm$ and $\tilde{\chi}_2^0$ of equal mass below 250 GeV is excluded.

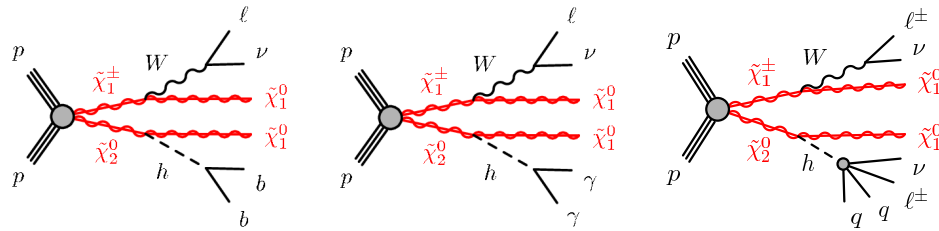


FIGURE 5.3: Diagrams for the direct production of $\tilde{\chi}_1^\pm \tilde{\chi}_2^0$ and the three decay modes studied in this note. For the same-sign dilepton channel (c), only the dominant decay mode is shown.

5.1.3.1 Introduction

Supersymmetry (SUSY) proposes the existence of supersymmetric particles, with spin differing by one half unit with respect to that of their Standard Model (SM) partners. Charginos, $\tilde{\chi}_{1,2}^\pm$, and neutralinos, $\tilde{\chi}_{1,2,3,4}^0$, are the ordered mass eigenstates formed from the linear superposition of the SUSY partners of the Higgs and electroweak gauge bosons (higgsinos, winos and binos). In R -parity-conserving models [43–46], SUSY particles are pair-produced in colliders and the lightest SUSY particle (LSP) is stable. In many models it is assumed to be the $\tilde{\chi}_1^0$, which is weakly interacting. Naturalness arguments [67, 68] suggest that the lightest of the charginos and neutralinos may have masses at the electroweak scale, and the direct production of charginos and neutralinos may be accessible at the LHC.

A simplified SUSY model [249] is considered for the optimization of the search and the interpretation of results. It describes the direct production of $\tilde{\chi}_1^\pm$ and $\tilde{\chi}_2^0$, where the masses and the decay modes of the relevant particles ($\tilde{\chi}_1^\pm$, $\tilde{\chi}_1^0$, $\tilde{\chi}_2^0$) are the only free parameters. It is assumed that the $\tilde{\chi}_1^\pm$ and $\tilde{\chi}_2^0$ are pure wino states and degenerate in mass, while the $\tilde{\chi}_1^0$ is a pure bino state. The prompt decays $\tilde{\chi}_1^\pm \rightarrow W^\pm \tilde{\chi}_1^0$ and $\tilde{\chi}_2^0 \rightarrow h \tilde{\chi}_1^0$ are assumed to have 100% branching fractions. The Higgs boson mass is set to the measured 125 GeV and its branching ratios are assumed to be the same as in the SM. The latter assumption is motivated by those SUSY models in which the mass of the pseudo-scalar Higgs boson is much larger than the Z -boson mass.

The search presented in this note targets three Higgs boson decay modes as illustrated in Fig. 5.3. The Higgs boson decays either into a pair of b -quarks, or a pair of photons, or a pair of W bosons where at least one of the bosons decays leptonically. The final states therefore contain missing transverse momentum from neutrinos and neutralinos, one lepton (e or μ), and one of the following: two b -quarks ($\ell b b$), or two photons ($\ell \gamma \gamma$), or an additional lepton with the same electric charge ($\ell^\pm \ell^\pm$). The $h \rightarrow ZZ$ and $h \rightarrow \tau \tau$ decays also contribute to the same-sign dilepton signature.

The analysis is based on a data sample of proton–proton collisions recorded by the ATLAS detector at a centre-of-mass energy of 8 TeV. Its integrated luminosity corresponds to 20.3 fb^{-1} . Previous searches for charginos and neutralinos have been reported by ATLAS [71, 182, 422] and CMS [72, 73]. Similar searches were conducted at the Tevatron [74, 75] and LEP [128–132].

The results of this note are combined with the ATLAS search using the three-lepton and missing transverse momentum final state, performed with the same dataset [182]. The three-lepton

TABLE 5.1: Simulated samples used for background estimates. “Tune” refers to the choices of parameters used for the underlying event generation.

Process	Generator	Cross section	Tune	PDF set
Single top, t -channel	ACERMC [141]+PYTHIA [357]	NNLO+NNLL [143]	AUET2B [144]	CTEQ6L1 [253]
Single top, s -channel	POWHEG [146, 147]+PYTHIA	NNLO+NNLL [148]	PERUGIA2011C [149]	CT10 [443]
tW	POWHEG+PYTHIA	NNLO+NNLL [151]	PERUGIA2011C	CT10
$t\bar{t}$	POWHEG+PYTHIA	NNLO+NNLL [152–157]	PERUGIA2011C	CT10
$t\bar{t}W, t\bar{t}Z$	MADGRAPH [158]+PYTHIA	NLO	AUET2B	CTEQ6L1
W, Z (bb channel)	SHERPA [159]	NLO	–	CT10
W, Z ($\ell^\pm\ell^\pm$ channel)	ALPGEN [160]+PYTHIA	NLO	PERUGIA2011C	CTEQ6L1
WW, WZ, ZZ	SHERPA	NLO	–	CT10
$W\gamma, W\gamma\gamma$	ALPGEN+PYTHIA	NLO	AUET2B	CTEQ6L1
$Z\gamma, Z\gamma\gamma$	SHERPA	NLO	–	CT10
$W^\pm W^\pm$	SHERPA	NLO	–	CT10
Wh, Zh	PYTHIA8 [161]	NNLO(QCD)+NLO(EW) [162]	AU2 [163]	CTEQ6L1
$t\bar{t}h$	PYTHIA8	NLO(QCD) [162]	AU2	CTEQ6L1

signal regions may contain up to two hadronically decaying τ leptons providing sensitivity to the $h \rightarrow \tau\tau/WW/ZZ$ Higgs boson decay modes. The statistical combination of the results is facilitated by the fact that all signal and control regions have been constructed not to overlap.

This note is organized in the following way: the description of the Monte Carlo simulation is in Sec. 5.1.3.2. In Sec. 5.1.3.3 the common aspects of the event reconstruction are illustrated; Sections 5.1.3.4, 5.1.3.5, and 5.1.3.6 describe the channel-specific features; Section 5.1.3.7 describes the systematic uncertainties; the results and conclusions follow in Secs. 5.1.3.8 and 5.1.3.9.

5.1.3.2 Monte Carlo simulation

The propagation of particles through the ATLAS detector is modelled with GEANT4 [135] using the full ATLAS detector simulation [137] for all Monte Carlo (MC) simulated samples, except for the $t\bar{t}$ POWHEG+PYTHIA and the SUSY signal samples in which the Higgs boson decays to two b -quarks, for which a fast simulation based on a parametric response of the electromagnetic and hadronic calorimeters is used [138]. The effect of multiple proton–proton collisions from the same or nearby beam bunch crossings (in-time or out-of-time pile-up) is incorporated into the simulation by overlaying additional minimum-bias events generated with PYTHIA8 [161] onto hard-scatter events. Simulated events are weighted to match the distribution of the average number of interactions per bunch crossing observed in data, but are otherwise reconstructed in the same manner as data.

The event generators, the accuracy of theoretical cross sections, the underlying event parameter tunes, and the parton distribution function (PDF) sets used for simulating the SM background processes are summarized in Table 5.1.

The SUSY signal samples are produced with HERWIG++ [164] using the CTEQ6L1 PDF set. Signal cross sections are calculated at next-to-leading order (NLO) in the strong coupling constant using PROSPINO2 [275]. These agree with the NLO calculations matched to resummation at next-to-leading logarithmic (NLL) accuracy within $\sim 2\%$ [166, 250]. The nominal cross section and the uncertainty are taken respectively from the centre and the spread of the cross section predictions using different PDF sets and their associated uncertainties, as well as from variations of factorisation and renormalisation scales, as described in Ref. [168].

5.1.3.3 Event reconstruction

The data sample considered in this analysis was collected with a combination of single-lepton, dilepton, and diphoton triggers. After applying beam, detector, and data-quality requirements, the dataset corresponds to an integrated luminosity of 20.3 fb^{-1} , with an uncertainty of 2.8%. The uncertainty is derived, following the methodology detailed in Ref. [169], from a preliminary calibration of the luminosity scale from beam-separation scans performed in November 2012.

Events are analysed if the primary vertex has five or more tracks with transverse momentum $p_T > 400 \text{ MeV}$ associated with it, unless stated otherwise. For this purpose, the primary vertex of an event is identified as the vertex with the largest $\sum p_T^2$ of associated tracks.

Electron candidates must satisfy “medium” identification criteria, following Ref. [185] (modified for 2012 data conditions), and are required to have $p_T > 10 \text{ GeV}$ and $|\eta| < 2.47$. Electron p_T and η are determined from the calibrated clustered energy deposits in the electromagnetic calorimeter and the matched ID track, respectively.

Muon candidates are reconstructed by combining tracks in the ID and tracks or segments in the MS [171] and are required to have $p_T > 10 \text{ GeV}$ and $|\eta| < 2.7$. To suppress cosmic-ray muon background, events are rejected if they contain a muon having transverse impact parameter with respect to the primary vertex $|d_0| > 0.2 \text{ mm}$ or longitudinal impact parameter with respect to the primary vertex $|z_0| > 1 \text{ mm}$.

Photon candidates are reconstructed from clusters of energy deposits in the electromagnetic calorimeter. Clusters without matching tracks as well as those matching one or two tracks consistent with a photon conversion are considered. The shape of the cluster must match that expected for an electromagnetic shower, using criteria tuned for robustness under the pile-up conditions of 2012 [172]. The cluster energy is calibrated, separately for converted and unconverted photon candidates, using simulation. In addition, η -dependent correction factors determined from $Z \rightarrow e^+e^-$ events are applied to the cluster energy, as described in Ref. [172]. The photon candidates must have $p_T > 20 \text{ GeV}$ and $|\eta| < 2.37$, excluding the gap of $1.37 < |\eta| < 1.56$ between the barrel and end-cap electromagnetic calorimeters.

Jets are reconstructed with the anti- k_t algorithm [269] with a radius parameter 0.4 using three-dimensional clusters of energy in the calorimeter [174] as input. The clusters are calibrated, weighting differently the energy deposits arising from the electromagnetic and hadronic components of the showers. The final jet energy calibration corrects the calorimeter response to the particle-level jet energy [175, 176], where correction factors are obtained from simulation and then refined and validated using data. Corrections for in-time and out-of-time pile-up are also applied, as described in Ref. [178]. Events containing jets failing the quality criteria described in Ref. [175] are rejected to suppress non-collision background and events with large noise in the calorimeters.

Jets with $p_T > 20 \text{ GeV}$ are considered in the central pseudorapidity ($|\eta| < 2.4$) region, and $p_T > 30 \text{ GeV}$ in the forward ($2.4 < |\eta| < 4.5$) region. For central jets, information from the ID makes it possible to suppress pile-up using the “jet vertex fraction” (JVF). It is defined as the p_T -weighted fraction of tracks within the jet that originate from the primary vertex of the event,

TABLE 5.2: Summary of the overlap removal procedure. Potential ambiguities are resolved by removing nearby objects in the indicated order, from top to bottom. Different ΔR separation requirements are used in the three channels. In the same-sign channel, e^+e^- and $\mu^+\mu^-$ pairs with $m_{\ell^+\ell^-} < 12$ GeV are also removed.

Candidates	ΔR threshold			Candidate removed
	$\ell b b$	$\ell \gamma \gamma$	$\ell^\pm \ell^\pm$	
$e - e$	0.1	—	0.05	lowest- p_T e
$e - \gamma$	—	0.4	—	e
jet- γ	—	0.4	—	jet
jet- e	0.2	0.2	0.2	jet
$\tau - e$ or $\tau - \mu$	—	—	0.2	τ
$\mu - \gamma$	—	0.4	—	μ
e -jet or μ -jet	0.4	0.4	0.4	e or μ
$e - \mu$	0.1	—	0.1	both
$\mu - \mu$	0.05	—	0.05	both
jet- τ	—	—	0.2	jet

and it is -1 if there are no tracks within the jet. Central jets can also be tagged as originating from bottom quarks (referred to as b -jets) using the MV1 multivariate b -tagging algorithm based on quantities related to impact parameters of tracks and reconstructed secondary vertices [444]. The efficiency of the b -tagging algorithm depends on the operating point chosen for each channel, and it is reported in Secs. 5.1.3.4 and 5.1.3.6.

Hadronically decaying τ leptons are reconstructed as 1- or 3-prong hadronic jets within $|\eta| < 2.47$, and are required to have $p_T > 20$ GeV after being calibrated to the τ energy scale [140]. Final states with hadronically decaying τ leptons are not considered here; however, they are used in the overlap removal procedure described below, as well as to make the same-sign lepton channel non-overlapping with the three-lepton search [182] that is included in the combined result.

Potential ambiguities between candidate leptons, photons and jets are resolved by removing one or both objects if they are separated by $\Delta R \equiv \sqrt{(\Delta\phi)^2 + (\Delta\eta)^2}$ below a threshold. This process eliminates duplicate objects reconstructed from a single particle, and suppresses leptons and photons contained inside hadronic jets. The thresholds and the order in which overlapping objects are removed are summarized in Table 5.2. The remaining leptons and photons are referred to as “preselected” objects.

Isolation criteria are applied to improve the quality of reconstructed objects. The criteria are based on the scalar sum of the transverse energies E_T of the calorimeter cell clusters within a radius ΔR of the object ($E_T^{\text{cone}\Delta R}$), and on the scalar sum of the p_T of the tracks within ΔR and associated with the primary vertex ($p_T^{\text{cone}\Delta R}$). The contribution due to the object itself is not included in either sum. The detailed values of the isolation criteria depend on the channel; they are specified in Secs. 5.1.3.4, 5.1.3.5 and 5.1.3.6.

The missing transverse momentum, \vec{p}_T^{miss} (with magnitude E_T^{miss}), is the negative vector sum of the transverse momenta of all preselected electrons, muons, and photons as well as jets and energy of calorimeter clusters with $|\eta| < 4.9$ not associated with these objects. Clusters that are associated with electrons, photons and jets are calibrated to the scale of the corresponding

objects; the ones that are not associated with any reconstructed object are calibrated at the hadronic scale [183, 190].

The efficiencies for electrons, muons, and photons to pass the reconstruction and identification criteria are measured in control samples, and corrections are applied to the simulated samples to reproduce the efficiencies in data. Similar corrections are also applied to the jet b -tagging efficiency and mis-identification probability.

5.1.3.4 One lepton and two b -jets channel

5.1.3.4.a Event selection

The events considered in the one lepton and two b -jets channel are recorded with a combination of single-lepton triggers. The offline event selection requires exactly one signal lepton (e or μ) with $p_T > 25$ GeV, to ensure that the event is triggered with a constant high efficiency. The signal electrons must satisfy the “tight” identification criteria of Ref. [185], $|d_0|/\sigma_{d_0} < 5$, where σ_{d_0} is the error on d_0 , and $|z_0 \sin \theta| < 0.4$ mm. The signal muons must satisfy $|\eta| < 2.4$, $|d_0|/\sigma_{d_0} < 3$, and $|z_0 \sin \theta| < 0.4$ mm. The signal electrons (muons) are required to satisfy the isolation criteria $E_T^{\text{cone}0.3}/p_T < 0.18$ (0.12) and $p_T^{\text{cone}0.3}/p_T < 0.16$ (0.12).

Events with two or three jets are selected, where the jets can be either central ($|\eta| < 2.4$) or forward ($2.4 < |\eta| < 4.9$). Central jets have $p_T > 25$ GeV, and forward jets have $p_T > 30$ GeV. For central jets with $p_T < 50$ GeV, the JVF must be > 0.5 . The two highest- p_T central jets must be b -tagged. The chosen operating point of the b -tagging algorithm identifies b -jets in simulated $t\bar{t}$ events with an efficiency of 70%; it mis-identifies charm and light-flavour (including gluon induced) jets 20% and $< 1\%$ of the time respectively.

The dominant background contributions in the $\ell b\bar{b}$ channel are $t\bar{t}$, W + jets, and single-top Wt production. Their contributions are suppressed using the kinematic selections described below, which defines the two signal regions SR $\ell b\bar{b}$ -1 and SR $\ell b\bar{b}$ -2 summarized in Table 5.3.

The contranverse mass m_{CT} [186, 295] is defined as

$$m_{CT} = \sqrt{(E_T^{b_1} + E_T^{b_2})^2 - |\vec{p}_T^{b_1} - \vec{p}_T^{b_2}|^2}, \quad (5.1)$$

TABLE 5.3: Selection requirements for the signal, control and validation regions of the one lepton and two b -jets channel.

	SR $\ell b\bar{b}$ -1	SR $\ell b\bar{b}$ -2	CR $\ell b\bar{b}$ -T	CR $\ell b\bar{b}$ -W	VR $\ell b\bar{b}$ -1	VR $\ell b\bar{b}$ -2
n_{lepton}	1	1	1	1	1	1
n_{jet}	2–3	2–3	2–3	2	2–3	2–3
$n_{b\text{-jet}}$	2	2	2	1	2	2
E_T^{miss} [GeV]	> 100	> 100	> 100	> 100	> 100	> 100
m_{CT} [GeV]	> 160	> 160	100–160	> 160	100–160	> 160
m_T^W [GeV]	100–130	> 130	> 100	> 40	40–100	40–100

where $E_T^{b_i}$ and $\vec{p}_T^{b_i}$ are the transverse energy and momentum of the i -th b jet. The SM $t\bar{t}$ background has an upper endpoint at m_{CT} of approximately m_t , and is efficiently suppressed by requiring $m_{CT} > 160$ GeV.

The transverse mass m_T^W , describing W candidates in background events, is defined as

$$m_T^W = \sqrt{2E_T^\ell E_T^{\text{miss}} - 2\vec{p}_T^\ell \cdot \vec{p}_T^{\text{miss}}}, \quad (5.2)$$

where E_T^ℓ and \vec{p}_T^ℓ are the transverse energy and momentum of the lepton. Requiring $m_T^W > 100$ GeV efficiently suppresses the $W + \text{jets}$ background. The two SRs are distinguished by $100 < m_T^W < 130$ GeV for SR lbb -1 and $m_T^W > 130$ GeV for SR lbb -2. The first signal region provides sensitivity to signal models with a mass splitting between the lightest neutralinos similar to the Higgs boson mass, while the second one targets larger mass splittings.

In each SR, events are classified into five bins of the invariant mass m_{bb} of the two b -jets as 45–75–105–135–165–195 GeV. In the SRs, about 70% of the signal events due to $h \rightarrow b\bar{b}$ populate the central bin of 105–135 GeV. The other four bins (sidebands) are used to constrain the background normalization, as described below.

5.1.3.4.b Background estimation

The contributions from the $t\bar{t}$ and $W + \text{jets}$ background sources are estimated from simulation, and normalized to data in dedicated control regions defined in the following paragraphs. The contribution from multi-jet production, where the signal lepton is a mis-identified jet or comes from a heavy-flavour hadron decay or photon conversion, is estimated using the ‘‘matrix method’’ described in Ref. [422], and is found to be less than 3% of the total background in all regions and is thus neglected. The remaining sources of background (single top, $Z + \text{jets}$, WW , WZ , ZZ , Zh and Wh production) are estimated from simulation.

Two control regions (CR), CR lbb -T and CR lbb -W, are designed to constrain the normalization of the $t\bar{t}$ and $W + \text{jets}$ backgrounds respectively. The acceptance for $t\bar{t}$ events is increased in CR lbb -T by modifying the requirement on m_{CT} to $100 < m_{CT} < 160$ GeV. The acceptance of $W + \text{jets}$ events is increased in CR lbb -W by requiring exactly two jets, of which only one is b -tagged, and $m_T^W > 40$ GeV. These two control regions are summarized in Table 5.3. The control regions are defined to be similar to the signal regions in order to reduce systematic uncertainties on the extrapolation to the signal regions; at the same time they are dominated by the targeted background processes and the expected signal contamination is small.

As in the signal regions, the control regions are binned in m_{bb} (m_{bj} in the case of CR lbb -W). In the ‘‘background-only’’ likelihood fit, a simultaneous fit is performed to the eight m_{bb} sideband bins of the SRs and the ten m_{bb} bins of the CRs. This fit, as well as the limit setting procedure, is performed using the HISTFITTER package described in Ref. [189]. The two free parameters of the fit, namely the normalizations of the $t\bar{t}$ and $W + \text{jets}$ background components, are constrained by the number of events observed in the control regions, where the number of events is described by a Poisson probability density function. The remaining nuisance parameters correspond to the systematic uncertainties described in Sec. 5.1.3.7. They are taken into account

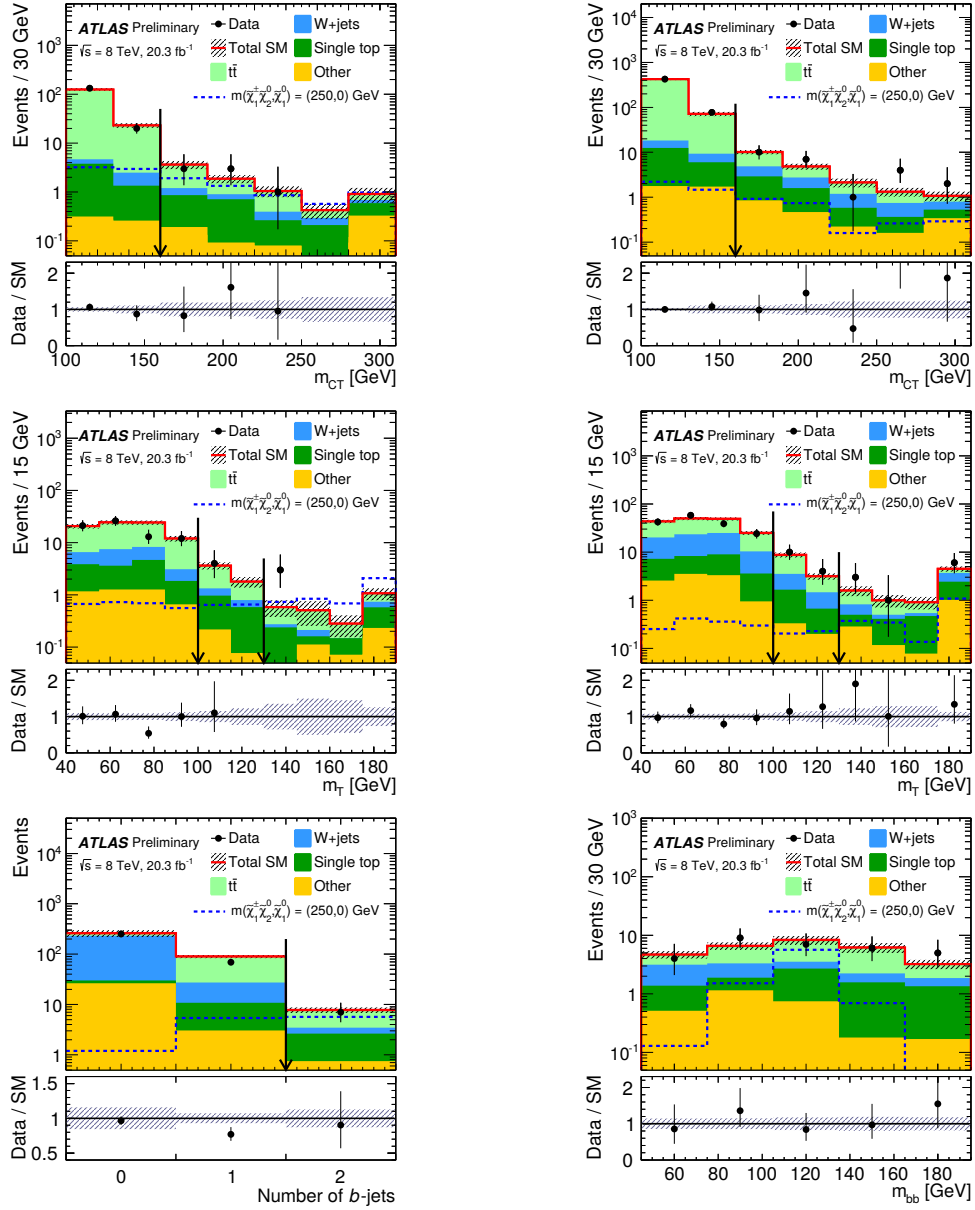


FIGURE 5.4: Distributions of m_{CT} , m_T^W , $n_{b\text{-jet}}$ and m_{bb} for the one lepton and two b -jets channel in the indicated regions. The background histograms are obtained from the background-only fit. The hatched regions represent the total uncertainties on the background estimates. The rightmost bin in (a)–(d) includes overflow. The distributions of a signal hypothesis are also shown. The vertical arrow indicates the boundary of the signal regions. The lower panel shows the ratio between data and the SM background prediction.

TABLE 5.4: Event yields and SM expectation in the one lepton and two b -jets channel obtained with the background-only fit. “Other” includes $Z + \text{jets}$, WW , WZ , ZZ , Zh and Wh processes. The errors shown include statistical and systematic uncertainties.

	SR lbb -1 $105 < m_{bb} < 135$	SR lbb -2	SR lbb -1 m_{bb} sidebands	SR lbb -2	CR lbb -T	CR lbb -W	VR lbb -1	VR lbb -2
Observed events	4	3	14	10	651	1547	885	235
SM expectation	6.0 ± 1.3	2.8 ± 0.8	13.1 ± 2.4	8.8 ± 1.7	642 ± 25	1560 ± 40	880 ± 90	245 ± 17
$t\bar{t}$	3.8 ± 1.2	1.4 ± 0.7	8.0 ± 2.4	3.1 ± 1.4	607 ± 25	680 ± 60	680 ± 90	141 ± 18
$W + \text{jets}$	0.6 ± 0.3	0.2 ± 0.1	2.7 ± 0.5	1.7 ± 0.3	11 ± 2	690 ± 60	99 ± 12	62 ± 8
Single top	1.3 ± 0.4	0.7 ± 0.4	1.9 ± 0.6	2.5 ± 1.1	20 ± 4	111 ± 14	80 ± 10	27 ± 4
Other	0.3 ± 0.1	0.5 ± 0.1	0.5 ± 0.1	1.5 ± 0.2	4 ± 1	76 ± 8	16 ± 2	15 ± 1

with their uncertainties, and adjusted to maximize the likelihood. The yields estimated with the background-only fit are reported in Table 5.4. While CR lbb -T is dominated by $t\bar{t}$ events, CR lbb -W is populated evenly by $t\bar{t}$ and $W + \text{jets}$ events, which causes the normalisation of the $t\bar{t}$ and $W + \text{jets}$ contributions to be negatively correlated after the fit. As a result, the uncertainties on individual background sources do not add up quadratically to the uncertainty on the total SM expectation. The normalization factors are found to be 1.03 ± 0.15 for $t\bar{t}$ and 0.79 ± 0.07 for $W + \text{jets}$, where the errors include statistical and systematic uncertainties.

To validate the background modelling, two validation regions (VR) are defined similarly to the SRs except for requiring $40 < m_{\text{T}}^W < 100$ GeV, and requiring $100 < m_{\text{CT}} < 160$ GeV for VR lbb -1 and $m_{\text{CT}} > 160$ GeV for VR lbb -2 as summarized in Table 5.3. The yields in the VRs are shown in Table 5.4 after the background-only fit, which does not use the data in the VRs to constrain the background. The data event yields are found to be consistent with background expectations. Figure 5.4 shows the distributions of m_{CT} , m_{T}^W , $n_{b\text{-jet}}$ and m_{bb} in various regions. The data agree well with the SM expectations in all distributions.

5.1.3.5 One lepton and two photons channel

5.1.3.5.a Event Selection

Events recorded with diphoton triggers are used in the one lepton and two photons channel. The transverse energy thresholds at trigger level for the most energetic (leading) and second most energetic (sub-leading) photons are 35 GeV and 25 GeV, respectively. In addition, events recorded with the single-lepton triggers used for the lepton + 2 b -jet channel are included. The event selection requires exactly one signal lepton (e or μ) and exactly two signal photons, with p_{T} thresholds of 15 GeV for electrons, 10 GeV for muons, and 40 (20) GeV for leading (sub-leading) photons. The isolation criteria for both electrons and muons are $E_{\text{T}}^{\text{cone}0.4}/p_{\text{T}} < 0.2$ and $p_{\text{T}}^{\text{cone}0.2}/p_{\text{T}} < 0.15$. Signal photons are required to satisfy $E_{\text{T}}^{\text{cone}0.4} < 6$ GeV and $p_{\text{T}}^{\text{cone}0.2} < 2.6$ GeV.

In this channel, a neural network algorithm, based on the momenta of the tracks associated to each vertex and the direction of flight of the photons, is used to select the primary vertex, similarly to the ATLAS SM $h \rightarrow \gamma\gamma$ analysis described in Ref. [191]. Signal muons must satisfy

TABLE 5.5: Selection requirements for the signal and validation regions of the one lepton and two photons channel.

	SR $\ell\gamma\gamma$ -1	SR $\ell\gamma\gamma$ -2	VR $\ell\gamma\gamma$ -1	VR $\ell\gamma\gamma$ -2
n_{lepton}	1	1	1	1
n_γ	2	2	2	2
E_T^{miss} [GeV]	> 40	> 40	< 40	—
$\Delta\phi(W, h)$	> 2.25	> 2.25	—	< 2.25
$m_T^{W\gamma^1}$ [GeV]	> 150	< 150	—	—
	and	or	—	—
$m_T^{W\gamma^2}$ [GeV]	> 80	< 80	—	—

$|d_0| < 1$ mm and $|z_0| < 10$ mm, with the impact parameters defined relative to the primary vertex.

The two largest background contributions are due to multi-jet and $Z\gamma$ production, with leptons or jets mis-reconstructed as photons. These background contributions are suppressed by requiring $E_T^{\text{miss}} > 40$ GeV.

The p_T of the $W \rightarrow \ell\nu$ system, reconstructed assuming background events with $p_T^\nu = E_T^{\text{miss}}$, is required to be back-to-back with the p_T of the $h \rightarrow \gamma\gamma$ candidate ($\Delta\phi(W, h) > 2.25$). Only events with a diphoton invariant mass $m_{\gamma\gamma}$ between 100 and 160 GeV are considered, and all such events are used in a signal plus background fit to the data, described in Sec. 5.1.3.5.b. Events in the sideband, outside the Higgs-mass window between 120 and 130 GeV, are included to constrain the non-Higgs background.

Selected events are split into two SRs with different expected signal sensitivities based on two variables $m_T^{W\gamma^1}$ and $m_T^{W\gamma^2}$, which are defined as

$$m_T^{W\gamma^i} = \sqrt{(m_T^W)^2 + 2E_T^W E_T^{\gamma^i} - 2\vec{p}_T^W \cdot \vec{p}_T^{\gamma^i}}, \quad (5.3)$$

where m_T^W , E_T^W and \vec{p}_T^W are the transverse mass, energy and momentum of the W candidate, and $E_T^{\gamma^i}$ and $\vec{p}_T^{\gamma^i}$ are the transverse energy and momentum of the i -th, p_T -ordered, photon. Including a photon in the transverse mass calculation provides a means to identify leptonically decaying W bosons in the presence of a final-state radiation photon. Events with $m_T^{W\gamma^1} > 150$ GeV and $m_T^{W\gamma^2} > 80$ GeV are classified into SR $\ell\gamma\gamma$ -1, and those with either $m_T^{W\gamma^1} < 150$ GeV or $m_T^{W\gamma^2} < 80$ GeV into SR $\ell\gamma\gamma$ -2. SR $\ell\gamma\gamma$ -1 provides the most sensitivity to the signal, while SR $\ell\gamma\gamma$ -2 assists in constraining systematic uncertainties.

Two overlapping validation regions are defined by inverting and relaxing the E_T^{miss} and $\Delta\phi(W, h)$ cuts relative to those of the signal regions. The first region VR $\ell\gamma\gamma$ -1 requires $E_T^{\text{miss}} < 40$ GeV and no cut on $\Delta\phi(W, h)$, and the second region VR $\ell\gamma\gamma$ -2 requires $\Delta\phi(W, h) < 2.25$ and no cut on E_T^{miss} . The signal and validation regions are summarized in Table 5.5.

The distributions in the Higgs window of the four kinematic variables used to define the SRs are shown in Fig. 5.5. For illustration purposes, the observed yield in the sideband region is shown for each distribution, scaled into the Higgs window by the relative widths of the sideband and Higgs window, $10 \text{ GeV} / 50 \text{ GeV} = 0.2$. Also shown, in each plot, is a simulation-based

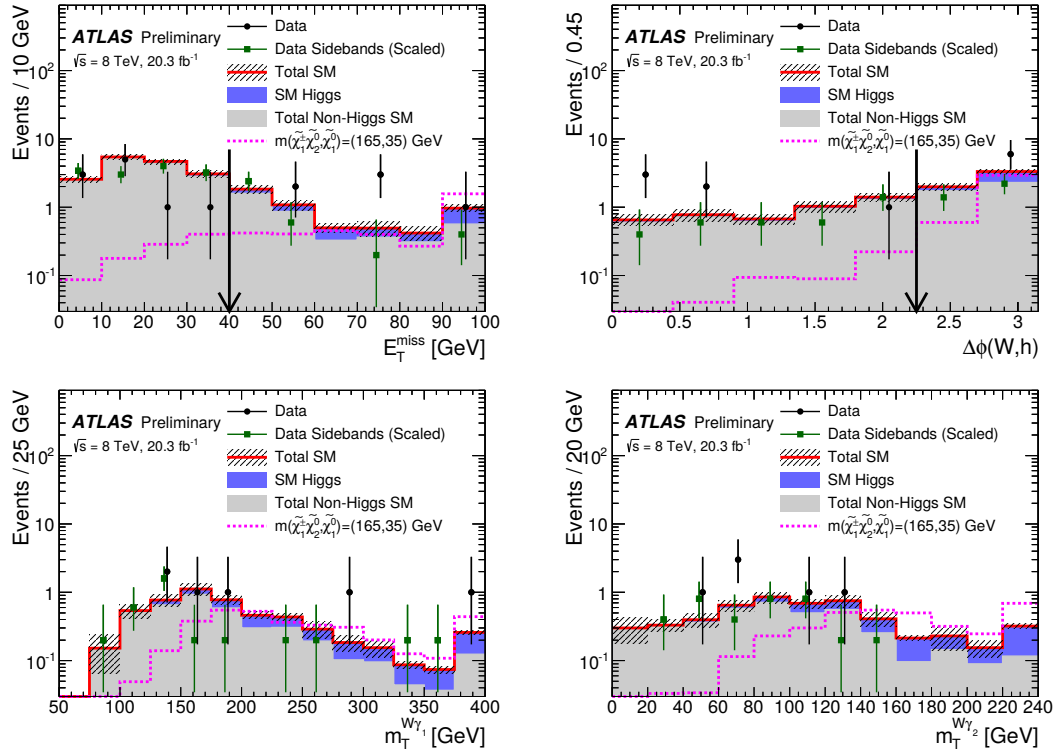


FIGURE 5.5: Distributions of E_T^{miss} , $\Delta\phi(W, h)$, $m_T^{W\gamma_1}$ and $m_T^{W\gamma_2}$ in the one lepton and two photons signal regions for the Higgs window ($120 < m_{\gamma\gamma} < 130$ GeV). The selections on E_T^{miss} and $\Delta\phi(W, h)$ have been removed for these distributions; their positions are indicated by arrows. The filled and hashed regions represent the yield and total uncertainties on the simulation-based background cross check. The contributions from non-Higgs backgrounds are scaled by $10 \text{ GeV} / 50 \text{ GeV} = 0.2$ from the $m_{\gamma\gamma}$ sideband ($100 < m_{\gamma\gamma} < 120$ GeV and $130 < m_{\gamma\gamma} < 160$ GeV) into the Higgs window. The rightmost bin in (a), (c), and (d) includes overflow. Scaled data in the sideband are shown as squares, while events in the Higgs window are shown as circles.

cross check of the background estimate. To reduce statistical uncertainties originating from the limited number of simulated events, the non-Higgs contributions are obtained in the Higgs sideband and scaled into the Higgs window by 0.2. The simulation-based prediction of the non-Higgs background is estimated from the $W/Z(\gamma, \gamma\gamma)+\text{jets}$ samples, after applying a data-driven correction for the probability of electrons or jets to be reconstructed as photons. A small contribution from backgrounds with jets reconstructed as leptons is determined by using the ‘fake factor’ method [192]. This simulation-based background estimate is only used as a cross check of the data sideband background estimate described below. It shows consistent results with the data estimate, but it is not used for limit setting.

5.1.3.5.b Background estimation

The contribution from background sources that do not contain a $h \rightarrow \gamma\gamma$ decay can be statistically separated by a template fit to the $m_{\gamma\gamma}$ distribution. A similar approach is followed as in Ref. [191]: the non-Higgs background is modeled as $\exp(-\alpha m_{\gamma\gamma})$, with the decay constant α as a free, positive parameter in the fit. Alternate functional models are used to evaluate the systematic uncertainty due to the choice of background modelling function. The $h \rightarrow \gamma\gamma$ template, used

TABLE 5.6: Event yields and SM expectation in the Higgs window of the lepton plus two photon channel ($120 < m_{\gamma\gamma} < 130$ GeV) after the background-only fit. The Higgs window is excluded from the fit in the two signal regions. The errors shown include statistical and systematic uncertainties.

	SR $l\gamma\gamma$ -1	SR $l\gamma\gamma$ -2	VR $l\gamma\gamma$ -1	VR $l\gamma\gamma$ -2
Observed events	1	5	30	26
SM expectation	1.6 ± 0.4	3.3 ± 0.8	30.2 ± 2.3	20.4 ± 1.9
Non-Higgs	0.6 ± 0.3	3.0 ± 0.8	29.2 ± 2.3	19.8 ± 1.9
Wh	0.85 ± 0.02	0.23 ± 0.01	0.71 ± 0.02	0.29 ± 0.01
Zh	0.04 ± 0.01	0.02 ± 0.01	0.14 ± 0.02	0.05 ± 0.01
$t\bar{t}h$	0.14 ± 0.01	0.02 ± 0.01	0.11 ± 0.01	0.25 ± 0.01

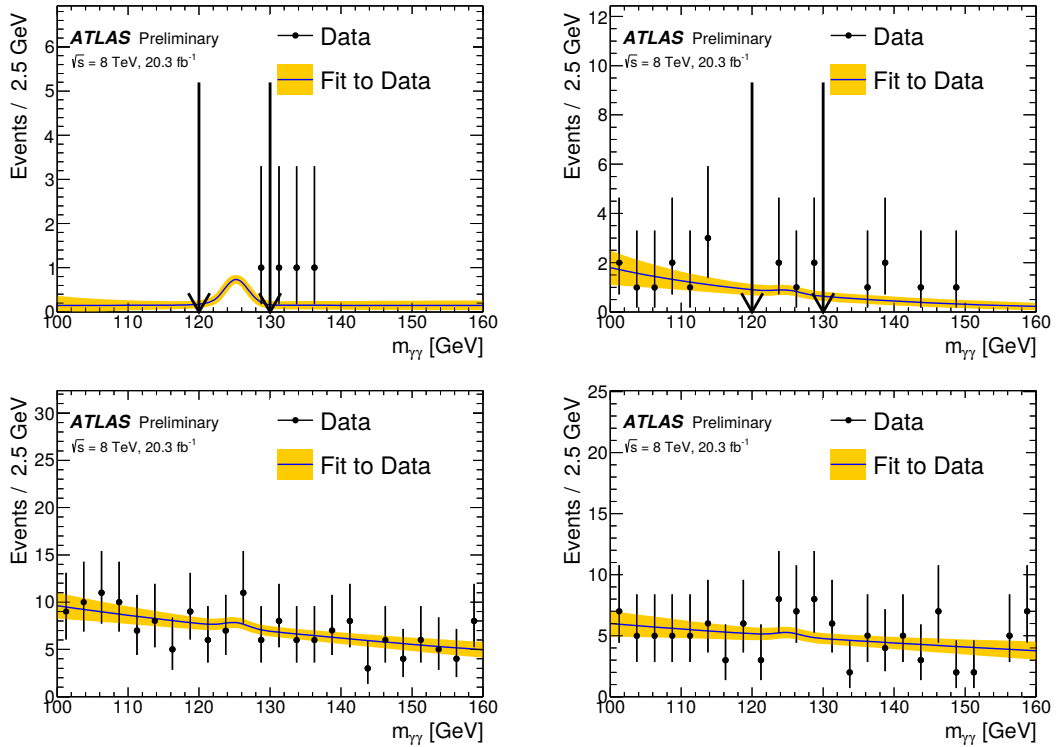


FIGURE 5.6: Results of the background-only fit to the $m_{\gamma\gamma}$ distribution in the one lepton and two photons signal and validation regions. The contributions from SM Higgs boson production are constrained to the MC prediction and associated systematic uncertainties. The band shows the systematic uncertainty in the fit. The fit is performed on events with $100 \text{ GeV} < m_{\gamma\gamma} < 160 \text{ GeV}$, with events in SR $l\gamma\gamma$ -1 or SR $l\gamma\gamma$ -2 in the Higgs window ($120 \text{ GeV} \leq m_{\gamma\gamma} \leq 130 \text{ GeV}$), indicated by the arrows, excluded from the fit.

for the Higgs background and signal, is defined by the sum of a Crystal Ball function [445] for the core of the distribution and a Gaussian function for the tails. This functional form follows the one used in the SM $h \rightarrow \gamma\gamma$ analysis [191], with the nominal values and uncertainties of the fit parameters determined by fits to the simulation in SR $\ell\gamma\gamma$ -1 and SR $\ell\gamma\gamma$ -2. The results of the fit to the simulation are used as an external constraint on the template during the fit to data. The width of the Gaussian core of the Crystal Ball quantifies the detector resolution and is determined in simulation to be approximately 3 GeV. This is comparable to the resolution found in the SM $h \rightarrow \gamma\gamma$ analysis [191].

Contributions from SM processes with a real Higgs boson decay are estimated by simulation and come primarily from Wh associated production, followed by $t\bar{t}h$ and Zh . Systematic uncertainties on the signal yield of these SM processes are discussed in Sec. 5.1.3.7. Figure 5.6 shows the background-only fits to the observed $m_{\gamma\gamma}$ distributions in the signal and validation regions, with the signal region Higgs window ($120 < m_{\gamma\gamma} < 130$ GeV) excluded from the fit. Table 5.6 summarizes the observed event yields in the Higgs window and the background estimates in the signal and validation regions. The errors are dominated by the statistical uncertainty due to the number of events in the $m_{\gamma\gamma}$ sidebands.

5.1.3.6 Same-sign dilepton channel

5.1.3.6.a Event Selection

Events recorded with a combination of dilepton triggers are used in the same-sign dilepton channel. The lowest unrescaled trigger p_T thresholds depend on the flavour of the leptons and are at most 25 GeV and 14 GeV for the leading and sub-leading lepton, respectively. The offline event selection requires two same-sign signal leptons (ee , $e\mu$ or $\mu\mu$) with $p_T > 30$ GeV and 20 GeV and no additional preselected lepton. The signal electrons must satisfy the ‘‘tight’’ identification criteria from Ref. [185], $|d_0|/\sigma_{d_0} < 3$, and $|z_0 \sin \theta| < 0.4$ mm. The signal muons must satisfy $|\eta| < 2.4$, $|d_0|/\sigma_{d_0} < 3$, and $|z_0 \sin \theta| < 1$ mm. The isolation criteria for electrons (muons) are $E_T^{\text{cone}0.3}/\min(p_T, 60 \text{ GeV}) < 0.13$ (0.14) and $p_T^{\text{cone}0.3}/\min(p_T, 60 \text{ GeV}) < 0.07$ (0.06). Events containing a hadronically decaying preselected τ lepton are rejected in order to avoid statistical overlap with the three-lepton final states [182].

Events are required to contain between one and three central ($|\eta| < 2.4$) jets with $p_T > 20$ GeV and $|\text{JVF}| > 0$ if $p_T < 50$ GeV. To reduce backgrounds with heavy-flavour decays, all the jets must fail the b -tagging criteria at the 80% efficiency operating point. There must be no forward ($2.4 < |\eta| < 4.9$) jet with $p_T > 30$ GeV.

The dominant background contributions in the $\ell^\pm\ell^\pm$ channel are due to SM diboson production (WZ and ZZ) leading to two ‘‘prompt’’ leptons and to events with ‘‘non-prompt’’ leptons (heavy-flavour decays, photon conversions and mis-identified jets). These backgrounds are suppressed with the tight identification criteria described above, and with the kinematic requirements summarized in Table 5.7. The requirements have been optimized separately for each lepton flavour combination (ee , $\mu\mu$, and $e\mu$), and for different numbers of reconstructed jets, leading to six signal regions.

TABLE 5.7: Selection requirements for the signal regions of the same-sign dilepton channel.

	SR ee -1	SR ee -2	SR $\mu\mu$ -1	SR $\mu\mu$ -2	SR $e\mu$ -1	SR $e\mu$ -2
Lepton flavours	ee	ee	$\mu\mu$	$\mu\mu$	$e\mu$	$e\mu$
n_{jet}	1	2 or 3	1	2 or 3	1	2 or 3
Leading lepton p_{T} [GeV]	> 30	> 30	> 30	> 30	> 30	> 30
Subleading lepton p_{T} [GeV]	> 20	> 20	> 20	> 30	> 30	> 30
$ m_{\ell\ell} - m_Z $ [GeV]	> 10	> 10	–	–	–	–
$\Delta\eta_{\ell\ell}$	–	–	< 1.5	< 1.5	< 1.5	< 1.5
$E_{\text{T}}^{\text{miss,rel}}$ [GeV]	> 55	> 30	–	–	–	–
m_{eff} [GeV]	> 200	–	> 200	> 200	> 200	> 200
$m_{\text{T}}^{\text{max}}$ [GeV]	–	> 110	> 110	–	> 110	> 110
$m_{\ell j}$ or $m_{\ell jj}$ [GeV]	< 90	< 120	< 90	< 120	< 90	< 120

The dilepton invariant mass $m_{\ell\ell}$ is required to differ by at least 10 GeV from the Z -boson mass for the ee channel, in which contamination due to electron charge mis-identification is significant.

The visible mass of the Higgs boson candidate is defined for the 1-jet signal regions as the invariant mass ($m_{\ell j}$) of the jet and the lepton that is closest to it in terms of ΔR , and for the two-or-three-jet signal regions as the invariant mass ($m_{\ell jj}$) of the two highest- p_{T} jets and the lepton that is closest to them as a system. In the signal regions, the cut $m_{\ell j} < 90$ GeV is required for SR $\ell\ell$ -1 and the cut $m_{\ell jj} < 120$ GeV for SR $\ell\ell$ -2.

Depending on the final state additional kinematic variables are used to further reduce the background. Requiring the pseudorapidity difference between the two leptons $\Delta\eta_{\ell\ell} < 1.5$ decreases the WZ and ZZ background. Requirements on $E_{\text{T}}^{\text{miss,rel}}$, defined as

$$E_{\text{T}}^{\text{miss,rel}} = \begin{cases} E_{\text{T}}^{\text{miss}} & \text{if } \Delta\phi > \pi/2, \\ E_{\text{T}}^{\text{miss}} \sin(\Delta\phi) & \text{if } \Delta\phi < \pi/2, \end{cases} \quad (5.4)$$

where $\Delta\phi$ is the azimuthal angle difference between $\vec{p}_{\text{T}}^{\text{miss}}$ and the nearest lepton or jet, reduce the $Z + \text{jets}$ and non-prompt lepton background in the ee channel. The $E_{\text{T}}^{\text{miss,rel}}$ is defined to reduce the impact on $E_{\text{T}}^{\text{miss}}$ of any potential mis-measurement, either from jets or from leptons. The scalar sum m_{eff} of the transverse energies of the leptons, jets and the missing transverse momentum is used to suppress the diboson background. Requiring $m_{\text{T}}^{\text{max}} > 110$ GeV, where $m_{\text{T}}^{\text{max}}$ is the larger of the two m_{T}^W values computed with one of the leptons and the missing transverse momentum, suppresses background events with one leptonically decaying W boson, whose transverse mass distribution has an end-point at m_W .

5.1.3.6.b Background estimation

The irreducible background in the same-sign dilepton channel is dominated by WZ and ZZ diboson productions, in which both vector bosons decay leptonically and one or two leptons do not satisfy the selection requirements, mostly the kinematic ones. These contributions are estimated from the simulation.

Background contributions due to non-prompt leptons are estimated with the matrix method. It takes advantage of the difference between the efficiencies for prompt and non-prompt leptons,

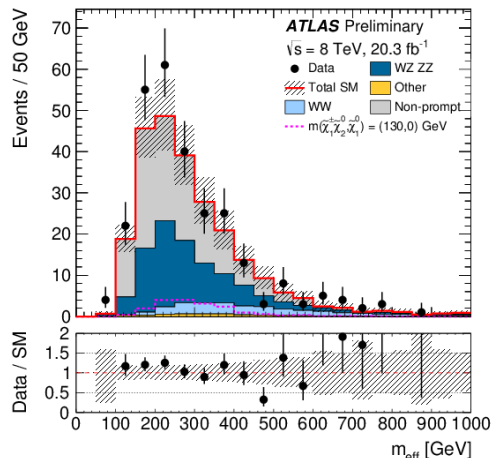


FIGURE 5.7: Distribution of m_{eff} in the validation region of the same-sign $e\mu$ channel. This validation region is defined by applying only the n_{jet} and p_{T} requirements from Table 5.7, and reversing the $m_{\ell j}$, $m_{\ell jj}$ criteria. The hashed regions represent the total uncertainties on the background estimates. The distribution of a signal hypothesis is also shown. The lower panel shows the ratio between data and the SM background prediction.

defined as the fractions of prompt and non-prompt preselected leptons, respectively, that pass the signal-lepton requirements. The number of events containing non-prompt leptons is obtained from these efficiencies and the observed number of events in each SR or VR using four categories of selection with preselected or signal leptons. The efficiencies for prompt and non-prompt leptons are derived, as a function of p_{T} and η , for each process leading to either prompt or non-prompt leptons using the truth information from simulated events. They are then corrected with simulation-to-data scale factors measured in control regions, as described in Ref. [422]. The contributions from each process leading to either prompt or non-prompt leptons are then used to compute a weighted-average efficiency, where the weight for each process is determined as its relative contribution to the number of preselected leptons in the region of interest.

Same-sign background events where the lepton charge is mis-measured are usually due to a hard bremsstrahlung photon with subsequent asymmetric pair production. The charge mis-measurement probability, which is negligible for muons, is measured in data as a function of electron p_{T} and $|\eta|$ using events from the $Z \rightarrow e^+e^-$ sample where the two electrons are reconstructed with the same sign. Such probability, which is below 1% for most of the p_{T} and η values, is then applied to the simulated opposite-sign ee and $e\mu$ pairs to estimate this background [177]. Although any process with the $e^\pm e^\mp$ or $e^\pm \mu^\mp$ final state can mimic the same-sign signature with charge mis-measurement, most of this background contribution is due to the production of $Z + \text{jets}$ events, amounting to less than 10% of the background yield in any of the $\ell^\pm \ell^\pm$ signal regions.

Estimates of non-prompt lepton and charge mis-measurement background are tested in validation regions obtained by applying only the n_{jet} and p_{T} requirements from Table 5.7 and requiring $m_{\ell j} > 90$ GeV or $m_{\ell jj} > 120$ GeV. The number of observed events agrees with the expected background in all validation regions. Figure 5.7 shows the distribution of m_{eff} in the validation region of the same-sign $e\mu$ channel. The number of observed and expected events in each signal region is reported in Table 5.8. Figure 5.8 shows the m_{eff} , $m_{\text{T}}^{\text{max}}$, $m_{\ell j}$, and $m_{\ell jj}$ distributions in

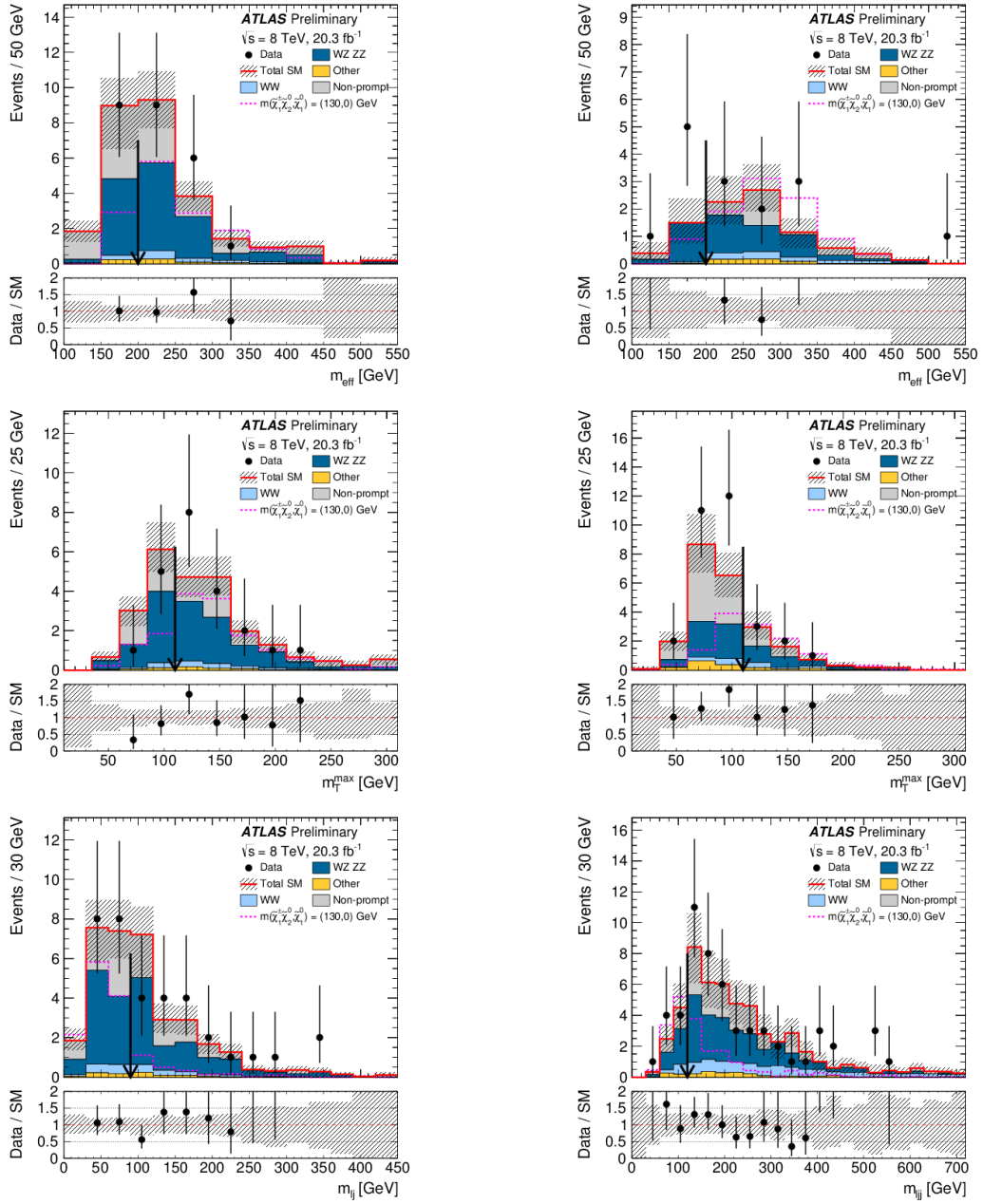


FIGURE 5.8: Distributions of m_{eff} , $m_{\text{T}}^{\text{max}}$, $m_{\ell j}$ and $m_{\ell j j}$ for the same-sign dilepton channel in the signal regions with 1-jet (left) and 2-or-3-jet (right). $\text{SR}_{\ell\ell-1}$ is the sum of SR_{ee-1} , $\text{SR}_{\mu\mu-1}$, and $\text{SR}_{\mu\mu-1}$; $\text{SR}_{\ell\ell-2}$ is the sum of SR_{ee-2} , $\text{SR}_{\mu\mu-2}$, and $\text{SR}_{\mu\mu-2}$. All selection criteria are applied, except for the one on the variable being shown. The value of the cut, which may not be applied in all flavor channels, is indicated by the vertical arrow. The hashed regions represent the total uncertainties on the background estimates. The distributions of a signal hypothesis are also shown. The lower panel shows the ratio between data and the SM background prediction. The rightmost bin of each plot includes overflow.

the same-sign dilepton signal regions. No significant excess is observed over the SM background expectations in any channel.

5.1.3.7 Systematic uncertainties

Table 5.9 summarizes the contributions of the dominant sources of systematic uncertainties on the total expected background yields in the six signal regions.

For the one lepton and two b -jets channel, theoretical uncertainties of the $t\bar{t}$ and single-top background estimates are the most important. They are evaluated by comparing different generators (POWHEG, MC@NLO and ACERMC) and parton shower algorithms (PYTHIA and HERWIG),

TABLE 5.8: Event yields and SM expectation in the same-sign dilepton channel signal regions. The WW background includes both $W^\pm W^\pm$ and $W^\pm W^\mp$ production, the latter due to electron charge mis-measurement. “Other” background includes $t\bar{t}$, single top, Z + jets, Zh and Wh production. The errors shown include statistical and systematic uncertainties.

	SRee-1	SRee-2	SR $\mu\mu$ -1	SR $\mu\mu$ -2	SRe μ -1	SRe μ -2
Observed events	2	1	6	4	8	4
SM expectation	6.0 \pm 1.2	2.8 \pm 0.8	3.8 \pm 0.9	2.6 \pm 1.1	7.0 \pm 1.3	1.9 \pm 0.7
Non-prompt	3.4 \pm 1.0	1.6 \pm 0.5	0.00 \pm 0.20	0.3 \pm 0.4	3.0 \pm 0.9	0.48 \pm 0.28
WZ, ZZ	2.2 \pm 0.6	0.7 \pm 0.4	3.4 \pm 0.8	1.8 \pm 0.9	3.3 \pm 0.8	1.1 \pm 0.5
WW	0.33 \pm 0.31	0.22 \pm 0.23	0.24 \pm 0.29	0.4 \pm 0.5	0.4 \pm 0.4	0.23 \pm 0.26
Other	0.13 \pm 0.13	0.31 \pm 0.31	0.14 \pm 0.14	0.06 \pm 0.06	0.19 \pm 0.17	0.09 \pm 0.08

TABLE 5.9: Summary of the statistical and of the main systematic uncertainties on the background estimates, expressed in per cent of the total background yields in each signal region. Uncertainties that are not considered for a particular channel are indicated by a “–”. Note that the individual uncertainties can be correlated, and do not necessarily add up quadratically to the total background uncertainty.

	SR lbb -1	SR lbb -2	SR $l\gamma\gamma$ -1	SR $l\gamma\gamma$ -2	SR ll -1	SR ll -2
Number of background events	6.0 \pm 1.3	2.8 \pm 0.8	1.6 \pm 0.4	3.3 \pm 0.8	16.8 \pm 2.8	7.3 \pm 1.5
Statistical	9	7	22	23	7	7
Modelling $t\bar{t}$	23	25	–	–	< 1	< 1
Modelling single top	5	11	–	–	< 1	< 1
Modelling $Wh, Zh, t\bar{t}h$	–	–	3	1	–	–
Modelling WZ	–	–	–	–	11	22
Electron reconstruction	3	3	1	1	< 1	< 1
Muon reconstruction	1	1	< 1	< 1	1	< 1
Photon reconstruction	–	–	4	5	–	–
Jet energy scale and resolution	6	14	1	3	2	11
b -jet identification	6	4	–	–	–	–
m_{bb} shape	8	12	–	–	–	–
Background $m_{\gamma\gamma}$ model	–	–	5	7	–	–
Non-prompt estimate	–	–	–	–	10	11
Charge mis-measurement estimate	–	–	–	–	2	3
Other sources	4	5	< 1	2	2	2

varying the QCD scales up and down by a factor of two, and taking the envelope of the background variations when using different PDF sets. Statistical uncertainties from the data in the CRs result in uncertainties on the normalization of the $t\bar{t}$ and $W + \text{jets}$ backgrounds, while the limited number of simulated events yields uncertainty on the shape of the background m_{bb} distributions. Experimental systematic uncertainties are dominated by the uncertainties on the jet energy scale [176] and resolution [193], that are derived from a combination of test-beam data and in-situ measurements, and followed by the uncertainty on the b -jet identification [194].

For the one lepton and two photons channel, the background uncertainties are dominated by the data statistics in the $m_{\gamma\gamma}$ sidebands. The only source of systematic uncertainty on the non-Higgs background estimate is the choice of the $m_{\gamma\gamma}$ model. The systematic uncertainties on the Higgs background estimates are dominated by the theoretical uncertainties on the Wh , Zh , and $t\bar{t}h$ production cross sections and the photon reconstruction. The main theoretical uncertainties arise from QCD scale variations and from parton distribution functions [162]. Scale variation uncertainties on the modelling of the Higgs boson production are evaluated by reweighting the Higgs boson p_T distribution. The experimental systematic uncertainty from photon reconstruction is determined with the tag-and-probe method using radiative Z decays [195].

For the same-sign dilepton channel, the two main sources of systematic uncertainties are related to the non-prompt lepton estimate, and to the modelling of the WZ background. The uncertainty on the non-prompt estimate originates mainly from the limited accuracy of the simulation-to-data scale factors, and on the production rate of non-prompt leptons, in particular their η dependence. The uncertainty on the WZ background modelling is determined using a same-sign, WZ -enriched sample used to validate the SHERPA prediction. This validation sample is selected by requiring three leptons, two of which must have same flavour, opposite sign, $|m_{\ell\ell} - m_Z| < 10 \text{ GeV}$, and then considering only the highest- p_T same-sign pair. None of the other requirements from Table 5.7 are applied, except for the lepton p_T and n_{jet} selections.

5.1.3.8 Results and interpretations

The event yields observed in data are consistent with the Standard Model expectations within uncertainties in all signal regions. The results are used to set exclusion limits with the frequentist

TABLE 5.10: From left to right, observed 95% CL_S upper limits ($\langle\sigma_{\text{vis}}\rangle_{\text{obs}}^{95}$) of the visible cross sections, the observed (S_{obs}^{95}) and expected (S_{exp}^{95}) 95% CL_S upper limits on the number of signal events with $\pm 1\sigma$ excursions of the expectation, the observed confidence level (CL_B) of the background-only hypothesis, and the discovery p -value (p_0), truncated at 0.5.

	$\langle\sigma_{\text{vis}}\rangle_{\text{obs}}^{95}[\text{fb}]$	S_{obs}^{95}	S_{exp}^{95}	CL_B	p_0
SR lbb -1	0.26	5.3	$6.3^{+3.4}_{-2.0}$	0.28	0.50
SR lbb -2	0.27	5.5	$5.1^{+2.6}_{-1.4}$	0.56	0.43
SR $l\gamma\gamma$ -1	0.18	3.6	$4.1^{+2.0}_{-0.7}$	0.25	0.50
SR $l\gamma\gamma$ -2	0.34	7.0	$5.9^{+2.0}_{-1.2}$	0.75	0.19
SR ll -1	0.51	10.4	$10.9^{+3.8}_{-3.1}$	0.51	0.50
SR ll -2	0.51	10.3	$8.1^{+3.3}_{-1.5}$	0.72	0.32

hypothesis tests based on the profile log likelihood ratio test statistic and approximated with the asymptotic formulae [196].

Exclusion upper limits at 95% CL on the number of beyond-the-SM (BSM) signal events, S , for each SR are derived using the CL_S prescription [197], assuming no signal yield in other signal and control regions. Normalizing these by the integrated luminosity of the data sample, they can be interpreted as upper limits on the visible BSM cross section, $\sigma_{\text{vis}} = \sigma \times A \times \epsilon$, where σ is the production cross section for the BSM signal, A is the acceptance defined by the fraction of events passing the geometric and kinematic selections at particle level, and ϵ is the detector reconstruction, identification and trigger efficiency.

Table 5.10 summarizes, for each SR, the observed 95% CL upper limits ($(\sigma_{\text{vis}})_{\text{obs}}^{95}$) of the visible cross section, the observed (S_{obs}^{95}) and expected (S_{exp}^{95}) 95% CL upper limits on the number of signal events with $\pm 1\sigma$ excursions of the expectation, the observed confidence level (CL_B) of the background-only hypothesis, and the discovery p -value (p_0), truncated at 0.5.

The obtained results are also used to set exclusion limits on the common mass of the $\tilde{\chi}_1^\pm$ and $\tilde{\chi}_2^0$ for various assumptions of the $\tilde{\chi}_1^0$ mass in the simplified model of $pp \rightarrow \tilde{\chi}_1^\pm \tilde{\chi}_2^0$ followed by $\tilde{\chi}_1^\pm \rightarrow W^\pm \tilde{\chi}_1^0$ and $\tilde{\chi}_2^0 \rightarrow h \tilde{\chi}_1^0$. In this hypothesis test, all the CRs and SRs of the considered

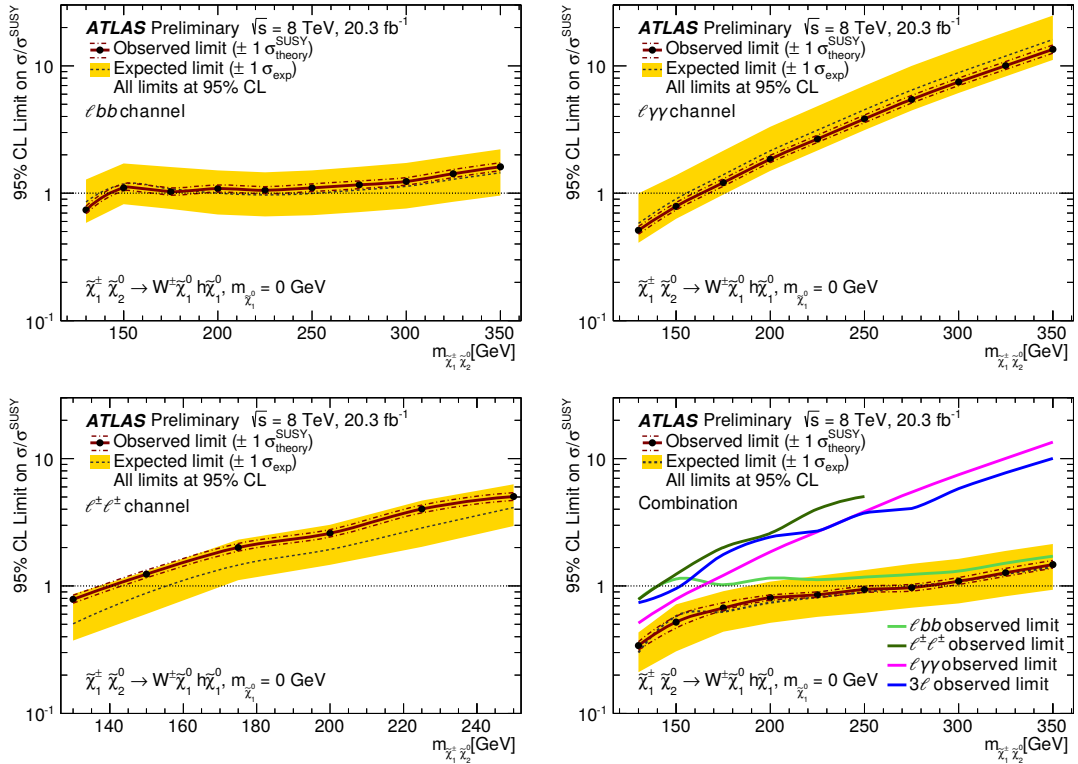


FIGURE 5.9: Observed (solid line) and expected (dashed line) 95% CL upper limits of the cross section normalized by the simplified model prediction for $m_{\tilde{\chi}_1^0} = 0$. The combination in (d) is obtained using the result from the ATLAS three-lepton search [182] in addition to the three channels reported in this note. The $\pm 1\sigma$ lines around the observed limit represent the results obtained when changing the nominal signal cross section up or down by the $\pm 1\sigma$ theoretical uncertainty. The solid band around the expected limit represents the $\pm 1\sigma$ uncertainty band where all uncertainties, except those on the signal cross sections, are considered.

channels are fitted simultaneously, taking into account correlated experimental and theoretical systematic uncertainties as common nuisance parameters. The signal contamination in the CRs is accounted for in the fit, where a single non-negative normalization parameter is used to describe the signal model in all channels.

Systematic uncertainties on the signal expectations stemming from detector effects are included in the fit in the same way as for the backgrounds. Theoretical systematic uncertainties on the signal cross section described in Sec. 5.1.3.2 are not included directly in the fit. In all resulting exclusions the dashed (black) and solid (red) lines show the 95% CL expected and observed limits, respectively, including all uncertainties except for the theoretical signal cross section uncertainty. The (yellow) bands around the expected limits show the $\pm 1\sigma$ expectations. The dotted $\pm 1\sigma$ (red) lines around the observed limit represent the results obtained when changing

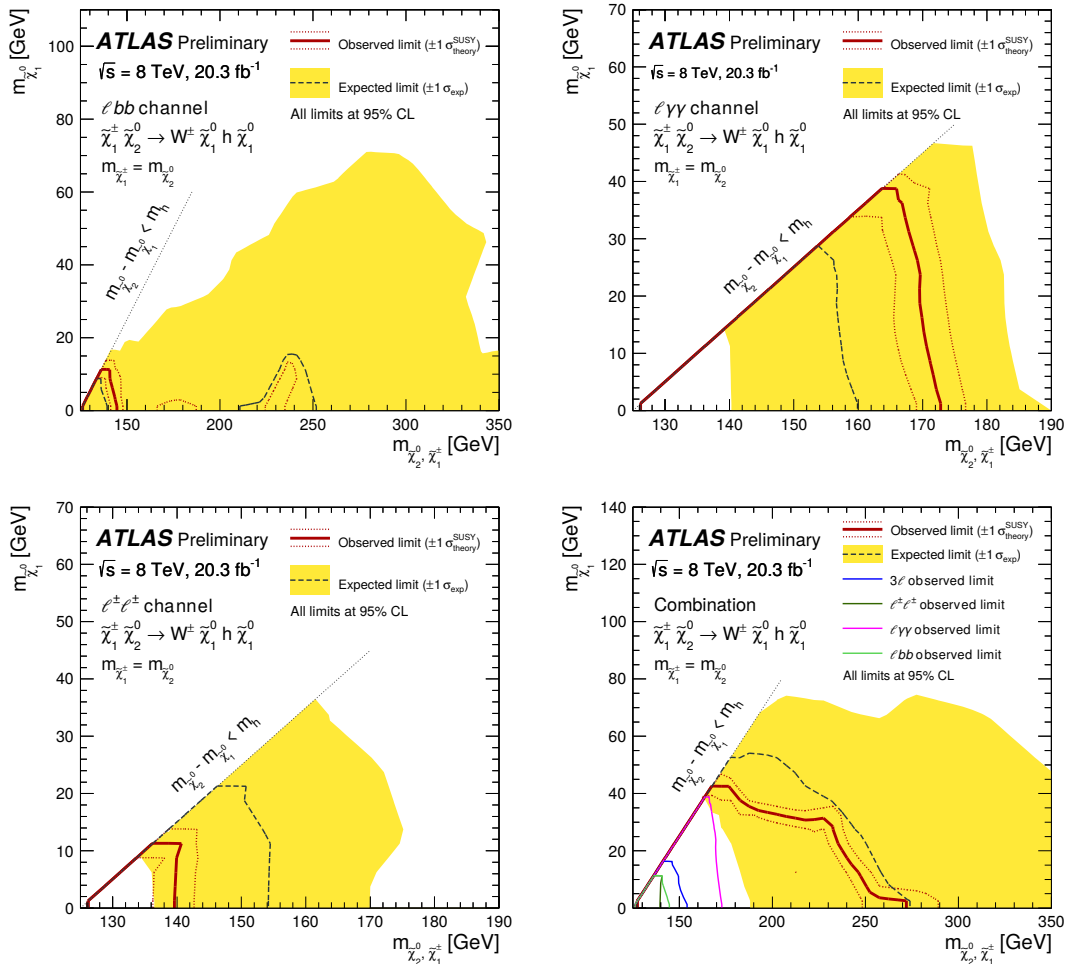


FIGURE 5.10: Observed (solid line) and expected (dashed line) 95% CL exclusion regions in the simplified model. The combination in (d) is obtained using the result from the ATLAS three-lepton search [182] in addition to the three channels reported in this note. The $\pm 1\sigma$ lines around the observed limit represent the results obtained when changing the nominal signal cross section up or down by the $\pm 1\sigma$ theoretical uncertainty. The solid band around the expected limit shows the $\pm 1\sigma$ uncertainty band where all uncertainties, except those on the signal cross sections, are considered.

the nominal signal cross section up or down by its theoretical uncertainties, and the limits are reported referring to the -1σ variation.

Figure 5.9 shows the 95% CL upper limits of the signal cross section normalized by the simplified model prediction as a function of $m_{\tilde{\chi}_2^0, \tilde{\chi}_1^\pm}$ for $m_{\tilde{\chi}_1^0} = 0$. The sensitivity of the individual one lepton and two b -jets, one lepton and two photons, and same-sign dilepton channels is illustrated on Figs. 5.9(a–c), respectively. The corresponding limit combining all channels and the ATLAS three-lepton search is shown in Fig. 5.9(d). For $m_{\tilde{\chi}_2^0, \tilde{\chi}_1^\pm} > 250$ GeV the same-sign dilepton channel is not considered. In Fig. 5.9(a), the expected exclusion region below $m_{\tilde{\chi}_2^0, \tilde{\chi}_1^\pm} = 140$ GeV is largely due to SR lbb -1 that targets models with small mass splitting between the neutralinos, while the expected exclusion region around $m_{\tilde{\chi}_2^0, \tilde{\chi}_1^\pm} = 240$ GeV is driven by SR lbb -2 designed for larger mass splittings. The upper limit shows slow variation with increasing $m_{\tilde{\chi}_2^0, \tilde{\chi}_1^\pm}$ as the acceptance of SR lbb -2 increases and compensates the decrease of the production cross section. Figure 5.9(d) shows that in the $m_{\tilde{\chi}_2^0, \tilde{\chi}_1^\pm} < 170$ GeV range all channels show similar sensitivity, while for $m_{\tilde{\chi}_2^0, \tilde{\chi}_1^\pm} > 170$ GeV the one lepton and two b -jets channel is the dominant one. Nevertheless, the contribution from the other channels to the combination is important to extend the excluded range significantly compared to Fig. 5.9(a).

Figures 5.10(a–c) show the 95% CL exclusion regions in the $(m_{\tilde{\chi}_2^0, \tilde{\chi}_1^\pm}, m_{\tilde{\chi}_1^0})$ mass plane of the simplified model obtained from the individual one lepton and two b -jets, one lepton and two photons, and same-sign dilepton signal regions, respectively. Figure 5.10(d) shows the corresponding exclusion region obtained by combining the three channels described in this note with the ATLAS three-lepton search, which by itself excludes $m_{\tilde{\chi}_2^0, \tilde{\chi}_1^\pm}$ up to 160 GeV for $m_{\tilde{\chi}_1^0} = 0$ GeV as seen in Fig. 5.10(d). The combination of these four independent searches improves the sensitivity significantly, and the 95% CL exclusion region for $m_{\tilde{\chi}_1^0} = 0$ is extended to 250 GeV. The wide uncertainty bands of the expected limits in Fig. 5.10 are due to the slow variation of the sensitivity with increasing $m_{\tilde{\chi}_2^0, \tilde{\chi}_1^\pm}$ and $m_{\tilde{\chi}_1^0}$, as can also be seen in Fig. 5.9.

5.1.3.9 Conclusions

A search for the direct pair production of charginos and neutralinos $pp \rightarrow \tilde{\chi}_1^\pm \tilde{\chi}_2^0$ followed by $\tilde{\chi}^\pm \rightarrow \tilde{\chi}_1^0(W^\pm \rightarrow \ell^\pm \nu)$ and $\tilde{\chi}_2^0 \rightarrow \tilde{\chi}_1^0(h \rightarrow bb/\gamma\gamma/\ell^\pm \nu qq)$ has been performed using 20.3 fb $^{-1}$ of $\sqrt{s} = 8$ TeV proton–proton collision data delivered by the Large Hadron Collider and recorded with the ATLAS detector. Three final state signatures are considered: one lepton and two b -jets, one lepton and two photons, and two same-sign leptons, each associated with missing transverse momentum. Observations are consistent with the Standard Model expectations. Limits are set in a simplified model, combining these results with the three-lepton search presented in Ref. [182]. For the simplified model, common masses of $\tilde{\chi}_1^\pm$ and $\tilde{\chi}_2^0$ are excluded up to 250 GeV for a massless $\tilde{\chi}_1^0$.

In this sub-section, I'll describe a novel method for indirect mass reconstruction of some particles produced at the LHC via charged-current processes.

5.1.4 New Method to Measure the Mass of a Chargino-Neutralino Pair

A New Method for Indirect Mass Measurements using the Integral Charge Asymmetry at the LHC

G. Steve Muanza, Thomas Serre

Aix Marseille Université, CNRS/IN2P3, CPPM UMR 7346, 13288, Marseille, France

Abstract

Processes producing a charged final state at the LHC have a positive or null integral charge asymmetry. We propose a novel method for an indirect measurement of the mass of these final states based upon the process integral charge asymmetry. We present this method in three stages. Firstly, the theoretical prediction of the integral charge asymmetry and its related uncertainties are studied through parton level cross sections calculations. Secondly, the experimental extraction of the integral charge asymmetry of a given signal, in the presence of some background, is performed using particle level simulations. Process dependent templates enable to convert the measured integral charge asymmetry into an estimated mass of the charged final state. Thirdly, a combination of the experimental and the theoretical uncertainties determines the full uncertainty of the indirect mass measurement.

This new method applies to all charged current processes at the LHC. In this article, we demonstrate its effectiveness at extracting the mass of the W boson, as a first step, and the sum of the masses of a chargino and a neutralino in case these supersymmetric particles are produced by pair, as a second step.

5.1.4.1 Introduction

Contrarily to most of the previous high energy particle colliders, the LHC is a charge asymmetric machine. For charged final states ², denoted FS^\pm , the integral charge asymmetry, denoted A_C ,

²We defined these as event topologies containing an odd number of high p_T charged and isolated leptons within the fiducial volume of the detector.

is defined by

$$A_C = \frac{N(FS^+) - N(FS^-)}{N(FS^+) + N(FS^-)} \quad (5.5)$$

where $N(FS^+)$ and $N(FS^-)$ represent respectively the number of events bearing a positive and a negative charge in the FS.

For a FS^\pm produced at the LHC in $p + p$ collisions, this quantity is positive or null, whilst it is always compatible with zero for a FS^\pm produced at the TEVATRON in $p + \bar{p}$ collisions.

To illustrate the A_C observable, let's consider the Drell-Yan production of W^\pm bosons in $p + p$ collisions. It is obvious for this simple $2 \rightarrow 2$ s-channel process that more W^+ than W^- are produced. Indeed, denoting y_W the rapidity of the W boson, the corresponding range of the Björken x's: $x_{1,2} = \frac{M_{W^\pm}}{\sqrt{s}} \times e^{\pm y_W}$, probes the charge asymmetric valence parton densities within the proton. This results in having more $U + \bar{D} \rightarrow W^+$ than $\bar{U} + D \rightarrow W^-$ configurations in the initial state (IS). Here U and D collectively and respectively represent the up and the down quarks.

In the latter case the dominant contribution to A_C comes from the difference in rate between the $u + \bar{d}$ and the $d + \bar{u}$ quark currents in the IS. Using the usual notation $f(x, Q^2)$ for the parton density functions (PDF) and within the leading order (LO) approximation, this can be expressed as:

$$A_C \approx \frac{u(x_{1,2}, M_W^2) \bar{d}(x_{2,1}, M_W^2) - \bar{u}(x_{1,2}, M_W^2) d(x_{2,1}, M_W^2)}{u(x_{1,2}, M_W^2) \bar{d}(x_{2,1}, M_W^2) + \bar{u}(x_{1,2}, M_W^2) d(x_{2,1}, M_W^2)} \quad (5.6)$$

where the squared four-momentum transfer Q^2 is set to M_W^2 .

From equation 5.6, we can see that the Q^2 evolution of the parton density functions (PDFs) govern the Q^2 evolution of A_C . The former are known, up-to the NNLO in QCD, as solutions of the DGLAP equations [238]. One could therefore think of using an analytical functional form to relate A_C to the squared mass of the s-channel propagator, here M_W^2 . However there are additional contributions to the W^\pm inclusive production. At the Born level, some come from other flavour combinations in the IS of the s-channel, and some come from the u and the t-channels. On top of this, there are higher order corrections. These extra contributions render the analytical expression of the Q^2 dependence of A_C much more complicated. Therefore we choose to build process-dependent numerical mass template curves for A_C by varying M_{FS^\pm} . These mass templates constitute inclusive and flexible tools into which all the above-mentioned contributions to A_C can be incorporated, they can very easily be built within restricted domain of the signal phase space imposed by kinematic cuts.

The A_C for the $W^\pm \rightarrow \ell^\pm \nu$ production at the LHC is large enough to be measured and it has relatively small systematic uncertainties since it's a ratio of cross sections. The differential charge asymmetry of this process in $p + p$ collisions have indeed been measured by the ATLAS [239], the CMS [285] [286] and the LHCb [242] experiments [243] for the first times in their 2011 datasets.

In this article we exploit the A_C to set a new type of constraint on the mass of the charged FS^\pm as initially proposed in [417][247].

We'll separate the study into two parts. The first one, in section 2, is dedicated to present in full length the method of indirect mass measurement that we propose on a known Standard Model (SM) process. We choose the $W^\pm \rightarrow \ell^\pm + \cancel{E}_T$ inclusive production at the LHC to serve as a test bench.

In the second part, in section 3, we shall repeat the method on a "Beyond the Standard Model" (BSM) process. We choose a SUSY search process of high interest, namely $\tilde{\chi}_1^\pm + \tilde{\chi}_2^0 \rightarrow 3\ell^\pm + \cancel{E}_T$.

For both the SM and the BSM processes, we obviously tag the sign of the FS by choosing a decay into one (or three) charged lepton(s) for which the sign is experimentally easily accessible.

It's obvious that for these two physics cases other mass reconstruction methods exist. These standard mass reconstruction techniques are all based on the kinematics of the FS. For the $W^\pm \rightarrow \ell^\pm + \cancel{E}_T$ process mass templates based upon the transverse mass allow to extract M_{W^\pm} with an excellent precision that the new technique proposed here cannot match. In contrast, for the $\tilde{\chi}_1^\pm + \tilde{\chi}_2^0 \rightarrow 3\ell^\pm + \cancel{E}_T$ process, even if astute extensions of the transverse mass enable to accurately measure some mass differences, no standard techniques is able to measure accurately the mass of the charged FS: $M_{FS^\pm} = M(\tilde{\chi}_1^\pm) + M(\tilde{\chi}_2^0)$.

Therefore this new mass reconstruction technique should not be viewed as an alternative to the standard techniques but rather as an unmined complement to them. In a few cases, especially where many FS particles escape detection, this new technique can be more accurate than the standard ones. It also has the advantage of being almost model independent.

For each signal process we sub-divide the method into four steps that are described in four sub-sections. In the first sub-sections 5.1.4.2.a and 5.1.4.3.a, we start by deriving the theoretical A_C template curves at the parton level.

In the second sub-sections 5.1.4.2.b and 5.1.4.3.b, we place ourselves in the situation of an experimental measurement of the A_C of the signal in the presence of some background. For that we generate samples of Monte Carlo (MC) events that we reconstruct using a fast simulation of the response of the ATLAS detector. This enables to account for the bias of the signal A_C induced by the event selection. In addition we can quantify the bias of A_C due to the residual contribution of some background processes passing this event selection.

Then, in the third sub-sections 5.1.4.2.c and 5.1.4.3.c, we convert the measured A_C into an estimated M_{FS} using fitted experimental A_C template curves that account for all the experimental uncertainties.

In the fourth sub-sections 5.1.4.2.d and 5.1.4.3.d, we combine the theoretical and the experimental uncertainties on the signal A_C to derive the full uncertainty of the indirect mass measurement. The conclusions are presented in section 5.1.4.4 and the prospects in section 5.1.4.5.

Note that we'll always express the integral charge asymmetry in % and the mass of the charged final state in GeV throughout this article. The uncertainty on the integral charge asymmetry

δA_C will also be expressed in % but will always represent an absolute uncertainty as opposed to a relative uncertainty with respect to A_C .

5.1.4.2 Inclusive Production of $W^\pm \rightarrow \ell^\pm \nu$

5.1.4.2.a Theoretical Prediction of $A_C(W^\pm \rightarrow \ell^\pm \nu)$

In this section we calculate separately the cross sections of the "signed processes", i.e. the cross sections of the positive and negative FS: $\sigma^+ = \sigma(p + p \rightarrow W^+ \rightarrow \ell^+ \nu)$ and $\sigma^- = \sigma(p + p \rightarrow W^- \rightarrow \ell^- \bar{\nu})$. The process integral charge asymmetry therefore writes:

$$A_C = \frac{\sigma^+ - \sigma^-}{\sigma^+ + \sigma^-} \quad (5.7)$$

5.3.4.2.a. 1). Sources of Theoretical Uncertainties on A_C

Since these cross sections integration are numerical rather than analytical, they each have an associated statistical uncertainty $\delta\sigma_{Stat}^\pm$ due to the finite sampling of the process phase space. Even though these are relatively small we explicitly include them and we calculate the resulting statistical uncertainty on the process integral charge asymmetry: $\delta(A_C)_{Stat}$ for which we treat $\delta\sigma_{Stat}^+$ and $\delta\sigma_{Stat}^-$ as uncorrelated uncertainties. Hence:

$$\delta(A_C)_{Stat} = \frac{2}{(\sigma^+ + \sigma^-)^2} \sqrt{(\sigma^- \cdot \delta\sigma_{Stat}^+)^2 + (\sigma^+ \cdot \delta\sigma_{Stat}^-)^2} \quad (5.8)$$

For each cross section calculation we choose the central Parton Density Function (PDF) from a PDF set (or just the single PDF when there's no associated uncertainty set). Whenever we use a PDF set, it contains $2N_{PDF}$ uncertainty PDFs on top of the central PDF fit, the PDF uncertainty is calculated as proposed in [259]:

$$\begin{cases} \delta(A_C)_{PDF}^{Up} = \sqrt{\sum_{i=1}^{N_{PDF}} (Max[A_C(i)^{up} - A_C(0), A_C(i)^{down} - A_C(0), 0])^2} \\ \delta(A_C)_{PDF}^{Down} = \sqrt{\sum_{i=1}^{N_{PDF}} (Max[A_C(0) - A_C(i)^{up}, A_C(0) - A_C(i)^{down}, 0])^2} \end{cases} \quad (5.9)$$

where $A_C(0)$, $A_C(i)^{up}$, and $A_C(i)^{down}$ represent the integral charge asymmetries calculated with σ_0 , σ_i^{up} , and σ_i^{down} , respectively. σ_0 represents the cross section calculated with the central PDF fit. σ_i^{up} represent the N_{PDF} upward uncertainty PDFs such that generally $\sigma_i^{up} > \sigma_0$, and σ_i^{down} represent the N_{PDF} downward uncertainty PDFs such that generally $\sigma_i^{down} < \sigma_0$.

We choose the QCD renormalization and factorization scales: $\mu_R = \mu_F = \mu_0$ to be equal, and we choose a process dependent dynamical option to adjust the value of μ_0 to the actual kinematics event by event. The scale uncertainty is evaluated using the usual factors 1/2 and 2 to calculate variations with respect to the central value μ_0 :

$$\begin{cases} \delta(A_C)_{Scale}^{Up} = A_C(\mu_0/2) - A_C(\mu_0) \\ \delta(A_C)_{Scale}^{Down} = A_C(2\mu_0) - A_C(\mu_0) \end{cases} \quad (5.10)$$

The total theoretical uncertainty is defined as the sum in quadrature of the 3 sources:

$$\begin{cases} \delta(A_C)_{Total}^{Up} = \sqrt{[\delta(A_C)_{PDF}^{Up}]^2 + [\delta(A_C)_{Scale}^{Up}]^2 + [\delta(A_C)_{Stat}]^2} \\ \delta(A_C)_{Total}^{Down} = \sqrt{[\delta(A_C)_{PDF}^{Down}]^2 + [\delta(A_C)_{Scale}^{Down}]^2 + [\delta(A_C)_{Stat}]^2} \end{cases} \quad (5.11)$$

5.3.4.2.a. 2). Setup and Tools for the Computation of A_C

We calculate the $\sigma^+ = \sigma(p + p \rightarrow W^+ \rightarrow \ell^+ \nu)$ and $\sigma^- = \sigma(p + p \rightarrow W^- \rightarrow \ell^- \bar{\nu})$ cross sections and their uncertainties at $\sqrt{s} = 7$ TeV using MCFM v5.8 [270][271][272]. We include both the $W^\pm + 0Lp$ and the $W^\pm + 1Lp$ matrix elements (ME) in the calculation in order to have a better representation of the W^\pm inclusive production (the notation "Lp" stands for "light parton", i.e. u/d/s quarks or gluons). We set the QCD scales as $\mu_R = \mu_F = \mu_0 = \sqrt{M^2(W^\pm) + p_T^2(W^\pm)}$ and we run the calculation at the QCD leading order (LO) and next-to-leading order (NLO). For both the phase space pre-sampling and the actual cross section integration, we run 10 times 20,000 sweeps of VEGAS [248]. We impose the following parton level cuts: $M(\ell^\pm \nu) > 10$ GeV, $|\eta(\ell^\pm)| < 2.4$ and $p_T(\ell^\pm) > 20$ GeV. We artificially vary the input mass of the W^\pm boson and we repeat the computations for the 3 following couples of respective LO and NLO PDFs: MRST2007lomod [264] - MRST2004nlo [256], CTEQ6L1 [253] - CTEQ6.6 [254], and MSTW2008lo68cl - MSTW2008nlo68cl [258] which are interfaced to MCFM through LHAPDF v5.7.1 [260]. As the LO is sufficient to present the method in detail, we'll restrict ourselves to LO MEs and LO PDFs throughout the article for the sake of simplicity. We shall however provide the theoretical A_C mass templates up to the NLO for the W process. And we recommend to establish them using the best theoretical calculations available for any use in a real data analysis, including at minimum the QCD NLO corrections.

The MRST2007lomod is chosen as the default PDF throughout this article. The two other LO PDFs serve for comparison of the central value and the uncertainty of A_C with respect to MRST2007lomod. In that regard, MSTW2008lo68cl is especially useful to estimate the impact of the $\delta(A_C)_{PDF}$.

5.3.4.2.a. 3). Modeling of the Theoretical $A_C(W^\pm \rightarrow e^\pm \nu_e)$ Template Curves

The theoretical MRST2007lomod and MRST2004nlo raw template curves are obtained by sampling A_C^{Raw} at different values of M_{W^\pm} . The corresponding theoretical uncertainties are also calculated: $A_C^{Raw} \pm \delta A_C^{Raw}$. This discrete sampling is then transformed into a continuous template curve through a fit using a functional form $A_C^{Fit} = f(M_{W^\pm})$ which is constrained by the theoretical uncertainties.

We have considered three different types of functional forms for these fits with f being either a:

1. polynomial of logarithms: $f(x) = \sum_{i=0}^{N_{FP}} A_i \times \{\text{Log}(x)\}^i$
2. polynomial of logarithms of logarithms: $f(x) = \sum_{i=0}^{N_{FP}} A_i \times \{\text{Log}[\text{Log}(x)]\}^i$
3. series of Laguerre polynomials: $f(x) = \sum_{i=0}^{N_{FP}} A_i \times L_n(x)$ where $L_n(x) = \frac{e^x}{n!} \frac{d^n}{dx^n} (e^{-x} x^n)$.

The types of functional forms that we're considering are not arbitrary, they are all related to parametrizations of solutions of the DGLAP equations for the evolution of the PDFs. The polynomial of logarithms of logarithms is inspired by an expansion of the PDF in series of $\text{Log}[\text{Log}(Q^2)]$ as suggested in [238]. The polynomial of logarithms was just the simplest approximation of the aforementioned series that we first considered. And the expansion of the PDF in series of Laguerre polynomials is proposed in [244].

In the Appendix A, we give a numerical example of the evolution of the $u(x, Q^2)$, $\bar{u}(x, Q^2)$, $d(x, Q^2)$, $\bar{d}(x, Q^2)$ proton density functions calculated with QCDNUM [245] and the MSTW2008nlo68cl PDF. We also provide a few toy models to justify the main properties of the functional forms used for A_C^{Fit} .

Ultimately, the model of the theoretical template curve uses the functional form f for the A_C^{Fit} central values and re-calculate their uncertainty δA_C^{Fit} by accounting for the correlations between the uncertainties of the fit parameters:

$$(\delta A_C^{Fit})^2 = (\delta f)^2 = \sum_{i=0}^{N_{FP}} \sum_{j>i}^{N_{FP}} \left(\frac{\partial f}{\partial A_i} \right)^2 \cdot \text{VAR}(A_i) + 2 \cdot \frac{\partial f}{\partial A_i} \cdot \frac{\partial f}{\partial A_j} \cdot \text{COVAR}(A_i, A_j) \quad (5.12)$$

The diagonal and off-diagonal elements of the fit uncertainty matrix are denoted $\text{VAR}(A_i)$ and $\text{COVAR}(A_i, A_j)$, they correspond to the usual variances of the parameters and the covariances amongst them, respectively.

The number of fit parameters N_{FP} is taken as the minimum integer necessary to get a good χ^2/Ndf for the fit and it is adjustable for each A_C template curve.

Comparing the three types of polynomials cited above as functional forms to fit all the A_C template curves of sub-sections 5.1.4.2.a and 5.1.4.3.a, we find that the polynomials of logarithms of logarithms of Q give the best fits. They are henceforth chosen as the default functional form to model the Q evolution of A_C throughout this article.

5.3.4.2.a. 4). $A_C(W^\pm \rightarrow e^\pm \nu_e)$ Template Curves for MRST

The theoretical MRST2007lomod and MRST2004nlo A_C template curves are obtained from the signed cross sections used for table 5.16. Since there is no MRST2007lomod PDF uncertainty set, we simply set $\delta(A_C)_{PDF} = 0$. In this case, $\delta_{Total}^{Theory} A_C = \sqrt{\delta_{Stat}^2 A_C + \delta_{Scale}^2 A_C}$. Figure 5.11 displays the fit to the A_C template curve using a polynomial of $\text{Log}(\text{Log}(Q))$. In the case of the MRST2007lomod PDF, it is sufficient to limit the polynomial to the degree $N_{FP} = 5$ to fit the A_C template curve in the following (default) range: $M_{W^\pm} \in [15, 1500]$ GeV.

M_{W^\pm} (GeV)	A_C (%)	$\delta(A_C)_{Stat}$ (%)	$\delta(A_C)_{Scale}$ (%)	$\delta(A_C)_{PDF}$ (%)	$\delta(A_C)_{Total}$ (%)
20.1	LO: 2.20	± 0.24	+0.47 +0.10	0.00	+0.52 -0.26
	NLO: 2.09	± 0.11	+0.04 -0.14	0.00	+0.12 -0.18
40.2	LO: 6.77	± 0.12	+0.02 -0.11	0.00	+0.12 -0.16
	NLO: 8.05	± 0.07	-0.18 -0.06	0.00	+0.19 -0.09
<u>80.4</u>	LO: 20.18	± 0.06	+0.05 -0.03	0.00	+0.08 -0.07
	NLO: 21.49	± 0.03	-0.08 -0.00	0.00	+0.09 -0.03
160.8	LO: 29.39	± 0.05	+0.00 +0.03	0.00	+0.05 -0.06
	NLO: 30.55	± 0.03	-0.02 -0.01	0.00	+0.04 -0.03
321.6	LO: 35.92	± 0.05	-0.11 +0.10	0.00	+0.11 -0.11
	NLO: 36.90	± 0.03	-0.05 -0.04	0.00	+0.06 -0.05
643.2	LO: 43.99	± 0.05	-0.14 +0.13	0.00	+0.15 -0.14
	NLO: 45.11	± 0.03	-0.05 -0.05	0.00	+0.06 -0.06
1286.4	LO: 52.36	± 0.06	+0.03 -0.02	0.00	+0.07 -0.07
	NLO: 55.33	± 0.04	+0.01 -0.02	0.00	+0.04 -0.04

TABLE 5.11: The MRST A_C table with the breakdown of the different sources of theoretical uncertainty. The MRST2007lomod PDF is used for the LO and the MRST2004nlo for the NLO.

M_{W^\pm} (GeV)	A_C^{Fit} (%)	δA_C^{Fit} (%)
20.1	LO: 1.35	± 0.10
	NLO: 2.00	± 0.12
40.2	LO: 7.27	± 0.07
	NLO: 8.31	± 0.08
<u>80.4</u>	LO: 19.93	± 0.05
	NLO: 21.12	± 0.05
160.8	LO: 29.46	± 0.04
	NLO: 30.49	± 0.04
321.6	LO: 36.29	± 0.04
	NLO: 37.29	± 0.04
643.2	LO: 43.07	± 0.05
	NLO: 44.61	± 0.04
1286.4	LO: 52.43	± 0.06
	NLO: 55.40	± 0.04

TABLE 5.12: The MRST A_C^{Fit} table with δA_C^{Fit} calculated using Eq. 5.12. The MRST2007lomod PDF is used at LO and the MRST2004nlo one is used at NLO.

5.3.4.2.a. 5). $A_C(W^\pm \rightarrow e^\pm \nu_e)$ Template Curves for CTEQ6

The theoretical CTEQ6L1 and CTEQ6.1 A_C template curves are obtained from the signed cross sections used for table 5.13.

5.3.4.2.a. 6). $A_C(W^\pm \rightarrow e^\pm \nu_e)$ Template Curves for MSTW2008

The theoretical MSTW2008lo68cl and MSTW2008nlo68cl A_C template curves are obtained from the signed cross sections used for table 5.15.

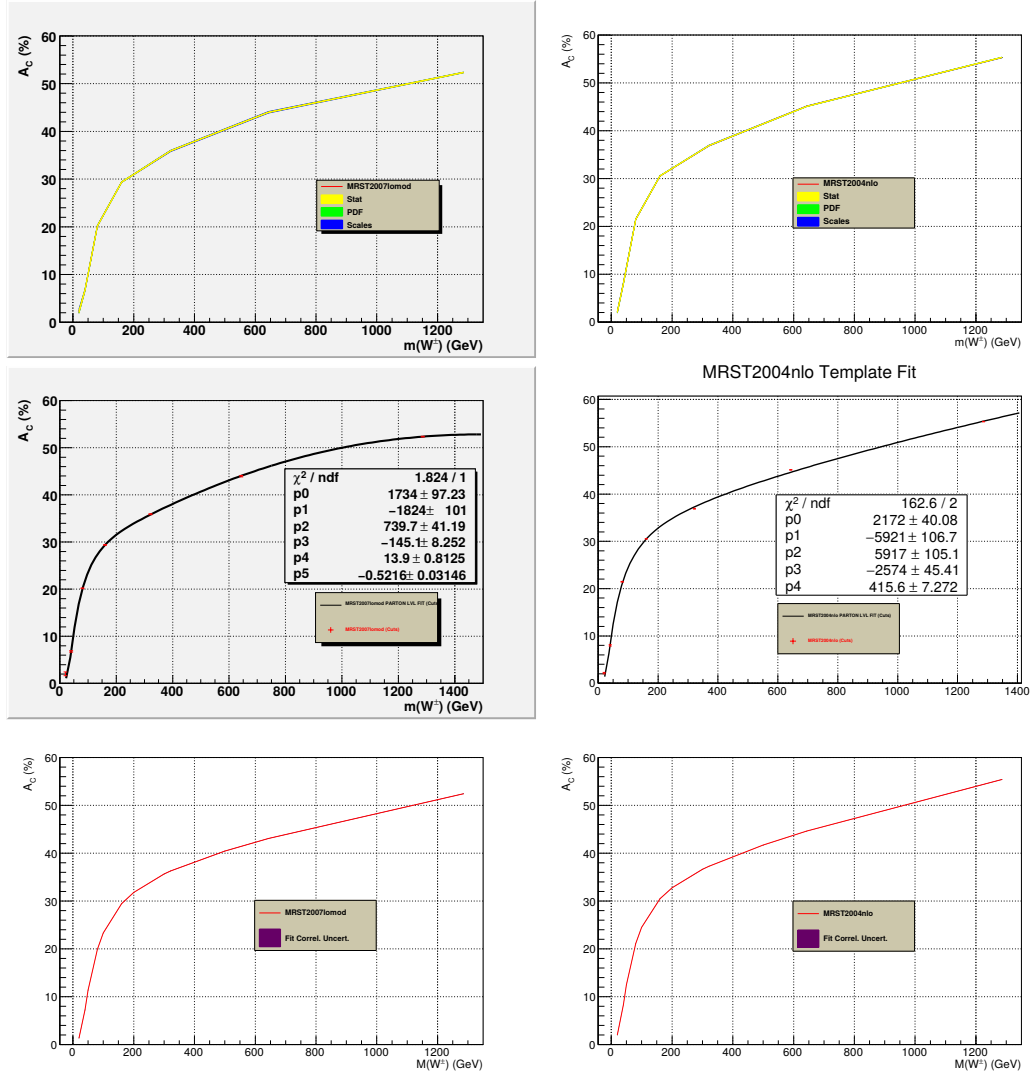


FIGURE 5.11: The theoretical MRST A_C template curves at LO with MRST2007lomod on the left-hand side (LHS) and NLO with the MRST2004nlo on the right-hand side (RHS). The raw curve with its uncertainty bands, the corresponding fitted curve and the fitted curve with the correlations between the fit parameters uncertainties are displayed on the top, the middle and the bottom rows, respectively.

In this case, the PDF uncertainty is provided and it turns out to be the dominant source of theoretical uncertainty on A_C .

5.3.4.2.a. 7). Comparing the Different A_C Template Curves At this stage, it's interesting to compare the A_C template curves produced with different PDFs using MCFM. From figure 5.14 we can see that the A_C of the different PDF used at LO and at NLO are in agreement at the $\pm 2\sigma$ level, provided that we switch the reference to a PDF set containing uncertainty PDFs. This figure also displays the $\frac{A_C^{NLO}}{A_C^{LO}}$ ratios for the three families of PDFs used. These ratios are almost flat with respect to M_{W^\pm} over the largest part of our range of interest. However at the low mass ends they vary rapidly. As we illustrate in the Appendix A, these integral charge asymmetry ratios can be fitted by the same functional forms as the A_C^{LO} and A_C^{NLO} .

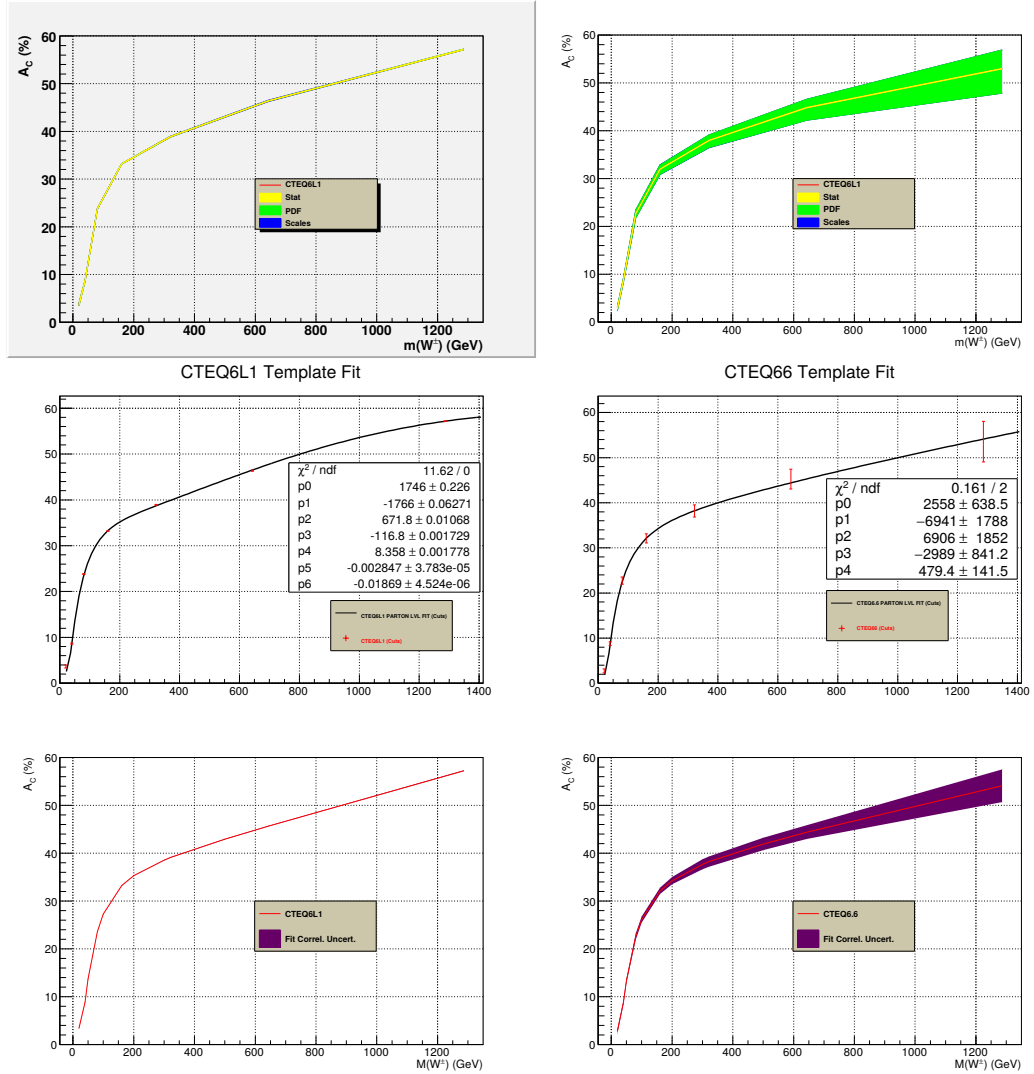


FIGURE 5.12: The theoretical CTEQ6 A_C template curves at LO with CTEQ6L1 (LHS) and NLO with the CTEQ6.6 (RHS). The raw curve with its uncertainty bands, the corresponding fitted curve and the fitted curve with the correlations between the fit parameters uncertainties are displayed on the top, the middle and the bottom rows, respectively.

5.1.4.2.b Experimental Measurement of $A_C(W^\pm \rightarrow \ell^\pm \nu)$

The aim of this sub-section is to study the biases on A_C due to two different sources: the event selection and the residual background remaining after the latter cuts are applied.

5.3.4.2.b. 1). Monte Carlo Generation

To quantify these biases we generate Monte Carlo (MC) event samples using the following LO generator: Herwig++ v2.5.0 [360]. We adopt a tune of the underlying event derived by the ATLAS collaboration [263] and we use accordingly the MRST2007lomod [264] PDF.

Herwig++ mainly uses $2 \rightarrow 2$ LO ME that we denote in the standard way: $1 + 2 \rightarrow 3 + 4$. For all the non-resonant processes, the production is splitted into bins of M , where $M = M(3, 4)$ is the invariant mass of the two outgoing particles.

M_{W^\pm} (GeV)	A_C (%)	$\delta(A_C)_{Stat}$ (%)	$\delta(A_C)_{Scale}$ (%)	$\delta(A_C)_{PDF}$ (%)	$\delta(A_C)_{Total}$ (%)
20.1	LO: 3.70	± 0.24	-0.27 +0.11	0.00	+0.36 -0.26
	NLO: 2.76	± 0.11	-0.24 -0.13	+0.37 -0.39	+0.45 -0.43
40.2	LO: 8.65	± 0.12	-0.02 -0.00	0.00	+0.12 -0.12
	NLO: 8.75	± 0.07	+0.09 -0.09	+0.38 -0.41	+0.40 -0.43
<u>80.4</u>	LO: 23.81	± 0.06	+0.07 -0.06	0.00	+0.09 -0.08
	NLO: 22.67	± 0.03	+0.14 -0.20	+0.74 -0.85	+0.75 -0.87
160.8	LO: 33.21	± 0.05	+0.01 -0.00	0.00	+0.05 -0.05
	NLO: 31.99	± 0.02	+0.23 -0.24	+0.86 -1.11	+0.89 -1.14
321.6	LO: 38.90	± 0.05	-0.09 +0.07	0.00	+0.10 -0.09
	NLO: 37.99	± 0.03	+0.18 -0.18	+1.11 -1.52	+1.12 -1.53
643.2	LO: 46.38	± 0.05	-0.14 0.13	0.00	+0.15 -0.14
	NLO: 44.83	± 0.03	+0.06 -0.09	+1.76 -2.64	+1.76 -2.64
1286.4	LO: 57.17	± 0.06	-0.06 +0.06	0.00	+0.08 -0.08
	NLO: 52.97	± 0.04	+0.05 +0.04	+3.90 -5.10	+3.90 -5.10

TABLE 5.13: The CTEQ6 A_C table with the breakdown of the different sources of theoretical uncertainty. The CTEQ6L1 PDF is used at LO and the CTEQ6.6 one is used at NLO.

M_{W^\pm} (GeV)	A_C^{Fit} (%)	δA_C^{Fit} (%)
20.1	LO: 3.40	± 0.09
	NLO: 2.76	± 0.44
40.2	LO: 8.85	± 0.06
	NLO: 8.76	± 0.42
<u>80.4</u>	LO: 23.59	± 0.04
	NLO: 22.57	± 0.64
160.8	LO: 33.24	± 0.04
	NLO: 32.11	± 0.66
321.6	LO: 39.11	± 0.04
	NLO: 38.23	± 1.08
643.2	LO: 45.67	± 0.05
	NLO: 44.41	± 1.43
1286.4	LO: 57.24	± 0.07
	NLO: 54.11	± 3.42

TABLE 5.14: The CTEQ6 A_C^{Fit} table with δA_C^{Fit} calculated using Eq. 5.12. The CTEQ6L1 PDF is used at LO and the CTEQ6.6 one is used at NLO.

For the single vector boson ("V+jets") production, where V stands for W^\pm and γ^*/Z , we mix in the same MC samples the contributions from the pure Drell-Yan process V+0Lp ME and the V+1Lp ME. For all the SM processes a common cut of $M > 10$ GeV is applied.

All the samples are normalized using the Herwig++ cross section multiplied by a K-factor that includes at least the NLO QCD corrections. We'll denote NLO (respectively NNLO) K-factor the ratio: $\frac{\sigma_{NLO}}{\sigma_{LO}}$ (respectively $\frac{\sigma_{NNLO}}{\sigma_{LO}}$). We choose not to apply such higher order corrections to the normalization of the following non-resonant inclusive processes:

- light flavor QCD (denoted QCD LF): $2 \rightarrow 2$ MEs involving $u/d/s/g$ partons
- heavy flavor QCD (denoted QCD HF): $c + \bar{c}$ and $b + \bar{b}$

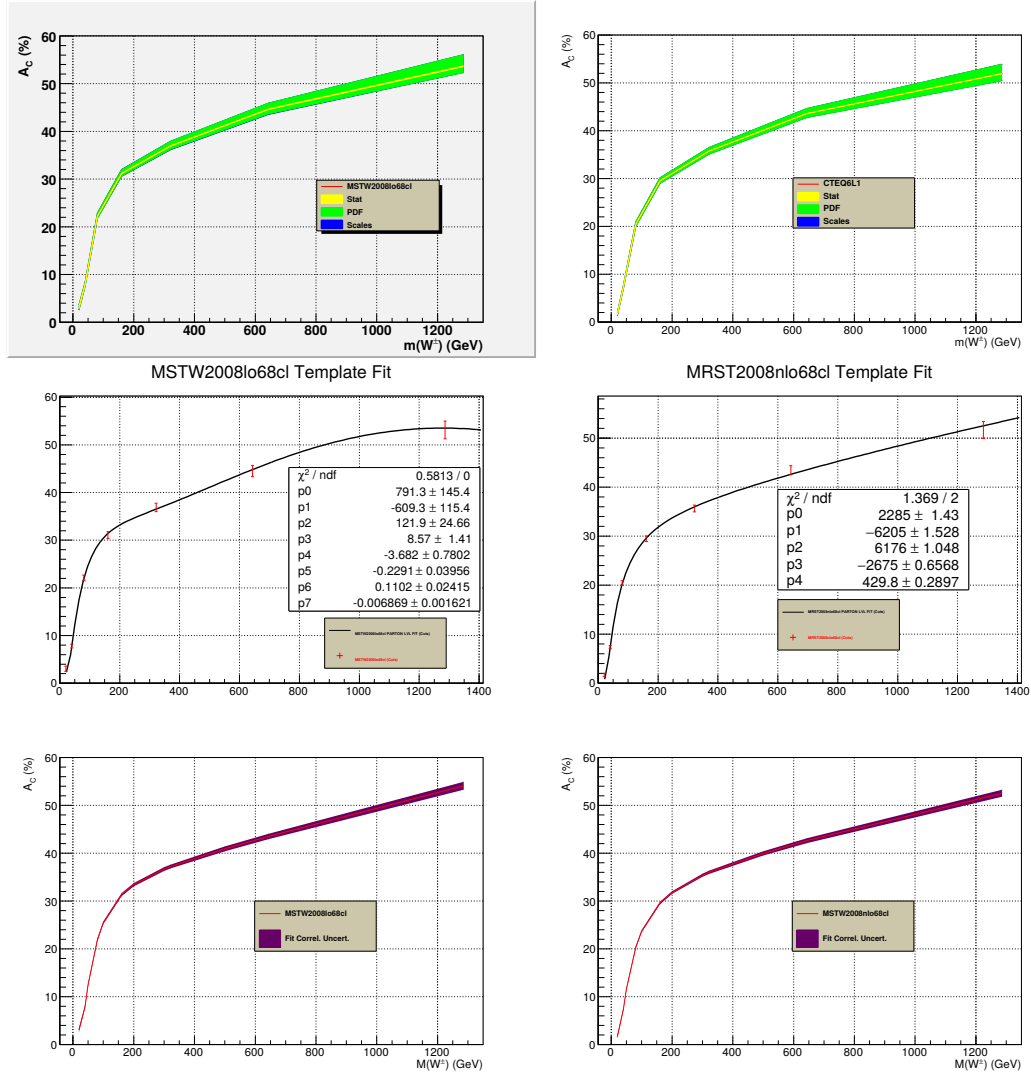


FIGURE 5.13: The theoretical MSTW2008 A_C template curves at LO with MSTW2008lo68cl (LHS) and NLO with the MSTW2008nlo68cl (RHS). The raw curve with its uncertainty bands and the corresponding fitted curve are displayed on the LHS and on the RHS, respectively.

- prompt photon productions: $\gamma + jets$ and $\gamma + \gamma$

Despite their large cross sections these non-resonant processes will turn out to have very low efficiencies and to represent a small fraction of the remaining background in the event selection used in the analyses we perform.

The NNLO K-factors for the $\gamma^*/Z(\rightarrow \ell^\pm \ell^\mp)$ process are derived from PHOZR [281] with $\mu_R = \mu_F = M(\ell^\pm \ell^\mp)$ and using the MSTW2008nlo68cl PDF for σ_{NNLO} and the MRST2007lomod one for σ_{LO} .

The top pairs and single top [283][282] NLO K-factors are obtained by running MCFM v5.8 using the MSTW2008nlo68cl and the MSTW2008lo68cl PDFs for the numerator and the denominator respectively, with the QCD scales set as follows: $\mu_R = \mu_F = \hat{s}$.

M_{W^\pm} (GeV)	A_C (%)	$\delta(A_C)_{Stat}$ (%)	$\delta(A_C)_{Scale}$ (%)	$\delta(A_C)_{PDF}$ (%)	$\delta(A_C)_{Total}$ (%)
20.1	LO: 3.07	± 0.24	-0.21 +0.14	+0.46 -0.40	+0.56 -0.49
	NLO: 1.64	± 0.12	-0.08 -0.17	+0.29 -0.31	+0.32 -0.37
40.2	LO: 7.85	± 0.12	+0.10 +0.07	+0.43 -0.33	+0.46 -0.36
	NLO: 7.35	± 0.07	+0.05 -0.06	+0.30 -0.33	+0.31 -0.34
<u>80.4</u>	LO: 22.24	± 0.06	+0.15 +0.13	+0.64 -0.42	+0.66 -0.44
	NLO: 20.47	± 0.03	-0.06 -0.01	+0.48 -0.46	+0.48 -0.46
160.8	LO: 31.19	± 0.05	+0.21 +0.19	+0.78 -0.53	+0.81 -0.57
	NLO: 29.52	± 0.03	-0.10 +0.02	+0.62 -0.51	+0.63 -0.51
321.6	LO: 36.96	± 0.05	+0.16 +0.33	+0.96 -0.70	+0.97 -0.77
	NLO: 35.73	± 0.03	-0.05 -0.05	+0.76 -0.59	+0.76 -0.59
643.2	LO: 44.63	± 0.06	+0.17 +0.41	+1.28 -0.96	+1.29 -1.05
	NLO: 43.58	± 0.03	-0.08 -0.03	+1.05 -0.78	+1.05 -0.78
1286.4	LO: 53.66	± 0.07	+0.31 +0.33	+2.39 -1.28	+2.42 -1.32
	NLO: 51.92	± 0.04	+0.03 +0.02	+1.99 -1.45	+1.99 -1.45

TABLE 5.15: The MSTW2008lo68cl A_C table with the breakdown of the different sources of theoretical uncertainty. The MSTW2008lo68cl PDF is used at LO and the MSTW2008nlo68cl one is used at NLO.

M_{W^\pm} (GeV)	A_C^{Fit} (%)	δA_C^{Fit} (%)
20.1	LO: 3.05	± 0.38
	NLO: 1.63	± 0.26
40.2	LO: 7.90	± 0.26
	NLO: 7.39	± 0.21
<u>80.4</u>	LO: 21.89	± 0.27
	NLO: 20.30	± 0.22
160.8	LO: 31.35	± 0.31
	NLO: 29.59	± 0.26
321.6	LO: 37.22	± 0.40
	NLO: 35.99	± 0.34
643.2	LO: 43.49	± 0.57
	NLO: 42.61	± 0.51
1286.4	LO: 54.08	± 0.83
	NLO: 52.53	± 0.74

TABLE 5.16: The MSTW2008lo68cl A_C^{Fit} table with δA_C^{Fit} calculated using equation 5.12. The MSTW2008lo68cl PDF is used at LO and the MSTW2008nlo68cl one is used at NLO.

5.3.4.2.b. 2). Fast Simulation of the Detector Response

We use the following setup of Delphes v1.9 [266] to get a fast simulation of the ATLAS detector response as well as a crude emulation of its trigger. The generated MC samples are written in the HepMC v2.04.02 format [267] and passed through Delphes.

For the object reconstruction we also use Delphes defaults, with the exception of utilizing the "anti-kT" jet finder [269] with a cone radius of $\Delta R = \sqrt{(\Delta\eta)^2 + (\Delta\phi)^2} = 0.4$.

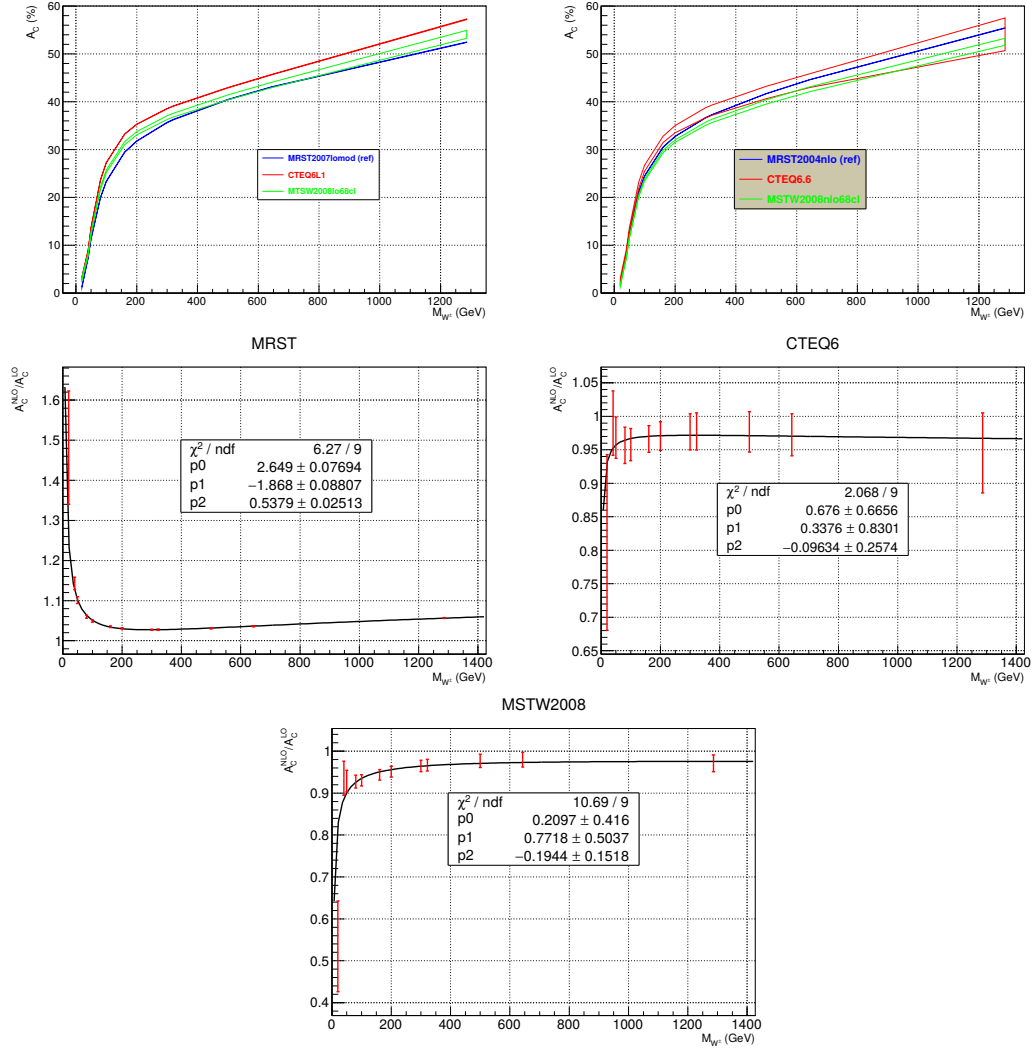


FIGURE 5.14: Comparison between the A_C template curves. The top LHS plot compares the LO PDFs: MRST2007lomod (blue, ref. curve), CTEQ6L1 (red), MSTW2008lo68cl (green). The top RHS plot compares the NLO PDFs: MRST2004nlo (blue, ref. curve), CTEQ6.6 (red), MSTW2008nlo68cl (green). The middle and the bottom rows display the $\frac{A_C^{NLO}}{A_C^{LO}}$ fitted by the same functional forms as the A_C^{LO} template curves.

5.3.4.2.b. 3). Analyses of the $W^\pm \rightarrow \ell^\pm \nu$ Process

We consider only the electron and the muon channels. For these analyses we set the integrated luminosity to $\int \mathcal{L} dt = 1 \text{ fb}^{-1}$.

Instead of trying to derive unreliable systematic uncertainties for these analyses using Delphes, we choose to use realistic values as quoted in actual LHC data analysis publications. We choose the analyses with the largest data samples so as to reduce as much as possible the statistical uncertainties in their measurements but also to benefit from the largest statistics for the data samples utilized to derive their systematic uncertainties. This choice leads us to quote systematic uncertainties from analyses performed by the CMS collaboration. Namely we use:

$$\delta_{Syst}A_C(W^\pm \rightarrow e^\pm\nu_e) = 1.0\% \quad (5.13)$$

$$\delta_{Syst}A_C(W^\pm \rightarrow \mu^\pm\nu_\mu) = 0.4\% \quad (5.14)$$

The values quoted in equations 5.13 and 5.14 come from references [285] and [286], respectively.

And to get an estimate of the uncertainty on a ratio of number of expected events we use the systematics related to the measurement of the following cross sections ratio

$$\sigma(pp \rightarrow W^\pm \rightarrow \ell^\pm\nu_\ell)/\sigma(pp \rightarrow \gamma^*/Z \rightarrow \ell^\pm\ell^\mp) \quad (5.15)$$

which amounts to 1.0% [287].

5.3.4.2.b. 3).A. The Electron Channel

5.3.4.2.b. 3).A.1. Event Selection in the Electron Channel

The following cuts are applied:

- $p_T(e^\pm) > 25$ GeV
- $|\eta(e^\pm)| < 1.37$ or $1.53 < |\eta(e^\pm)| < 2.4$
- Tracker Isolation: reject events with additional tracks of $p_T > 2$ GeV within a cone of $\Delta R = 0.5$ around the direction of the e^\pm track
- Calorimeter Isolation: the ratio of, the scalar sum of E_T deposits in the calorimeter within a cone of $\Delta R = 0.5$ around the direction of the e^\pm , to the $p_T(e^\pm)$, must be less than 1.2
- $\cancel{E}_T > 25$ GeV
- $M_T = \sqrt{2p_T(\ell^\pm)\cancel{E}_T[1 - \cos\Delta\phi(\ell^\pm, \cancel{E}_T)]} > 40$ GeV
- Reject events with an additional leading isolated muon: μ_1^\pm
- Reject events with an additional trailing isolated electron: e_2^\pm
- Reject events with an additional second track ($Track_2$) such that:

$$\begin{cases} Q(e_1^\pm) = -Q(Track_2) \\ 3 < p_T(Track_2) < 10 \text{ GeV} \\ M[e_1^\pm, Track_2] > 50 \text{ GeV} \end{cases}$$

The corresponding selection efficiencies and event yields (expressed in thousandths of events) are reported in table 5.17. Figure 5.15 displays the \cancel{E}_T distribution after the event selection in the electron channel (LHS) and in the muon channel (RHS).

Process	ϵ (%)	N_{exp} (k evts)	$A_C \pm \delta A_C^{Stat}$ (%)
Signal: $W^\pm \rightarrow e^\pm \nu_e$			
$M(W^\pm) = 40.2$ GeV	0.81 ± 0.01	290.367	9.66 ± 1.57
$M(W^\pm) = 60.3$ GeV	13.69 ± 0.05	2561.508	11.22 ± 0.38
$M(W^\pm) = 80.4$ GeV	29.59 ± 0.04	3343.195	16.70 ± 0.18
$M(W^\pm) = 100.5$ GeV	39.19 ± 0.07	2926.093	20.77 ± 0.22
$M(W^\pm) = 120.6$ GeV	44.84 ± 0.07	2357.557	23.19 ± 0.21
$M(W^\pm) = 140.7$ GeV	48.66 ± 0.07	1899.820	25.29 ± 0.20
$M(W^\pm) = 160.8$ GeV	51.28 ± 0.07	1527.360	26.87 ± 0.19
$M(W^\pm) = 201.0$ GeV	54.54 ± 0.07	1.032	29.06 ± 0.18
Background	-	91.614 ± 1.706	10.07 ± 0.15
$W^\pm \rightarrow \mu^\pm \nu_\mu / \tau^\pm \nu_\tau / q\bar{q}'$	0.211 ± 0.003	71.350	12.92 ± 1.25
$t\bar{t}$	5.76 ± 0.02	6.600	1.00 ± 0.37
$t + b, t + q(+b)$	3.59 ± 0.01	1.926	28.97 ± 0.35
$W + W, W + \gamma^*/Z, \gamma^*/Z + \gamma^*/Z$	2.94 ± 0.01	2.331	10.65 ± 0.35
$\gamma + \gamma, \gamma + jets, \gamma + W^\pm, \gamma + Z$	0.201 ± 0.001	0.759	17.25 ± 0.53
γ^*/Z	0.535 ± 0.001	5.746	4.43 ± 0.23
QCD HF	$(0.44 \pm 0.17) \times 10^{-4}$	1.347	14.29 ± 37.41
QCD LF	$(0.87 \pm 0.33) \times 10^{-4}$	1.555	71.43 ± 26.45

TABLE 5.17: Selection efficiencies, event yields and integral charge asymmetries for the $W^\pm \rightarrow e^\pm \nu_e$ analysis.

The non-resonant background processes represent just $\sim 4\%$ of the total background after the event selection, this justifies the approximation of not to include the NLO QCD corrections to their normalizations.

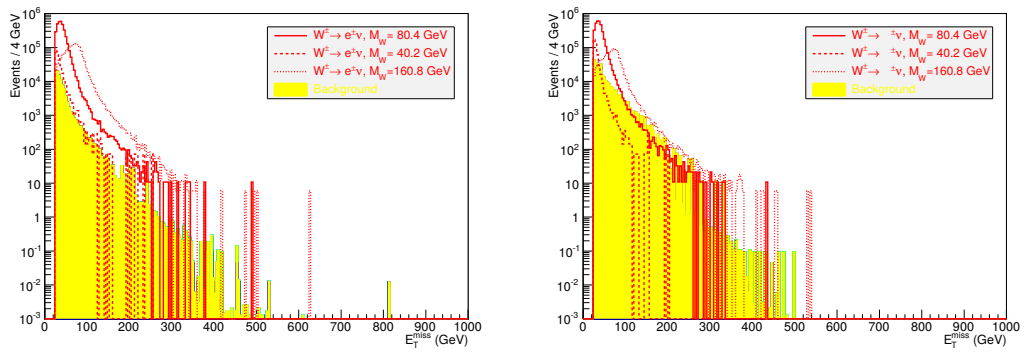


FIGURE 5.15: E_T^{miss} distribution after the event selection is applied for the $W^\pm \rightarrow e^\pm \nu_e$ (LHS) and for the $W^\pm \rightarrow \mu^\pm \nu_\mu$ (RHS) analysis.

5.3.4.2.b. 3).A.2. Common Procedure for the Background Subtraction and the Propagation of the Experimental Uncertainty

If we were to apply such an analysis on real collider data, we would get in the end the measured integral charge asymmetry A_C^{Meas} of the data sample passing the selection cuts. And obviously we wouldn't know which event come from which sub-process. Since the MC enables to separate the different contributing sub-processes, it's possible to extract the integral charge asymmetry

of the signal (S), knowing that of the total background (B). If we denote $\alpha^{Exp} = \frac{N_B^{Exp}}{N_S^{Exp}}$ the ratio of the expected number of background events to the expected number of signal events, we can express $A_C^{Exp}(S+B)$, the integral charge asymmetry of all remaining events either from signal or from background, with respect to that quantity for signal only events $A_C^{Exp}(S)$, and for background only events $A_C^{Exp}(B)$. This writes:

$$A_C^{Exp}(S+B) = \frac{A_C^{Exp}(S) + \alpha^{Exp} \cdot A_C^{Exp}(B)}{1 + \alpha^{Exp}} \quad (5.16)$$

where the upper script "Exp" stands for "Expected".

This formula can easily be inverted to extract $A_C^{Exp}(S)$ in what we'll refer to as the "background subtraction equation":

$$A_C^{Exp}(S) = (1 + \alpha^{Exp}) \cdot A_C^{Exp}(S+B) - \alpha^{Exp} \cdot A_C^{Exp}(B) \quad (5.17)$$

Note that these expressions involve only ratios hence their experimental systematic uncertainty remains relatively small. The uncertainty on $A_C^{Exp}(S)$ is calculated by taking account the correlation between the uncertainties of α^{Exp} , $A_C^{Exp}(B)$, and $A_C^{Exp}(S+B)$.

$$\begin{aligned} [\delta A_C(S)]^2 &= [A_C(S+B) - A_C(B)]^2 \cdot [\delta\alpha]^2 + (1 + \alpha)^2 \cdot [\delta A_C(S+B)]^2 + \alpha^2 \cdot [\delta A_C(B)]^2 \\ &\quad + 2 \cdot [A_C(S+B) - A_C(B)] \cdot (1 + \alpha) \cdot COV[\alpha, A_C(S+B)] \\ &\quad - 2 \cdot [A_C(S+B) - A_C(B)] \cdot \alpha \cdot COV[\alpha, A_C(B)] \\ &\quad - 2 \cdot \alpha \cdot (1 + \alpha) \cdot COV[A_C(B), A_C(S+B)] \end{aligned} \quad (5.18)$$

In order to propagate the experimental uncertainties from equations 5.13, 5.14, and 5.15 to $\delta A_C(S)$, we perform pseudo-experiments running 10,000,000 trials for each. In these trials all quantities involved in the background subtraction equation 5.17 is allowed to fluctuate according to a gaussian smearing that has its central value as a mean and its total uncertainty as an RMS. In each of these pseudo-experiments, the signal S and the background B float separately. For each of the events categories (S or B) separately, the numbers of positively and negatively charged events also fluctuate but in full anti-correlation. This procedure enables to estimate numerically the values of the variances and covariances appearing in equation 5.18.

In a realistic analysis context, $A_C^{Exp}(S)$ can be obtained from a full simulation of the signal, $A_C^{Exp}(B)$ and α^{Exp} can also be obtained this way or through data-driven techniques. The experimental systematic uncertainties can be propagated as usually done to each of these quantities. And one can extract $A_C^{Obs}(S)$ from a data sample using the following form of equation 5.17:

$$A_C^{Obs}(S) = (1 + \alpha^{Meas}) \cdot A_C(Data) - \alpha^{Meas} \cdot A_C^{Meas}(B) \quad (5.19)$$

provided a good estimate of the number of remaining signal and background events after the event selection as well as the integral charge asymmetries of the signal and of the background are established. The upper script "Obs" stands for observed.

5.3.4.2.b. 3).A.3. The Measured A_C in the Electron Channel

For the nominal W mass, we calculate $A_C^{Meas}(S)$ using the inputs from the analysis in the electron channel only with their statistical uncertainties:

- $A_C^{Exp}(S) = (16.70 \pm 0.18)\%$
- $A_C^{Exp}(B) = (10.07 \pm 0.15)\%$
- $A_C^{Exp}(S + B) = (16.52 \pm 0.11)\%$
- $\alpha^{Exp} = (2.74 \pm 0.05) \times 10^{-2}$

After the background subtraction and the propagation of the experimental systematic uncertainties, we get:

$$A_C^{Meas}(S) = (16.70 \pm 0.76)\% \quad (5.20)$$

5.3.4.2.b. 3).A.4. The A_C Template Curve in the Electron Channel

In order to establish the experimental A_C template curve, we apply a "multitag and probe method". We consider all the $W^\pm \rightarrow e^\pm \nu_e$ MC samples with a non-nominal W mass as the multitag and the one with the nominal W mass as the probe. We apply equation 5.17 to each of the multitag samples and plot their $A_C^{Meas}(S)$ as a function of M_{W^\pm} . A second degree polynomial of logarithms of logarithms is well suited to fit the template curve as shown in the LHS of figure 5.16, for the electron channel. The fit to this template curve can be expressed by equation 5.21. Note that we do not include the probe sample in the template curve since we want to estimate the accuracy of its indirect mass measurement.

$$A_C^{Meas}(W^\pm \rightarrow e^\pm + \nu_e) = -107.1 - 183.5 \times \text{Log}(\text{Log}(M_{W^\pm})) + 82.69 \times \text{Log}(\text{Log}(M_{W^\pm}))^2 \quad (5.21)$$

Process	$\alpha^{Exp} \pm \delta\alpha^{Stat}$	Z_N (σ)	$A_C^{Meas.}$ (%)	$\delta A_C^{Meas.}$ (%)	$\delta A_C^{Meas.Fit}$ (%)
Signal: $W^\pm \rightarrow e^\pm \nu_e$					
$M(W^\pm) = 40.2$ GeV	$(31.55 \pm 0.77) \times 10^{-2}$	37.25	9.66	1.05	0.60
$M(W^\pm) = 60.3$ GeV	$(3.58 \pm 0.07) \times 10^{-2}$	$\gg 5.00$	11.22	0.78	0.52
$M(W^\pm) = 80.4$ GeV	$(2.74 \pm 0.05) \times 10^{-2}$	$\gg 5.00$	16.70	0.76	0.35
$M(W^\pm) = 100.5$ GeV	$(3.13 \pm 0.06) \times 10^{-2}$	$\gg 5.00$	20.77	0.77	0.33
$M(W^\pm) = 120.6$ GeV	$(3.89 \pm 0.07) \times 10^{-2}$	$\gg 5.00$	23.19	0.78	0.35
$M(W^\pm) = 140.7$ GeV	$(4.82 \pm 0.09) \times 10^{-2}$	$\gg 5.00$	25.29	0.78	0.39
$M(W^\pm) = 160.8$ GeV	$(6.00 \pm 0.11) \times 10^{-2}$	$\gg 5.00$	26.86	0.79	0.42
$M(W^\pm) = 201.0$ GeV	$(88.77 \pm 1.66) \times 10^0$	0.19	29.07	2.03	0.48

TABLE 5.18: Noise to signal ratio, signal statistical significance, and expected and measured integral charge asymmetries for the signal after the event selection in the electron channel.

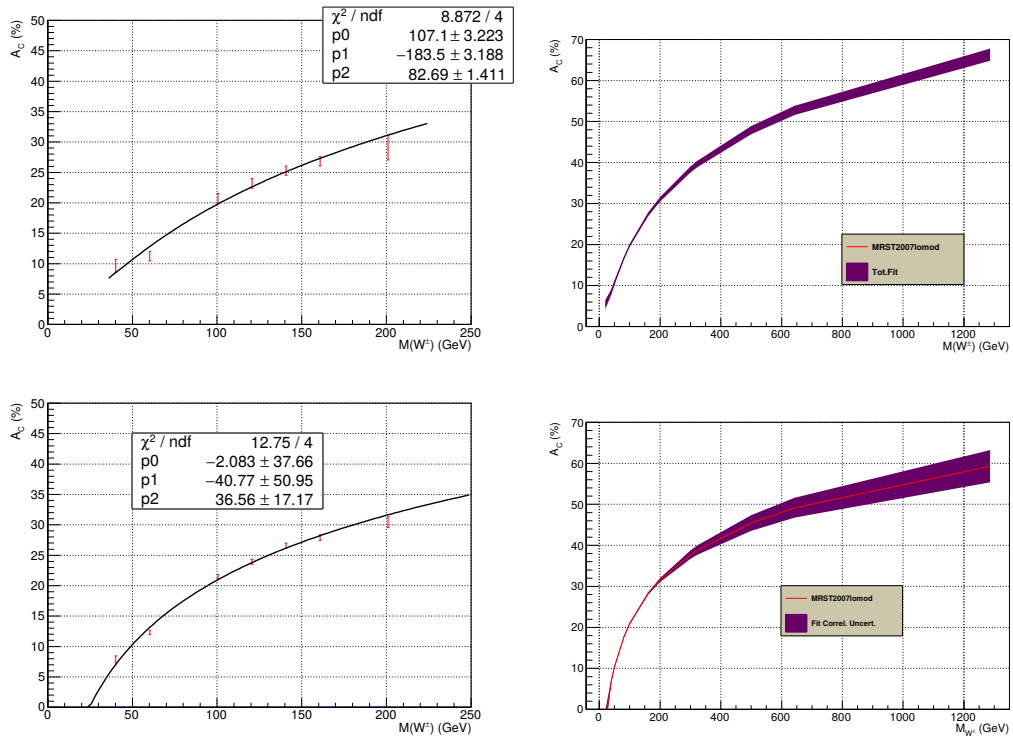


FIGURE 5.16: The A_C^{Meas} template curves for the electron channel (top) and the muon channel (bottom). The fits to the $A_C^{Meas}(S)$ are presented on the LHS. These fits with uncertainty bands accounting for the correlation between the uncertainties of the fit parameters are shown on the RHS.

The values of the noise to signal ratio (α^{Exp}), the signal statistical significance (Z_N , defined in the next paragraph), the expected (A_C^{Exp}), and the measured (A_C^{Meas}) integral charge asymmetries for the signal after the event selection in the electron channel are reported in table 5.18.

The signal significances reported are calculated using a conversion of the confidence level of the signal plus background hypothesis CL_{S+B} into an equivalent number of one-sided gaussian standard deviations Z_N as proposed in [291] and implemented in RooStats [292]. For these calculations the systematic uncertainty of the background was set to 5%, which completely covers the total uncertainty for the measurement of the inclusive cross section $\sigma(p + p \rightarrow W^\pm \rightarrow \ell^\pm \nu)$ as reported in [287].

We recalculate the uncertainty on $A_C^{Meas}(S)$ accounting for the correlation between the parameters when fitting the $A_C^{Meas}(S)$ template curve by applying equation 5.18. This results in a slightly reduced uncertainty as shown in equation 5.22.

$$A_C^{Meas.Fit}(S) = (16.70 \pm 0.35)\% \quad (5.22)$$

5.3.4.2.b. 3).B. The Muon Channel

5.3.4.2.b. 3).B.1. Event Selection in the Muon Channel

The following cuts are applied:

- $p_T(\mu) > 20$ GeV
- $|\eta(\mu)| < 2.4$
- Tracker Isolation: reject events with additional tracks of $p_T > 2$ GeV within a cone of $\Delta R = 0.5$ around the direction of the μ^\pm track
- Calorimeter Isolation: the ratio of, the scalar sum of E_T deposits in the calorimeter within a cone of $\Delta R = 0.5$ around the direction of the μ^\pm , to the $p_T(\mu^\pm)$ must be less than 0.25
- $\cancel{E}_T > 25$ GeV
- $M_T > 40$ GeV
- Reject events with an additional trailing isolated muon: μ_2^\pm
- Reject events with an additional leading isolated electron: e_1^\pm
- Reject events with an additional second track ($Track_2$) such that :

$$\begin{cases} Q(\mu_1^\pm) = -Q(Track_2) \\ 3 < p_T(Track_2) < 10 \text{ GeV} \\ M[\mu_1^\pm, Track_2] > 50 \text{ GeV} \end{cases}$$

The corresponding selection efficiencies and event yields are reported in table 5.19. The RHS of figure 5.15 displays the \cancel{E}_T distribution after the event selection. The non-resonant background processes represent $\sim 3\%$ of the total background after the event selection.

5.3.4.2.b. 3).B.2. The Measured A_C in the Muon Channel

The $A_C^{Meas}(S)$ treatment described in paragraph 2.2.4. a.2. is applied to the probe sample in the muon channel, starting from the following inputs:

- $A_C^{Exp}(S) = (17.42 \pm 0.18)\%$
- $A_C^{Exp}(B) = (7.36 \pm 0.15)\%$
- $A_C^{Exp}(S + B) = (16.64 \pm 0.12)\%$
- $\alpha^{Exp} = (8.38 \pm 0.65) \times 10^{-2}$

For the nominal W mass, this leads to a measured integral charge asymmetry of:

$$A_C^{Meas}(S) = (17.42 \pm 0.34)\% \quad (5.23)$$

where the uncertainty is also dominated by the value in equation 5.14.

<i>Process</i>	ϵ (%)	N_{exp} (k evts)	$A_C(S) \pm \delta A_C^{Stat}(S)$ (%)
Signal: $W^\pm \rightarrow \mu^\pm \nu_\mu$			
$M(W^\pm) = 40.2$ GeV	1.22 ± 0.02	439.192	7.86 ± 1.28
$M(W^\pm) = 60.3$ GeV	12.27 ± 0.05	2295.224	12.30 ± 0.40
$M(W^\pm) = \underline{80.4}$ GeV	29.32 ± 0.04	3313.642	17.42 ± 0.18
$M(W^\pm) = 100.5$ GeV	54.03 ± 0.07	4034.779	21.48 ± 0.19
$M(W^\pm) = 120.6$ GeV	31.30 ± 0.07	1645.675	23.93 ± 0.25
$M(W^\pm) = 140.7$ GeV	33.71 ± 0.07	1316.121	26.56 ± 0.23
$M(W^\pm) = 160.8$ GeV	35.37 ± 0.07	1053.514	27.90 ± 0.23
$M(W^\pm) = 201.0$ GeV	82.84 ± 0.05	1.568	30.44 ± 0.15
Background	-	277.787 ± 21.555	7.36 ± 0.15
$W^\pm \rightarrow e^\pm \nu_e / \tau^\pm \nu_\tau / q\bar{q}'$	0.291 ± 0.003	177.500	8.70 ± 1.07
$t\bar{t}$	4.27 ± 0.02	4.895	-0.14 ± 0.43
$t + b, t + q(+b)$	0.485 ± 0.005	0.264	27.14 ± 0.96
$W + W, W + \gamma^*/Z, \gamma^*/Z + \gamma^*/Z$	3.25 ± 0.01	2.478	11.39 ± 0.33
$\gamma + \gamma, \gamma + jets, \gamma + W^\pm, \gamma + Z$	0.135 ± 0.001	0.497	17.48 ± 0.65
γ^*/Z	0.727 ± 0.001	43.382	5.79 ± 0.20
QCD HF	$(2.13 \pm 0.37) \times 10^{-4}$	17.983	-17.65 ± 16.88
QCD LF	$(1.38 \pm 0.41) \times 10^{-4}$	30.788	9.09 ± 30.03

TABLE 5.19: Event selection efficiencies, event yields and integral charge asymmetries for the $W^\pm \rightarrow \mu^\pm \nu_\mu$ analysis.

5.3.4.2.b. 3).B.3. The Template Curve in the Muon Channel

After applying the $A_C^{Meas}(S)$ treatment to the tag samples in the muon channel, we get the $A_C^{Meas}(S)$ template curve shown in the RHS of figure 5.16. The fit to this template curve is reported in equation 5.24.

$$A_C^{Meas}(W^\pm \rightarrow \mu^\pm \nu_\mu) = -2.08 - 40.77 \times \text{Log}(\text{Log}(M_{W^\pm})) + 36.56 \times \text{Log}(\text{Log}(M_{W^\pm}))^2 \quad (5.24)$$

The values of the noise to signal ratio (α^{Exp}), the signal statistical significance (Z_N), and the expected (A_C^{Exp}) and the measured (A_C^{Meas}) integral charge asymmetries for the signal after the event selection in the muon channel are reported in table 5.20.

<i>Process</i>	$\alpha^{Exp} \pm \delta\alpha^{Stat}$	Z_N (σ)	$A_C^{Meas.}$ (%)	$\delta A_C^{Meas.}$ (%)	$\delta A_C^{Meas.Fit}$ (%)
Signal: $W^\pm \rightarrow \mu^\pm \nu_\mu$					
$M(W^\pm) = 40.2$ GeV	$(63.25 \pm 4.97) \times 10^{-2}$	11.19	7.86	0.59	0.45
$M(W^\pm) = 60.3$ GeV	$(12.10 \pm 0.94) \times 10^{-2}$	2295.22	12.30	0.37	0.27
$M(W^\pm) = \underline{80.4}$ GeV	$(8.38 \pm 0.65) \times 10^{-2}$	3313.64	17.42	0.34	0.27
$M(W^\pm) = 100.5$ GeV	$(6.88 \pm 0.53) \times 10^{-2}$	4034.78	21.48	0.35	0.22
$M(W^\pm) = 120.6$ GeV	$(16.88 \pm 1.31) \times 10^{-2}$	1645.68	23.93	0.40	0.19
$M(W^\pm) = 140.7$ GeV	$(21.11 \pm 1.64) \times 10^{-2}$	1316.12	26.56	0.42	0.22
$M(W^\pm) = 160.8$ GeV	$(26.37 \pm 2.05) \times 10^{-2}$	1053.51	27.90	0.45	0.27
$M(W^\pm) = 201.0$ GeV	$(17.72 \pm 1.37) \times 10^1$	1.57	30.44	0.87	0.40

TABLE 5.20: Noise to signal ratio, signal statistical significance, and expected and measured integral charge asymmetries for the signal after the event selection in the muon channel.

Again, accounting for the correlation between the parameters when fitting the $A_C^{Meas}(S)$ template curve enables to reduce the uncertainty as shown in equation 5.25.

$$A_C^{Meas.Fit}(S) = (17.42 \pm 0.27)\% \quad (5.25)$$

5.1.4.2.c Indirect Determination of M_{W^\pm}

5.3.4.2.c. 1). Results in the Individual Channels

The $A_C^{Meas.}(S) \pm \delta A_C^{Meas.}(S)$ in the electron and in the muon channels translate into indirect $M_{W^\pm}^{Meas.} \pm \delta M_{W^\pm}$ measurements using the experimental A_C template curves from the RHS of figure 5.16 in each of these channels:

$$A_C^{Meas.}(S) = (16.70 \pm 0.35)\% \Rightarrow M^{Meas.}(W^\pm \rightarrow e^\pm \nu_e) = 81.07_{-2.01}^{+2.06} \text{ GeV}, \quad (5.26)$$

$$A_C^{Meas.}(S) = (17.42 \pm 0.27)\% \Rightarrow M^{Meas.}(W^\pm \rightarrow \mu^\pm \nu_\mu) = 79.67_{-1.39}^{+3.56} \text{ GeV}. \quad (5.27)$$

5.3.4.2.c. 2). Combination of the Electron and the Muon Channels

We combine the electron and muon channels using a weighted mean for the measured W^\pm mass, the weight is the inverse of the uncertainty on the measured mass. In order to account for the asymmetric uncertainties, we slightly modify the expressions for the weighted mean and the weighted RMS of a quantity x as follows:

$$\langle x \rangle = \frac{\sum_{i=1}^N \frac{x_i}{\delta_i^2}}{\sum_{i=1}^N \frac{1}{\delta_i^2}} \rightarrow \langle x \rangle = \frac{\sum_{i=1}^N \left[\frac{x_i}{(\delta_i^{Up})^2} + \frac{x_i}{(\delta_i^{Down})^2} \right]}{\sum_{i=1}^N \left[\frac{1}{(\delta_i^{Up})^2} + \frac{1}{(\delta_i^{Down})^2} \right]} \quad (5.28)$$

$$\delta^2(\langle x \rangle) = \frac{1}{\sum_{i=1}^N \frac{x_i}{\delta_i^2}} \rightarrow \delta^2(\langle x \rangle) = \frac{1}{\sum_{i=1}^N \left[\frac{x_i}{(\delta_i^{Up})^2} + \frac{x_i}{(\delta_i^{Down})^2} \right]} \quad (5.29)$$

where x_i , δ_i^{Up} and δ_i^{Down} are respectively the central value, the upward uncertainty and the downward uncertainty of the mass derived in the channel i .

The result of the combination is:

$$M^{Comb.Meas.}(W^\pm) = 80.30 \pm 0.96 \text{ GeV [Expt. Comb.]} \quad (5.30)$$

5.1.4.2.d Final Result for MRST2007lomod

The next step is to estimate the theoretical uncertainty corresponding to the measured mass and to combine it with the experimental uncertainty. We simply use the central value of the measured W^\pm mass and we read-off the theoretical template curve the intervals, defined by the intercepts with upper and lower fit curves.

$$M_{Theory}(W^\pm) = 80.30_{-0.21}^{+0.19} \text{ GeV [MRST2007lomod]} \quad (5.31)$$

Finally we just sum in quadrature the theoretical and experimental upward and downward uncertainties:

$$\delta_{Tot.} M(W^\pm) = 80.30 \begin{cases} +\sqrt{(0.96)^2 + (0.19)^2} = +0.98 \\ -\sqrt{(0.96)^2 + (0.21)^2} = -0.98 \end{cases} \text{ GeV} \quad (5.32)$$

Therefore the final result for the MRST2007lomod PDF reads:

$$M_{W^\pm} = 80.30_{-0.98}^{+0.98} \text{ GeV [Total MRST2007lomod]}. \quad (5.33)$$

This constitutes an indirect M_{W^\pm} measurement with a relative accuracy of 1.2%, where the experimental uncertainty largely dominates over the (underestimated) theoretical uncertainty.

5.1.4.2.e Final Results for the Other Parton Density Functions

Since Delphes v1.9 does not store the set of variables $(x_1, x_2, flav_1, flav_2, Q^2)$ necessary to access the PDF information from the generator, we slightly modify it so as to retrieve the "HepMC::PdfInfo" object from the HepMC event record and to store it within the Delphes GEN branch as described in [288].

Based upon these variables we can apply PDF re-weightings so as to make experimental A_C predictions for the CTEQ6L1 and the MSTW2008lo68cl PDFs. The new event weight is calculated in the standard way:

$$\text{PDFweight(New PDF)} = \frac{f_{\text{Flav}_1}^{\text{New PDF}}(x_1, Q^2)}{f_{\text{Flav}_1}^{\text{Old PDF}}(x_1, Q^2)} \times \frac{f_{\text{Flav}_2}^{\text{New PDF}}(x_2, Q^2)}{f_{\text{Flav}_2}^{\text{Old PDF}}(x_2, Q^2)} \quad (5.34)$$

where the "Old PDF" is the default one, MRST2007lomod, and the "New PDF" is either CTEQ6L1 or MSTW2008lo68cl.

We re-run the electron and muon channel analyses and just change the weights of all the selected events. This results in signal event yields, and $A_C^{Exp}(S)$, $A_C^{Exp}(B)$ as reported in tables 5.21 and 5.22 for the CTEQ6L1 PDF and in tables 5.23 and 5.24 for the MSTW2008lo68cl one.

Then we produce the experimental A_C template curves for CTEQ6L1 and MSTW2008lo68cl and both analysis channels as displayed in figures 5.17 and 5.18.

For the CTEQ6L1 PDF, we find:

$$A_C^{Meas.Fit}(S) = (15.78 \pm 0.50)\% \Rightarrow M^{Meas}(W^\pm \rightarrow e^\pm \nu_e) = 73.39_{-2.30}^{+2.40} \text{ GeV}, \quad (5.35)$$

$$A_C^{Meas.Fit}(S) = (17.42 \pm 0.18)\% \Rightarrow M^{Meas}(W^\pm \rightarrow \mu^\pm \nu_\mu) = 79.82_{-0.92}^{+0.94} \text{ GeV} \quad (5.36)$$

which leads to the following combined value:

$$M^{Comb.Meas.}(W^\pm \rightarrow \ell^\pm \nu_\ell) = (78.95 \pm 0.61) \text{ GeV [Expt. CTEQ6L1]} \quad (5.37)$$

M_{W^\pm} (GeV)	$N_{Exp}(S)$ (k Evts)	$A_C^{Exp}(S)$ (%)
40.2 e^\pm	288.688±5.866	11.26±2.06
40.2 μ^\pm	947.643±11.535	7.86±1.28
60.3 e^\pm	2491.955±10.746	10.65±0.49
60.3 μ^\pm	5285.294±16.847	12.30±0.40
80.4 e^\pm	3766.569±8.423	15.78±0.29
80.4 μ^\pm	5551.710±6.752	17.42±0.18
100.5 e^\pm	4106.984±5.009	20.64±0.19
100.5 μ^\pm	4188.292±4.997	21.48±0.19
120.6 e^\pm	2739.825±4.796	23.54±0.26
120.6 μ^\pm	3777.497±4.730	23.93±0.25
140.7 e^\pm	2284.590±3.512	25.52±0.25
140.7 μ^\pm	3020.544±3.268	26.56±0.23
160.8 e^\pm	1584.146±2.512	27.07±0.24
160.8 μ^\pm	2461.819±2.255	27.90±0.23
201.0 e^\pm	1.259±0.002	29.57±0.23
201.0 μ^\pm	1.628±0.001	30.64±0.15

TABLE 5.21: Number of expected signal events and expected signal A_C as a function of $M(W^\pm)$ for the electron and muon analyses reweighted to the CTEQ6L1 PDF predictions.

W^\pm Decay Channel	$N_{Exp}(B)$ (k Evts)	$A_C^{Exp}(B)$ (%)
e^\pm	352.660 ± 7.996	9.74 ± 0.23
μ^\pm	707.617 ± 29.944	7.45 ± 0.15

TABLE 5.22: Number of expected background events and expected background A_C for the electron (upper line) and the muon (lower line) analyses reweighted to the CTEQ6L1 PDF predictions.

To this measured central value of the mass correspond the following theoretical uncertainties:

$$M(W^\pm) = 78.95^{+0.11}_{-0.13} \text{ GeV [Theory CTEQ6L1]}, \quad (5.38)$$

Therefore the final result for the CTEQ6L1 PDF reads:

$$M(W^\pm) = 78.95^{+0.62}_{-0.62} \text{ GeV [Total CTEQ6L1]} \quad (5.39)$$

and it's dominant uncertainty is also experimental, since its theoretical uncertainty is underestimated. This represents an indirect measurement of the W^\pm mass with a relative accuracy of 0.8%.

For the MSTW2008lo68cl PDF:

$$A_C^{Meas.Fit}(S) = (15.78 \pm 0.52)\% \Rightarrow M^{Meas}(W^\pm \rightarrow e^\pm \nu_e) = 76.91^{+2.80}_{-2.74} \text{ GeV}, \quad (5.40)$$

$$A_C^{Meas.Fit}(S) = (17.42 \pm 0.18)\% \Rightarrow M^{Meas}(W^\pm \rightarrow \mu^\pm \nu_\mu) = 82.07^{+1.11}_{-1.10} \text{ GeV} \quad (5.41)$$

which leads to the following combined value:

$$M^{Comb.Meas.}(W^\pm \rightarrow \ell^\pm \nu_\ell) = (81.36 \pm 0.73) \text{ GeV} \quad (5.42)$$

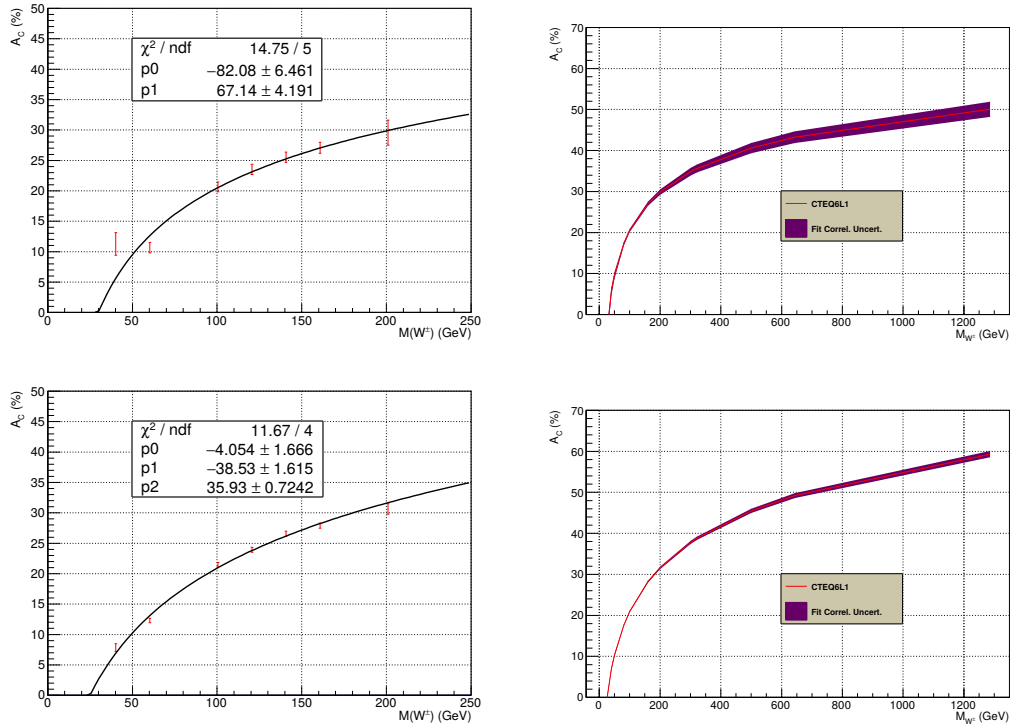


FIGURE 5.17: The CTEQ6L1 A_C template curves for the $W^\pm \rightarrow e^\pm \nu_e$ (top) and the $W^\pm \rightarrow \mu^\pm \nu_\mu$ (bottom) analyses. The fits to the $A_C^{Exp}(S)$ are presented on the LHS. These fits with uncertainty bands accounting for the correlation between the uncertainties of the fit parameters are shown on the RHS.

M_{W^\pm} (GeV)	$N_{Exp}(S)$ (k EvtS)	$A_C^{Exp}(S)$ (%)
40.2 e^\pm	280.257 ± 5.781	11.26 ± 2.06
40.2 μ^\pm	913.868 ± 11.334	7.86 ± 1.28
60.3 e^\pm	2469.515 ± 10.705	10.65 ± 0.49
60.3 μ^\pm	5219.408 ± 16.783	12.30 ± 0.40
80.4 e^\pm	3663.615 ± 8.363	15.78 ± 0.29
80.4 μ^\pm	5711.468 ± 6.753	17.42 ± 0.18
100.5 e^\pm	4053.288 ± 5.016	20.64 ± 0.19
100.5 μ^\pm	4165.175 ± 5.000	21.48 ± 0.19
120.6 e^\pm	2665.994 ± 4.800	23.54 ± 0.26
120.6 μ^\pm	3811.380 ± 4.697	23.93 ± 0.25
140.7 e^\pm	2221.101 ± 3.530	25.52 ± 0.25
140.7 μ^\pm	3033.091 ± 3.252	26.56 ± 0.23
160.8 e^\pm	1539.501 ± 2.516	27.07 ± 0.24
160.8 μ^\pm	2446.996 ± 2.280	27.90 ± 0.23
201.0 e^\pm	1.230 ± 0.002	29.57 ± 0.23
201.0 μ^\pm	1.645 ± 0.001	30.64 ± 0.15

TABLE 5.23: Number of expected signal events and expected signal A_C as a function of $M(W^\pm)$ for the electron and muon analyses reweighted to the MSTW2008lo68cl PDF predictions.

The corresponding theoretical uncertainties are:

$$M(W^\pm) = 81.36_{-1.32}^{+1.50} \text{ GeV [Theory MSTW2008lo68cl]}, \quad (5.43)$$

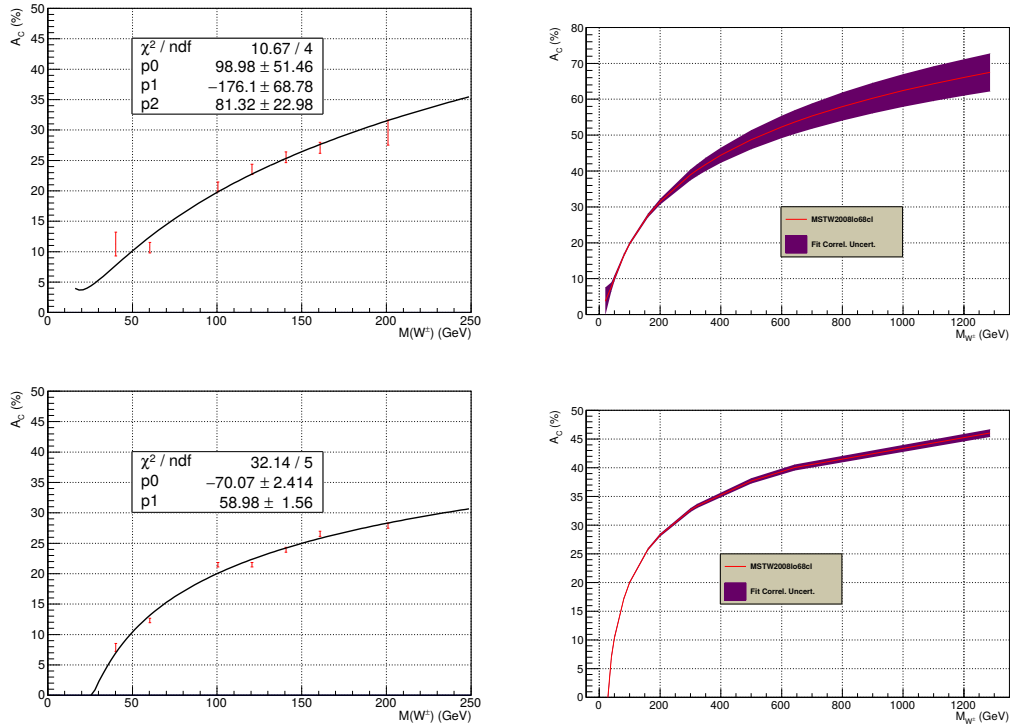


FIGURE 5.18: The MSTW2008lo68cl A_C template curves for the $W^\pm \rightarrow e^\pm \nu_e$ (top) and the $W^\pm \rightarrow \mu^\pm \nu_\mu$ (bottom) analyses. The fits to the $A_C^{Exp}(S)$ are presented on the LHS. These fits with uncertainty bands accounting for the correlation between the uncertainties of the fit parameters are shown on the RHS.

W^\pm Decay Channel	$N_{Exp}(B)$ (k Evt)	$A_C^{Exp}(B)$ (%)
e^\pm	371.956 ± 8.081	9.74 ± 0.23
μ^\pm	721.196 ± 29.968	7.45 ± 0.15

TABLE 5.24: Number of expected background events and expected background A_C for the electron (upper line) and muon (lower line) analyses reweighted to the MSTW2008lo68cl PDF predictions.

Therefore the final result for the MSTW2008lo68cl PDF reads:

$$M(W^\pm) = 81.36^{+1.67}_{-1.51} \text{ GeV [Total MSTW2008lo68cl]} \quad (5.44)$$

and it's dominant uncertainty comes from $\delta_{PDF}^{Theory} A_C$. In this case, this represents an indirect measurement of the W^\pm mass with a relative accuracy of 2.1%.

5.1.4.2.f Summary of the M_{W^\pm} Measurements and their Accuracy

We sum up the indirect mass measurements of M_{W^\pm} extracted from the integral charge asymmetry of the $W^\pm \rightarrow \ell^\pm \nu$ inclusive process within table 5.25. Therein we also present a few figures of merit of the accuracy of these measurements:

1. $\frac{\delta M_{W^\pm}^{Fit}}{M_{W^\pm}^{Fit}}$
2. $\frac{(M_{W^\pm}^{Fit} - M_{W^\pm}^{True})}{M_{W^\pm}^{True}}$
3. $\frac{(M_{W^\pm}^{Fit} - M_{W^\pm}^{True})}{\delta M_{W^\pm}^{Fit}}$

In this notation, $M_{W^\pm}^{Fit}$ and $\delta M_{W^\pm}^{Fit}$ represent the indirectly measured M_{W^\pm} and its uncertainty, and $M_{W^\pm}^{True}$ stands for the nominal W^\pm boson mass.

The first figure of merit (1.) reflects the intrinsic resolution power of the indirect mass measurement, irrespective of its possible biases, it's expressed in %. The second and the third ones measure the accuracy with respect to the nominal W^\pm boson mass: firstly as a relative uncertainty in % irrespective of the method precision (2.) and secondly as a compatibility between the nominal and the predicted masses given the method precision (3.), expressed in number of standard deviations (σ).

Figure of Merit of the Accuracy	Considered LO PDFs		
	MRST2007lomod	CTEQ6L1	MSTW2008lo68cl
1. $\frac{\delta M_{W^\pm}^{Fit}}{M_{W^\pm}^{Fit}}$	1.2%	0.8%	2.1%
2. $\frac{(M_{W^\pm}^{Fit} - M_{W^\pm}^{True})}{M_{W^\pm}^{True}}$	-0.1%	-1.8%	+1.2%
3. $\frac{(M_{W^\pm}^{Fit} - M_{W^\pm}^{True})}{\delta M_{W^\pm}^{Fit}}$	-0.1 σ	-2.3 σ	+0.6 σ

TABLE 5.25: Summary of the indirect mass measurements of M_{W^\pm} extracted from the integral charge asymmetry of the $W^\pm \rightarrow \ell^\pm \nu$ process. Different figures of merit of the accuracy of these measurements are presented.

The values of the figures of merit in table 5.25 show that already at LO, this new method enables to get a good estimate of the W^\pm boson mass.

5.1.4.3 Inclusive Production of $\tilde{\chi}_1^\pm + \tilde{\chi}_2^0 \rightarrow 3\ell^\pm + \cancel{E}_T$

5.1.4.3.a Theoretical Prediction of $A_C(\tilde{\chi}_1^\pm + \tilde{\chi}_2^0)$

In this section we repeat the types of calculations done in section 5.1.4.2.a but now for a process of interest in R-parity conserving SUSY searches, namely the $p + p \rightarrow \tilde{\chi}_1^\pm + \tilde{\chi}_2^0 \rightarrow 3\ell^\pm + \cancel{E}_T$ inclusive production.

We use Resummino v1.0.0 [250] to calculate the $p + p \rightarrow \tilde{\chi}_1^\pm + \tilde{\chi}_2^0$ cross sections at different levels of theoretical accuracy. At fixed order in QCD we run these calculations at the LO and the NLO. In addition, we also run them starting from the NLO MEs and including the "Next-to-Leading Log" (NLL) analytically resummed corrections. The latter, sometimes referred to as "NLO+NLL" will simply be denoted "NLL" in the following.

We calculate these cross sections at $\sqrt{s} = 8$ TeV using "Simplified Models" [249] for the following masses:

$$M(\tilde{\chi}_1^\pm) = M(\tilde{\chi}_2^0) = 100, 105, 115, 125, 135, 145, 150, 200, 250, 300, 400, 500, 600, 700 \text{ GeV}$$

and using the PDFs reported in table 5.26. We set the QCD scales as $\mu_R = \mu_F = \mu_0 = M(\tilde{\chi}_1^\pm) + M(\tilde{\chi}_2^0)$. Regarding the phase space sampling, a statistical precision of 0.1% is requested for the numerical integration of the cross sections.

LO	NLO & NLL
MRST2007lomod CTEQ6L1	MRST2004nlo CTEQ6.1
MSTW2008lo68cl	MSTW2008nlo68cl

TABLE 5.26: PDFs used for the calculations of $\sigma(\tilde{\chi}_1^\pm + \tilde{\chi}_2^0)$ at the LO in QCD and the NLO and the NLL.

The integral charge asymmetries as functions of $M(\tilde{\chi}_1^\pm) + M(\tilde{\chi}_2^0)$ for this process are presented in tables 5.27, 5.29, and 5.31 for the MRST2007lomod/MRST2004nlo, the CTEQ6L1/CTEQ6.1, and the MSTW2008lo68cl/MSTW2008nlo68cl PDFs, respectively.

$A_C(\tilde{\chi}_1^\pm + \tilde{\chi}_2^0)$ Template Curves for MRST The theoretical MRST A_C template curves are obtained by computing the A_C based upon the cross sections of the signed processes used for table 5.27. They are displayed in figure 5.19.

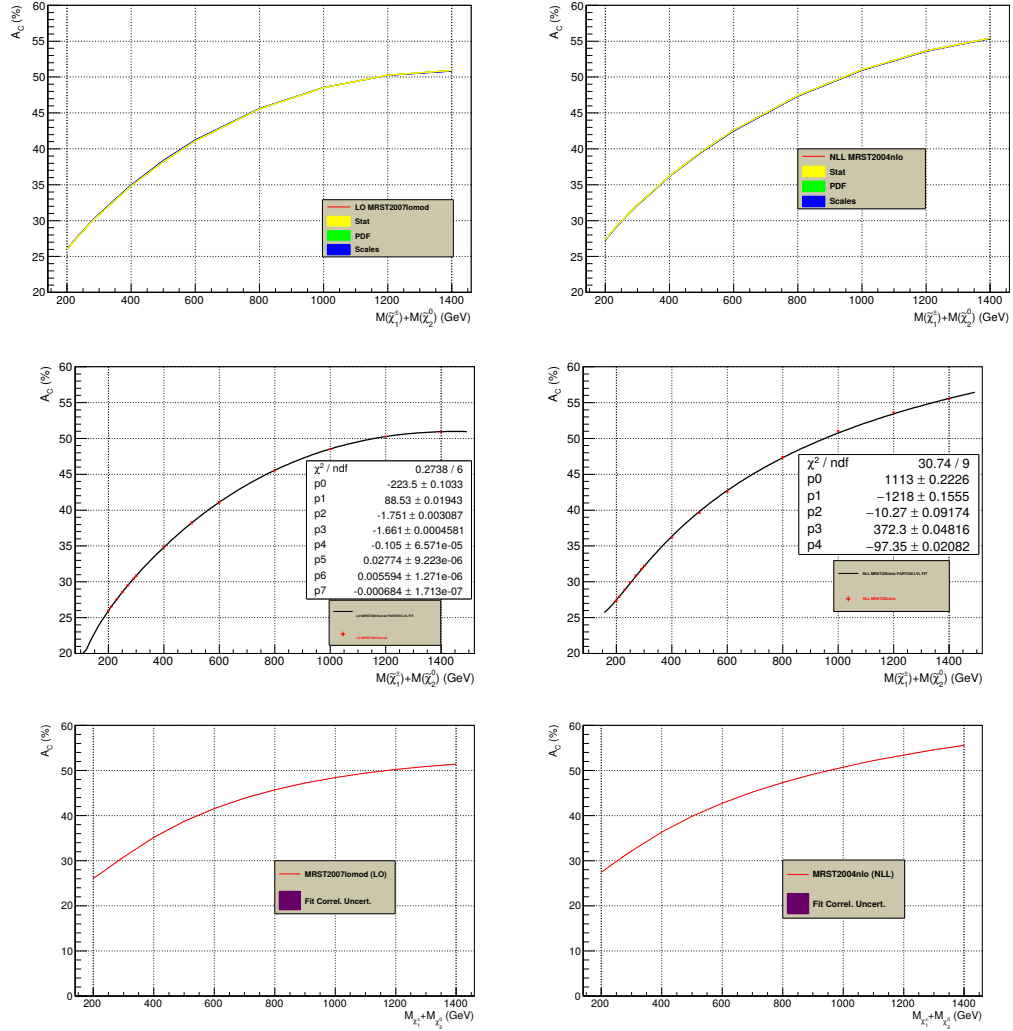


FIGURE 5.19: The theoretical MRST A_C template curves. The raw curve with its uncertainty bands and the corresponding fitted curve with uncorrelated and with correlated uncertainties are displayed on the top, the middle and the bottom rows, respectively. The LHS concerns the LO calculations based upon the MRST2007lomod PDF and the RHS concerns the NLL calculations using the MRST2004nlo PDF.

$A_C(\tilde{\chi}_1^\pm + \tilde{\chi}_2^0)$ Template Curves for CTEQ6 The theoretical CTEQ6 A_C template curves are obtained by computing the A_C based upon the cross sections of the signed processes used for table 5.29. They are displayed in figure 5.20.

$M_{\tilde{\chi}_1^\pm} + M_{\tilde{\chi}_2^0}$ (GeV)	A_C (%)	$\delta(A_C)_{Stat}$ (%)	$\delta(A_C)_{Scale}$ (%)	$\delta(A_C)_{PDF}$ (%)	$\delta(A_C)_{Total}$ (%)
200.	LO: 25.991	± 0.004	-0.037	0.000	+0.037
	NLL: 27.363	± 0.011	+0.056 +0.092 -0.074	not quoted	-0.056 +0.093 -0.075
210.	LO: 26.52	± 0.003	-0.046	0.000	+0.046
	NLL: 27.904	± 0.009	+0.063 +0.100 -0.066	not quoted	-0.063 +0.101 -0.067
230.	LO: 27.562	± 0.002	-0.061	0.000	+0.061
	NLL: 28.938	± 0.006	+0.074 +0.098 -0.056	not quoted	-0.074 +0.099 -0.057
250.	LO: 28.549	± 0.002	-0.073	0.000	+0.073
	NLL: 29.934	± 0.004	+0.085 +0.084 -0.072	not quoted	-0.085 +0.084 -0.073
270.	LO: 29.495	± 0.001	-0.084	0.000	+0.084
	NLL: 30.877	± 0.003	+0.094 +0.085 -0.088	not quoted	-0.094 +0.085 -0.088
290.	LO: 30.403	± 0.001	-0.094	0.000	+0.094
	NLL: 31.786	± 0.002	+0.102 +0.079 -0.091	not quoted	-0.102 +0.079 -0.091
300.	LO: 30.844	± 0.001	-0.098	0.000	+0.098
	NLL: 32.229	± 0.002	+0.106 +0.076 -0.093	not quoted	-0.106 +0.076 -0.093
400.	LO: 34.847	± 0.000	-0.125	0.000	+0.125
	NLL: 36.213	± 0.001	+0.126 +0.086 -0.069	not quoted	-0.126 +0.086 -0.069
500.	LO: 38.230	± 0.000	-0.132	0.000	+0.132
	NLL: 39.648	± 0.000	+0.131 +0.101 -0.100	not quoted	-0.131 +0.101 -0.100
600.	LO: 41.101	± 0.000	-0.127	0.000	+0.127
	NLL: 42.600	± 0.000	+0.124 +0.104 -0.129	not quoted	-0.124 +0.104 -0.129
800.	LO: 45.548	± 0.000	-0.091	0.000	+0.091
	NLL: 47.420	± 0.000	+0.086 +0.118 -0.073	not quoted	-0.086 +0.118 -0.073
1000.	LO: 48.528	± 0.000	-0.038	0.000	+0.038
	NLL: 51.035	± 0.000	+0.033 +0.116 -0.063	not quoted	-0.033 +0.116 -0.063
1200.	LO: 50.264	± 0.000	+0.024	0.000	+0.024
	NLL: 53.658	± 0.000	-0.025 +0.101 +0.021	not quoted	-0.025 +0.101 -0.021
1400.	LO: 50.924	± 0.000	+0.088	0.000	+0.088
	NLL: 55.404	± 0.000	-0.081 +0.008 -0.083	not quoted	-0.081 +0.008 -0.083

TABLE 5.27: The MRST $A_C(\tilde{\chi}_1^\pm \tilde{\chi}_2^0)$ table with the breakdown of the different sources of theoretical uncertainty.

$M_{\tilde{\chi}_1^\pm} + M_{\tilde{\chi}_2^0}$ (GeV)	A_C^{Fit} (%)	δA_C^{Fit} (%)
200.	LO: 25.984 NLL: 27.435	± 0.025 ± 0.031
210.	LO: 26.530 NLL: 27.927	± 0.024 ± 0.030
230.	LO: 27.571 NLL: 28.904	± 0.024 ± 0.028
250.	LO: 28.557 NLL: 29.866	± 0.023 ± 0.027
270.	LO: 29.498 NLL: 30.807	± 0.023 ± 0.027
290.	LO: 30.400 NLL: 31.724	± 0.022 ± 0.026
300.	LO: 30.838 NLL: 32.172	± 0.022 ± 0.026
400.	LO: 34.824 NLL: 36.286	± 0.021 ± 0.025
500.	LO: 38.215 NLL: 39.768	± 0.020 ± 0.027
600.	LO: 41.102 NLL: 42.720	± 0.019 ± 0.029
800.	LO: 45.562 NLL: 47.400	± 0.016 ± 0.034
1000.	LO: 48.532 NLL: 50.881	± 0.015 ± 0.041
1200.	LO: 50.261 NLL: 53.508	± 0.017 ± 0.049
1400.	LO: 50.945 NLL: 55.501	± 0.022 ± 0.057

TABLE 5.28: The MRST $A_C^{Fit}(\tilde{\chi}_1^\pm, \tilde{\chi}_2^0)$ table with its theoretical uncertainty accounting for the correlations between the parameters fitting the A_C^{Raw} template curves.

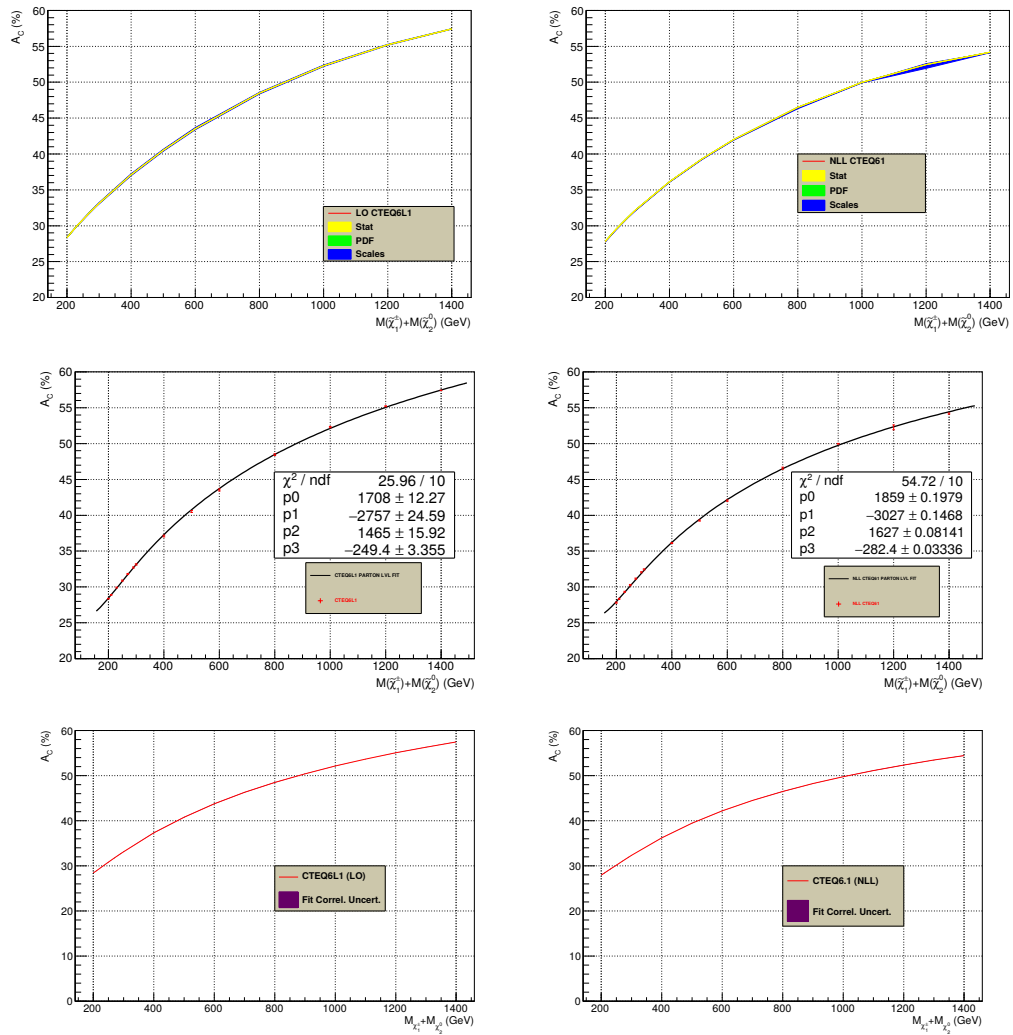


FIGURE 5.20: The theoretical CTEQ6 A_C template curves. The raw curve with its uncertainty bands and the corresponding fitted curve with uncorrelated and with correlated uncertainties are displayed on the top, the middle and the bottom rows, respectively. The LHS concerns the LO calculations based upon the CTEQ6L1 PDF and the RHS concerns the NLL calculations using the CTEQ6.1 PDF.

$M_{\tilde{\chi}_1^\pm} + M_{\tilde{\chi}_2^0}$ (GeV)	A_C (%)	$\delta(A_C)_{Stat}$ (%)	$\delta(A_C)_{Scale}$ (%)	$\delta(A_C)_{PDF}$ (%)	$\delta(A_C)_{Total}$ (%)
200.	LO: 28.367	± 0.003	-0.030	0.000	+0.030
	NLL: 27.822	± 0.010	+0.045 +0.076 -0.074	not quoted	-0.045 +0.077 -0.075
210.	LO: 28.896	± 0.003	-0.038	0.000	+0.038
	NLL: 28.345	± 0.008	+0.051 +0.084 -0.069	not quoted	-0.051 +0.084 -0.069
230.	LO: 29.911	± 0.002	-0.053	0.000	+0.053
	NLL: 29.333	± 0.006	+0.064 +0.102 -0.054	not quoted	-0.064 +0.102 -0.054
250.	LO: 30.880	± 0.001	-0.066	0.000	+0.066
	NLL: 30.273	± 0.004	+0.074 +0.093 -0.064	not quoted	+0.074 +0.093 -0.064
270.	LO: 31.808	± 0.001	-0.077	0.000	+0.077
	NLL: 31.169	± 0.003	+0.084 +0.078 -0.070	not quoted	-0.084 +0.078 -0.070
290.	LO: 32.701	± 0.001	-0.087	0.000	+0.087
	NLL: 32.026	± 0.002	+0.092 +0.065 -0.090	not quoted	-0.092 +0.065 -0.090
300.	LO: 33.135	± 0.001	-0.091	0.000	+0.091
	NLL: 32.434	± 0.002	+0.096 +0.065 -0.089	not quoted	-0.096 +0.065 -0.089
400.	LO: 37.104	± 0.000	-0.121	0.000	+0.121
	NLL: 36.136	± 0.001	+0.121 +0.080 -0.055	not quoted	-0.121 +0.080 -0.055
500.	LO: 40.531	± 0.000	-0.134	0.000	+0.134
	NLL: 39.285	± 0.000	+0.131 +0.088 -0.057	not quoted	-0.131 +0.088 -0.057
600.	LO: 43.527	± 0.000	-0.137	0.000	+0.137
	NLL: 42.023	± 0.000	+0.132 +0.056 -0.119	not quoted	-0.132 +0.056 -0.119
800.	LO: 48.473	± 0.000	-0.121	0.000	+0.121
	NLL: 46.514	± 0.000	+0.116 +0.094 -0.194	not quoted	-0.116 +0.094 -0.194
1000.	LO: 52.293	± 0.000	-0.094	0.000	+0.094
	NLL: 49.985	± 0.000	+0.090 +0.054 -0.053	not quoted	-0.090 +0.054 -0.053
1200.	LO: 55.219	± 0.000	-0.063	0.000	+0.063
	NLL: 52.447	± 0.000	+0.061 +0.528 +0.147	not quoted	-0.061 +0.528 -0.147
1400.	LO: 57.428	± 0.000	-0.034	0.000	+0.034
	NLL: 54.190	± 0.000	+0.033 +0.069 -0.081	not quoted	-0.033 +0.069 -0.081

TABLE 5.29: The CTEQ6 $A_C(\tilde{\chi}_1^\pm \tilde{\chi}_2^0)$ table with the breakdown of the different sources of theoretical uncertainty.

$M_{\tilde{\chi}_1^\pm} + M_{\tilde{\chi}_2^0}$ (GeV)	A_C^{Fit} (%)	δA_C^{Fit} (%)
200.	LO: 28.407 NLL: 27.811	± 0.034 ± 0.027
210.	LO: 28.900 NLL: 28.340	± 0.027 ± 0.026
230.	LO: 29.876 NLL: 29.342	± 0.023 ± 0.024
250.	LO: 30.832 NLL: 30.282	± 0.027 ± 0.023
270.	LO: 31.766 NLL: 31.172	± 0.032 ± 0.022
290.	LO: 32.674 NLL: 32.018	± 0.037 ± 0.022
300.	LO: 33.119 NLL: 32.428	± 0.038 ± 0.022
400.	LO: 37.203 NLL: 36.126	± 0.046 ± 0.023
500.	LO: 40.687 NLL: 39.287	± 0.048 ± 0.026
600.	LO: 43.675 NLL: 42.041	± 0.052 ± 0.027
800.	LO: 48.507 NLL: 46.558	± 0.058 ± 0.030
1000.	LO: 52.220 NLL: 49.977	± 0.052 ± 0.033
1200.	LO: 55.133 NLL: 52.477	± 0.034 ± 0.041
1400.	LO: 57.447 NLL: 54.189	± 0.032 ± 0.052

TABLE 5.30: The CTEQ $A_C^{Fit}(\tilde{\chi}_1^\pm, \tilde{\chi}_2^0)$ table with its theoretical uncertainty accounting for the correlations between the parameters fitting the A_C^{Raw} template curves.

$A_C(\tilde{\chi}_1^\pm + \tilde{\chi}_2^0)$ Template Curves for MSTW2008 The theoretical MSTW2008lo68cl A_C template curves are obtained by computing the A_C based upon the cross sections of the signed processes used for table 5.31. They are displayed in figure 5.21.

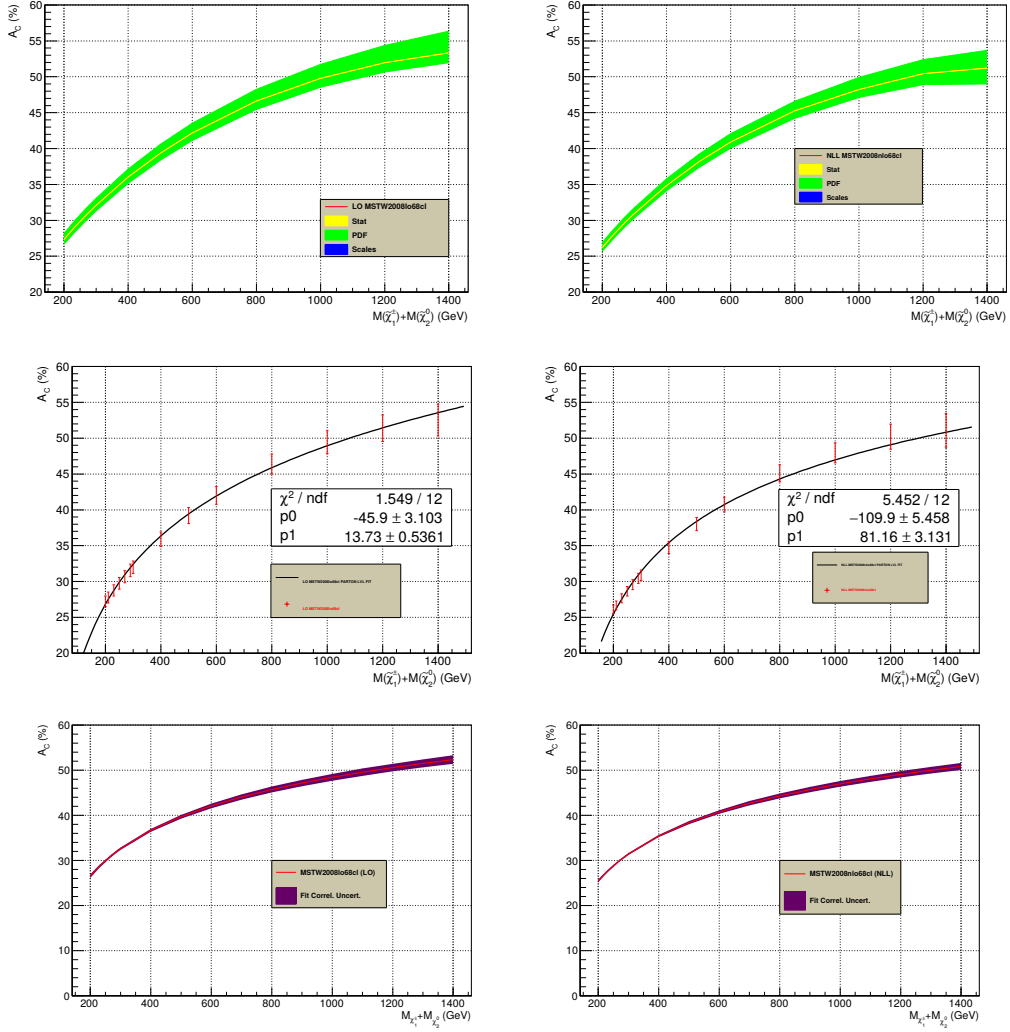


FIGURE 5.21: The theoretical MSTW2008 A_C template curves. The raw curve with its uncertainty bands and the corresponding fitted curve with uncorrelated and with correlated uncertainties are displayed on the top, the middle and the bottom rows, respectively. The LHS concerns the LO calculations based upon the MSTW2008lo68cl PDF and the RHS concerns the NLL calculations using the MSTW2008nl68cl PDF.

$M_{\tilde{\chi}_1^\pm} + M_{\tilde{\chi}_2^0}$ (GeV)	A_C (%)	$\delta(A_C)_{Stat}$ (%)	$\delta(A_C)_{Scale}$ (%)	$\delta(A_C)_{PDF}$ (%)	$\delta(A_C)_{Total}$ (%)
200.	LO: 27.330	± 0.003	-0.034 +0.049	+0.827 -0.649	+0.828 -0.651
	NLL: 26.215	± 0.011	+0.091 -0.067	+0.682 -0.518	+0.688 -0.522
210.	LO: 27.857	± 0.003	-0.042 +0.056	+0.845 -0.663	+0.846 -0.665
	NLL: 26.744	± 0.009	+0.080 -0.056	+0.694 -0.530	+0.698 -0.533
230.	LO: 28.872	± 0.002	-0.068 +0.085	+0.878 -0.690	+0.880 -0.693
	NLL: 27.757	± 0.006	+0.040 -0.069	+0.722 -0.549	+0.727 -0.550
250.	LO: 29.842	± 0.001	-0.078 +0.073	+0.911 -0.716	+0.913 -0.720
	NLL: 28.730	± 0.004	+0.053 -0.080	+0.747 -0.573	+0.751 -0.575
270.	LO: 30.770	± 0.001	-0.087 +0.063	+0.942 -0.742	+0.945 -0.747
	NLL: 29.658	± 0.003	+0.069 -0.088	+0.773 -0.595	+0.775 -0.599
290.	LO: 31.662	± 0.001	-0.094 +0.058	+0.972 -0.766	+0.976 -0.772
	NLL: 30.540	± 0.002	+0.080 -0.092	+0.802 -0.608	+0.804 -0.613
300.	LO: 32.096	± 0.001	-0.097 +0.068	+0.987 -0.778	+0.991 -0.784
	NLL: 30.969	± 0.002	+0.089 -0.117	+0.802 -0.625	+0.805 -0.632
400.	LO: 36.028	± 0.000	-0.117 +0.117	+1.123 -0.885	+1.129 -0.893
	NLL: 34.846	± 0.001	+0.105 -0.043	+0.929 -0.713	+0.935 -0.714
500.	LO: 39.351	± 0.000	-0.123 +0.122	+1.250 -0.971	+1.256 -0.979
	NLL: 38.145	± 0.000	+0.097 -0.093	+1.042 -0.803	+1.047 -0.808
600.	LO: 42.179	± 0.000	-0.118 +0.116	+1.372 -1.043	+1.377 -1.050
	NLL: 40.906	± 0.000	+0.121 -0.103	+1.171 -0.841	+1.177 -0.847
800.	LO: 46.628	± 0.000	-0.088 +0.085	+1.627 -1.161	+1.629 -1.164
	NLL: 45.265	± 0.000	+0.101 -0.080	+1.352 -1.027	+1.356 -1.030
1000.	LO: 49.793	± 0.000	-0.051 +0.046	+1.953 -1.242	+1.953 -1.243
	NLL: 48.243	± 0.000	+0.112 -0.019	+1.674 -1.124	+1.678 -1.125
1200.	LO: 51.956	± 0.000	-0.014 +0.013	+2.407 -1.301	+2.408 -1.301
	NLL: 50.430	± 0.000	+0.031 -0.000	+1.966 -1.534	+1.966 -1.534
1400.	LO: 53.328	± 0.000	-0.018 -0.013	+3.019 -1.375	+3.019 -1.375
	NLL: 51.216	± 0.000	+0.082 +0.060	+2.470 -2.216	+2.472 -2.217

TABLE 5.31: The MSTW2008 $A_C(\tilde{\chi}_1^\pm \tilde{\chi}_2^0)$ table with the breakdown of the different sources of theoretical uncertainty.

Comparing the different A_C Template Curves

Here again we compare the A_C template curves produced with different PDFs using Resummino this time. From figure 5.22 we can see that the A_C of the different PDF used at LO and at NLO are in agreement only at the $\pm 3\sigma$ level. This figure also displays the $\frac{A_C^{NLL}}{A_C^{LO}}$ ratios for the three families of PDFs used.

$M_{\tilde{\chi}_1^\pm} + M_{\tilde{\chi}_2^0}$ (GeV)	A_C^{Fit} (%)	δA_C^{Fit} (%)
200.	LO: 26.841746 NLL: 25.767	± 0.358 ± 0.304
210.	LO: 27.512 NLL: 26.426	± 0.341 ± 0.286
230.	LO: 28.761 NLL: 27.656	± 0.310 ± 0.257
250.	LO: 29.905 NLL: 28.783	± 0.287 ± 0.235
270.	LO: 30.962 NLL: 29.824	± 0.271 ± 0.220
290.	LO: 31.943 NLL: 30.790	± 0.261 ± 0.212
300.	LO: 32.409 NLL: 31.248	± 0.258 ± 0.211
400.	LO: 36.358 NLL: 35.138	± 0.282 ± 0.251
500.	LO: 39.422 NLL: 38.1545	± 0.350 ± 0.328
600.	LO: 41.925 NLL: 40.619	± 0.423 ± 0.405
800.	LO: 45.875 NLL: 44.509	± 0.554 ± 0.537
1000.	LO: 48.939 NLL: 47.526	± 0.663 ± 0.644
1200.	LO: 51.442 NLL: 49.991	± 0.754 ± 0.733
1400.	LO: 53.559 NLL: 52.075	± 0.832 ± 0.810

TABLE 5.32: The MSTW $A_C^{Fit}(\tilde{\chi}_1^\pm \tilde{\chi}_2^0)$ table with its theoretical uncertainty accounting for the correlations between the parameters fitting the A_C^{Raw} template curve.

5.1.4.3.b Experimental Measurement of $A_C(\tilde{\chi}_1^\pm + \tilde{\chi}_2^0 \rightarrow 3\ell^\pm + \cancel{E}_T)$

The aim of this sub-section is to repeat, in the context of the considered SUSY signal, a study similar to that of section 5.1.4.2.b.

We use Simplified Models to generate our signal in the two configurations shown in figure 5.23.

The first signal configuration, denoted S1, supposes that the lightest part of the SUSY mass spectrum is made of $\tilde{\chi}_1^\pm$, $\tilde{\chi}_2^0$, $\tilde{\ell}^\pm$ (i.e. \tilde{e}^\pm or $\tilde{\mu}^\pm$), and $\tilde{\chi}_1^0$, in order of decreasing mass. In addition, the following decays (and their charge conjugate) are all supposed to have a branching ratio of 100%: $\tilde{\chi}_1^\pm \rightarrow \tilde{\ell}^\pm (\rightarrow \ell^\pm \tilde{\chi}_1^0) + \nu$, $\tilde{\chi}_2^0 \rightarrow \tilde{\ell}^\pm (\rightarrow \ell^\pm \tilde{\chi}_1^0) + \ell^\mp$. In practice, within the MSSM, very large branching ratios for these decays are guaranteed by the envisaged mass hierarchy.

The second signal configuration, denoted S2, supposes that the lightest part of the SUSY mass spectrum is made of $\tilde{\chi}_1^\pm$, $\tilde{\chi}_2^0$, and $\tilde{\chi}_1^0$, in order of decreasing mass. The charged sleptons are supposed to be much heavier. In addition, the following SUSY decays are all supposed to have a branching ratio of 100%: $\tilde{\chi}_1^\pm \rightarrow W^\pm (\rightarrow \ell^\pm \nu) + \tilde{\chi}_1^0$, $\tilde{\chi}_2^0 \rightarrow Z^0 (\rightarrow \ell^\pm \ell^\mp) + \tilde{\chi}_1^0$. In practice, within the MSSM, these branching ratios not only depend on the envisaged mass hierarchy, but also on the fields composition of the $\tilde{\chi}_2^0$, the $\tilde{\chi}_1^\pm$, and the $\tilde{\chi}_1^0$. Regarding the SM leptonic decays of the

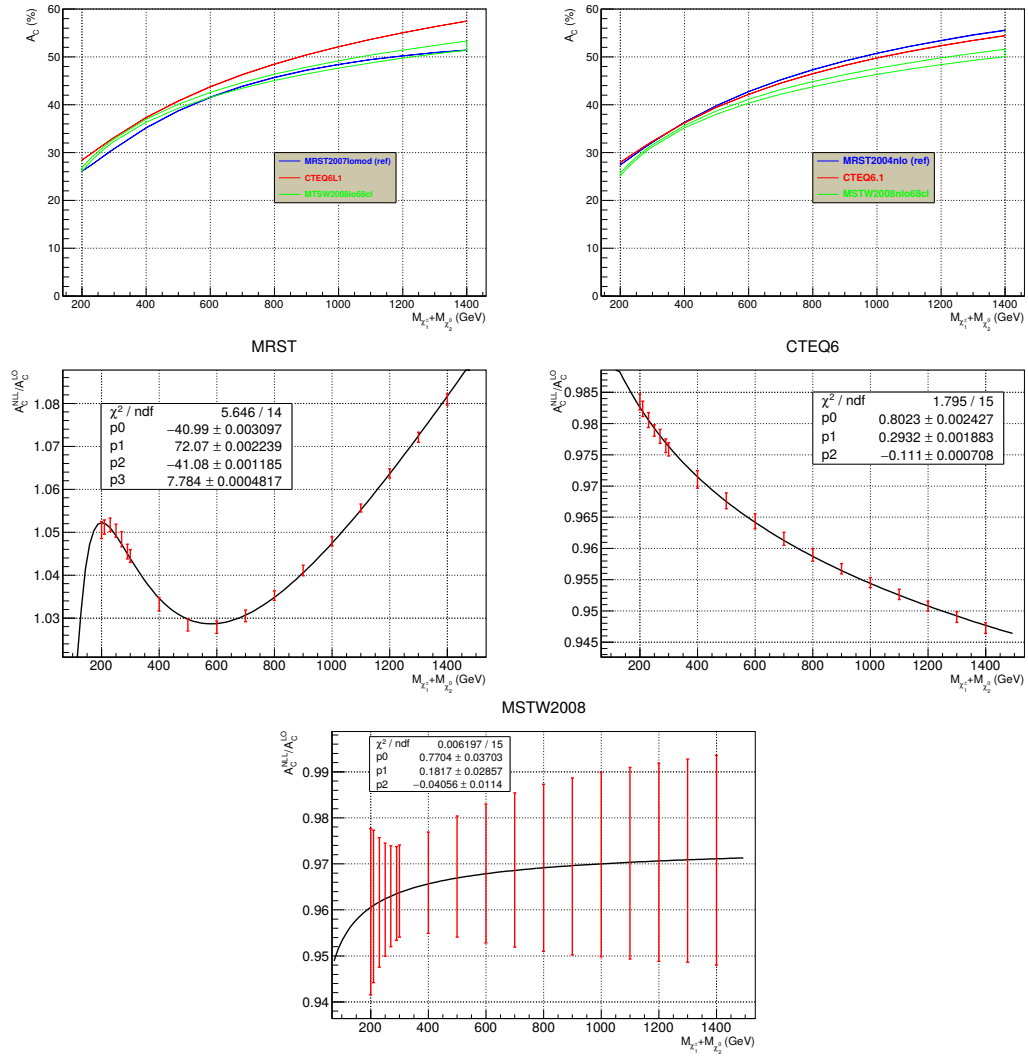


FIGURE 5.22: Comparison between the A_C template curves. The top LHS plot compares the LO PDFs: MRST2007lomod (blue, ref. curve), CTEQ6L1 (red), MSTW2008lo68cl (green). The top RHS plot compares the NLO PDFs: MRST2004nlo (blue, ref. curve), CTEQ6.1 (red), MSTW2008nlo68cl (green). The middle and the bottom rows display the $\frac{A_C^{NLL}}{A_C^{LO}}$ fitted by the same functional forms as the A_C^{LO} template curves.

W^\pm and the Z^0 gauge bosons, we used their actual SM branching ratios. This will have the obvious consequence of a much smaller event yield for the S2 signals compared to the S1 signals of same mass.

The hypotheses common to configurations S1 and S2 are that the lightest SUSY particle (LSP) is the $\tilde{\chi}_1^0$, and that the $\tilde{\chi}_2^0$ and the $\tilde{\chi}_1^\pm$ are mass degenerate.

At this stage, it's interesting to remind that the usual kinematical techniques applied to the R-parity conserving SUSY processes in general, and to the $\tilde{\chi}_1^\pm \tilde{\chi}_2^0 \rightarrow 3\ell^\pm + \cancel{E}_T$ in particular, only enable to reconstruct mass differences. More precisely, the mass of the same-flavor and opposite sign dilepton that comes from the $\tilde{\chi}_2^0$ decay have an end-point: $M^{Max}(\ell^\pm \ell^\mp)$ [297] which takes the values defined in table 5.33 depending on the mass hierarchy.



FIGURE 5.23: The sketch of the Simplified Models used to generate the signal samples: the S1 signal (LHS) has a $\tilde{\ell}^\pm$ NLSP whereas for the S2 signal (RHS) the mass degenerate $\tilde{\chi}_1^\pm$ and $\tilde{\chi}_2^0$ are the NLSPs. Both signals share the $\tilde{\chi}_1^0$ as the LSP.

Configuration	Kinematic End-Point	Condition
S1	$M^{Max}(\ell^\pm \ell^\mp) = \sqrt{\frac{[M^2(\tilde{\chi}_2^0) - M^2(\tilde{\ell}^\pm)][M^2(\tilde{\ell}^\pm) - M^2(\tilde{\chi}_1^0)]}{M^2(\tilde{\ell}^\pm)}}$	$M(\tilde{\chi}_2^0) > M(\tilde{\ell}^\pm) > M(\tilde{\chi}_1^0)$
S2	$M^{Max}(\ell^\pm \ell^\mp) = M(\tilde{\chi}_2^0) - M(\tilde{\chi}_1^0)$	$M(\tilde{\chi}_2^0) - M(\tilde{\chi}_1^0) < M_Z$ (S2a)
	$M(\ell^\pm \ell^\mp) \approx M_Z$	$M(\tilde{\chi}_2^0) - M(\tilde{\chi}_1^0) \geq M_Z$ (S2b)

TABLE 5.33: Kinematic end-points of the $\tilde{\chi}_2^0 \rightarrow \ell^\pm \ell^\mp \tilde{\chi}_1^0$ decays.

Monte Carlo Generation

We generate a new set of MC samples. We report here only the MC parameters that are different from those used in sub-section 5.1.4.2.b. We use the following LO generator: Herwig++ v2.5.2 for the SUSY signal and for most of the background processes.

The other background processes: $W^+ + W^- + W^\pm$, $W^+ + W^- + \gamma^*/Z$, $W^\pm + \gamma^*/Z + \gamma^*/Z$, $\gamma^*/Z + \gamma^*/Z + \gamma^*/Z$, $W^\pm + 1c + 0Lp$, $W^\pm + 1c + 1Lp$, $W^\pm + c\bar{c} + 0Lp$, $W^\pm + b\bar{b} + 0Lp$, $W^\pm + t\bar{t} + 0Lp$ are generated using Alpgen v2.14 at the parton level. Those samples are passed on to Pythia v8.170 for the parton showering, the fragmentation of the colored particles, the modelling of the underlying event and the decay of the unstable particles.

For the $W^\pm + HF$ process, and the VVV processes in Alpgen the only decay mode generated is $\gamma^*/Z (\rightarrow f\bar{f})$ where $f = \ell^\pm, \tau^\pm, \nu, q$ and $75 < M(f\bar{f}) < 125$ GeV, whereas for the $W^\pm (\rightarrow e^\pm \nu_e / \mu^\pm \nu_\mu / \tau^\pm \nu_\tau)$ process no mass cuts are applied.

For the $W + HF$ processes, the renormalization scale is set to

$$\mu_R = \mu_F = \sqrt{M^2(W) + \sum_{i=1}^{N_p^{FS}} M_T^2(i)}$$

where the i index runs over the number of FS partons N_p^{FS} , and where $M_T^2 = M^2 + p_T^2$.

In particular for the signal samples, we test distinct mass hypotheses in different configurations.

For the S1 signal, we vary $M(\tilde{\chi}_2^0)$ in the range [100,700] GeV by steps of 100 GeV, and we set $M(\tilde{\chi}_1^0) = M(\tilde{\chi}_2^0)/2$ and $M(\tilde{\ell}^\pm) = [M(\tilde{\chi}_2^0) + M(\tilde{\chi}_1^\pm)]/2$.

For the S2 signal, we produce a single "S2a" sample, i.e. with $M(\tilde{\chi}_2^0) - M(\tilde{\chi}_1^0) < M_Z$, for which we set $M(\tilde{\chi}_2^0) = 100$ GeV, $M(\tilde{\chi}_1^0) = 50$ GeV. This enables to explore the case where the $\tilde{\chi}_1^\pm$ and the $\tilde{\chi}_2^0$ decay through a W^\pm and through a Z that are both off-shell. For the other S2 samples, denoted "S2b" and described in the following paragraph, both the W^\pm and the Z bosons are on-shell. In addition, we vary $M(\tilde{\chi}_2^0)$ in the range [200,700] GeV by steps of 100 GeV, setting $M(\tilde{\chi}_1^0) = M(\tilde{\chi}_2^0)/2$. We also vary $M(\tilde{\chi}_2^\pm)$ in the range [105,145] GeV by steps of 10 GeV with a fixed value of $M(\tilde{\chi}_1^0) = 13.8$ GeV. And finally, we added two samples: $[M(\tilde{\chi}_2^0), M(\tilde{\chi}_1^0)] = [150,50]$ GeV and [250,125] GeV.

Analysis of the $\tilde{\chi}_1^\pm \tilde{\chi}_2^0 \rightarrow 3\ell^\pm + \cancel{E}_T$ Process

We considered only the electron and the muon channels. For these analyses we set the integrated luminosity to $\int \mathcal{L} dt = 20 \text{ fb}^{-1}$.

1). Event Selection in the Trilepton Channel

A first set of requirements related to the leptons are applied for the event selection as mentioned hereafter:

1. $N(\ell^\pm) \geq 3$

2. Electron candidates:

- (a) $|\eta(e^\pm)| < 1.37$ or $1.53 < |\eta(e^\pm)| < 2.47$

- (b) $p_T(e^\pm) > 10$ GeV

3. Muon candidates:

- (a) $|\eta(\mu^\pm)| < 2.4$

- (b) $p_T(\mu^\pm) > 10$ GeV

4. $p_T(\ell_1^\pm) > 20$ GeV

5. $p_T(\ell_2^\pm) > 10$ GeV

6. $p_T(\ell_3^\pm) > 10$ GeV

7. Tracker Isolation: reject events with additional tracks of $p_T > 2$ GeV within a cone of $\Delta R = 0.5$ around the direction of the ℓ^\pm track

8. Calorimeter Isolation: ratio of the scalar sum of E_T deposits in the calorimeter within a cone of $\Delta R = 0.5$ around the direction of the ℓ^\pm , to the $p_T(\ell^\pm)$ must be less than 1.2 for e^\pm and less than 0.25 for μ^\pm

9. $\cancel{E}_T > 35$ GeV

10. $M_{T2} > 75$ GeV

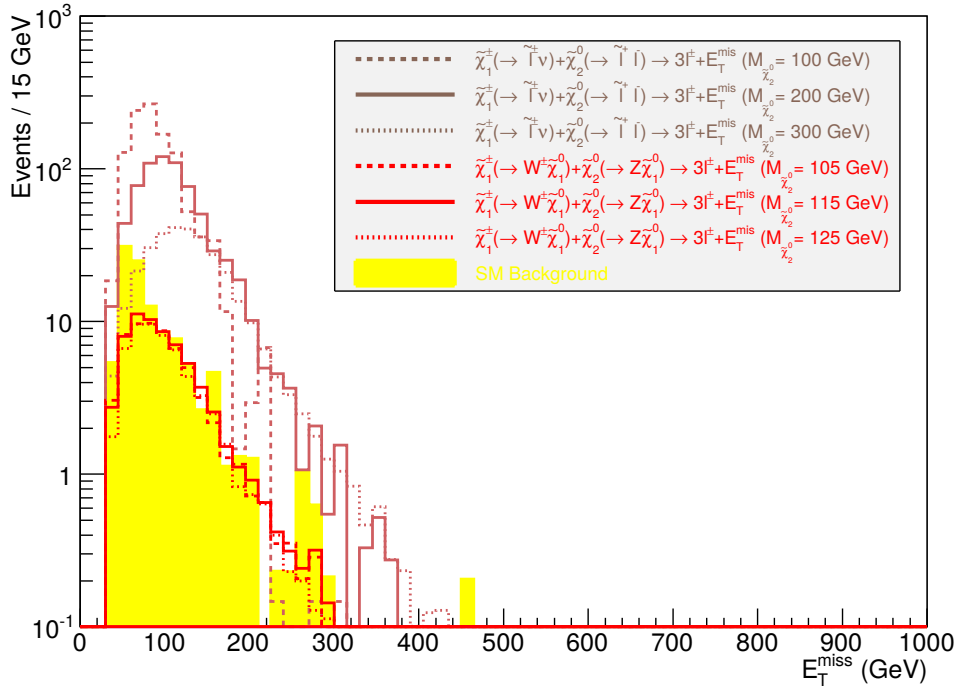


FIGURE 5.24: Distribution of the \cancel{E}_T after the event selection. The background, the S1, and the S2 signals are the filled yellow, the hollow brown, and the hollow red histograms, respectively.

The latter cut is applied on the so-called "stransverse mass": M_{T2} . We used a boost-corrected calculation of this variable as described in [295] and implemented in MCTLib [296].

The event selection efficiencies, event yields, signal significances and the expected integral charge asymmetries are reported in table 5.34. Figure 5.24 displays the \cancel{E}_T distribution after the event selection.

We note that the S1 signal significance exceeds 5σ for $M(\tilde{\chi}_2^0) = M(\tilde{\chi}_1^\pm)$ in the $[100,400]$ GeV interval, whereas the S2 signal significance reaches only the 3σ for $100 < M(\tilde{\chi}_2^0) = M(\tilde{\chi}_1^\pm) < 150$ GeV.

In this simple version of the analysis, we keep the same event selection for both the S1 and the S2 signals. Therefore these signal samples share the same residual background as well as the same bias from the event selection. In these conditions, we could use a common A_C template curve for both of them. However, because we choose many overlapping masses between these two signal samples, we split them into two separate sets of experimental A_C template curves. The S1 A_C template curve, that include the propagation of the realistic experimental uncertainties into each term of equation 5.17, are displayed in figure 5.25, the S2 ones are displayed in figure 5.26. And the final signal template curves for which the uncertainties account for the correlations between the parameters used to fit the A_C^{Meas} template curves are shown in figure 5.27, on the LHS for S1 and on the RHS for S2.

<i>Process</i>	ϵ (%)	N_{exp} (EvtS)	Z_N	$A_C^{Exp} \pm \delta A_C^{Stat}$ (%)
S1 Signal				
$[M(\tilde{\chi}_2^0), M(\tilde{\ell}^\pm), M(\tilde{\chi}_1^0)]$ GeV				
[100, 75, 50]	0.45 ± 0.01	1097.43	31.70	(7.70 ± 0.27)
[200, 150, 100]	4.39 ± 0.02	702.98	23.86	(16.06 ± 0.20)
[300, 225, 150]	11.41 ± 0.03	319.48	13.79	(21.30 ± 0.17)
[400, 300, 200]	16.15 ± 0.04	113.02	6.04	(24.40 ± 0.18)
[500, 375, 250]	18.98 ± 0.04	37.96	2.25	(27.21 ± 0.16)
[600, 450, 300]	21.01 ± 0.04	12.60	0.74	(27.20 ± 0.14)
[700, 525, 350]	22.66 ± 0.04	4.53	0.23	(29.06 ± 0.15)
S2 Signal				
$[M(\tilde{\chi}_2^0), M(\tilde{\chi}_1^0)]$ GeV				
[100, 50]	0.26 ± 0.01	0.14	-0.06	(7.62 ± 0.38)
[105, 13.8]	2.10 ± 0.01	61.75	3.55	(7.84 ± 0.23)
[115, 13.8]	3.17 ± 0.02	65.46	3.74	(7.73 ± 0.21)
[125, 13.8]	3.85 ± 0.02	57.49	3.32	(9.34 ± 0.21)
[135, 13.8]	4.95 ± 0.02	54.84	3.18	(10.43 ± 0.17)
[145, 13.8]	5.85 ± 0.02	49.05	2.87	(11.50 ± 0.19)
[150, 50]	3.90 ± 0.02	28.65	1.71	(12.06 ± 0.19)
[200, 100]	4.59 ± 0.02	10.70	0.62	(16.66 ± 0.20)
[250, 125]	8.53 ± 0.03	7.79	0.44	(18.28 ± 0.18)
[300, 150]	12.42 ± 0.03	5.06	0.26	(20.98 ± 0.18)
[400, 200]	17.67 ± 0.04	1.80	0.05	(24.11 ± 0.17)
[500, 250]	20.09 ± 0.04	0.58	-0.03	(27.51 ± 0.16)
[600, 300]	21.70 ± 0.04	0.19	-0.06	(27.25 ± 0.18)
[700, 350]	22.17 ± 0.04	0.06	-0.07	(27.91 ± 0.17)
Background				
$W^\pm(\rightarrow e^\pm \nu_e / \mu^\pm \nu_\mu / \tau^\pm \nu_\tau / qq') + LF$	-	109.51	-	(28.04 ± 0.20)
$W^\pm(\rightarrow e^\pm \nu_e / \mu^\pm \nu_\mu / \tau^\pm \nu_\tau) + HF$	0.00 ± 0.00	0.00	-	-
$W^\pm(\rightarrow e^\pm \nu_e / \mu^\pm \nu_\mu / \tau^\pm \nu_\tau) + HF$	0.082 ± 0.004	0.96	-	(36.93 ± 1.76)
$t\bar{t}$	0.00 ± 0.00	0.00	-	-
$t + b, t + q(+b)$	0.00 ± 0.00	0.00	-	-
$W + W, W + \gamma^*/Z, \gamma^*/Z + \gamma^*/Z$	0.283 ± 0.002	106.78	-	(26.95 ± 0.25)
$W^+ + W^- + W^\pm, W^+ + W^- + \gamma^*/Z,$ $W^\pm + \gamma^*/Z + \gamma^*/Z, \gamma^*/Z + \gamma^*/Z + \gamma^*/Z$	0.576 ± 0.004	1.77	-	(29.84 ± 0.34)
$\gamma + \gamma, \gamma + jets, \gamma + W^\pm, \gamma + Z$	0.00 ± 0.00	0.00	-	-
$\gamma^*/Z + LF$	0.00 ± 0.00	0.00	-	-
$\gamma^*/Z + HF$	0.00 ± 0.00	0.00	-	-
QCD HF	0.00 ± 0.00	0.00	-	-
QCD LF	0.00 ± 0.00	0.00	-	-

TABLE 5.34: Event selection efficiencies, event yields, signal significances and charge asymmetries for the $p + p \rightarrow \tilde{\chi}_1^\pm \tilde{\chi}_2^0 \rightarrow 3\ell^\pm + \cancel{E}_T$ analysis.

5.1.4.3.c Indirect Determination of $M(\tilde{\chi}_1^\pm) + M(\tilde{\chi}_2^0)$

Experimental Result for the S1 Signal

Using the S1 signal experimental A_C template curves of figure 5.25, we can get the central values and the uncertainties of the indirectly measured $M(\tilde{\chi}_1^\pm) + M(\tilde{\chi}_2^0)$ for each input mass as reported in table 5.40.

<i>Process</i>	$\alpha^{Exp} \pm \delta\alpha^{Stat}$	Z_N (σ)	$A_C^{Meas.}$ (%)	$\delta A_C^{Tot.}$ (%)	$\delta A_C^{Meas.Fit}$ (%)
S1 Signal					
$[M_{\tilde{\chi}_2^0}, M_{\tilde{\ell}^\pm}, M_{\tilde{\chi}_1^0}]$ GeV					
[100, 75, 50]	$(9.98 \pm 0.26) \times 10^{-2}$	31.70	7.70	0.83	0.74
[200, 150, 100]	$(15.58 \pm 0.36) \times 10^{-2}$	23.86	16.06	0.85	0.44
[300, 225, 150]	$(34.28 \pm 0.79) \times 10^{-2}$	13.79	21.30	0.96	0.48
[400, 300, 200]	$(96.89 \pm 2.22) \times 10^{-2}$	6.04	24.40	1.29	0.58
[500, 375, 250]	$(288.49 \pm 6.61) \times 10^{-2}$	2.25	27.21	1.75	0.69
[600, 450, 300]	$(869.13 \pm 19.89) \times 10^{-2}$	0.74	27.20	1.97	0.77
[700, 525, 350]	$(241.74 \pm 5.55) \times 10^{-1}$	0.23	29.06	2.02	0.85
S2 Signal					
$[M_{\tilde{\chi}_2^0}, M_{\tilde{\chi}_1^0}]$ GeV					
[100, 50]	$(78.22 \pm 6989.64) \times 10^1$	-0.06	7.62	0.88	0.59
[105, 13.8]	$(177.34 \pm 4.21) \times 10^{-2}$	3.55	7.85	1.58	0.56
[115, 13.8]	$(167.29 \pm 3.91) \times 10^{-2}$	3.74	7.73	1.55	0.52
[125, 13.8]	$(190.49 \pm 4.44) \times 10^{-2}$	3.32	9.34	1.60	0.49
[135, 13.8]	$(199.69 \pm 4.61) \times 10^{-2}$	3.18	10.43	1.62	0.46
[145, 13.8]	$(223.26 \pm 5.16) \times 10^{-2}$	2.87	11.50	1.67	0.45
[150, 50]	$(382.23 \pm 8.90) \times 10^{-2}$	1.71	12.06	1.85	0.44
[200, 100]	$(102.35 \pm 2.34) \times 10^{-1}$	0.62	16.66	2.00	0.46
[250, 125]	$(140.58 \pm 3.23) \times 10^{-1}$	0.44	18.28	2.01	0.52
[300, 150]	$(216.42 \pm 4.96) \times 10^{-1}$	0.26	20.98	2.02	0.60
[400, 200]	$(608.39 \pm 13.89) \times 10^{-1}$	0.05	24.11	2.03	0.74
[500, 250]	$(18.88 \pm 0.43) \times 10^{-5}$	-0.03	27.51	2.03	0.86
[600, 300]	$(57.64 \pm 1.32) \times 10^{-5}$	-0.06	27.25	2.03	0.96
[700, 350]	$(182.52 \pm 4.17) \times 10^{-5}$	-0.07	27.91	2.03	1.04

TABLE 5.35: Noise to signal ratio, signal statistical significance, and expected and measured integral charge asymmetries for the S1 and S2 signal samples for the $p+p \rightarrow \tilde{\chi}_1^\pm \tilde{\chi}_2^0 \rightarrow 3\ell^\pm + \cancel{E}_T$ analysis.

This enables us to perform a closure test of our method on the S1 signal sample as displayed at the top of figure 5.28, where we can fit of the input versus the measured $M(\tilde{\chi}_1^\pm) + M(\tilde{\chi}_2^0)$ by a linear function.

This fit indicates, given the uncertainties, that the indirect measurement is:

$$\begin{cases} \text{linear : the slope of the fit function is compatible with 1} \\ \text{unbiased : the y - intercept of the fit function is compatible with 0} \end{cases} \quad (5.45)$$

Further elementary checks, forcing the parameters of the fit functions, tend to confirm these indications, as presented in table 5.37.

Experimental Result for the S2 Signal

As in the previous sub-section, using the S2 signal A_C template curves 5.26, we can get the results reported in table 5.41. The closure test on the S2 signal samples is displayed at the bottom of figure 5.28.

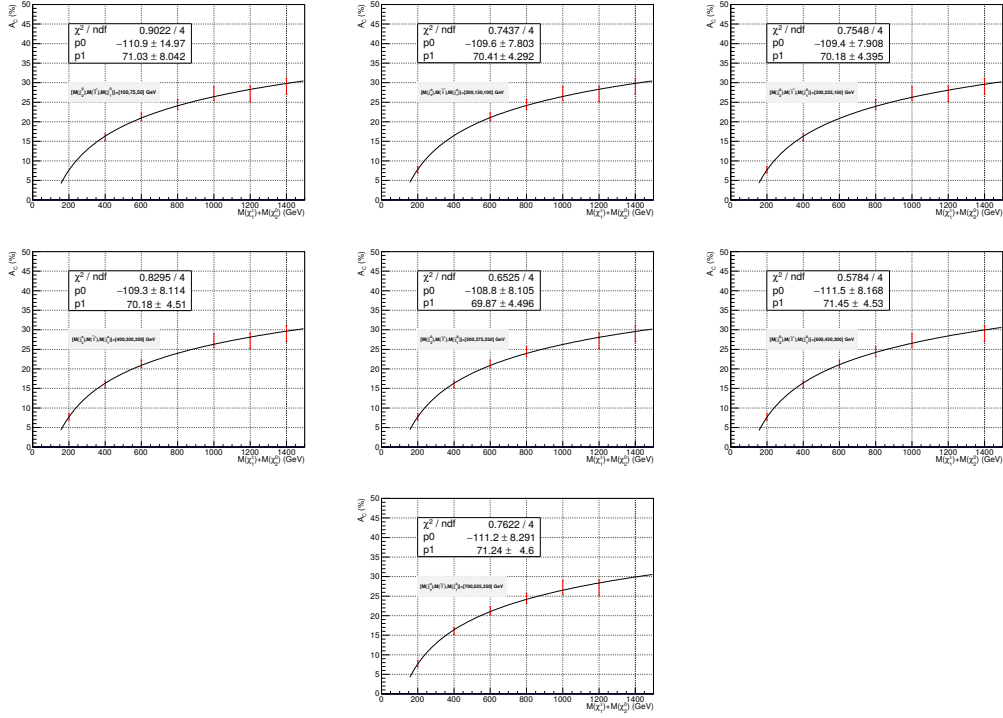


FIGURE 5.25: Experimental A_C template curves for the S1 signal samples, as they are listed, in table 5.34 from the top to the bottom rows. Here, they appear ordered by increasing $\tilde{\chi}_2^0$ mass, from the top to the bottom row and from left to right.

$M(\tilde{\chi}_1^\pm) + M(\tilde{\chi}_2^0)$ Input Mass (GeV)	$A_C^{Meas.} \pm \delta A_C^{Meas. Fit}$ (%)	$M(\tilde{\chi}_1^\pm) + M(\tilde{\chi}_2^0)$ Measured Mass (GeV)
200.	7.70 ± 0.74	$200.37^{+11.51}_{-10.78}$
400.	16.06 ± 0.44	$390.18^{+14.83}_{-14.21}$
600.	21.30 ± 0.48	$617.94^{+27.70}_{-26.34}$
800.	24.40 ± 0.58	$824.61^{+46.98}_{-44.09}$
1000.	27.21 ± 0.69	$1083.15^{+76.95}_{-71.18}$
1200.	27.20 ± 0.77	$1082.08^{+86.18}_{-78.99}$
1400.	29.06 ± 0.85	$1304.01^{+118.38}_{-107.31}$

TABLE 5.36: Measured $A_C(S)$ of the S1 signal samples with their full experimental uncertainty. Indirect mass measurement and their full experimental uncertainty as a function of the signal sample.

Forced Parameter	Fit $\chi^2/Ndof$	Fit Y-Intercept	Fit Slope
Slope	5.328/6	-1.67 ± 8.26	1.0 ± 0.0
Y-Intercept	5.260/6	0.0 ± 0.0	0.9933 ± 0.0203

TABLE 5.37: Closure tests with a forced fit parameter for the S1 signal samples.

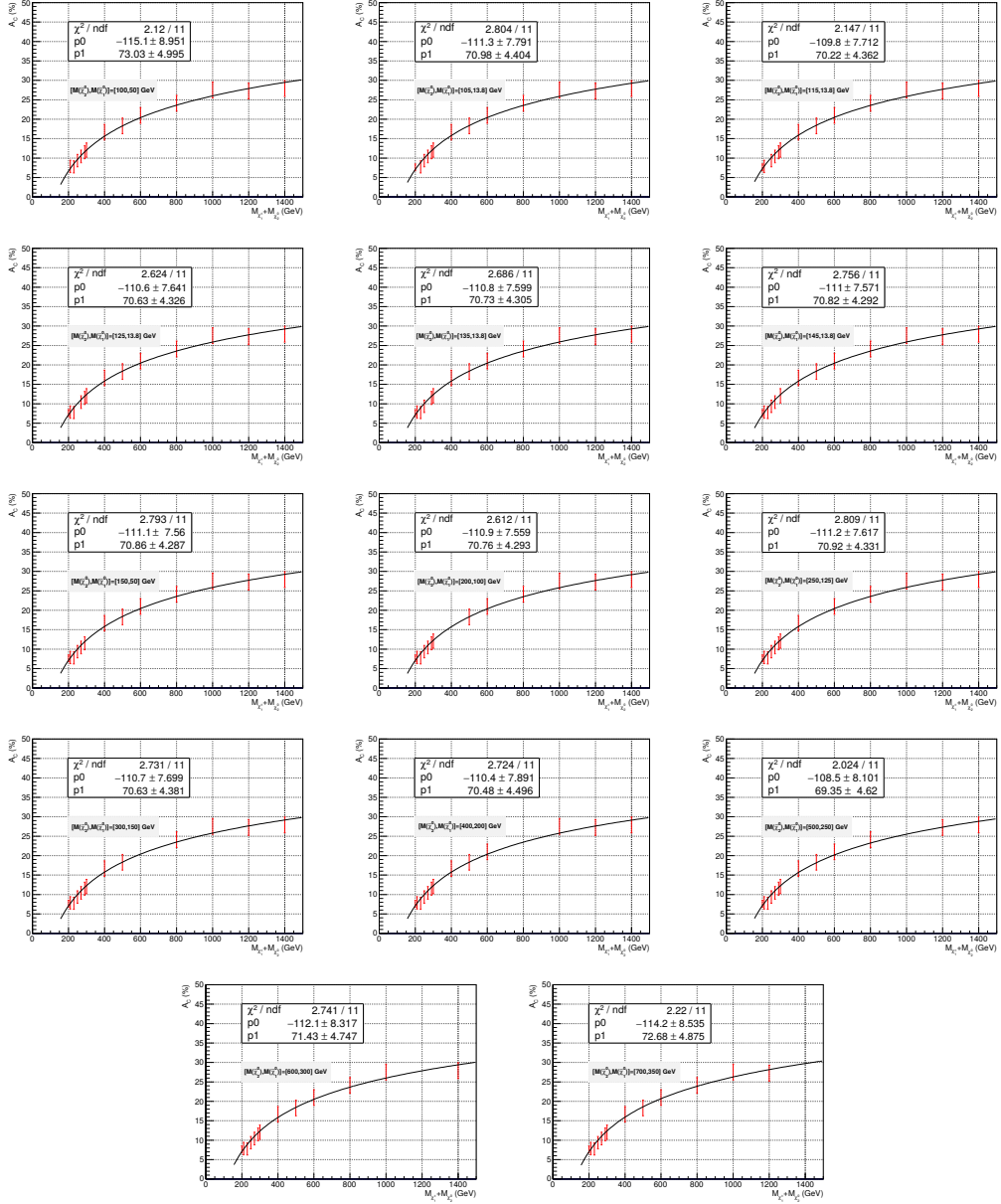


FIGURE 5.26: Experimental A_C template curves for the S2 signal samples, as they are listed, in table 5.34 from the top to the bottom rows. Here, they appear ordered by increasing $\tilde{\chi}_2^0$ mass, from the top to the bottom row and from left to right.

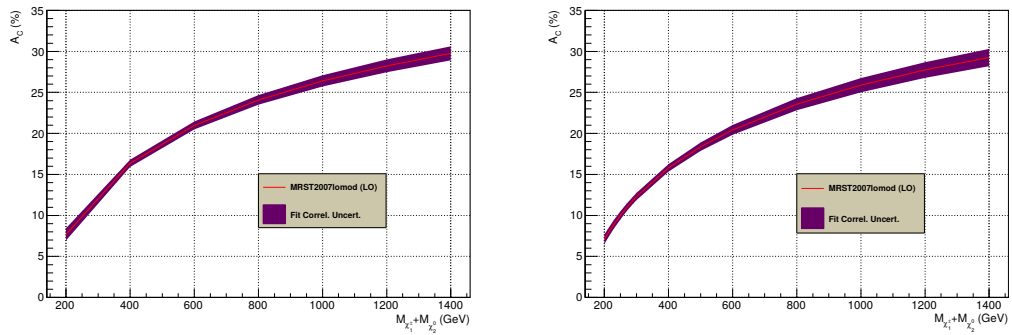


FIGURE 5.27: Fitted A_C template curves for the S1 (LHS) and the S2 (RHS) signal samples. The uncertainty accounts for the correlations between the parameters used to fit the A_C^{Meas} template curves.

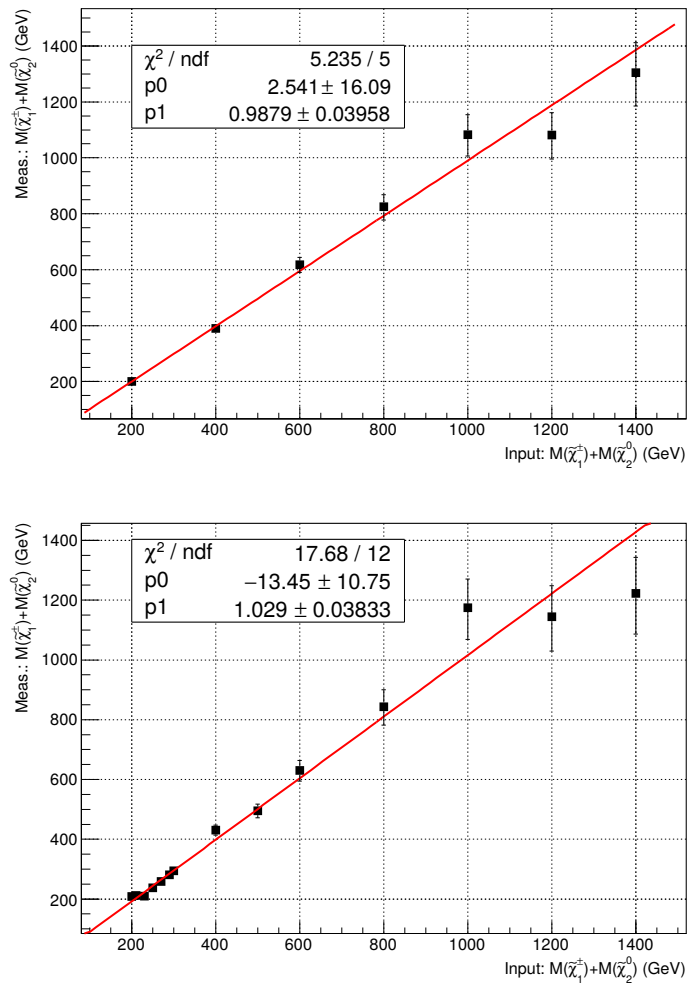


FIGURE 5.28: Closure test of the indirect measurement of $M(\tilde{\chi}_1^\pm) + M(\tilde{\chi}_2^0)$ for the S1 (top) and S2 (bottom) signal samples with only experimental uncertainties.

$M(\tilde{\chi}_1^\pm) + M(\tilde{\chi}_2^0)$ Input Mass (GeV)	$A_C^{Meas.} \pm \delta A_C^{Meas. Fit}$ (%)	$M(\tilde{\chi}_1^\pm) + M(\tilde{\chi}_2^0)$ Measured Mass (GeV)
200.	7.62 ± 0.59	$208.34^{+9.51}_{-9.01}$
210.	7.85 ± 0.56	$211.99^{+9.20}_{-8.75}$
230.	7.73 ± 0.52	$210.08^{+8.43}_{-8.05}$
250.	9.34 ± 0.49	$237.72^{+9.01}_{-8.97}$
270.	10.43 ± 0.46	$258.55^{+9.52}_{-9.13}$
290.	11.50 ± 0.45	$281.34^{+10.29}_{-9.86}$
300.	12.06 ± 0.44	$294.21^{+10.60}_{-10.17}$
400.	16.66 ± 0.46	$430.69^{+17.35}_{-16.57}$
500.	18.28 ± 0.52	$495.51^{+23.17}_{-21.97}$
600.	20.98 ± 0.60	$630.50^{+35.51}_{-33.34}$
800.	24.11 ± 0.74	$843.48^{+61.79}_{-57.00}$
1000.	27.51 ± 0.86	$1174.45^{+105.82}_{-95.96}$
1200.	27.25 ± 0.96	$1144.45^{+115.34}_{-103.44}$
1400.	27.91 ± 1.04	$1222.38^{+135.40}_{-120.22}$

TABLE 5.38: Measured $A_C(S)$ of the S2 signal samples with their full experimental uncertainty. Indirect mass measurement and their full experimental uncertainty as a function of the signal sample.

Here again the fit indicates, within the uncertainties, that the indirect mass measurement is linear and unbiased. The checks, forcing the parameters of the fit functions, tend to confirm these indications, as presented in table 5.39.

Forced Parameter	Fit $\chi^2/Ndof$	Fit Y-Intercept	Fit Slope
Slope	18.27/13	-5.601 ± 3.349	1.0 ± 0.0
Y-Intercept	19.25/13	0.0 ± 0.0	0.9838 ± 0.0120

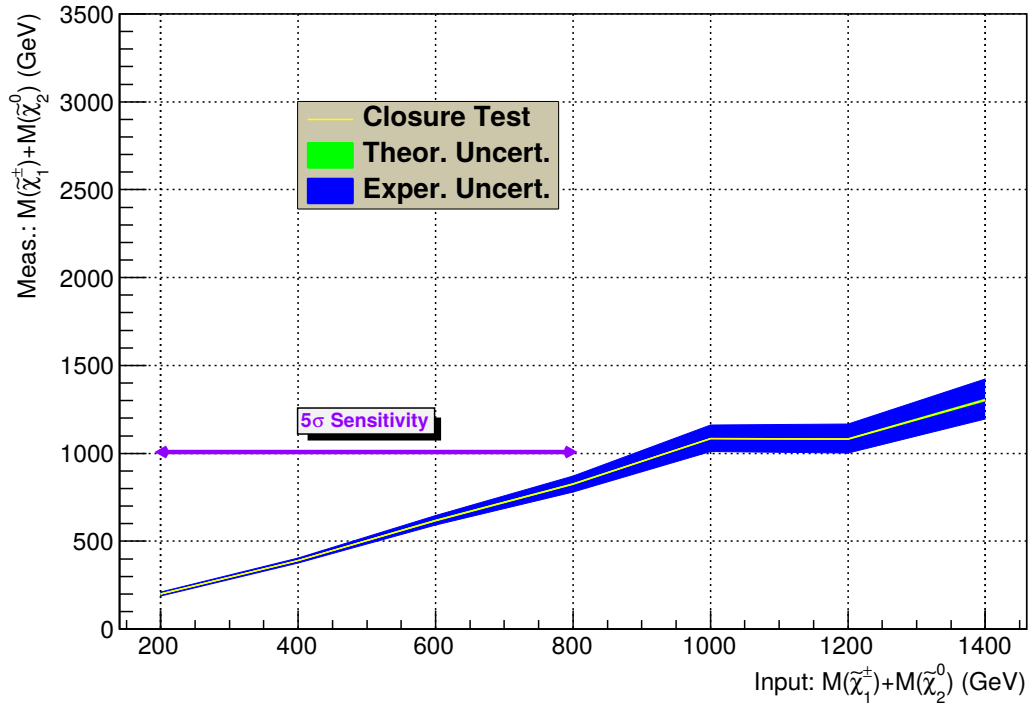
TABLE 5.39: Closure tests with a forced fit parameter for the S2 signal samples.

5.1.4.3.d Final Result for MRST2007lomod

Final Result for the S1 Signal

Meas. $M(\tilde{\chi}_1^\pm) + M(\tilde{\chi}_2^0)$	Expt. Uncert. (GeV)	Theor. Uncert. (GeV)	Total Uncert. (GeV)
200.37	+11.51 -10.78	+0.90 -0.90	+11.55 -10.82
390.18	+14.83 -14.21	+1.07 -1.12	+14.87 -14.25
617.94	+27.70 -26.34	+2.15 -2.24	+27.78 -26.44
824.61	+46.98 -44.09	+2.69 -2.70	+47.06 -44.17
1083.15	+76.95 -71.18	+2.13 -2.24	+76.98 -71.22
1082.08	+86.18 -78.99	+2.16 -2.24	+86.21 -79.02
1304.01	+118.38 -107.31	+5.76 -5.38	+118.52 -107.44

TABLE 5.40: Final results for the S1 samples with experimental and theoretical uncertainties.

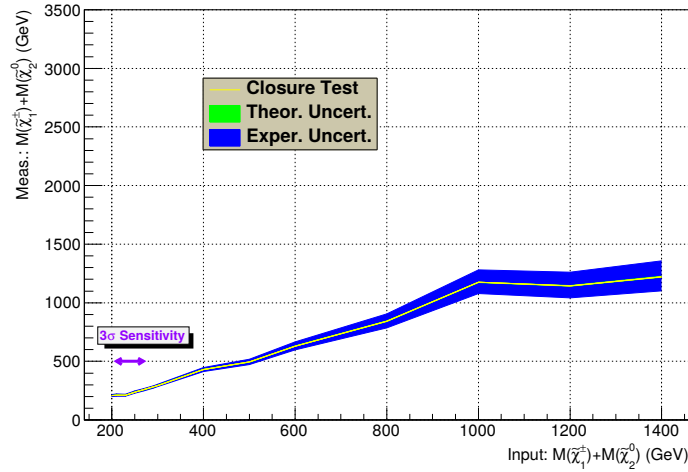
FIGURE 5.29: Closure test of the indirect measurement of $M(\tilde{\chi}_1^\pm) + M(\tilde{\chi}_2^0)$ for the S1 signal samples with both theoretical and experimental uncertainties. The sub-range with a signal sensitivity of 5σ is highlighted.

For the S1 sub-samples with a signal significance in excess of 5σ , the indirect measurements of $M(\tilde{\chi}_1^\pm) + M(\tilde{\chi}_2^0)$ are performed with an overall accuracy better than 6% for input masses $M(\tilde{\chi}_2^0) = M(\tilde{\chi}_1^\pm)$ in the [100,300] GeV interval, and better than 10% for $M(\tilde{\chi}_2^0) = M(\tilde{\chi}_1^\pm) \geq 400$ GeV. This is reported in table 5.40 and displayed in figure 5.29.

Final Result for the S2 Signal

Meas. $M(\tilde{\chi}_1^\pm) + M(\tilde{\chi}_2^0)$	Expt. Uncert. (GeV)	Theor. Uncert. (GeV)	Total Uncert. (GeV)
208.34	+9.51 -9.01	+0.70 -0.76	+9.54 -9.04
211.99	+9.20 -8.75	+0.66 -0.69	+9.22 -8.78
210.08	+8.43 -8.05	+0.55 -0.76	+8.45 -8.09
237.72	+9.01 -8.97	+0.61 -0.64	+9.03 -8.99
258.55	+9.52 -9.13	+0.65 -0.76	+9.54 -9.16
281.34	+10.29 -9.86	+0.77 -0.86	+10.32 -9.90
294.21	+10.60 -10.17	+0.86 -0.87	+10.63 -10.21
430.69	+17.35 -16.57	+1.34 -1.44	+17.40 -16.63
495.51	+23.17 -21.97	+1.37 -1.46	+23.21 -22.02
630.50	+35.51 -33.34	+2.12 -2.24	+35.57 -33.42
843.48	+61.79 -57.00	+2.57 -2.74	+61.84 -57.07
1174.45	+105.82 -95.96	+2.44 -2.47	+105.85 -95.99
1144.45	+115.34 -103.44	+2.40 -2.53	+115.36 -103.47
1222.38	+135.40 -120.22	+3.38 -3.34	+135.44 -120.27

TABLE 5.41: Final results for the S2 samples with experimental and theoretical uncertainties.

FIGURE 5.30: Closure test of the indirect measurement of $M(\tilde{\chi}_1^\pm) + M(\tilde{\chi}_2^0)$ for the S2 signal samples with both theoretical and experimental uncertainties. The sub-range with a signal sensitivity of 3σ is highlighted.

For the S2 sub-samples with a signal significance in excess of 3σ , the indirect measurements of $M(\tilde{\chi}_1^\pm) + M(\tilde{\chi}_2^0)$ are performed with an overall accuracy better than 4.5% for respective input masses $M(\tilde{\chi}_2^0) = M(\tilde{\chi}_1^\pm)$ in the [105,145] GeV interval and better than 11.1% for considered masses outside this interval. This is reported in table 5.41 and displayed in figure 5.30.

5.1.4.3.e Summary of the $M(\tilde{\chi}_1^\pm) + M(\tilde{\chi}_2^0)$ Measurements and their Accuracy

We sum up the indirect mass measurements of $M_{(\tilde{\chi}_1^\pm) + M_{\tilde{\chi}_2^0}}$ extracted from the integral charge asymmetry of the $\tilde{\chi}_1^\pm + \tilde{\chi}_2^0 \rightarrow 3\ell^\pm + \cancel{E}_T$ inclusive process within tables 5.42 (S1 signal) and 5.43 (S2 signal).

S1 Signal Input $M_{\tilde{\chi}_1^\pm} + M_{\tilde{\chi}_2^0}$ (GeV)	Figure of Merit		
	1. $\frac{\delta M_{W^\pm}^{Fit}}{M_{W^\pm}^{Fit}}$	2. $\frac{(M_{W^\pm}^{Fit} - M_{W^\pm}^{True})}{M_{W^\pm}^{True}}$	3. $\frac{(M_{W^\pm}^{Fit} - M_{W^\pm}^{True})}{\delta M_{W^\pm}^{Fit}}$
200.	5.8%	+0.2%	+0.03 σ
400.	3.8%	-2.5%	-0.7 σ
600.	4.5%	+3.0%	+0.7 σ
800.	5.7%	+3.1%	+0.5 σ
1000.	7.1%	+8.3%	+1.1 σ
1200.	8.0%	-9.8%	-1.4 σ
1400.	9.1%	-6.9%	-0.8 σ

TABLE 5.42: Summary of the indirect mass measurements of $M_{\tilde{\chi}_1^\pm} + M_{\tilde{\chi}_2^0}$ extracted from the integral charge asymmetry of the S1 signal samples. Different figures of merit of the accuracy of these measurements are presented.

S2 Signal Input $M_{\tilde{\chi}_1^\pm} + M_{\tilde{\chi}_2^0}$ (GeV)	Figure of Merit		
	1. $\frac{\delta M_{W^\pm}^{Fit}}{M_{W^\pm}^{Fit}}$	2. $\frac{(M_{W^\pm}^{Fit} - M_{W^\pm}^{True})}{M_{W^\pm}^{True}}$	3. $\frac{(M_{W^\pm}^{Fit} - M_{W^\pm}^{True})}{\delta M_{W^\pm}^{Fit}}$
200.	4.6%	+4.2%	+0.9 σ
210.	4.4%	+1.0%	+0.2 σ
230.	4.0%	-8.7%	-2.4 σ
250.	3.8%	-4.9%	-1.4 σ
270.	3.7%	-4.2%	-1.2 σ
290.	3.7%	-3.0%	-0.8 σ
300.	3.6%	-1.9%	-0.5 σ
400.	4.0%	+7.7%	+1.8 σ
500.	4.7%	-0.9%	-0.2 σ
600.	5.6%	+5.1%	+0.9 σ
800.	7.3%	+5.4%	+0.7 σ
1000.	9.0%	+17.5%	+1.7 σ
1200.	10.1%	-4.6%	-0.5 σ
1400.	11.1%	-12.7%	-1.3 σ

TABLE 5.43: Summary of the indirect mass measurements of $M_{\tilde{\chi}_1^\pm} + M_{\tilde{\chi}_2^0}$ extracted from the integral charge asymmetry of the S2 signal samples. Different figures of merit of the accuracy of these measurements are presented.

For the S1 signal at LO, this new method enables to get an accuracy better than 6% for the range with 5 σ sensitivity to the signal and better than 10% elsewhere. Whereas for the S2 signal at LO, we get an accuracy better than 4.5% for the range with 3 σ sensitivity to the signal and better than 11.2% elsewhere. All these indirect measurements are statistically compatible with the total uncertainty of the method.

One should bear in mind however that these results do not account for the dominant theoretical uncertainty ($\delta(A_C)_{PDF}$).

5.1.4.4 Conclusions

We propose a new method to measure the mass of charged final states using the integral charge asymmetry A_C at the LHC.

At first we detail and test this method on the $p + p \rightarrow W^\pm \rightarrow \ell^\pm \nu$ inclusive process. Then we apply it on a SUSY search of interest, namely the $p + p \rightarrow \tilde{\chi}_1^\pm + \tilde{\chi}_2^0 \rightarrow 3\ell^\pm + \cancel{E}_T$ inclusive process. For each process, we start by calculating the central values of A_C using cross section integrators with LO MEs and with three different LO PDFs. MCFM is used for the SM process and Resummino is used for the SUSY process. The same tools are also used to estimate the theoretical uncertainties on A_C . These calculations are repeated varying the mass of the charged final state. Over the studied mass ranges we find that A_C is a monotonically increasing function of $M(FS^\pm)$. This function is well described by a polynomial of logarithms of logarithms of $M(FS^\pm)$. The PDF uncertainty turns out to be the dominant source of the theoretical uncertainty.

The experimental extraction of A_C requires a quantitative estimate of the biases caused by the event selection and by the residual background. To this end MC samples are generated for the considered signal and its related background processes. These samples are passed through a fast simulation of the ATLAS detector response. Realistic values for the systematic uncertainties are taken from publications of LHC data analyses. The full experimental uncertainties as well as the effect of the residual background are consistently propagated through a central value and uncertainties of the measured A_C . This way the measured A_C of each signal sample can be translated into a central value and uncertainties of an indirect measurement of the corresponding $M(FS^\pm)$. The theoretical uncertainties of each measured $M(FS^\pm)$ is summed in quadrature with the experimental uncertainties so as to provide the full uncertainty for this new method.

For the $p + p \rightarrow W^\pm \rightarrow \ell^\pm \nu$ inclusive process, M_{W^\pm} can be indirectly measured with an overall accuracy better than 1.2%. We note that the dispersion of the central values of M_{W^\pm} indirectly measured with the three PDFs are compatible with the total uncertainty of the MSTW2008lo68cl prediction.

For the $p + p \rightarrow \tilde{\chi}_1^\pm + \tilde{\chi}_2^0 \rightarrow 3\ell^\pm + \cancel{E}_T$ inclusive process, without accounting for $\delta(A_C)_{PDF}$, $M(\tilde{\chi}_1^\pm) + M(\tilde{\chi}_2^0)$ can be measured with an overall accuracy better than 6% for a sensitivity to the signal in excess of 5σ and with an accuracy better than 4.5% for a sensitivity to the signal in excess of 3σ . These indirect mass measurements are independent of the details of the decay chains of the signal samples. For the considered SUSY process, basic closure tests indicate the indirect mass estimate does not need any linearity nor offset corrections.

We recommend to apply this method using at least NLO A_C templates both for the theoretical and the experimental parts. Indeed, the most precise cross sections and event generations constitute more reliable theory predictions and are in better agreement with the data than LO predictions. NLO or NLL theoretical templates reduce the theoretical uncertainty, as shown in table 5.31 for example. Besides, the measurements of $\frac{dA_C(W^\pm \rightarrow \ell^\pm \nu)}{d\eta(\ell^\pm)}$ by the LHC experiments

[239] [285] [286] [242] [243] were found to agree well with NLO theory predictions. However, even if our asymmetry ratios of the A_C theoretical templates: $\frac{A_C^{NLO}}{A_C^{LO}}$ in Fig. 5.14 and $\frac{A_C^{NLL}}{A_C^{LO}}$ in Fig. 5.22, reveal important shape difference of the higher orders with respect to LO, nevertheless the size of the corrections seems quite modest.

5.1.4.5 Prospects

In this article we have envisaged two production processes for which the mass measurement from the integral charge asymmetry is applicable. One SM inclusive process $p + p \rightarrow W^\pm \rightarrow 1\ell^\pm + \cancel{E}_T$ and one SUSY inclusive process $p + p \rightarrow \tilde{\chi}_1^\pm + \tilde{\chi}_2^0 \rightarrow 3\ell^\pm + \cancel{E}_T$. Here are the typical physics cases where we think the indirect mass measurement is applicable and complementary with respect to usual mass reconstruction techniques:

- Initial state (IS): processes induced by $q + \bar{q}$, or $q + g$
- Final state (FS): situations where the clasiscal reconstruction techniques are degraded because of
 - bad energy resolution for some objects (τ_{had}^\pm , jets, b-jets,...) combined with a limited statistical significance
(i.e. channels with τ_{had}^\pm compared to channels with e^\pm or μ^\pm)
 - and especially where many particles are undetected

For models with an extended Higgs sector: the $H^{\pm\pm}(\rightarrow W^\pm W^\pm) + H^\mp(\rightarrow \ell^\mp \nu) \rightarrow \ell^\pm \ell^\pm + \ell^\mp + \cancel{E}_T$ channel could be a good physics case because there are 3 undetected neutrinos. On the contrary, for $H^{\pm\pm} + H^\mp \rightarrow \ell^\pm \ell^\pm + \ell^\mp + \cancel{E}_T$, M_T templates should be more accurate.

Other physics cases could be searches for $W'^\pm \rightarrow \mu^\pm \nu$ and for $W'^\pm \rightarrow t\bar{b}$.

In SUSY models, here's a non-exhaustive list of processes of interest:

- For "semi-weak" processes:
 - $\tilde{\chi}_1^\pm + \tilde{q}$, for which $M_{\tilde{\chi}_1^\pm} + M_{\tilde{q}}$ could be measured
 - $\tilde{\chi}_1^\pm + \tilde{g}$, for which $M_{\tilde{\chi}_1^\pm} + M_{\tilde{g}}$ could be measured
- For "weak" processes:
 - Slepton sector: $\tilde{\ell}^\pm + \tilde{\nu}$, for which $M_{\tilde{\ell}^\pm} + M_{\tilde{\nu}}$ could be measured
 - Chargino-neutralino sector: $\tilde{\chi}_1^\pm + \tilde{\chi}_{1,2,3}^0$, to measure $M_{\tilde{\chi}_1^\pm} + M_{\tilde{\chi}_{1,2,3}^0}$

Note, that with the increasing center-of-mass energies and the increasing integrated luminosities of the LHC runs in the years to come, all the vector boson fusion production modes of the above cited processes could also become testable.

This new method only applies after a given event selection and it is indicative of the mass of the final state produced by a charged current process, only when the event selection provides a good statistical significance for that process. Further studies should determine wether a differential

charge asymmetry can be used to improve the separation between a given signal and its related background processes and therefore improve the sensitivity to some of this signal properties.

Differential charge asymmetries have been extensively used in other search contexts. For example, in attempts to explain the large forward-backward asymmetries of the $t\bar{t}$ production measured at the TEVATRON by both the CDF [432] and the D0 [433] experiments, some studies were carried out at the LHC to constrain possible contributions from an extra W'^{\pm} boson. See for example [434][435], using a differential charge asymmetry with respect to a three-body invariant mass, and also [436], using an integral charge asymmetry, and the references therein. Such analyses, using charge asymmetries with respect to the $t\bar{t}$ system rapidity, invariant mass and transverse momentum, have also been performed by the ATLAS and CMS collaborations, see [437] and [438], respectively. We should also mention the differential charge asymmetry with respect to a two-body invariant mass which served as a discriminant between some BSM underlying models [439][440], namely SUSY versus Universal Extra Dimension [441] models, in the study of some specific decay chains.

For what concerns the current article, a first look at the differential charge asymmetry versus the pseudo-rapidity of the charged lepton coming from the chargino decay, reveals promising shape differences between the SM background and the $p + p \rightarrow \tilde{\chi}_1^{\pm} + \tilde{\chi}_2^0$ SUSY signals. However detailed results are awaiting further studies.

Acknowledgments

We would like to thank the CCIN2P3 computing facility in Lyon where we produced, stored and analyzed our MC samples. The corresponding author thanks Ben O'Leary, Abdelhak Djouadi, and Gordon Watts for useful discussions. He also addresses a special word of thanks to the authors of Resummino, of MCFM, and of Delphes for their help and availability.

5.1.4.6 Appendix: Toy Models for the Evolution of A_C

This section is by no mean a formal proof of the properties of the functional forms utilized to fit the different A_C template curves. It's rather a numerical illustration that render these properties plausible.

5.1.4.6.a Numerical Example of Evolution of the PDFs, the Quark Currents and A_C

In this paragraph, we describe in a simplified scheme, the choice of these functional forms aimed at fitting:

1. the proton u and d quarks and anti-quarks density functions,
2. the quark currents in the initial state,
3. the dominant flavour contribution to the LO expression of A_C which is recalled in Eq. 5.46.

$$A_C \approx \frac{u(x_{1,2}, Q^2)\bar{d}(x_{2,1}, Q^2) - \bar{u}(x_{1,2}, Q^2)d(x_{2,1}, Q^2)}{u(x_{1,2}, Q^2)\bar{d}(x_{2,1}, Q^2) + \bar{u}(x_{1,2}, Q^2)d(x_{2,1}, Q^2)} \quad (5.46)$$

In order to illustrate numerically the Q evolution of the different quantities listed above, we used QCDNUM and the MSTW2008nlo68cl PDF. We set the Björken momentum fractions to arbitrary values (compatible with the W^\pm production in p+p collisions at $\sqrt{s} = 7$ TeV), $x_1 = 0.15$ and $x_2 = 8.79 \times 10^{-4}$, and varied Q . The quark density functions $x_1 \cdot u(x_1, Q^2)$, $x_1 \cdot \bar{u}(x_1, Q^2)$, $x_1 \cdot d(x_1, Q^2)$, $x_1 \cdot \bar{d}(x_1, Q^2)$, and $x_2 \cdot u(x_2, Q^2)$, $x_2 \cdot \bar{u}(x_2, Q^2)$, $x_2 \cdot d(x_2, Q^2)$, $x_2 \cdot \bar{d}(x_2, Q^2)$ are shown in the top RHS and LHS of Fig. 5.31, respectively. At the bottom row of the same figure the positively and negatively charged currents $x_{1,2} \cdot x_{2,1} \cdot u(x_{1,2}, Q^2) \cdot \bar{d}(x_{2,1}, Q^2)$, and $x_{1,2} \cdot x_{2,1} \cdot \bar{u}(x_{1,2}, Q^2) \cdot d(x_{2,1}, Q^2)$ as well as A_C are displayed on the LHS, with a zoom on the low Q end on the RHS.

In sub-section 5.1.4.2.a we consider different polynomials of functions of Q as fit functions to describe the Q evolution of the PDFs. Let's consider here a polynomial of $\text{Log}(\text{Log}(Q))$, in this example, the momentum fractions carried by the incoming quarks: $x_i \cdot f(x_i, Q^2)$ can be fitted by first degree polynomials of $\text{Log}(\text{Log}(Q))$ (though $x_2 \cdot f(x_2, Q^2)$ fits are actually improved by using a second degree polynomial). First degree polynomials of $\text{Log}(\text{Log}(Q))$ give very good fits of the evolution of the "quark currents": $x_1 \cdot x_2 \cdot f_{flav1}(x_1, Q^2) \cdot f_{flav2}(x_2, Q^2)$ c, and, given the hierarchy of the coefficients of these quark currents polynomials, of the A_C as well.

5.1.4.6.b Toy Models for the Main Properties of A_C^{Fit}

Hereafter, we make the hypothesis that quark currents and A_C can be fitted by the different polynomials of functions of Q evoked above. We want to figure out how the coefficients of such

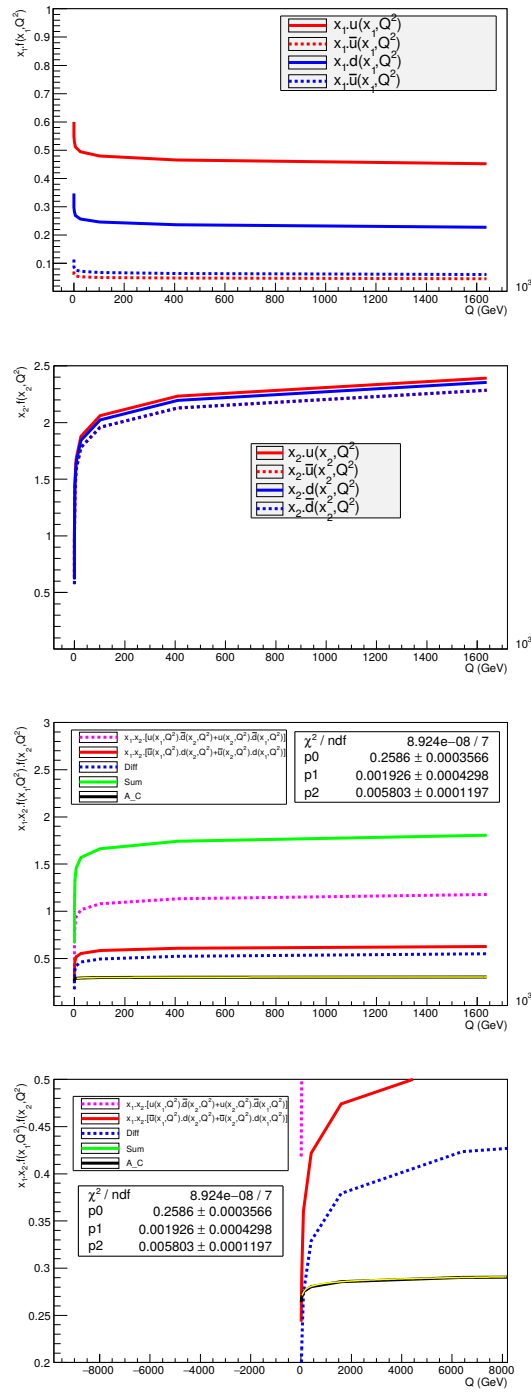


FIGURE 5.31: Evolutions of the quark PDFs (top), of the quark currents in the IS and of A_C (bottom) calculated with QCDNUM using the MSTW2008nlo68cl parametrization.

polynomials arrange so as to give the A_C template curves presented in sub-section 5.1.4.2.a, i.e. monotonically increasing functions of Q with a monotonically decreasing slope.

Again, let's consider the simplest case where the first degree polynomials are sufficient. If we denote $x = Q$, and $f(x)$ the fit function, we can write the charged cross sections:

$$\begin{cases} \sigma^+(x) = P_0 + P_1 \cdot f(x) \\ \sigma^-(x) = M_0 + M_1 \cdot f(x) \end{cases} \quad (5.47)$$

therefore

$$A_C(x) = \frac{(P_0 - M_0) + (P_1 - M_1) \cdot f(x)}{(P_0 + M_0) + (P_1 + M_1) \cdot f(x)} \quad (5.48)$$

Provided that $\lim_{x \rightarrow +\infty} |f(x)| = +\infty$ (which holds for all the fit functions we considered), it appears that A_C has an asymptote given by:

$$\lim_{x \rightarrow +\infty} A_C(x) = \frac{(P_1 - M_1)}{(P_1 + M_1)} \quad (5.49)$$

The derivative of $A_C(x)$ can be expressed as:

$$\frac{dA_C(x)}{dx} = \frac{2 \cdot (P_1 M_0 - P_0 M_1) \cdot f'(x)}{[(P_0 + M_0) + (P_1 + M_1) \cdot f(x)]^2} \quad (5.50)$$

Hence the condition to get a monotonically increasing $A_C(x)$ writes:

$$\frac{dA_C(x)}{dx} \geq 0 \iff (P_1 M_0 - P_0 M_1) \cdot f'(x) \geq 0 \quad (5.51)$$

And finally, that fact that A_C can be fitted with the same functional form as $\sigma^+(x)$ and $\sigma^-(x)$ relies on the (approximate) fulfillment of the following second degree functional equation:

$$(A_1 M_1) \cdot (f(x))^2 + (A_0 M_1 + A_1 M_0 - P_1) \cdot f(x) + (A_0 M_0 - P_0) = 0 \quad (5.52)$$

This equation has an analytical solution if its determinant is positive or null:

$$\Delta = \sqrt{(A_0 M_1 + A_1 M_0 - P_1)^2 - 4 \cdot (A_1 M_1) \cdot (A_0 M_0 - P_0)} \geq 0.$$

The fits of $\sigma^+(x)$, $\sigma^-(x)$ and A_C with the 3 considered functional forms are performed and the corresponding values of the fit parameters are presented in table 5.44.

Fit Parameter	Polynomial of $\text{Log}(Q)$	Polynomial of $\text{Log}(\text{Log}(Q))$	Laguerre Polynomials
P_0	0.33 ± 0.03	0.01 ± 0.03	0.79 ± 0.08
P_1	0.064 ± 0.004	0.43 ± 0.02	$(-2.9 \pm 1.5) \times 10^{-7}$
M_0	0.21 ± 0.02	0.04 ± 0.01	0.44 ± 0.04
M_1	0.032 ± 0.002	0.220 ± 0.006	$(-1.4 \pm 0.8) \times 10^{-7}$
A_0	0.258 ± 0.002	0.242 ± 0.002	0.283 ± 0.004
A_1	0.0036 ± 0.0002	0.023 ± 0.001	$(-1.6 \pm 0.8) \times 10^{-8}$

TABLE 5.44: Values of the fits parameters.

5.1.4.6.c Polynomials of $\text{Log}(x)$

In this case, our toy model writes:

$$A_C(x) = \frac{(P_0 - M_0) + (P_1 - M_1) \cdot \text{Log}(x)}{(P_0 + M_0) + (P_1 + M_1) \cdot \text{Log}(x)} \quad (5.53)$$

with

$$\frac{dA_C(x)}{dx} = \frac{2 \cdot (P_1 M_0 - P_0 M_1)}{x \cdot [(P_0 + M_0) + (P_1 + M_1) \cdot \text{Log}(x)]^2} \quad (5.54)$$

and, since $x \geq 0$,

$$\frac{dA_C(x)}{dx} \geq 0 \iff (P_1 M_0 - P_0 M_1) \geq 0 \quad (5.55)$$

Given the values of the fits parameters:

- the asymptoteic A_C is 33.0%
- $P_1 M_0 - P_0 M_1 = 2.51 \times 10^{-3} \geq 0$
- $\Delta = 3.12 \times 10^{-3} \geq 0$

Therefore $A_C(x)$ can be fitted by a first order polynomial of $\text{Log}(x)$, it's a monotonically increasing function, yet its has an asymptote.

5.1.4.6.d Polynomials of $\text{Log}(\text{Log}(x))$

In this case, our toy model writes:

$$A_C(x) = \frac{(P_0 - M_0) + (P_1 - M_1) \cdot \text{Log}(\text{Log}(x))}{(P_0 + M_0) + (P_1 + M_1) \cdot \text{Log}(\text{Log}(x))} \quad (5.56)$$

with

$$\frac{dA_C(x)}{dx} = \frac{2 \cdot (P_1 M_0 - P_0 M_1)}{x \cdot \text{Log}(x) \cdot [(P_0 + M_0) + (P_1 + M_1) \cdot \text{Log}(\text{Log}(x))]^2} \quad (5.57)$$

and, since $x \geq 0$ (in practice $x \geq 10$ GeV) and $\text{Log}(x) \geq 0$,

$$\frac{dA_C(x)}{dx} \geq 0 \iff (P_1 M_0 - P_0 M_1) \geq 0 \quad (5.58)$$

Given the values of the fits parameters:

- the asymptotic A_C is 32.6%
- $P_1 M_0 - P_0 M_1 = 1.57 \times 10^{-2} \geq 0$
- $\Delta = 0.144 \geq 0$

Therefore $A_C(x)$ can be fitted by a first order polynomial of $\text{Log}(\text{Log}(x))$, it's a monotonically increasing function, yet its has an asymptote.

5.1.4.6.e Laguerre Polynomials $L_n(x)$

The toy model writes:

$$A_C(x) = \frac{(P_0 - M_0) + (P_1 - M_1) \cdot (1 - x)}{(P_0 + M_0) + (P_1 + M_1) \cdot (1 - x)} \quad (5.59)$$

with

$$\frac{dA_C(x)}{dx} = \frac{-2 \cdot (P_1 M_0 - P_0 M_1)}{[(P_0 + M_0) + (P_1 + M_1) \cdot (1 - x)]^2} \quad (5.60)$$

and,

$$\frac{dA_C(x)}{dx} \geq 0 \iff (P_1 M_0 - P_0 M_1) \leq 0 \quad (5.61)$$

Given the values of the fits parameters:

- the asymptoteic A_C is 34.2%
- $P_1 M_0 - P_0 M_1 = -1.46 \times 10^{-3} \leq 0$
- $\Delta = 6.3 \times 10^{-14} \geq 0$

Therefore $A_C(x)$ can be fitted by a first order polynomial of $(1-x)$, it's a monotonically increasing function, yet its has an asymptote.

We verified that for the case without longitudinal boost: $x_1 = x_2 = 1.15 \times 10^{-2}$, the conclusions listed above remain valid.

Appendix A

Rapport Détaillé sur l'Activité Post-Doctorale

A.1 Formation Doctorale

J'ai effectué ma thèse au LPC Clermont-Ferrand d'octobre 1992 à mai 1996 dans l'expérience ATLAS au LHC du CERN. Mes travaux de thèse [308][309][310] concernaient principalement la recherche de particules supersymétriques, des jauginos électrofaibles, mais aussi la recherche et le développement (R&D) sur le calorimètre hadronique à tuile (TILECAL) [311][312][313][314] de l'expérience ATLAS.

A.2 Recherches Post-Doctorales

A.2.1 Entrée au CNRS

Je suis entré au CNRS en octobre 1996 et ai été affecté à l'Institut d Physique Nucléaire (IPN) de Lyon, unité mixte dépendant du CNRS (IN2P3) et de l'université de Lyon I.

A.2.2 Expérience CMS au LHC du CERN

- Période: octobre 1996 - janvier 1998
- Lieu: IPN Lyon
- Type d'activité: Instrumentation sur le trajectographe externe de CMS

Mes activités consistaient à participer à la R&D de détecteurs gazeux à micropistes (MSGC: pour Micro-Strip Gas Chamber) [315][316][317] qui étaient sensés équiper le trajectographe externe de l'expérience CMS.

J'ai participé à des tests locaux de prototypes avec un canon à rayons X et à des tests en faisceaux au PSI à Villigen et au CERN à Genève. Je me suis particulièrement intéressé aux corrélations entre les modules endommagés et les conditions de leur production et de leurs tests. J'ai participé à la reproduction et aux études des claquages provoqués par les particules hautement ionisantes et parfois favorisés par la mauvaise qualité de la production des modules. Ces claquages qui détruisaient les pistes représentaient le principal problème de ce type de détecteurs pour un fonctionnement dans l'environnement du LHC. Et, bien que d'importants progrès aient été réalisés pour assurer la survie des pistes, ces détecteurs n'ont finalement pas été retenus pour équiper le trajectographe externe de CMS.

A.2.3 Expérience L3 au LEP du CERN

- Période: janvier 1998 - juillet 2001
- Lieu: IPN Lyon
- Type d'activité: Analyse de données

J'ai effectué des recherches de boson(s) de Higgs produit(s) principalement par le processus de Björken: $e^+e^- \rightarrow HZ$, dans les topologies inclusives comprenant deux jets et de l'énergie manquante $HZ \rightarrow 2j + \cancel{E}$. Ces topologies ont été étudiées avec et sans étiquetage des jets de quarks b:

A.2.3.1 Désintégrations Invisibles du boson de Higgs

Je me suis particulièrement intéressé aux modes de désintégrations invisibles du boson de Higgs: $h \rightarrow invisible$, prévues dans certaines extensions du Modèle Standard (MS), notamment en supersymétrie: $h \rightarrow \tilde{\chi}_1^0 \tilde{\chi}_1^0$ ou $h \rightarrow \tilde{\nu} \tilde{\nu}$. Conjointement, Patrice Lebrun de l'IPN Lyon étudiait la réaction $e^+e^- \rightarrow h(\rightarrow invisible)Z(\rightarrow \ell^\pm \ell^\mp)$ avec $\ell^\pm = e^\pm$ ou μ^\pm . Nous avons donc pris la responsabilité pour la collaboration L3 de ces analyses jusqu'à la fin du LEP [318][319].

A.2.3.2 Désintégrations du boson de Higgs en quarks b

Parallèlement, j'ai proposé et encadré le stage de M2 et la thèse de Daniel Teyssier sur la recherche du boson de Higgs du MS [320][321][322][323]: $e^+e^- \rightarrow H(\rightarrow b\bar{b})Z(\rightarrow \nu\bar{\nu})$. Cette analyse a également été exploitée pour établir des limites dans le cadre du Modèle Standard Supersymétrique Minimal (MSSM) [325][326][327][328] et, en enlevant l'étiquetage des jets de b, dans le cadre des recherches indépendantes de la saveur [329].

Pendant toute cette période, j'ai participé au contrôle des prises de données du calorimètre électromagnétique à cristaux de l'expérience L3 au CERN.

A.2.4 Expérience D0 au TEVATRON du FNAL

- Période: février 2000 - décembre 2010
- Lieu: IPN Lyon, FNAL (USA), LAL Orsay, CPPM Marseille
- Types d'activité: Etalonnage hors-ligne des calorimètres, Générateurs Monte Carlo, Analyse de données

Au début de l'année 2000, après un long travail à contre courant à l'IPN de Lyon, j'ai convaincu deux collègues de L3 de former un nouveau groupe pour participer à l'expérience D0 auprès du TEVATRON du Fermi National Accelerator Laboratory (FNAL, dans la banlieue de Chicago). J'ai effectué un premier voyage de prise de contact au FNAL en février 2000, puis nous avons reçu en avril 2000 l'approbation du Conseil Scientifique de l'IPN de Lyon pour participer officiellement à la collaboration D0, en intégrant le groupe "D0-France" qui comprenait les autres laboratoires du CNRS et du CEA déjà impliqués.

Mes activités ont principalement porté sur trois axes:

A.2.4.1 L'étalonnage hors-ligne des objets calorimétriques

Pour le Run II du TEVATRON (2001-2011), l'étalonnage hors-ligne des objets calorimétriques (électrons et jets) de l'expérience D0 a démarré dans le groupe D0-France. D'une part, il s'agissait d'établir l'échelle absolue d'énergie électromagnétique (EM) à partir de résonances bien connues telles que le $Z \rightarrow e^+e^-$ et de l'appliquer pour corriger, après reconstruction, l'énergie des électrons et des photons. D'autre part, il s'agissait d'établir l'échelle d'énergie des jets, relative à l'échelle absolue d'énergie EM, essentiellement grâce à l'équilibre des impulsions transverses dans le processus: $\gamma + jets$. Ces corrections affectent d'autres quantités telle que l'énergie transverse manquante: \cancel{E}_T et sont donc absolument indispensables pour produire le moindre résultat de physique. J'ai co-dirigé cette activité dite de "Calorimeter Offline Calibration" [330] d'avril 2000 à juillet 2001 avant qu'elle ne soit re-distribuée dans les groupes "EM ID" et "Jet Energy Scale (JES)" de la collaboration D0 au cours de l'été 2001. J'ai également été responsable du MC du groupe "Calorimeter Offline Calibration" pendant cette période.

J'ai été détaché au FNAL entre septembre 2001 et septembre 2002. J'y ai poursuivi les activités d'étalonnage de l'énergie des jets dans le groupe JES. J'ai pris la responsabilité de la correction de l'énergie sous-jacente des jets d'octobre 2001 à janvier 2003. Ce travail a constitué l'essentiel de la thèse de Jérôme Coss [431] que j'ai proposée et encadrée. Par ailleurs, j'ai été le responsable MC du groupe JES de septembre 2001 à février 2003. Enfin, j'ai proposé et démarré des études MC pour l'étalonnage de la réponse des jets de quarks b à l'aide du processus: $\gamma + b$ entre décembre 2003 et mars 2005. Cette méthode d'étalonnage de la réponse toute à fait nouvelle, a été reprise et développée par un autre collègue de D0, Jochen Cammin entre 2004 et 2008. Mais le reste des corrections de la b-JES n'ont jamais été finalisées faute de main d'oeuvre. Aucune b-JES générique n'a donc pas pu être utilisée dans les analyses.

L'échelle d'énergie des jets de D0 au Run II a fait l'objet de plusieurs notes internes, mais n'a été publiée qu'en 2014, donc après mon départ de la collaboration. On peut en trouver un

résumé dans la référence publique suivante: [331]. J'ai co-signé 3 des notes internes sur ce sujet: [332][333][334].

A.2.4.2 Les outils de prédictions théoriques

Outre le MC de l'étalonnage des objets calorimétriques, je me suis impliqué d'avril 2000 jusqu'à décembre 2010 sur tous les aspects de l'utilisation des outils de prédictions théoriques dans la collaboration D0: calculateurs de spectre de masse pour de la physique au-delà du MS (BSM: "Beyond the Standard Model"), intégrateurs de sections efficaces, générateurs d'événements, codes de désintégration, ainsi que leurs scripts de production, leurs méta-données, leur accès dans la base de données SAM [340], ... et toutes les interfaces afférentes.

Ces travaux consistaient à intégrer des outils développés par des théoriciens dans l'environnement informatique de l'expérience D0, à en faire la maintenance, la documentation [339] ainsi que des recommandations aux groupes de physique et l'assistance aux utilisateurs individuels. Il fallait aussi assurer un dialogue avec la communauté des théoriciens, auteurs de ces outils, en leur remontant les desiderata de la collaboration, éventuellement des erreurs que nous avions détectées et en leur demandant des explications et éclaircissements à retransmettre à l'intérieur de la collaboration, ce pour tous les processus du MS ainsi que tous les phénomènes nouveaux (NP: "New Phenomena") recherchés en BSM.

Je me suis impliqué dans de nombreux projets:

- le déverminage de l'outil de production MC de la collaboration *mc_runjob* [341] avec Catherine Biscarat
- la gestion et le développement des outils fixant les paramètres physiques de la génération d'événements, les *cardfiles* [342]
- la définition d'une convention de nommage (*naming scheme* [343]) utilisée dans toute la collaboration pour les fichiers de paramètres et pour les méta-données des générateurs
- la définition d'une nouvelle table de la base de données centrale de D0, appelée *SAM*: "Sequential Access via Metadata", concernant les générateurs à éléments de matrice à ordre fixé (*FOME*: "Fixed Order Matrix Elements" [337])
- la gestion et l'amélioration des interfaces des générateurs [344] les plus utilisés: Pythia, Herwig (intégration de Jimmy et mise en oeuvre des interfaces avec Tauola [345] et EvtGen [346])
- définition de la liste de hadrons beaux [347] à faire désintégrer par EvtGen pour tous les générateurs qui lui étaient interfacés
- maintien des outils et paquetages suivants: PDFLIB [350], MCFM [361], *cardfiles*
- développement d'outils permettant d'accéder aux échantillons MC: *MC Catalog* [353], *REILM*: "Request ID List Maker" [354]

- introduction en 2002 des paramètres ajustés pour la simulation des événements sous-jacents ("UE: Underlying Event") uniquement par les cardfiles dans Pythia [348] et en introduisant Jimmy dans Herwig. J'avais invité R. Field, phénoménologue et membre de la collaboration CDF, à présenter ses ajustements pour la première fois dans la collaboration [349] D0
- coordination d'outils communs à toute la collaboration pour la simulation des processus du MS (*CSMC*: "Common Sample Monte Carlo" [352])
- supervision des outils de la production centralisée avec le générateur Alpgen v1 ("*CAPS*: Common Alpgen+Pythia Studies" et son script ComAlpPI.sh, développé par Catherine Biscarat à partir de mars 2004 [335])
- découverte d'une erreur (affectant la production MC officielle de D0) dans l'interface Alpgen entre v1.2 et Pythia v6.202 [430] en 2003
- supervision des outils de la production centralisée avec le générateur Alpgen v2 (paquetage *alpgen_prod* développé par Gérard Grenier à partir de mars 2005 [336])
- calcul de sections efficaces LO et NLO avec MCFM pour permettre une normalisation au NLO-QCD pour tous les processus du MS dans D0. Ces sections efficaces compilées dans une note interne [351] constitue la principale source de normalisation au NLO dans les analyses du Run II dans D0.
- production au format des générateurs de D0 et simulation+reconstruction des échantillons MC Madgraph+Pythia produits par S. Mrenna [338] et stockés sous le format MCFIO dans ENSTORE
- ...

J'ai été le responsable du MC du groupe NP de novembre 2000 à janvier 2003 et je décrirai dans le paragraphe suivant les activités MC spécifiques à la physique BSM. Enfin, j'ai été co-responsable de la simulation de la collaboration D0 de janvier 2003 à janvier 2005.

A.2.4.3 La recherche de la Supersymétrie

Dans le groupe NP, j'ai principalement contribué aux outils de prédictions théoriques. Les activités liées aux processus du MS, qui constituent des bruits de fond pour la physique BSM, ont été décrites dans le paragraphe précédent.

Pour la plupart des analyses recherchant des signaux BSM, SUSY avec conservation de la R-parité (RPC), leptoquark, Z' , W' , technicouleur,... la génération d'événements utilisait le programme Pythia dans les versions suivantes:

- 6.129 et 6.155 pour mcp05, mcp06, mcp08 et mcp10
- 6.203 pour mcp11, mcp13
- 6.319 pour mcp17, mcp20

- 6.413 pour mcp20

Les mcpXX représentent les versions de production des distributions informatiques de D0. Je m'en suis occupé pour le groupe NP pendant les périodes suivantes: mcp05 à partir de novembre 2000, mcp06 à partir d'avril 2001, mcp08 à partir d'octobre 2001, mcp10 à partir de janvier 2002, mcp11 à partir d'août 2002 et mcp13 à partir décembre 2002.

Pour les signaux SUSY, les versions de Pythia jusqu'à la 6.1 ne contenaient pas d'interface avec des programmes calculant les spectres de masse et les couplages des particules SUSY (sparticules) comme Isasusy [362]. J'ai donc travaillé sur l'interface appelée Pyfris [363], écrite à ma demande par S. Mrenna et que j'ai contribué à la maintenir au fils des modifications dans les programmes Isajet (contenant Isasusy) et Pythia pour garder la compatibilité. Ceci a permis de générer les échantillons MC de signaux SUSY.

Pyfris a été complètement intégré à Pythia à partir de la version 6.2 et j'ai pu contrôler la génération SUSY de D0 directement à partir des *cardfiles*. Grâce à ces outils et avec le concours de mes étudiants, Jérôme Coss puis Thomas Millet, j'ai pu fournir au groupe NP entre janvier 2001 et octobre 2005 des ntuples ROOT [416] contenant les masses et les couplages des sparticules, les taux d'embranchement, les largeurs et les sections efficaces de production NLO-QCD pour des échantillonnages [364] des 3 principaux modèles SUSY (mSUGRA, mGMSB et mAMSB). Ces ntuples ont été utilisés par plusieurs membres du groupe NP pour estimer la sensibilité de D0 par rapport à divers signaux SUSY avant d'en entamer l'analyse et ont aussi permis d'établir des limites d'exclusion à l'issue de ces analyses.

Pour fournir les sections efficaces de production au NLO-QCD, j'ai utilisé le programme Prospino v1 [365] dont j'étais responsable pour D0 [366].

Par la suite, j'ai ajouté des outils tels que Sdecay [367][368], le programme le plus précis pour le calcul au NLO-QCD des désintégrations des sparticules dans le MSSM et NMHdecay [369][370], son équivalent pour le modèle NMSSM. Mais également Suspect [371], un programme alternatif de calcul de spectre et de couplages SUSY et les versions plus récentes d'Isajet. Entre août 2003 et février 2006, j'ai intégré tous ces programmes dans un paquetage D0 appelé *susy_tools* dont j'ai eu la responsabilité [372]. En novembre 2003, les phénoménologues, auteurs de tous ces programmes, ont adopté le "SUSY Les Houches Accord" (SLHA) [374] qui est une interface universelle entre les calculateurs de spectres et de couplages, les codes de désintégration et les générateurs d'événements pour la SUSY. Cette convention a entraîné d'énormes progrès en permettant des échanges simplifiés entre ces programmes sans avoir à maintenir toutes les interfaces explicites. A compter de ce moment, je n'ai plus fourni d'échantillonnages de modèles SUSY au groupe NP, mais plutôt des outils produisant des fichiers SLHA contenant chacun un modèle explicite de SUSY.

J'ai encadré la thèse de Thomas Millet dont l'analyse portait sur la recherche de la SUSY dans la production de paires de gluinos se désintégrant dans la topologie: $4b + \cancel{E}_T$.

Je me suis naturellement occupé de la génération du signal SUSY pour cette analyse, pour laquelle Patrice Verdier a contribué à l'encadrement. En raison d'un retard important dans la

finalisation de l'analyse par rapport à la collaboration CDF et du fait que nous n'ayons analysé que 1 fb^{-1} de données, cette analyse n'a pas donné lieu à une publication.

De 2000 à 2005, j'ai participé au contrôle des prises de données des calorimètres à argon liquide de l'expérience D0 au FNAL. De septembre 2005 à novembre 2010, j'ai participé à distance au contrôle des bases de données du FNAL (*shifts SAM*).

A.2.5 Expérience ATLAS au LHC du CERN

D'avril à juin 2010, j'ai encadré le stage de M2 de Spyridon Argyropoulos intitulé "Contributions à la mesure de la section efficace $p + p \rightarrow b\bar{b} + X$ dans les données ATLAS à $\sqrt{s} = 7 \text{ TeV}$ " [373]. Ce stage concernait principalement le calcul de la prédiction théorique la plus précise de $\sigma(p + p \rightarrow b\bar{b} + X)$ en incluant les incertitudes théoriques. Ce calcul a été effectué à l'aide de l'intégrateur de sections efficaces FONLL [375][376] qui combine un calcul à ordre fixe au NLO-QCD avec une resommation précise à l'ordre des logarithmes sub-dominants. L'objectif était de proposer une repondération de la simulation du processus $p + p \rightarrow b\bar{b} + X$ par Pythia 6.4 [357], basée sur des éléments de matrice LO ("Leading Order") augmentés d'une douche partonique qui simule en partie de la resommation à l'ordre des logarithmes dominants. Ce pour permettre une comparaison, en normalisation et surtout en forme, aux données. Finalement, le groupe en charge de cette analyse [358] n'a pas retenu cette option et a comparé les données aux récents générateurs NLO: POWHEG [355] et MC@NLO [356]. Ce stage concernait également la validation des corrections d'énergie des jets de b semi-muoniques qui avaient établies sur le MC à $\sqrt{s} = 14 \text{ TeV}$ [359] et qui allaient être appliquées aux données et au MC à $\sqrt{s} = 7 \text{ TeV}$. Des tests de fermeture sur un échantillon MC du processus $p + p \rightarrow W^\pm(\rightarrow \ell^\pm\nu) + H(\rightarrow b\bar{b})$ avec $mH = 120 \text{ GeV}$ ont été réalisés montrant une échelle d'énergie bien rétablie (augmentation de l'ordre de 60%) après les corrections d'énergie des jets, incluant les corrections semi-muoniques, avec une légère amélioration (l'ordre de 25%) de la résolution relative.

De février à juin 2011, j'ai encadré le stage de M2 de Thomas Serre sur l'utilisation de l'asymétrie de charge pour contraindre des masses au LHC. A l'issue de ce stage, j'ai continué à développer cette méthode qui est incluse dans le chapitre 5 de ce mémoire d'habilitation et dont j'ai diffusé un preprint [428] avant de le soumettre pour publication dans le "Journal of High Energy Physics".

Entre septembre 2011 et septembre 2012, j'ai été responsable du générateur Herwig++ [360] dans la collaboration ATLAS.

Entre octobre 2011 et octobre 2014, j'ai co-encadré avec Pascal Pralavorio (CPPM Marseille) la thèse de Thomas Serre concernant l'identification des électrons et la recherche de la SUSY dans la topologie $\ell^\pm\ell^\mp + \cancel{E}_T$ [422]. Pascal Pralavorio était le directeur de thèse et le principal encadrant.

De même, je co-encadré la thèse de Michael Ughetto entre octobre 2011 et novembre 2014, avec Jean-Loïc Kneur et Gilbert Moutaka du LCC Montpellier pour sa partie phénoménologique, et avec Laurent Vacavant pour l'identification des jets de quarks b. Cette thèse a également eu comme objet la recherche de la SUSY dans le canal $\tilde{\chi}_1^\pm + \tilde{\chi}_2^0 \rightarrow W^\pm(\rightarrow \ell^\pm\nu)\tilde{\chi}_1^0 + h^0(\rightarrow b\bar{b})\tilde{\chi}_1^0$ [423][424][425][442]. Cette analyse constitue la première recherche dans ATLAS qui utilise un

boson de Higgs comme sonde pour la recherche de la SUSY et c'est la plus sensible à la production de paires de gauginos électrofaibles ("Electroweakinos").

Entre mai 2010 et novembre 2012, j'ai participé au contrôle des prises de données des calorimètres de l'expérience ATLAS au CERN.

Enfin, le paragraphe suivant (en anglais), décrit le travail d'intérêt général que j'ai effectué pour la collaboration ATLAS en vue de redevenir signataire de ses publications. Ce travail a été réalisé dans le groupe de travail sur les générateurs MC entre novembre 2011 et septembre 2013 (avec quelques interruptions). Je n'ai pas placé les références dans la bibliographie globale de ce mémoire parce qu'il s'agit exclusivement de références internes à la collaboration ATLAS.

A.2.5.1 ATLAS Authorship Project

A.2.5.1.a Validation of Tauola++

I essentially demonstrated that stand-alone Pythia v8 and Herwig++ v2.5 are handling tau decays in a satisfactory way with respect to Tauola++, both for the branching ratios and the shapes, see: <https://indico.cern.ch/event/187156/>

"Update on Parton LVL Pythia8 + Tauola++ and Photos++ Studies".

I also reproduced the following MC generator bug reported in:

<https://savannah.cern.ch/bugs/?93972> within

<http://indico.cern.ch/getFile.py/access?contribId=4&resId=1&materialId=slides&confId=187947>

"Update on Parton LVL Pythia8 + Tauola++ and Photos++ Studies". And fixed it in:

<http://indico.cern.ch/getFile.py/access?contribId=5&resId=0&materialId=slides&confId=187951>

"Short Update on Pythia8 Interfaces".

A.2.5.1.b Setup for CKKW-L matching

The goal was to setup Pythia v8 so that it could implement the CKKW-L matching between partons from a multileg ME generators to partons from the Pythia parton shower (PS) as stated in:

<https://its.cern.ch/jira/browse/AGENE-740>. I tested the new variable introduced by J. Monk into the Py8 Athena interface aimed at storing the ME-PS matching weight, see again:

<http://indico.cern.ch/getFile.py/access?contribId=5&resId=0&materialId=slides&confId=187951>

"Short Update on Pythia8 Interfaces".

Finally I did some short developments and tests on my side and handed them over to George Azuelos in June 2012 when he was ready to implement CKKW-L in the Athena Pythia v8 interface, see:

</afs/cern.ch/user/m/muanza/public/Pythia8Interfaces/CKKW-L/CKKW-L.tar.gz>.

A.2.5.1.c Validation of Photos++

I compared QED radiations in Herwig++, Pythia v8 stand-alone and Pythia v8 & Photos++ with external tools, see:

<http://indico.cern.ch/event/183026> "Pythia8 + Tauola++ and Photos++";

<http://indico.cern.ch/event/187156> "Update on Parton LVL Pythia8 + Tauola++ and Photos++ Studies";

<http://indico.cern.ch/event/187947> "Update on Parton LVL Pythia8 + Tauola++ and Photos++ Studies".

I also performed some comparisons of Pythia v8 and Pythia v8 & Photos++ in Athena, see the latest version in:

<https://indico.cern.ch/event/220985> "Update on QED model/data comparison studies".

I also worked on a data vs MC comparison with my student T. Serre, see:

<http://indico.cern.ch/event/202764> "Confronting Photos++ to ATLAS 2012 data";

<http://indico.cern.ch/event/209127> "Data/MC in 2e+gamma";

<http://indico.cern.ch/event/217662> "Photos++ - Data/MC".

The final version of these studies can be found at:

<https://indico.cern.ch/event/271453> " $Z \rightarrow \ell\pm\ell^\mp$ QED MC modelling comparisons". In this updated version of the Pythia v8 & Photos++ study was performed into 2 steps. The common new feature was to produce hadronized events where photons could come from hadron decays and to make a full usage of the parenthood links in the event record to identify the FSR photons in pure Pythia v8, in Pythia v8 & Photos++ and in Herwig++. In the first stage the event topologies were defined using the individual EM truth particles, whilst in the second stage, those were, for the first time, IRC-safely clustered into EM-jets using FastJet jet finder library. The code used to analyze the NTUP_Truth is available at:

[/afs/cern.ch/user/m/muanza/public/Pythia8Interfaces/PHOTOS](https://afs.cern.ch/user/m/muanza/public/Pythia8Interfaces/PHOTOS)

the sub-directories EM_Part_LVL and EM_Jets_LVL contain versions of the studies based on single EM particles and on InfraRed and Collinear safe clustering of the EM particles into EM-jets.

A.2.6 Groupements de Recherche sur la Physique Au-Delà du Modèle Standard

Depuis 1997, j'ai participé aux Groupements de Recherche (GDR) centré sur la SUSY mais ouvert sur toute la physique BSM.

A.2.6.1 GDR 501 sur la Supersymétrie

J'ai participé aux activités des groupes de travail sur le MSSM et sur les Outils dans le GDR SUSY de 1997 à 2000. A l'époque l'un des sujets dominants était la comparaison et le déverminage des calculateurs de spectre SUSY. J'ai directement ré-utilisé les outils que j'ai développé dans ce

cadre pour les besoins du MC SUSY dans la collaboration D0. Les travaux du groupe MSSM ont fait l'objet du document suivant: [417] qui n'a pas été publié, mais qui est devenu un preprint de référence. J'ai également contribué aux deux notes internes suivantes: [407] et [408].

A.2.6.2 EuroGDR 2305 sur la Supersymétrie

En raison de mon détachement aux USA, j'ai un peu moins contribué au GDR européen 2305 sur la Supersymétrie [404] de 2001 à 2004.

A.2.6.3 GDR 2305 sur la Supersymétrie

Au sein du GDR 2305 sur la Supersymétrie [405] de 2005 à 2008, j'ai été co-responsable du groupe "Outils et Méthodes Communs" avec Margarete Mülleitner et membre du Conseil de Groupement du GDR. Nous avons eu une activité assez riche, accessible à la référence suivante: [409]. J'ai notamment été le principal organisateur de l'atelier sur les bruits de fond du MS [387] et j'ai proposé et animé le projet de recherche en aveugle d'un signal SUSY: [410].

A.2.6.4 GDR 3262 Terascale

J'ai été co-responsable du groupe "Outils et Méthodes Communs" avec Sabine Kraml et Benjamin Fuks et membre du Conseil de Groupement du GDR 3262 Terascale [406] qui a démarré début 2009 et qui a couvert la physique BSM jusqu'à fin à 2012. J'ai été le principal organisateur de sa réunion générale au CPPM Marseille du 11-13 octobre 2011 [388].

A.2.6.5 Prolongement du GDR 3262 Terascale

Je suis membre du Conseil de Groupement du prolongement du GDR 3262 Terascale [406] qui a démarré début 2012 et qui couvrira la physique BSM jusqu'à fin à 2015.

A.3 Encadrement

A.3.1 Stages de M1

- Emmanuel Bourgeois, ENS Lyon, mai-juillet 2003,
"Recherche d'événements hémisphériques comme signature de la SUSY au LHC"
- Clément Bâty, Université Lyon I, mai-juillet 2005,
"L'asymétrie de charge au LHC"
- Abdel Khaoudi, Université J. Fourier Grenoble, avril-juin 2007,
"Recherche de la SUSY au LHC dans le canal trilepton"
- William Creus, Université Lyon I, juin-juillet 2007,
"Recherche en aveugle d'un signal supersymétrique au LHC"

A.3.2 Stages de M2

- Daniel Teyssier, Université Lyon I, mars-juillet 1999,
"Utilisation d'un réseau de neurones dans l'analyse $e^+e^- \rightarrow H(\rightarrow b\bar{b}) + Z(\rightarrow \nu\bar{\nu})$ avec l'expérience L3 au LEP"
- Jérôme Coss, Université Clermont-Ferrand II, mars-juillet 2000,
"Recherche des squarks et gluinos à grande $\tan\beta$ au Run II du TEVATRON"
- Thomas Millet, ENS Lyon, avril-juillet 2004,
"Recherche d'événements hémisphériques avec ATLAS au LHC et D0 au TEVATRON"
- Spyridon Argyropoulos, ENS Lyon, avril-juillet 2010,
"Contributions à la mesure de la section efficace $\sigma(p+p \rightarrow b\bar{b}+X)$ dans les données ATLAS à $\sqrt{s} = 7$ TeV"
- Thomas Serre, Université Clermont-Ferrand II, février-juin 2011,
"Utilisation de l'asymétrie de charge dans les recherches BSM au LHC"

A.3.3 Thèses

- Daniel Teyssier, IPN Lyon, Université Lyon I, septembre 1999 - mars 2002,
"Recherche du boson de Higgs standard et non-minimal à LEP2 dans l'expérience L3"
[377],
Directeur de thèse: Jean Paul Martin
Encadrant: S. Muanza
- Jérôme Coss, IPN Lyon, Université Lyon I, septembre 2000 - décembre 2003,
"L'étalonnage de l'énergie des jets avec le détecteur D0 au Run II du TEVATRON" [378],
Directeur de thèse: Jean Paul Martin
Encadrant: S. Muanza
- Thomas Millet, IPN Lyon, Université Lyon I, septembre 2004 - mai 2007,
"Recherche de gluinos dans la topologie à jets de quarks b et énergie transverse manquante avec le détecteur D0 au TeVatron" [379],
Directeur de thèse: Aldo Deandrea
Encadrant: S. Muanza
- Thomas Serre, CPPM Marseille, Université Aix-Marseille, octobre 2011 - octobre 2014,
Directeur de thèse: Pascal Pralavorio,
Co-Encadrant: S. Muanza
- Michael Ughetto, CPPM Marseille et LCC Montpellier, Université de Montpellier II, octobre 2011 - novembre 2014,
Directeur de thèse: Jean-Loïc Kneur,
Co-Encadrants: Gilbert Moulta, L. Vacavant, S. Muanza

A.3.4 Jurys

- M2 de Jérôme Coss, LPC Clermont-Ferrand, Université Clermont-Ferrand II, juillet 2000
- Thèse de Daniel Teyssier, IPN Lyon, Université Lyon I, 28 mars 2002
- Thèse de Jérôme Coss, IPN Lyon, Université Lyon I, 18 décembre 2003
- Thèse de Vincent Lesné, LPC Clermont-Ferrand, Université Clermont-Ferrand II, 11 juillet 2006
- M2 de Thomas Le Grand et A. Espargilière, ENS Lyon, 6 septembre 2007 [380]
- M1 de Jacques Arhan et William Creus, Université Lyon I, 7 septembre 2007
- Thèse de Thomas Millet, IPN Lyon, Université Lyon I, 11 mai 2007
- Thèse de Cément Bâty, IPN Lyon, Université Lyon I, 26 novembre 2009
- M2 de Spyridon Argyropoulos, ENS Lyon, 7 septembre 2010 [381]
- M2 de Thomas Serre, LPC Clermont-Ferrand, Université Clermont-Ferrand II, 15 juin 2011
- Thèse de Julien Chasserat, IPN Lyon, Université Lyon I, 5 mars 2014
- Master 2 de "Physique Théorique et Mathématique, Physique des Particules et Astrophysique" (P3TMA) de l'université Aix-Marseille, CPPM, juin 2012
- Thèse de Thomas Serre, CPPM et AMU, 9 octobre 2014
- Thèse de Michael Ughetto, LCC Montpellier et CPPM Marseille, Université Montpellier II, 7 novembre 2014

A.4 Enseignement

- "LA PHYSIQUE: La mécanique newtonnienne", 2h, 5 octobre 1999, Université Ouverte de Lyon
- "LA PHYSIQUE: L'électromagnétisme", 2h, 12 octobre 1999, Université Ouverte de Lyon
- "LA PHYSIQUE: Le monde de l'invisible", 2h, 26 octobre 1999, Université Ouverte de Lyon
- T.D. Electricité, DEUG A1, groupe B6, 9h, 1999-2000, Université Lyon I
- T.P. Informatique, DEUG A1, groupe D2, 12h, 1999-2000, Université Lyon I
- "LA PHYSIQUE de l'AN 2000: Le LHC", 2h, 12 janvier 2000, Université Ouverte de Lyon
- "VERS LA GRANDE UNIFICATION: L'instrumentation", 2h, 2000, Université Ouverte de Lyon

- "LA PHYSIQUE: La mécanique newtonnienne", 2h, 2000, Université Ouverte de Lyon
- "LA PHYSIQUE: L'électromagnétisme", 2h, 2000, Université Ouverte de Lyon
- "LA PHYSIQUE: Le monde de l'invisible", 2h, 2000, Université Ouverte de Lyon
- "LA PHYSIQUE: L'après LEP", 2h, 2000, Université Ouverte de Lyon
- "La Supersymétrie", 2h, 15 juin 2001, Université Ouverte de Lyon
- "Premiers Instants", 2h, 10 mars 2004, Université Ouverte de Lyon
- "MC Generators for Hadron Colliders", 8h, 30 janvier - 15 mai 2009, (cours informel) Groupe ATLAS CPPM Marseille
- "Experimental Particle Physics", 3h, août 2010, Ecole Africaine de Physique, Université de Stellenbosch, Afrique du Sud [401]
- "Introduction to Supersymmetry", 6h, 19 janvier 2010 - 28 janvier 2011, (cours informel) CPPM Marseille
Cours informel destiné aux étudiants en thèse et aux chercheurs dans groupes ATLAS, LHCb et ANTARES
- "Introduction à la Supersymétrie" (avec R. Grimm du CPT Marseille), 20h, janvier-février 2012, Cours de l'Ecole Doctorale 352, AMU
- "Introduction to Supersymmetry", 4h, février 2014, cours option M2 P3TMA, AMU
- "Introduction to Supersymmetry", 4h, août 2014, Ecole Africaine de Physique ASP2014, UCAD Dakar, Sénégal
- "Introduction to Supersymmetry", 4h, février 2015, cours option M2 P3TMA, AMU

A.5 Séminaires, Ateliers et Conférences

A.5.0.1 Séminaires

- "Report on the Searches for New Particles presented at ICHEP 2000", IPN Lyon, 3 octobre 2000 (avec G. Smadja)
- "Higgs searches with L3 at LEP", Brookhaven National Laboratory, Long Island NY, USA, 2 mai 2002
- "Non SUSY Searches at the TEVATRON", IPN Lyon, 17 juin 2004 (avec T. Kurca)
- "New Particle Searches at the TEVATRON Run II", IPN Lyon, 10 April 2007

A.5.0.2 Ateliers

Depuis 2005, j'ai participé et co-organisé un grand nombre de réunions nationales et européennes pour le GDR SUSY et pour le GDR Terascale. J'ai par exemple été le principal organisateur de:

- "EuroGDR Supersymmetry Workshop on SM Backgrounds", IPN Lyon, 13-14 octobre 2005 [387]
- "Réunion Générale du GDR Terascale", CPPM Marseille, 11-13 octobre 2011 [388]

Par ailleurs, voici une liste non-exhaustive d'ateliers où j'ai été orateur invité:

- "L3 Analysis Workshop", 28 mai 2001, Balatonfüred, Hungary,
Présentation: "Search for Invisible Higgs Boson Decays" (travail en collaboration avec P. Lebrun et D. Teyssier)
- "D0 Winter Physics Workshop", 24 février 2004, FNAL, Batavia IL, USA,
Présentation: "Event generator and detector simulation"
- "D0 Workshop 2004", 11 juin 2004, Fresno CA, USA,
Présentations: "Generators for p17", "MC Production", "Status Report on Common Alpgen+Pythia Studies"
- "D0 Grid Workshop", 29 avril - 1 mai 2005, FNAL, Batavia IL, USA,
Présentation: "Evolution of the Cardfiles package" (présenté par T. Kurca, préparé par moi)
- "Physics at TeV Colliders", 2-20 mai 2005, Les Houches, [411]
Co-responsable du groupe BSM, représentant la collaboration D0 [412],
Présentation: "A Search for Gluino Decays into 2 b-jets and a dilpeton at the LHC" (travail en collaboration avec T. Millet),
Actes: "Beyond the Standard Model Working Group: Summary Report," [413]
- "D0 New Phenomena Workshop", 5 décembre 2005, FNAL, Batavia IL, USA,
Présentation: "Status and Pending Issues of the p17 MC"
- "Top Workshop IN2P3 : From Dzero to ATLAS", 9-10 Octobre 2006, LPSC Grenoble,
Présentation: "MC for V+jets"
- "Physics at TeV Colliders", 11-29 juin 2007, Les Houches, [414]
Présentation: "Status of the Blind SUSY Analysis Project", 15 juin 2007
Actes: "Physics Beyond the Standard Model: Supersymmetry," [415]
- "Workshop on Top Physics: from the TeVatron to the LHC", 18-20 October 2007, LPSC Grenoble,
Présentation: "MC Validation for W/Z+jets Production"
- "D0 Workshop: Review of 1 fb⁻¹ Analyses", 29 octobre 2008, FNAL, Batavia IL, USA,
Présentation: "Gluino in bbbb+met"

- "CosmoRetreat", 12-13 mars 2009, Gemenos, France,
Présentation: "Interplay between LHC and Cosmology" [396]
- "MC4BSM", 14-16 avril 2010, Niels Bohr Institute, Copenhagen, Danemark,
Présentation: "D0 BSM Searches" [393]
- "BSM and the Early LHC Data", 13-17 décembre 2010, IPN Lyon,
Présentation: "ATLAS Searches for Extra Gauge Bosons and for SUSY in the Early LHC Data" [397]
- "Rencontre de Physique des Particules 2011", 13-14 janvier 2011, LPC Clermont-Ferrand,
Présentation: "ATLAS SUSY searches: preliminary results and short term prospects" [398]
- "Mini Workshop on neutrino indirect detection of Dark Matter", 13-14 décembre 2011, CPPM Marseille
Présentation: "Status of the RPC SUSY Searches at the LHC" [418]
- "Workshop Tools for SM and the New Physics", 18-21 juin 2012, Stockholm, Suède
Présentation: "Global Charge Asymmetry: a New Method for Indirect Mass Constraints at the LHC" [419]

A.5.0.3 Conférences

J'ai été orateur invité dans les conférences suivantes:

- "31st Rencontres de Moriond: QCD and High-Energy Hadronic Interactions", 23-30 mars 1996, Bourg-St-Maurice, France
Présentation: "The Search For Charginos And Neutralinos With ATLAS Detector At LHC" [309]
- "3rd International Workshop on Diquarks and other Models of Compositeness (DIQUARKS III)", Turin, Italy, 28-30 octobre 1996
Présentation: "The search for chargino-neutralino pairs with the ATLAS detector at the LHC" [310]
- "American Physical Society Centennial Meeting", 20-26 mars 1999, Atlanta GA, USA
Présentations: "Search for the Standard Model Higgs Boson in e^+e^- Interactions at $\sqrt{s} = 189$ GeV",
"Search for Neutral Higgs Bosons of the MSSM in e^+e^- Interactions at $\sqrt{s} = 130 - 189$ GeV" [394]
- "PHENO 2000 Symposium", avril 2000, Madison WI, USA
Présentation: "Search for Higgs Bosons in e^+e^- Interactions with the L3 detector at LEP" [395]
- "37th Rencontres de Moriond: QCD and High-Energy Hadronic Interactions", 17-24 mars 2002, Bourg-St-Maurice, France
Présentation: "Searches at the Tevatron" [382]

- "15th International Topical Conference on Hadron Collider Physics", 14-18 juin 2004, East-Lansing MI, USA
Présentation: "Searches for Strong Dynamics at the TEVATRON" [383]
- "42nd Rencontres de Moriond: QCD and High-Energy Hadronic Interactions", 17-24 mars 2007, La Thuile, Italie
Présentation: "Non-SUSY Searches at the Tevatron" [384]
- "Physics at the LHC", 29 septembre - 4 octobre 2008, Split, Croatia
Présentation: "D0 SUSY/BSM Searches" [385]
- "XXII. International Workshop on Deep-Inelastic Scattering and Related Subjects", 28 April - 2 May 2014, Varsovie, Pologne
Présentation: "Search for 3rd generation squarks with ATLAS detector" [420]

Enfin, j'ai fait partie du "Scientific Advisory Committee" et l'"Editorial Board" de la conférence Kruger2010, "Workshop on Discovery Physics at the LHC" qui s'est tenue du 5-10 décembre 2010 à Mpumalanga en Afrique du Sud [386].

A.6 Administration de la Recherche

- Membre élu du Conseil de Laboratoire de l'IPN Lyon de 1998 à 2003
- Membre élu du Conseil Scientifique de l'IPN Lyon de 2005 à 2007
- Responsable du groupe D0 de l'IPN Lyon du 1 septembre 2006 au 1 septembre 2008
- Membre de l'Institutional Board de la collaboration D0 de 2006 à 2008
- Membre élu du Conseil Scientifique du CPPM Marseille depuis 2009
- Membre du Conseil de Groupement du GDR 2305 sur la Supersymétrie de 2005 à 2008
- Responsable de l'Ecole Africaine de Physique 2010
- Membre de l'International Organizing Committee de l'Ecole Africaine de Physique depuis 2012
- Membre du Conseil de Groupement du GDR Terascale de 2009 à 2012
- Membre du Conseil de Groupement du GDR Terascale depuis 2012
- Membre élu du Conseil Scientifique du Labex OCEVU depuis juillet 2012
- Représentant du groupe ATLAS-CPPM dans le comité de Physique ATLAS-France de mai 2012 à juillet 2013
- Représentant du groupe ATLAS-CPPM dans le comité de programme du 1^{er} workshop "LHC France 2013" [429]

A.7 Vulgarisation de la Recherche

- Animation de l'exposition de l'IN2P3 "Sur les traces de l'invisible" dans le cadre de la Semaine de la Science, 12 octobre 1998, Bât. Astrée, Université Lyon I
- Accompagnement et animation de visites du CERN par des groupes de l'Université Ouverte Lyon-I: 3 février 1999, 5 juin 1999, 27 mai 2005
- Organisateur d'une visite du CERN, pour un groupe d'une quarantaine de personnes de l'IPNL, d'étudiants de Lyon I et d'accompagnants à l'occasion du cinquantenaire du CERN (16 Octobre 2004)
- "Fête dans les étoiles", CRAL, l'Observatoire de Lyon, 25 juin 2005
Présentation: "Le Big Bang en laboratoire".
- "Café des Sciences", Lyon, 5 novembre 2007, "Bientôt l'accélérateur de particule géant du CERN : le Big Bang en éprouvette!" [390]
- "Particle Physics" (avec John Ellis et Christine Darve), 6 août 2010, Canal Walk Science Centre, Cape Town, Afrique du Sud [402]
- "Café des Sciences", Avignon, 8 juin 2011
"Comprendre les secrets de la matière, le LHC... arme ultime?" [391]
- "Conférence Grand Public", CPPM Marseille, 15 octobre 2011
"La supersymétrie : 40 ans d'illusion ou avenir de la physique des particules? Le dénouement approche" [392]
- "Conférence Grand Public", Centre Castelvieux, Marseille, 27 novembre 2012
"Voyage au coeur de la matière. La découverte du boson de Higgs" [421]
- Visite du CERN avec des classes de 1^{ère} et terminale scientifiques de l'IST Marseille, décembre 2013
- "Conférence Grand Public", IST Marseille, 8 décembre 2014
"Marie Sklodowska-Curie: Parcours et Découvertes d'une Femme d'Exception" [427]

Bibliography

- [1] J. C. Ward, Phys. Rev. **78** (1950) 182.
- [2] Y. Takahashi, Nuovo Cim. **6** (1957) 371.
- [3] J. C. Taylor, Nucl. Phys. B **33** (1971) 436.
- [4] A. A. Slavnov, Theor. Math. Phys. **10** (1972) 99 [Teor. Mat. Fiz. **10** (1972) 153].
- [5] S. L. Glashow, Nucl. Phys. **22** (1961) 579.
- [6] S. Weinberg, Phys. Rev. Lett. **19** (1967) 1264.
- [7] A. Salam, Conf. Proc. C **680519** (1968) 367.
- [8] J.H. Poincaré, “Sur la dynamique de l’électron”. Comptes rendus Acad. Sci. Paris, 140 (1905) 1504-1508.
- [9] J.H. Poincaré, “Sur la dynamique de l’électron”. Rendiconti del Circolo Matematico di Palermo, 21 (1906) 129-175.
- [10] E. P. Wigner, “On Unitary Representations of the Inhomogeneous Lorentz Group,” Annals Math. **40** (1939) 149 [Nucl. Phys. Proc. Suppl. **6** (1989) 9].
- [11] O. Laporte and W.F. Meggers, “Some rules of spectral structure”. J. of the Optical Society of America 11 5 (1925) 459-460.
- [12] T.D. Lee and C.N. Yang, “Question of Parity Conservation in Weak Interactions”. Phys. Rev. 104 (1956) 254-258
- [13] C.S. Wu, E. Ambler, R.W. Hayward, D.D. Hoppes and R.P. Hudson, “Experimental Test of Parity Conservation in Beta Decay”. Phys. Rev. 105 (1957) 1413-1415.
- [14] R.L. Garwin, L.M. Lederman and M. Weinrich, “Observations of the Failure of Conservation of Parity and Charge Conjugation in Meson Decays: the Magnetic Moment of the Free Muon”. Phys. Rev. 105,(1957) 1415-1417
- [15] J.H. Christenson, J.W. Cronin, V.L. Fitch and R. Turlay, Phys. Rev. Lett. **13** (1964) 138.
- [16] J. Schwinger, “The Theory of Quantized Fields I”. Phys. Rev. 82, (1951) 914-927
- [17] W. Pauli, “Exclusion principle, Lorentz group and reflection of space-time and charge” in Niels Bohr and the Development of Physics (Pergamon Press, New York) (1955) 30.

-
- [18] J. S. Bell, “Time reversal in field theory”, Proc. of the Royal Society of London. Series A, Math. and Phys. Sc. 231, (1955) 479.
- [19] G. Lüders, Ann. of Physics, 2 (1) (1957) 1-15
- [20] R. Jost, Helv. Phys. Act. 30 (1957) 409.
- [21] J. S. Bell and R. Jackiw, Nuovo Cim. A **60** (1969) 47.
- [22] S. L. Adler, Phys. Rev. **177** (1969) 2426.
- [23] P. W. Higgs, Phys. Rev. Lett. **13** (1964) 508.
- [24] F. Englert and R. Brout, Phys. Rev. Lett. **13** (1964) 321.
- [25] G. S. Guralnik, C. R. Hagen and T. W. B. Kibble, Phys. Rev. Lett. **13** (1964) 585.
- [26] P. W. Anderson, Phys. Rev. **130** (1963) 439.
- [27] M. Baak *et al.* [Gfitter Group Collaboration], Eur. Phys. J. C **74** (2014) 3046 [arXiv:1407.3792 [hep-ph]].
- [28] G. Aad *et al.* [ATLAS Collaboration], Phys. Lett. B **716** (2012) 1 [arXiv:1207.7214 [hep-ex]].
- [29] S. Chatrchyan *et al.* [CMS Collaboration], Phys. Lett. B **716** (2012) 30 [arXiv:1207.7235 [hep-ex]].
- [30] Y. A. Golfand and E. P. Likhtman, JETP Lett. **13** (1971) 323 [Pisma Zh. Eksp. Teor. Fiz. **13** (1971) 452].
- [31] D. V. Volkov and V. P. Akulov, Phys. Lett. B **46** (1973) 109.
- [32] S. R. Coleman and J. Mandula, Phys. Rev. **159** (1967) 1251.
- [33] R. Haag, J. T. Lopuszanski and M. Sohnius, Nucl. Phys. B **88** (1975) 257.
- [34] J. Wess and B. Zumino, Phys. Lett. B **49** (1974) 52.
- [35] P. Fayet and J. Iliopoulos, Phys. Lett. B **51** (1974) 461.
- [36] L. O’Raifeartaigh, Nucl. Phys. B **96** (1975) 331.
- [37] S. Ferrara, L. Girardello and F. Palumbo, Phys. Rev. D **20** (1979) 403.
- [38] S. Dimopoulos and H. Georgi, Nucl. Phys. B **193** (1981) 150.
- [39] M. Guchait, Z. Phys. C **57** (1993) 157 [Z. Phys. C **61** (1994) 178].
- [40] G. Aad *et al.* [ATLAS Collaboration], JINST **3** (2008) S08003.
- [41] L. Evans and P. Bryant, JINST **3** (2008) S08001.
- [42] G. Aad *et al.* [ATLAS Collaboration], Eur. Phys. J. C **72** (2012) 1849 [arXiv:1110.1530 [hep-ex]].
- [43] P. Fayet, Phys. Lett. B **64** (1976) 159.

- [44] P. Fayet, Phys. Lett. B **69** (1977) 489.
- [45] G. R. Farrar and P. Fayet, Phys. Lett. B **76** (1978) 575.
- [46] P. Fayet, Phys. Lett. B **84** (1979) 416.
- [47] S. Weinberg, Phys. Rev. D **13** (1976) 974.
- [48] E. Gildener, Phys. Rev. D **14** (1976) 1667.
- [49] S. Weinberg, Phys. Rev. D **19** (1979) 1277.
- [50] L. Susskind, Phys. Rev. D **20** (1979) 2619.
- [51] S. Dimopoulos and S. Raby, Nucl. Phys. B **192** (1981) 353.
- [52] E. Witten, Nucl. Phys. B **188** (1981) 513.
- [53] M. Dine, W. Fischler and M. Srednicki, Nucl. Phys. B **189** (1981) 575.
- [54] N. Sakai, Z. Phys. C **11** (1981) 153.
- [55] R. K. Kaul and P. Majumdar, Nucl. Phys. B **199** (1982) 36.
- [56] H. Goldberg, Phys. Rev. Lett. **50** (1983) 1419 [Erratum-ibid. **103** (2009) 099905].
- [57] J. R. Ellis, J. S. Hagelin, D. V. Nanopoulos, K. A. Olive and M. Srednicki, Nucl. Phys. B **238** (1984) 453.
- [58] S. Dimopoulos, S. Raby and F. Wilczek, Phys. Rev. D **24** (1981) 1681.
- [59] L. E. Ibanez and G. G. Ross, Phys. Lett. B **105** (1981) 439.
- [60] M. B. Einhorn and D. R. T. Jones, Nucl. Phys. B **196** (1982) 475.
- [61] W. J. Marciano and G. Senjanovic, Phys. Rev. D **25** (1982) 3092.
- [62] C. Giunti, C. W. Kim and U. W. Lee, Mod. Phys. Lett. A **6** (1991) 1745.
- [63] J. R. Ellis, S. Kelley and D. V. Nanopoulos, Phys. Lett. B **260** (1991) 131.
- [64] U. Amaldi, W. de Boer and H. Furstenaue, Phys. Lett. B **260** (1991) 447.
- [65] P. Langacker and M. x. Luo, Phys. Rev. D **44** (1991) 817.
- [66] A. H. Chamseddine, R. L. Arnowitt and P. Nath, Phys. Rev. Lett. **49** (1982) 970.
- [67] R. Barbieri and G. F. Giudice, Nucl. Phys. B **306** (1988) 63.
- [68] B. de Carlos and J. A. Casas, In *Kazimierz 1993, Proceedings, New physics with new experiments* 340-343. and CERN Geneva - TH. 7024 (93/09,rec.Dec.) 6 p. Madrid Inst. Estruct. Mater. - IEM-FT-93-78 (93/09,rec.Dec.) 6 p [hep-ph/9310232].
- [69] G. Aad *et al.* [ATLAS Collaboration], JHEP **1404** (2014) 169 [arXiv:1402.7029 [hep-ex]].
- [70] G. Aad *et al.* [ATLAS Collaboration], JHEP **1405** (2014) 071 [arXiv:1403.5294 [hep-ex]].
- [71] G. Aad *et al.* [ATLAS Collaboration], JHEP **1410** (2014) 96 [arXiv:1407.0350 [hep-ex]].

- [72] V. Khachatryan *et al.* [CMS Collaboration], *Eur. Phys. J. C* **74** (2014) 9, 3036 [arXiv:1405.7570 [hep-ex]].
- [73] V. Khachatryan *et al.* [CMS Collaboration], *Phys. Rev. D* **90** (2014) 092007 [arXiv:1409.3168 [hep-ex]].
- [74] V. M. Abazov *et al.* [D0 Collaboration], *Phys. Lett. B* **680** (2009) 34 [arXiv:0901.0646 [hep-ex]].
- [75] T. Aaltonen *et al.* [CDF Collaboration], *Phys. Rev. Lett.* **101** (2008) 251801 [arXiv:0808.2446 [hep-ex]].
- [76] Y.A. Gol'fand and E.P. Likhman, *JETP Lett.* **13** (1971), 323.
D. Volkov and V.P. Akulov, *Phys. Lett.* **46B** (1973), 109.
J. Wess and B. Zumino, *Nucl. Phys.* **B70** (1974), 39.
J. Iliopoulos and B. Zumino, *Nucl. Phys.* **B76** (1974), 310.
P. Fayet and S. Ferrara, *Phys. Rep.* **32** (1977), 249.
- [77] S. Abachi *et al.* (D0 Collaboration), "Search for Squarks and Gluinos at $\sqrt{s} = 1.8TeV$ ", *Phys. Rev. Lett.* **75**, 618 (1995).
B. Abbott *et al.* (D0 Collaboration), "Search for Squarks and Gluinos in Events Containing Jets and a Large Imbalance in Transverse Momentum", *Phys. Rev. Lett.* **83**, 4937 (1999).
- [78] V.M. Abazov *et al.* (D0 Collaboration), "Search for Squarks and Gluinos in Events with Jets and Missing Transverse Energy in pbarp Collisions at $\sqrt{s} = 1.96TeV$ " *Phys. Lett. B* **638**, 119 (2006).
- [79] P. Verdier *et al.*, "Search for squarks and gluinos in events with jets and missing transverse energy with the DO detector using $1fb^{-1}$ of RunIIa data", D0 Note 5312.
- [80] M.L. Mangano *et al.*, "ALPGEN, a generator for hard multiparton processes in hadronic collisions", *JHEP* 0307:001,2003, hep-ph/0206293.
- [81] S. Muanza,
http://www-d0.fnal.gov/computing/MonteCarlo/generator_tools/prospino.html
<http://cdcvs0.fnal.gov/cgi-bin/public-cvs/cvsweb-public.cgi/PROSPINO/?cvsroot=d0cvs>
- [82] S. Dimopoulos and H. Georgi, "Softly Broken Supersymmetry and SU(5)", *Nucl. Phys. B* **193**, 150-162 (1981).
H.P. Nilles, *Phys. Rep.* **110** (1984) 1.
H.E. Haber and G.L. Kane, *Phys. Rep.* **117** (1985) 75.
- [83] A.H. Chamseddine, R. Arnowitt and P. Nath, *Phys. Rev. Lett.* **49**, (1982) 970.
J. Wess and J. Bagger, "Supersymmetry and Supergravity", Princeton University Press, Princeton 1983; revised edition 1992.
- [84] S. Abachi *et al.* [D0 Collaboration], *Nucl. Instrum. Meth. A* **338** (1994) 185.
- [85] V.M. Abazov *et al.*, (D0Collaboration), "The Upgraded D0detector", *Nucl. Instrum. Methods Phys. Res. A* **565**, 463 (2006).

- [86] V. M. Abazov *et al.*, Nucl. Instrum. Meth. A **552** (2005) 372 [physics/0503151].
- [87] Common Samples Group, "p17 PASS3 Data Samples",
<http://www-d0.fnal.gov/Run2Physics/cs/skimming/fixPass2p170903.html#skimmed>.
- [88] Reconstruction Group
<http://www-d0.fnal.gov/computing/algorithms/status/index.html>
<http://www-d0.hef.kun.nl//fullAgenda.php?ida=a052237>.
- [89] T. Andeen *et al.*, "Luminosity Constant for D0Run II", D0 Note 4496.
- [90] A. Zabi *et al.*, "A Trigger for Jets and Missing E_T ", D0 Note 4315, (2004).
- [91] T. Millet *et al.*, "Jets and MET triggers for the New Phenomena group in the V14 and V15 trigger lists", D0 Note 5120.
- [92] Particle Data Group reference:
W.-M. Yao *et al.*, Journal of Physics G **33**, 1 (2006).
- [93] GEANT reference:
R. Brun and F. Carminati, CERN Program Library Long Writeup W5013, 1993 (unpublished).
- [94] PYTHIA reference:
T. Sjöstrand *et al.*, Comput. Phys. Commun. **135**, 238 (2001).
- [95] P.Z. Skands *et al.*, "SUSY Les Houches Accord: Interfacing SUSY Spectrum Calculators, Decay Packages, and Event Generators", JHEP 0407 (2004) 036.
S. Muanza, "Susy Tools with SLHA"
<http://www-d0.hef.kun.nl//fullAgenda.php?ida=a06427&fid=33>
http://cdcv0.fnal.gov/cgi-bin/public-cvs/cvswb-public.cgi/susy_tools/?cvsroot=d0cvs.
- [96] G. Brooijmans, http://www-d0.fnal.gov/gusbroo/d0_private/060620-mc.pdf.
- [97] S. Muanza, "NLO Normalization of V+jets Samples"
<http://www-d0.hef.kun.nl//askArchive.php?base=agenda&categ=a062091&id=a062091s1t106/transparent>
- [98] J. Pumplin *et al.*, JHEP **0207** 012 (2002), hep-ph/0201195.
- [99] D. Stump *et al.*, JHEP **0310** 046 (2003), hep-ph/0303013.
- [100] M. Muhlleitner, A. Djouadi, Y. Mambrini
"SDECAY: a Fortran code for the decays of the supersymmetric particles in the MSSM"
Comput.Phys.Commun. 168 (2005) 46-70, hep-ph/0311167.
- [101] E.Boos *et al.*, [CompHEP Collaboration], "CompHEP 4.4: Automatic computations from Lagrangians to events, Nucl. Instrum. Meth. A534(2004), p250.
A.S. Belyaev *et al.*, "CompHEP - PYTHIA interface", hep-ph/0101232.
P. Bargassa, S. Desai and G. Brooijmans
<http://www-d0.fnal.gov/d0dist/dist/packages/comphep/devel>.

- [102] R.K. Ellis, J. Campbell *et al.*,
Phys. Rev. D60:011501 (1999), Phys. Rev. D60:113006 (1999), Phys. Rev. D62:114012 (2000),
Phys. Rev. D65:113007 (2002), Phys. Rev. D67:095002 (2003), Phys. Rev. D68:094021 (2003),
Phys. Rev. D69:074021 (2004), Phys.Rev.D70:094012,2004, Nucl.Phys.B726:109-130,2005.
- [103] S. Muanza, "A Compilation of MCFM v5.1 Cross Sections", D0 Note 5300.
- [104] The Tevatron Electroweak Working Group for the CDF and D0 Collaborations,
"Combination of CDF and D0 Results on the Mass of the Top Quark", hep-ex/0608032.
- [105] B. Casey and G. Snow for the D0 Luminosity group, "Improved Determination of the D0 Luminosity",
D0 Note 5140.
- [106] A. Schwartzman, <http://www-d0.hef.kun.nl//fullAgenda.php?ida=a05321&fid=64>.
- [107] The Simulation Group, "Proposed settings in mcp17 for V(=W/Z)+jets processes",
http://www-d0.fnal.gov/computing/MonteCarlo/generators/common_alpgen.html.
- [108] T. Junk, Nucl. Instrum. Methods A **434**, 435 (1999).
- [109] The CDF Collaboration, "Search for Gluino Pairs Decaying into Sbottom Bottom",
Phys. Rev. Lett. **96**, 171802 (2006), hep-ex/0512072.
- [110] L. Duflot, P. Verdier <http://www-d0.hef.kun.nl//fullAgenda.php?ida=a061360&fid=70>
L. Duflot, P. Verdier <http://www-d0.hef.kun.nl//fullAgenda.php?ida=a061369&fid=32>.
- [111] M. Petteni, "The mjcaf_par_trigger Package",
http://cdcv0.fnal.gov/cgi-bin/public-cvs/cvsweb-public.cgi/mjcaf_par_trigger/?cvsroot=d0cvs,
<http://www-d0.hef.kun.nl//fullAgenda.php?ida=a06844&fid=93>,
<http://www-d0.hef.kun.nl//fullAgenda.php?ida=a06940&fid=33>.
- [112] J.B. de Vivie de Régie, J.-F. Grivaz for the LEP SUSY Working Group, "Combined Lower Bound of the Neutralino Mass in a Constrained MSSM Model",
LEPSUSYWG/04-07.1, http://lepsusy.web.cern.ch/lepsusy/www/lsp_cmssm_summer04/cmSSM_final.html.
- [113] The JES Group, "Jet energy scale at D0 Run II using p17 data (v7.1)",
D0 Note 5248.
- [114] A. Duperrin *et al.*, "The V13 physics trigger list and New Phenomena Triggers",
D0 Note 4641.
- [115] L. Duflot *et al.*, "The cal_event_quality package",
D0 Note 4614.
- [116] S. Park *et al.*, "Efficiency of the data quality calorimeter flags",
D0 Note 5324.

- [117] B. Andrieu *et al.*, "Jet-ID Certification for Run IIa Data in p17", D0 Note 5170.
A. Harel *et al.*, "Combined JetID efficiency for p17", D0 Note 5218.
B. Andrieu *et al.*, "Measuring Reconstruction*Jet-ID efficiencies using the tag and probe method in p17", D0 Note 5250.
- [118] N. Makovec and J.-F. Grivaz, "Shifting, Smearing and Removing Simulated Jets", D0 Note 4914.
- [119] N. Makovec, "Search for New Physics in the Jets + Missing ET Topology", Ph.D. Thesis, Paris XI University, May 2006.
- [120] S. Trincaz-Duvoid and P. Verdier, "Missing ET Reconstruction in p17", D0 Note 4474.
- [121] M. Pangilinan, "First look at cable swap data",
<http://www-d0.hef.kun.nl//fullAgenda.php?ida=a061610&fid=35>.
M. Pangilinan, "Jet trigger turn-ons in cable swap data",
<http://www-d0.hef.kun.nl//fullAgenda.php?ida=a061750&fid=35>.
- [122] D. Gillberg, "Heavy Flavour Removal and Determination of Weighting Factors for ALPGEN W+jet Monte Carlo",
D0 Note 5129.
- [123] M. Anastasoae, S. Robinson, T. Scanlon, "Performance of the NN b-tagging Tool on p17 Data",
D0 Note 5213.
- [124] S. Calvet, A. Duperrin, E. Kajfasz, "Search for Pair Production of Scalar Bottom Quarks with the D0 in $p\bar{p}$ Collisions at $\sqrt{s} = 1.96$ TeV",
D0 Note 5074.
- [125] V. M. Abazov *et al.* [D0 Collaboration], Phys. Rev. Lett. **101** (2008) 062001 [arXiv:0802.2400 [hep-ex]].
- [126] M.L. Mangano,
<http://mlm.web.cern.ch/mlm/talks/lund-alpgen.pdf>
- [127] M.L. Mangano, M. Moretti, F. Piccinini and M. Treccani, JHEP **0701** (2007) 013 [hep-ph/0611129].
- [128] LEP SUSY Working Group. ALEPH, DELPHI, L3 and OPAL Experiments
"Combined LEP Chargino Results up to 208 GeV for large m_0 "
http://lepsusy.web.cern.ch/lepsusy/www/inos_moriond01/charginos_pub.html
- [129] A. Heister *et al.* [ALEPH Collaboration], Phys. Lett. B **583** (2004) 247.
- [130] J. Abdallah *et al.* [DELPHI Collaboration], Eur. Phys. J. C **31** (2003) 421 [hep-ex/0311019].
- [131] M. Acciarri *et al.* [L3 Collaboration], Phys. Lett. B **472** (2000) 420 [hep-ex/9910007].
- [132] G. Abbiendi *et al.* [OPAL Collaboration], Eur. Phys. J. C **35** (2004) 1 [hep-ex/0401026].

- [133] V. M. Abazov *et al.* [D0 Collaboration], Phys. Lett. B **638** (2006) 119 [hep-ex/0604029].
- [134] G. Aad *et al.* [ATLAS Collaboration], JINST **3** (2008) S08003.
- [135] S. Agostinelli *et al.* [GEANT4 Collaboration], Nucl. Instrum. Meth. A **506** (2003) 250.
- [136] G. Aad *et al.* [ATLAS Collaboration], JINST **3** (2008) S08003.
- [137] G. Aad *et al.* [ATLAS Collaboration], Eur. Phys. J. C **70** (2010) 823 [arXiv:1005.4568 [physics.ins-det]].
- [138] ATLAS Collaboration [ATLAS Collaboration], ATL-PHYS-PUB-2010-013, ATL-COM-PHYS-2010-838.
- [139] T. Sjostrand, S. Mrenna and P. Z. Skands, Comput. Phys. Commun. **178** (2008) 852 [arXiv:0710.3820 [hep-ph]].
- [140] The ATLAS collaboration, ATLAS-CONF-2013-044, ATLAS-COM-CONF-2013-040.
- [141] B. P. Kersevan and E. Richter-Was, Comput. Phys. Commun. **184** (2013) 919 [hep-ph/0405247].
- [142] T. Sjostrand, S. Mrenna and P. Z. Skands, JHEP **0605** (2006) 026 [hep-ph/0603175].
- [143] N. Kidonakis, Phys. Rev. D **83** (2011) 091503 [arXiv:1103.2792 [hep-ph]].
- [144] [ATLAS Collaboration], ATL-PHYS-PUB-2011-009, ATL-COM-PHYS-2011-744.
- [145] J. Pumplin, D. R. Stump, J. Huston, H. L. Lai, P. M. Nadolsky and W. K. Tung, JHEP **0207** (2002) 012 [hep-ph/0201195].
- [146] P. Nason, JHEP **0411** (2004) 040 [hep-ph/0409146].
- [147] S. Frixione, P. Nason and C. Oleari, JHEP **0711** (2007) 070 [arXiv:0709.2092 [hep-ph]].
- [148] N. Kidonakis, Phys. Rev. D **81** (2010) 054028 [arXiv:1001.5034 [hep-ph]].
- [149] P. Z. Skands, Phys. Rev. D **82** (2010) 074018 [arXiv:1005.3457 [hep-ph]].
- [150] H. L. Lai, M. Guzzi, J. Huston, Z. Li, P. M. Nadolsky, J. Pumplin and C.-P. Yuan, Phys. Rev. D **82** (2010) 074024 [arXiv:1007.2241 [hep-ph]].
- [151] N. Kidonakis, Phys. Rev. D **82** (2010) 054018 [arXiv:1005.4451 [hep-ph]].
- [152] M. Cacciari, M. Czakon, M. Mangano, A. Mitov and P. Nason, Phys. Lett. B **710** (2012) 612 [arXiv:1111.5869 [hep-ph]].
- [153] P. Bärnreuther, M. Czakon and A. Mitov, Phys. Rev. Lett. **109** (2012) 132001 [arXiv:1204.5201 [hep-ph]].
- [154] M. Czakon and A. Mitov, JHEP **1212** (2012) 054 [arXiv:1207.0236 [hep-ph]].
- [155] M. Czakon and A. Mitov, JHEP **1301** (2013) 080 [arXiv:1210.6832 [hep-ph]].
- [156] M. Czakon, P. Fiedler and A. Mitov, Phys. Rev. Lett. **110** (2013) 252004 [arXiv:1303.6254 [hep-ph]].

- [157] M. Czakon and A. Mitov, *Comput. Phys. Commun.* **185** (2014) 2930 [arXiv:1112.5675 [hep-ph]].
- [158] J. Alwall, P. Demin, S. de Visscher, R. Frederix, M. Herquet, F. Maltoni, T. Plehn and D. L. Rainwater *et al.*, *JHEP* **0709** (2007) 028 [arXiv:0706.2334 [hep-ph]].
- [159] T. Gleisberg, S. Hoeche, F. Krauss, M. Schonherr, S. Schumann, F. Siegert and J. Winter, *JHEP* **0902** (2009) 007 [arXiv:0811.4622 [hep-ph]].
- [160] M. L. Mangano, M. Moretti, F. Piccinini, R. Pittau and A. D. Polosa, *JHEP* **0307** (2003) 001 [hep-ph/0206293].
- [161] T. Sjostrand, S. Mrenna and P. Z. Skands, *Comput. Phys. Commun.* **178** (2008) 852 [arXiv:0710.3820 [hep-ph]].
- [162] S. Heinemeyer *et al.* [LHC Higgs Cross Section Working Group Collaboration], arXiv:1307.1347 [hep-ph].
- [163] [ATLAS Collaboration], ATL-PHYS-PUB-2012-003, ATL-COM-PHYS-2012-738.
- [164] M. Bahr, S. Gieseke, M. A. Gigg, D. Grellscheid, K. Hamilton, O. Latunde-Dada, S. Platzer and P. Richardson *et al.*, *Eur. Phys. J. C* **58** (2008) 639 [arXiv:0803.0883 [hep-ph]].
- [165] W. Beenakker, R. Hopker, M. Spira and P. M. Zerwas, *Nucl. Phys. B* **492** (1997) 51 [hep-ph/9610490].
- [166] B. Fuks, M. Klasen, D. R. Lamprea and M. Rothering, *JHEP* **1210** (2012) 081 [arXiv:1207.2159 [hep-ph]].
- [167] B. Fuks, M. Klasen, D. R. Lamprea and M. Rothering, *Eur. Phys. J. C* **73** (2013) 2480 [arXiv:1304.0790 [hep-ph]].
- [168] M. Kramer, A. Kulesza, R. van der Leeuw, M. Mangano, S. Padhi, T. Plehn and X. Portell, arXiv:1206.2892 [hep-ph].
- [169] G. Aad *et al.* [ATLAS Collaboration], *Eur. Phys. J. C* **73** (2013) 8, 2518 [arXiv:1302.4393 [hep-ex]].
- [170] G. Aad *et al.* [ATLAS Collaboration], *Eur. Phys. J. C* **74** (2014) 7, 2941 [arXiv:1404.2240 [hep-ex]].
- [171] G. Aad *et al.* [ATLAS Collaboration], *Eur. Phys. J. C* **74** (2014) 11, 3130 [arXiv:1407.3935 [hep-ex]].
- [172] G. Aad *et al.* [ATLAS Collaboration], *Eur. Phys. J. C* **74** (2014) 10, 3071 [arXiv:1407.5063 [hep-ex]].
- [173] M. Cacciari, G. P. Salam and G. Soyez, *JHEP* **0804** (2008) 063 [arXiv:0802.1189 [hep-ph]].
- [174] W. Lampl, S. Laplace, D. Lelas, P. Loch, H. Ma, S. Menke, S. Rajagopalan and D. Rousseau *et al.*, ATL-LARG-PUB-2008-002, ATL-COM-LARG-2008-003.

-
- [175] G. Aad *et al.* [ATLAS Collaboration], *Eur. Phys. J. C* **73** (2013) 3, 2304 [arXiv:1112.6426 [hep-ex]].
- [176] G. Aad *et al.* [ATLAS Collaboration], arXiv:1406.0076 [hep-ex].
- [177] G. Aad *et al.* [ATLAS Collaboration], *JHEP* **1406** (2014) 035 [arXiv:1404.2500 [hep-ex]].
- [178] The ATLAS collaboration, ATLAS-CONF-2013-083, ATLAS-COM-CONF-2013-097.
- [179] [ATLAS Collaboration], ATLAS-CONF-2011-102, ATLAS-COM-CONF-2011-110.
- [180] [ATLAS Collaboration], ATLAS-CONF-2012-054, ATLAS-COM-CONF-2012-064.
- [181] [ATLAS Collaboration], ATLAS-CONF-2012-054, ATLAS-COM-CONF-2012-064.
- [182] G. Aad *et al.* [ATLAS Collaboration], *JHEP* **1404** (2014) 169 [arXiv:1402.7029 [hep-ex]].
- [183] G. Aad *et al.* [ATLAS Collaboration], *Eur. Phys. J. C* **72** (2012) 1844 [arXiv:1108.5602 [hep-ex]].
- [184] The ATLAS collaboration, ATLAS-CONF-2013-082, ATLAS-COM-CONF-2013-075.
- [185] G. Aad *et al.* [ATLAS Collaboration], *Eur. Phys. J. C* **74** (2014) 7, 2941 [arXiv:1404.2240 [hep-ex]].
- [186] D. R. Tovey, *JHEP* **0804** (2008) 034 [arXiv:0802.2879 [hep-ph]].
- [187] G. Polesello and D. R. Tovey, *JHEP* **1003** (2010) 030 [arXiv:0910.0174 [hep-ph]].
- [188] G. Aad *et al.* [ATLAS Collaboration], *JHEP* **1405** (2014) 071 [arXiv:1403.5294 [hep-ex]].
- [189] M. Baak, G. J. Besjes, D. Cote, A. Koutsman, J. Lorenz and D. Short, arXiv:1410.1280 [hep-ex].
- [190] The ATLAS collaboration, ATLAS-CONF-2013-082, ATLAS-COM-CONF-2013-075.
- [191] G. Aad *et al.* [ATLAS Collaboration], *Phys. Lett. B* **726** (2013) 88 [Erratum-ibid. *B* **734** (2014) 406] [arXiv:1307.1427 [hep-ex]].
- [192] G. Aad *et al.* [ATLAS Collaboration], *Phys. Rev. D* **87** (2013) 5, 052002 [arXiv:1211.6312 [hep-ex]].
- [193] G. Aad *et al.* [ATLAS Collaboration], *Eur. Phys. J. C* **73**, no. 3, 2306 (2013) [arXiv:1210.6210 [hep-ex]].
- [194] The ATLAS collaboration, ATLAS-CONF-2014-004, ATLAS-COM-CONF-2014-003.
- [195] [ATLAS Collaboration], ATLAS-CONF-2012-123, ATLAS-COM-CONF-2012-139.
- [196] G. Cowan, K. Cranmer, E. Gross and O. Vitells, *Eur. Phys. J. C* **71** (2011) 1554 [Erratum-ibid. *C* **73** (2013) 2501] [arXiv:1007.1727 [physics.data-an]].
- [197] A. L. Read, *J. Phys. G* **28** (2002) 2693.

- [198] L3 Collaboration, B. Adeva *et al.*, Phys. Lett. **B 248** (1990) 203; L3 Collaboration, B. Adeva *et al.*, Phys. Lett. **B 252** (1990) 518; L3 Collaboration, B. Adeva *et al.*, Phys. Lett. **B 257** (1991) 450; L3 Collaboration, B. Adeva *et al.*, Phys. Lett. **B 283** (1992) 454; L3 Collaboration, B. Adeva *et al.*, Phys. Lett. **B 303** (1993) 391; L3 Collaboration, M. Acciarri *et al.*, Phys. Lett. **B 383** (1996) 487
- [199] L3 Collaboration, M. Acciarri *et al.*, Phys. Lett. **B 411** (1997) 373
- [200] L3 Collaboration, M. Acciarri *et al.*, Phys. Lett. **B 431** (1998) 437
- [201] L3 Collaboration, M. Acciarri *et al.*, Phys. Lett. **B 461** (1999) 376
- [202] L3 Collaboration, M. Acciarri *et al.*, Phys. Lett. **B 508** (2001) 225
- [203] L3 Collaboration, M. Acciarri *et al.*, Phys. Lett. **B 495** (2000) 18
- [204] L3 Collaboration, M. Acciarri *et al.*, Eur. Phys. J. **C16** (2000) 1
- [205] ALEPH Collaboration, R. Barate *et al.*, Phys. Lett. **B 499** (2001) 53
- [206] ALEPH Collaboration, R. Barate *et al.*, Phys. Lett. **B 495** (2000) 1; DELPHI Collaboration, P. Abreu *et al.*, Phys. Lett. **B 499** (2001) 23; OPAL Collaboration, G. Abbiendi *et al.*, Phys. Lett. **B 499** (2001) 38
- [207] L3 Collaboration, B. Adeva *et al.*, Nucl. Inst. Meth. **A 289** (1990) 35; J. A. Bakken *et al.*, Nucl. Inst. Meth. **A 275** (1989) 81; O. Adriani *et al.*, Nucl. Inst. Meth. **A 302** (1991) 53; B. Adeva *et al.*, Nucl. Inst. Meth. **A 323** (1992) 109; K. Deiters *et al.*, Nucl. Inst. Meth. **A 323** (1992) 162; M. Chemarin *et al.*, Nucl. Inst. Meth. **A 349** (1994) 345; M. Acciarri *et al.*, Nucl. Inst. Meth. **A 351** (1994) 300; G. Basti *et al.*, Nucl. Inst. Meth. **A 374** (1996) 293; A. Adam *et al.*, Nucl. Inst. Meth. **A 383** (1996) 342; L3 Collaboration, O. Adriani *et al.*, Phys. Rep. **236** (1993) 1
- [208] P. Janot, “The HZHA generator”, in “Physics at LEP2”, CERN Report 96-01 (1996)
- [209] PYTHIA versions 5.722 and 6.1 are used.
T. Sjöstrand, Preprint CERN-TH/7112/93 (1993), revised August 1995; Comp. Phys. Comm. **82** (1994) 74; Preprint hep-ph/0001032 (2000)
- [210] KK2f version 4.13 is used;
S. Jadach, B.F.L. Ward and Z. Wąs, Comp. Phys. Comm. **130** (2000) 260
- [211] KORALW version 1.33 is used.
S. Jadach *et al.*, Comp. Phys. Comm. **94** (1996) 216;
S. Jadach *et al.*, Phys. Lett. **B 372** (1996) 289
- [212] PHOJET version 1.05 is used.
R. Engel, Z. Phys. **C 66** (1995) 203;
R. Engel and J. Ranft, Phys. Rev. **D 54** (1996) 4244
- [213] F.A. Berends, R. Kleiss and R. Pittau, Comp. Phys. Comm. **85** (1995) 437

- [214] GEANT Version 3.15 is used,
R. Brun *et al.*, Preprint CERN-DD/EE/84-1 (1984), revised 1985
- [215] H. Fesefeldt, Preprint PITHA 85/02, RWTH Aachen (1985)
- [216] LEP Working Group for Higgs Boson Searches and ALEPH, DELPHI, L3, OPAL Collaborations, "Searches for Higgs bosons: preliminary combined results using LEP data collected at energies up to 202 GeV", Preprint CERN-EP/2000-55 (2000)
- [217] S. Catani *et al.*, Phys. Lett. **B 269** (1991) 432; S. Bethke *et al.*, Nucl. Phys. **B 370** (1992) 310
- [218] K. Griest and H.E. Haber, Phys. Rev. **D 37** (1998) 719; A. Djouadi *et al.* Phys. Lett. **B 376** (1996) 220.
- [219] L3 Collab., B. Adeva *et al.*, Nucl. Instr. Meth. **A 289** (1990) 35; J.A. Bakken *et al.*, Nucl. Instr. Meth. **A 275** (1989) 81; O. Adriani *et al.*, Nucl. Instr. Meth. **A 302** (1991) 53; B. Adeva *et al.*, Nucl. Instr. Meth. **A 323** (1992) 109; K. Deiters *et al.*, Nucl. Instr. Meth. **A 323** (1992) 162; M. Chemarin *et al.*, Nucl. Instr. Meth. **A 349** (1994) 345; M. Acciarri *et al.*, Nucl. Instr. Meth. **A 351** (1994) 300; G. Basti *et al.*, Nucl. Instr. Meth. **A 374** (1996) 293; A. Adam *et al.*, Nucl. Instr. Meth. **A 383** (1996) 342.
- [220] L3 Collab., M. Acciarri *et al.*, Phys. Lett. **B 418** (1997) 389.
- [221] ALEPH Coll., R. Barate *et al.*, Phys. Lett. **B 450** (1999) 301; DELPHI Collab., P. Abreu *et al.*, Phys. Lett. **B 459** (1999) 367; OPAL Collab., G. Abbiendi *et al.*, Eur. Phys. J. **C 7** (1999) 407.
- [222] T. Sjöstrand, preprint CERN-TH/7112/93 (1993), revised August 1995; T. Sjöstrand, Comp. Phys. Comm. **82** (1994) 74.
- [223] M. Skrzypek *et al.*, Comp. Phys. Comm. **94** (1996) 216; M. Skrzypek *et al.*, Phys. Lett. **B 372** (1996) 289.
- [224] S. Jadach, B.F.L. Ward, Z. Wąs, Comp. Phys. Comm. **79** (1994) 503.
- [225] R. Engel, Z. Phys. **C 66** (1995) 203; R. Engel, J. Ranft and S. Roesler, Phys. Rev. **D 52** (1995) 1459.
- [226] F.A. Berends, P.H. Daverfeldt, R. Kleiss, Nucl. Phys. **B 253** (1985) 441.
- [227] S. Jadach, W. Placzek, B.F.L. Ward, Phys. Rev. **D 40** (1989) 3582; Comp. Phys. Comm. **70** (1992) 305; Phys. Lett. **B 390** (1997) 298.
- [228] F.A. Berends, R. Kleiss and R. Pittau, Comp. Phys. Comm. **85** (1995) 447.
- [229] R. Brun *et al.*, preprint CERN DD/EE/84-1 (Revised 1987).
- [230] H. Fesefeldt, RWTH Aachen Report PITHA 85/02 (1985).
- [231] S. Catani *et al.*, Phys. Lett. **B 269** (1991) 432; S. Bethke *et al.*, Nucl. Phys. **B 370** (1992) 310.

- [232] J.F. Grivaz and F. Le Diberder, preprint LAL-92-37 (1992).
- [233] A. Favara and M. Pieri, preprint hep-ex/9706016 (1997).
- [234] P. Janot, “The HZHA generator”, in “Physics at LEP2”, Eds. G. Altarelli, T. Sjöstrand and F. Zwirner, CERN 96-01 (1996) Vol.2, 309.
- [235] V. M. Abazov *et al.* [D0 Collaboration], Phys. Lett. B **660** (2008) 449 [arXiv:0712.3805 [hep-ex]].
- [236] T. Millet, FERMILAB-THESIS-2007-22, LYCEN-T-2007-09.
- [237] A. D. Martin, W. J. Stirling, R. S. Thorne and G. Watt, Eur. Phys. J. C **63** (2009) 189 [arXiv:0901.0002 [hep-ph]].
- [238] A. Cafarella, C. Coriano and M. Guzzi, Nucl. Phys. B **748** (2006) 253 [hep-ph/0512358].
- [239] G. Aad *et al.* [ATLAS Collaboration], Phys. Lett. B **701** (2011) 31 [arXiv:1103.2929 [hep-ex]].
- [240] S. Chatrchyan *et al.* [CMS Collaboration], Phys. Rev. Lett. **109** (2012) 111806 [arXiv:1206.2598 [hep-ex]].
- [241] S. Chatrchyan *et al.* [CMS Collaboration], arXiv:1312.6283 [hep-ex].
- [242] The LHCb Collaboration [LHCb Collaboration], “Updated measurements of W and Z production at $\sqrt{s} = 7$ TeV with the LHCb experiment,” LHCb-CONF-2011-039.
- [243] [ATLAS Collaboration], ATLAS-CONF-2011-129.
- [244] L. Schoeffel, Nucl. Instrum. Meth. A **423** (1999) 439.
- [245] M. Botje, Comput. Phys. Commun. **182** (2011) 490 [arXiv:1005.1481 [hep-ph]].
- [246] A. Djouadi *et al.* [MSSM Working Group Collaboration], hep-ph/9901246.
- [247] S. Muanza, GDR SUSY Internal Note, May 2000. Unpublished.
http://susy.in2p3.fr/GDR-Notes/GDR_SUSY_PUBLIC/GDR-S-076.ps.
- [248] G. P. Lepage, CLNS-80/447.
- [249] J. Alwall, P. Schuster and N. Toro, Phys. Rev. D **79** (2009) 075020 [arXiv:0810.3921 [hep-ph]].
- [250] B. Fuks, M. Klasen, D. R. Lamprea and M. Rothering, Eur. Phys. J. C **73** (2013) 2480 [arXiv:1304.0790 [hep-ph]].
- [251] C. Anastasiou, K. Melnikov and F. Petriello, “Fully differential Higgs boson production and the di-photon signal through next-to-next-to-leading order,” Nucl. Phys. B **724** (2005) 197 [arXiv:hep-ph/0501130].
- [252] S. Catani, L. Cieri, G. Ferrera, D. de Florian and M. Grazzini, “Vector boson production at hadron colliders: a fully exclusive QCD calculation at NNLO,” Phys. Rev. Lett. **103** (2009) 082001 [arXiv:0903.2120 [hep-ph]].

- [253] J. Pumplin, D. R. Stump, J. Huston, H. L. Lai, P. M. Nadolsky and W. K. Tung, JHEP **0207** (2002) 012 [hep-ph/0201195].
- [254] P. M. Nadolsky, H. L. Lai, Q. H. Cao, J. Huston, J. Pumplin, D. Stump, W. K. Tung and C.-P. Yuan, Phys. Rev. D **78** (2008) 013004 [arXiv:0802.0007 [hep-ph]].
- [255] A. Sherstnev and R. S. Thorne, Eur. Phys. J. C **55** (2008) 553 [arXiv:0711.2473 [hep-ph]].
- [256] A. D. Martin, R. G. Roberts, W. J. Stirling and R. S. Thorne, Phys. Lett. B **604** (2004) 61 [hep-ph/0410230].
- [257] T. Sjostrand, S. Mrenna and P. Z. Skands, “PYTHIA 6.4 Physics and Manual,” JHEP **0605** (2006) 026 [arXiv:hep-ph/0603175].
- [258] A.D. Martin, W.J. Stirling, R.S. Thorne, G. Watt, “Parton distributions for the LHC,” Eur. Phys. J. C63 (2009) 189-285.
- [259] J. M. Campbell, J. W. Huston and W. J. Stirling, “Hard Interactions of Quarks and Gluons: A Primer for LHC Physics,” Rept. Prog. Phys. **70** (2007) 89 [arXiv:hep-ph/0611148].
- [260] M. R. Whalley, D. Bourilkov and R. C. Group, hep-ph/0508110.
- [261] G. Miu and T. Sjostrand, Phys. Lett. B **449** (1999) 313 [arXiv:hep-ph/9812455].
- [262] C. Balazs, J. Huston and I. Puljak, Phys. Rev. D **63** (2001) 014021 [arXiv:hep-ph/0002032].
- [263] G. Aad *et al.* [ATLAS Collaboration], arXiv:1103.1816 [hep-ex].
- [264] A. Sherstnev and R. S. Thorne, Eur. Phys. J. C **55**, 553 (2008) [arXiv:0711.2473 [hep-ph]].
- [265] K. Nakamura *et al.* [Particle Data Group], J. Phys. G **37** (2010) 075021.
- [266] S. Ovnyn, X. Rouby and V. Lemaitre, arXiv:0903.2225 [hep-ph].
- [267] M. Dobbs, J. B. Hansen, Comput. Phys. Commun. **134** (2001) 41-46.
- [268] T. Schörner-Sadenius and S. Tapprogge, ATL-DAQ-2003-004.
- [269] M. Cacciari, G. P. Salam and G. Soyez, JHEP **0804** (2008) 063 [arXiv:0802.1189 [hep-ph]].
- [270] J. M. Campbell and R. K. Ellis, Phys. Rev. D **60** (1999) 113006 [arXiv:hep-ph/9905386].
- [271] J. M. Campbell and R. K. Ellis, Phys. Rev. D **62** (2000) 114012 [arXiv:hep-ph/0006304].
- [272] J. M. Campbell and R. K. Ellis, Phys. Rev. D **65** (2002) 113007 [arXiv:hep-ph/0202176].
- [273] W. Beenakker, M. Klasen, M. Kramer, T. Plehn, M. Spira and P. M. Zerwas, Phys. Rev. Lett. **83** (1999) 3780 [Erratum-ibid. **100** (2008) 029901] [arXiv:hep-ph/9906298].
- [274] W. Beenakker, M. Kramer, T. Plehn, M. Spira and P. M. Zerwas, Nucl. Phys. B **515** (1998) 3 [arXiv:hep-ph/9710451].
- [275] W. Beenakker, R. Hopker, M. Spira and P. M. Zerwas, Nucl. Phys. B **492** (1997) 51 [arXiv:hep-ph/9610490].

- [276] M. Spira, arXiv:hep-ph/0211145.
- [277] T. Plehn, Czech. J. Phys. **55** (2005) B213 [arXiv:hep-ph/0410063].
- [278] S. Gieseke *et al.*, arXiv:1102.1672 [hep-ph].
- [279] <http://cc.in2p3.fr/docenligne/13/en>
- [280] J. Ohnemus, Phys. Rev. D **47**, 940 (1993).
- [281] R. Hamberg, W. L. van Neerven and T. Matsuura, Nucl. Phys. B **359** (1991) 343 [Erratum-
ibid. B **644** (2002) 403].
- [282] J. M. Campbell, R. Frederix, F. Maltoni and F. Tramontano, Phys. Rev. Lett. **102** (2009) 182003 [arXiv:0903.0005 [hep-ph]].
- [283] J. M. Campbell, R. K. Ellis and F. Tramontano, Phys. Rev. D **70** (2004) 094012 [arXiv:hep-ph/0408158].
- [284] R. Gavin, Y. Li, F. Petriello and S. Quackenbush, arXiv:1011.3540 [hep-ph].
- [285] S. Chatrchyan *et al.* [CMS Collaboration], Phys. Rev. Lett. **109** (2012) 111806 [arXiv:1206.2598 [hep-ex]].
- [286] S. Chatrchyan *et al.* [CMS Collaboration], arXiv:1312.6283 [hep-ex].
- [287] S. Chatrchyan *et al.* [CMS Collaboration], JHEP **1110** (2011) 132 [arXiv:1107.4789 [hep-ex]].
- [288] Delphes ticket submitted and solved by S. Muanza,
<https://cp3.irmp.ucl.ac.be/projects/delphes/ticket/44>
- [289] M.L. Mangano,
<http://mlm.web.cern.ch/mlm/talks/lund-alpgen.pdf>
- [290] M.L. Mangano, M. Moretti, F. Piccinini and M. Treccani, JHEP **0701** (2007) 013 [hep-ph/0611129].
- [291] K. Cranmer, Statistical Problems in Particle Physics, Astrophysics and CosmoLogy, Conf. Proc. (2006) 112
- [292] RooStats Tutorial, K. Cranmer (2009)
http://root.cern.ch/root/html/tutorials/roostats/rs_numbercountingutils.C.html
- [293] G. Aad *et al.* [ATLAS Collaboration], Eur. Phys. J. C **72** (2012) 2173 [arXiv:1208.1390 [hep-ex]].
- [294] G. Aad *et al.* [ATLAS Collaboration], ATLAS-CONF-2013-021.
- [295] G. Polesello and D. R. Tovey, JHEP **1003** (2010) 030 [arXiv:0910.0174 [hep-ph]].
- [296] D. R. Tovey, <http://projects.hepforge.org/mctlib>.
- [297] H. Baer, C. h. Chen, F. Paige and X. Tata, Phys. Rev. D **50** (1994) 4508 [hep-ph/9404212].

- [298] T. Aaltonen *et al.* [CDF Collaboration], Phys. Rev. D **83** (2011) 112003 [arXiv:1101.0034 [hep-ex]].
- [299] V. M. Abazov *et al.* [D0 Collaboration], Phys. Rev. D **84** (2011) 112005 [arXiv:1107.4995 [hep-ex]].
- [300] S. Knapen, Y. Zhao and M. J. Strassler, Phys. Rev. D **86** (2012) 014013 [arXiv:1111.5857 [hep-ph]].
- [301] S. Chatrchyan *et al.* [CMS Collaboration], Phys. Lett. B **717** (2012) 351 [arXiv:1206.3921 [hep-ex]].
- [302] N. Craig, C. Kilic and M. J. Strassler, Phys. Rev. D **84** (2011) 035012 [arXiv:1103.2127 [hep-ph]].
- [303] G. Aad *et al.* [ATLAS Collaboration], JHEP **1402** (2014) 107 [arXiv:1311.6724 [hep-ex]].
- [304] S. Chatrchyan *et al.* [CMS Collaboration], JHEP **1404** (2014) 191 [arXiv:1402.3803 [hep-ex]].
- [305] A. J. Barr, Phys. Lett. B **596** (2004) 205 [hep-ph/0405052].
- [306] J. M. Smillie and B. R. Webber, JHEP **0510** (2005) 069 [hep-ph/0507170].
- [307] T. Appelquist, H. C. Cheng and B. A. Dobrescu, Phys. Rev. D **64** (2001) 035002 [hep-ph/0012100].
- [308] S. Muanza, PhD Thesis
"La recherche des charginos et des neutralinos avec le détecteurs ATLAS au LHC"
http://tel.archives-ouvertes.fr/index.php?halsid=5ihrpla1httj8ucodalupjt465&view_this_doc=tel-00011022&version=1
- [309] S. Muanza [ATLAS Collaboration],
"The Search For Charginos And Neutralinos With Atlas Detector At LHC,"
<http://www.slac.stanford.edu/spires/find/hep/www?irn=4978030>
*Prepared for 31st Rencontres de Moriond:
QCD and High-Energy Hadronic Interactions, Les Arcs, France, 23-30 Mar. 1996*
- [310] S. Muanza,
"The search for chargino-neutralino pairs with the ATLAS detector at the LHC,"
<http://www.slac.stanford.edu/spires/find/hep/www?irn=3989631>
*3rd International Workshop on Diquarks and other Models of Compositeness (DIQUARKS III),
Turin, Italy, 28-30 Oct. 1996*
- [311] A. Gomes *et al.* [RD34 Collaboration],
*Prepared for Workshop on Scintillating Fiber Detectors (SCIFI 93),
Notre Dame, IN, 24-28 Oct. 1993*
- [312] Z. Ajaltouni *et al.*, Nucl. Instrum. Meth. A **388** (1997) 64.
- [313] S. Agnvall *et al.* [ATLAS Collaboration], Nucl. Instrum. Meth. A **403** (1998) 98.

- [314] S. Akhmadalev *et al.* [ATLAS Collaboration], Nucl. Instrum. Meth. A **480** (2002) 508 [arXiv:hep-ex/0104002].
- [315] V. Chorowicz, J. F. Clergeau, D. Contardo, R. Haroutunian, L. Mirabito, S. Muanza and G. Smadja, Nucl. Instrum. Meth. A **401** (1997) 238.
- [316] V. Chorowicz, J. F. Clergeau, D. Contardo, R. Haroutunian, L. Mirabito, S. Muanza and G. Smadja, Nucl. Instrum. Meth. A **419** (1998) 464.
- [317] S. Chatrchyan *et al.* [CMS Collaboration], JINST **3** (2008) S08004.
- [318] M. Acciarri *et al.* [L3 Collaboration], Phys. Lett. B **485** (2000) 85 [arXiv:hep-ex/0004006].
- [319] P. Achard *et al.* [L3 Collaboration], Phys. Lett. B **609** (2005) 35 [arXiv:hep-ex/0501033].
- [320] M. Acciarri *et al.* [L3 Collaboration], Phys. Lett. B **461** (1999) 376 [arXiv:hep-ex/9909004].
- [321] M. Acciarri *et al.* [L3 Collaboration], Phys. Lett. B **508** (2001) 225 [arXiv:hep-ex/0012019].
- [322] M. Acciarri *et al.* [L3 Collaboration], Phys. Lett. B **495** (2000) 18 [arXiv:hep-ex/0011043].
- [323] P. Achard *et al.* [L3 Collaboration], Phys. Lett. B **517** (2001) 319 [arXiv:hep-ex/0107054].
- [324] R. Barate *et al.* [LEP Working Group for Higgs boson searches and ALEPH Collaboration and and], Phys. Lett. B **565** (2003) 61 [arXiv:hep-ex/0306033].
- [325] M. Acciarri *et al.* [L3 Collaboration], Phys. Lett. B **471** (1999) 321 [arXiv:hep-ex/9910053].
- [326] M. Acciarri *et al.* [L3 Collaboration], Phys. Lett. B **503** (2001) 21 [arXiv:hep-ex/0012017].
- [327] P. Achard *et al.* [L3 Collaboration], Phys. Lett. B **545** (2002) 30 [arXiv:hep-ex/0208042].
- [328] S. Schael *et al.* [ALEPH Collaboration and DELPHI Collaboration and L3 Collaboration and], Eur. Phys. J. C **47** (2006) 547 [arXiv:hep-ex/0602042].
- [329] P. Achard *et al.* [L3 Collaboration], Phys. Lett. B **583** (2004) 14 [arXiv:hep-ex/0402003].
- [330] U. Bassler et S. Muanza,
http://d0-france.in2p3.fr/WORKING_GROUPS/CALORIMETRY/CALO_CAL_OFF/calocaloff.html
- [331] D0 Jet Energy Scale Group,
http://www-d0.fnal.gov/phys_id/jes/public_RunIIa/
- [332] F. Canelli, J. Coss, A. Goussiou, I. Iashvili, B. Kehoe, A. Kupco, S. Muanza, V. O'Dell, N. Parua, M. Petteni, A. Schwartzman
D0 Note 4110, "First Jet Energy Scale at D0 in Run II (for p10 Data and Monte Carlo)", 30 september 2002

- [333] J. Coss, A. Goussiou, I. Iashvili, S. Muanza, V. O'Dell, N. Parua, P. Perea, A. Schwartzman
D0 Note 4112, "Jet Energy Scale for p11 Data", 31 october 2002
- [334] J. Coss, S. Fatakia, A. Goussiou, U. Heintz, I. Iashvili, M. Kopal,
A. Kupco, S. Muanza, V. O'Dell, N. Parua, P. Perea
D0 Note 4115, "Jet Energy Scale and Resolution for p13 Data and Monte Carlo", 3 march
2003
- [335] C. Biscarat, D0 Note 4939,
"A package for ALPGEN MC event generation", 8 october 2005
C. Biscarat,
[http://cdcv0.fnal.gov/cgi-bin/public-cvs/cvswweb-public.cgi/cardfiles/common_alpgen_proposal/
tools/?cvsroot=d0cvs&hideattic=0#dirlist](http://cdcv0.fnal.gov/cgi-bin/public-cvs/cvswweb-public.cgi/cardfiles/common_alpgen_proposal/tools/?cvsroot=d0cvs&hideattic=0#dirlist)
http://www-clued0.fnal.gov/lancs/biscarat/common_alpgen_feb04/
- [336] G. Grenier, D0 Note 5148, "Integration of ALPGEN in the D0 software environment", 21
june 2006
G. Grenier, D0 Note 5589, "ALPGEN cross section in FOME metadata", 8 february 2008
- [337] S. Muanza,
http://www-d0.fnal.gov/computing/MonteCarlo/generators/FOME_MD.html
- [338] S. Muanza,
<http://www-d0.fnal.gov/computing/MonteCarlo/generators/enstore.html>
S. Mrenna,
http://home.fnal.gov/~mrenna/ME-PS_Matching.html
http://home.fnal.gov/~mrenna/Matched_Dataset_Description.html
- [339] S. Muanza,
<http://www-d0.fnal.gov/computing/MonteCarlo/MonteCarlo.html>
- [340] <http://www-d0.fnal.gov/computing/sam/>
- [341] <http://www-clued0.fnal.gov/runjob/>
- [342] <http://cdcv0.fnal.gov/cgi-bin/public-cvs/cvswweb-public.cgi/cardfiles/?cvsroot=d0cvs>
- [343] S. Muanza,
http://www-d0.fnal.gov/computing/MonteCarlo/generator_tools/cardfiles_doc.html
http://www-d0.fnal.gov/computing/MonteCarlo/generators/fome_cardfiles.html
- [344] http://cdcv0.fnal.gov/cgi-bin/public-cvs/cvswweb-public.cgi/mcpp_gen/?cvsroot=d0cvs
- [345] S. Muanza,
http://www-d0.fnal.gov/computing/MonteCarlo/generator_tools/tauola.html
- [346] S. Muanza,
http://www-d0.fnal.gov/computing/MonteCarlo/generator_tools/evtgen.html
- [347] S. Muanza,
http://www-d0.fnal.gov/computing/MonteCarlo/generators/pythia6203_HF-hadrons.html

- [348] <http://www-d0.fnal.gov/computing/releases/changes/p14.07.00.changes>
- [349] R. Field,
http://www.phys.ufl.edu/~rfield/cdf/D0_9-6-02.pdf
- [350] S. Muanza,
http://www-d0.fnal.gov/computing/MonteCarlo/generator_tools/pdfflib.html
- [351] S. Muanza, D0 Note 5300, "A Compilation of MCFM v5.1 Cross Sections", 4 december 2006
- [352] http://www-d0.fnal.gov/computing/MonteCarlo/generator_tools/common_samples/cs_mc.html
- [353] C. Biscarat, S. Muanza,
http://d0-france.in2p3.fr/WORKING_GROUPS/MONTECARLO/Catalog/current/
- [354] S. Muanza,
http://www-clued0.fnal.gov/~muanza/REILM/Running_Instructions.html
- [355] S. Alioli, P. Nason, C. Oleari and E. Re, JHEP **1006** (2010) 043 [arXiv:1002.2581 [hep-ph]].
- [356] S. Frixione and B. R. Webber, arXiv:hep-ph/0207182.
- [357] T. Sjostrand, S. Mrenna and P. Z. Skands, JHEP **0605** (2006) 026 [arXiv:hep-ph/0603175].
- [358] ATLAS Collaboration, ATLAS-CONF-2011-057,
"Measurement of the b-jet production cross section using muons in jets with ATLAS in pp collisions at $\sqrt{s} = 7$ TeV"
- [359] E. Lòpez Mateos, E.W. Hughes, A. Schwartzmann,
"Jet Energy Scale Correction to Semileptonic b-jets from Missing Neutrino Energy",
ATL-PHYS-INT-2008-047, ATL-COM-PHYS-2008-86
- [360] S. Gieseke *et al.*, arXiv:1102.1672 [hep-ph].
- [361] R. K. Ellis and S. Veseli, Phys. Rev. D **60** (1999) 011501 [hep-ph/9810489].
- [362] H. Baer, F. E. Paige, S. D. Protopopescu and X. Tata, arXiv:hep-ph/9305342.
- [363] S. Mrenna,
<http://home.fnal.gov/~mrenna/spythia.html>
S. Muanza,
http://www-d0.fnal.gov/computing/MonteCarlo/generator_tools/pyfris.html
- [364] S. Muanza,
http://www-d0.fnal.gov/computing/MonteCarlo/generator_tools/pyfris.html
T. Millet,
http://www-clued0.fnal.gov/~millet/susy_scans/index.php
- [365] W. Beenakker, R. Hopker and M. Spira, arXiv:hep-ph/9611232.
- [366] S. Muanza,
http://www-d0.fnal.gov/computing/MonteCarlo/generator_tools/prospino.html
<http://cdcvs0.fnal.gov/cgi-bin/public-cvs/cvsweb-public.cgi/PROSPINO/?cvsroot=d0cvs>

- [367] M. Muhlleitner, A. Djouadi and Y. Mambrini, *Comput. Phys. Commun.* **168** (2005) 46 [arXiv:hep-ph/0311167].
- [368] M. Muhlleitner, *Acta Phys. Polon. B* **35** (2004) 2753 [arXiv:hep-ph/0409200].
- [369] U. Ellwanger, J. F. Gunion and C. Hugonie, *JHEP* **0502** (2005) 066 [arXiv:hep-ph/0406215].
- [370] U. Ellwanger and C. Hugonie, *Comput. Phys. Commun.* **175** (2006) 290 [arXiv:hep-ph/0508022].
- [371] A. Djouadi, J. L. Kneur and G. Moultaka, *Comput. Phys. Commun.* **176** (2007) 426 [arXiv:hep-ph/0211331].
- [372] S. Muanza,
http://cdcvcs0.fnal.gov/cgi-bin/public-cvs/cvswweb-public.cgi/susy_tools/?cvsroot=d0cvs
http://www-d0.fnal.gov/computing/MonteCarlo/generator_tools/susy_tools.html
- [373] Stage de ME de S. Argyropoulos
ENS Lyon, 2010
http://www.ens-lyon.fr/DSM/SDMsite/M2/stages_M2/Argyropoulos.pdf
- [374] P. Z. Skands *et al.*, *JHEP* **0407** (2004) 036 [arXiv:hep-ph/0311123].
- [375] M. Cacciari, M. Greco and P. Nason, *JHEP* **9805** (1998) 007 [arXiv:hep-ph/9803400].
- [376] M. Cacciari, S. Frixione and P. Nason, *JHEP* **0103** (2001) 006 [arXiv:hep-ph/0102134].
- [377] D. Teyssier,
<http://tel.archives-ouvertes.fr/tel-00001929/fr/>
- [378] J. Coss,
<http://tel.archives-ouvertes.fr/tel-00008636/fr/>
- [379] T. Millet,
<http://tel.archives-ouvertes.fr/tel-00175297/fr/>
- [380] http://www.ens-lyon.fr/DSM/SDMsite/M2/stages_M2/Stages2007.htm
- [381] http://www.ens-lyon.fr/DSM/SDMsite/M2/stages_M2/Stages2010.html
- [382] <http://moriond.in2p3.fr/QCD/2002/indext.html>
- [383] <http://www.pa.msu.edu/hcp2004/program.html>
- [384] <http://moriond.in2p3.fr/QCD/2007/MorQCD07Prog.html>
- [385] <http://www.fesb.hr/physicslh/>
- [386] <http://events.saip.org.za/kruger2010/index.html>
- [387] B. Laforge, M. Mullheitner, S. Muanza,
<http://lyoinfo.in2p3.fr/gdrsusy05/>
- [388] <http://indico.in2p3.fr/conferenceDisplay.py?confId=5701>

- [389] <http://www.phy.bnl.gov/~partsem/01-02.html>
- [390] http://www.cafe-de-la-cloche.org/index.php?option=com_content&view=article&id=381:bientot-lacceleateur-de-particule-geant-du-ern-le-big-bang-en-eprouvette-&catid=98:cafe-science-archives&Itemid=98
- [391] <http://cafesciences.avignon.free.fr/>
http://cafesciences-avignon.fr/index.php?option=com_content&view=article&id=872:le-lhc-du-ern-arme-ultime-&catid=72:archives-2010-2011&Itemid=58
- [392] S. Muanza,
<http://indico.in2p3.fr/conferenceDisplay.py?confId=5143>
- [393] <https://indico.nbi.ku.dk/conferenceTimeTable.py?confId=124#20100414>
- [394] <http://l3.web.cern.ch/l3/conferences/talks99.html>
- [395] <http://l3.web.cern.ch/l3/conferences/talks2000.html>
- [396] <http://lamwvs.oamp.fr/cosmowiki/CosmoRetreat>
- [397] <http://indico.in2p3.fr/conferenceDisplay.py?confId=4228>
- [398] <http://indico.in2p3.fr/conferenceDisplay.py?confId=4451>
- [399] S. Muanza et al.,
<http://cern.ch/AfricanSchoolofPhysics>
- [400] S. Muanza et al.,
<http://indico.cern.ch/conferenceDisplay.py?confId=78565>
- [401] S. Muanza,
<http://indico.cern.ch/conferenceTimeTable.py?confId=78565#20100811.detailed>
- [402] C. Darve, J. Ellis, S. Muanza,
<http://indico.cern.ch/materialDisplay.py?contribId=135&sessionId=13&materialId=slides&confId=78565>
- [403] <http://susy.in2p3.fr/GDR-old/index.html>
- [404] <http://susy.in2p3.fr/GDR-2003/EuroGDR/General/index.html>
- [405] <http://susy.in2p3.fr/GDR-2005/Actualites/index.html>
- [406] <http://terascale.in2p3.fr/>
- [407] M.-B. Causse et S. Muanza,
"Certaines règles de Feynman pour l'extension Supersymétrique Minimale du Modèle Standard dans la jauge de T'Hooft-Feynman", 22 juillet 1999 http://susy.in2p3.fr/GDR-Notes/GDR_SUSY_PUBLIC/GDR-S-020.ps
- [408] S. Muanza,
"Using charge asymmetry in the search for chargino-neutralino pairs at the LHC - Introducing the new observable -", 18 mai 2000 http://susy.in2p3.fr/GDR-Notes/GDR_SUSY_PUBLIC/GDR-S-076.ps

- [409] http://www-clued0.fnal.gov/~muanza/SUSY_Tools_Group.html
- [410] http://www-clued0.fnal.gov/~muanza/Blind_SUSY_Analysis.html
- [411] <http://phystev.in2p3.fr/Houches2005/>
- [412] <http://phystev.in2p3.fr/Houches2005/wg.html#BSM>
- [413] B. C. Allanach, C. Grojean, P. Z. Skands, E. Accomando, G. Azuelos, H. Baer, C. Balazs and G. Belanger *et al.*, hep-ph/0602198.
- [414] <http://phystev.in2p3.fr/Houches2007/>
- [415] M. M. Nojiri, T. Plehn, G. Polesello, J. M. Alexander, B. C. Allanach, A. J. Barr, K. Benakli and F. Boudjema *et al.*, arXiv:0802.3672 [hep-ph].
- [416] R. Brun and F. Rademakers, Nucl. Instrum. Meth. A **389** (1997) 81.
- [417] A. Djouadi *et al.* [MSSM Working Group], arXiv:hep-ph/9901246.
- [418] S. Muanza, <http://indico.in2p3.fr/conferenceDisplay.py?confId=5983>
- [419] S. Muanza,
<http://agenda.albanova.se/contributionDisplay.py?contribId=271&sessionId=262&confId=3239>
- [420] S. Muanza,
Slides: <https://cds.cern.ch/record/1700090>
Proceedings: http://pos.sissa.it/archive/conferences/203/111/DIS2014_111.pdf
- [421] S. Muanza, http://marseille.catholique.fr/IMG/lettre/lettre_20121115_ece62_fr.html
- [422] G. Aad *et al.* [ATLAS Collaboration],
JHEP **1405** (2014) 071 [arXiv:1403.5294 [hep-ex]].
- [423] The ATLAS collaboration, ATLAS-CONF-2013-093, ATLAS-COM-CONF-2013-102.
- [424] B. Butler *et al.*,
ATLAS Internal Note, ATLAS-COM-PHYS-2013-1640.
- [425] The ATLAS collaboration, ATLAS-CONF-2014-062, ATLAS-COM-CONF-2014-086.
- [426] ATLAS-COM-PHYS-2013-1640, ATLAS-CONF-2014-062
Paper combining three different search channels currently in preparation.
- [427] <http://www.sainte-trinite.fr/blogist/index.php?post/2014/INFO-CONFERENCE>
- [428] G. S. Muanza and T. Serre, “A New Method for Indirect Mass Measurements using the Integral Charge Asymmetry at the LHC,” arXiv:1412.6695 [hep-ph].
- [429] <https://indico.in2p3.fr/event/6838/>
- [430] <http://mlm.web.cern.ch/mlm/alpgen/update4.html>
http://www-d0.fnal.gov/computing/MonteCarlo/generator_tools/mc_requests/11306-dir/11306-comments.txt

-
- [431] J. Coss, LYCEN-T-2003-48.
- [432] T. Aaltonen *et al.* [CDF Collaboration], Phys. Rev. D **83** (2011) 112003 [arXiv:1101.0034 [hep-ex]].
- [433] V. M. Abazov *et al.* [D0 Collaboration], Phys. Rev. D **84** (2011) 112005 [arXiv:1107.4995 [hep-ex]].
- [434] S. Knapen, Y. Zhao and M. J. Strassler, Phys. Rev. D **86** (2012) 014013 [arXiv:1111.5857 [hep-ph]].
- [435] S. Chatrchyan *et al.* [CMS Collaboration], Phys. Lett. B **717** (2012) 351 [arXiv:1206.3921 [hep-ex]].
- [436] N. Craig, C. Kilic and M. J. Strassler, Phys. Rev. D **84** (2011) 035012 [arXiv:1103.2127 [hep-ph]].
- [437] G. Aad *et al.* [ATLAS Collaboration], JHEP **1402** (2014) 107 [arXiv:1311.6724 [hep-ex]].
- [438] S. Chatrchyan *et al.* [CMS Collaboration], JHEP **1404** (2014) 191 [arXiv:1402.3803 [hep-ex]].
- [439] A. J. Barr, Phys. Lett. B **596** (2004) 205 [hep-ph/0405052].
- [440] J. M. Smillie and B. R. Webber, JHEP **0510** (2005) 069 [hep-ph/0507170].
- [441] T. Appelquist, H. C. Cheng and B. A. Dobrescu, Phys. Rev. D **64** (2001) 035002 [hep-ph/0012100].
- [442] G. Aad *et al.* [ATLAS Collaboration], arXiv:1501.07110 [hep-ex].
- [443] J. Gao *et al.*, Phys. Rev. D **89** (2014) 3, 033009 [arXiv:1302.6246 [hep-ph]].
- [444] [ATLAS Collaboration], ATLAS-CONF-2011-102.
- [445] M. Oreglia, SLAC Stanford - SLAC-236 (80,REC.APR. 81) 226p